The University Of Sheffield.

Constrained Aerodynamic Adjoint Optimisation of Supersonic Manoeuvre Wings.

Thomas Pratt, MSc

Supervised by Professor Ning Qin

Department of Mechanical Engineering
University of Sheffield

This thesis is submitted to the University of Sheffield in partial fulfillment of the requirement for the degree of Doctor of Philosophy (PhD)

January 2020

Abstract

Supersonic manoeuvring aircraft are designed to be efficient during aerobatic or high-load flight conditions at supersonic speeds, but are also usually required to also be efficient at other flight conditions. For example, transonic and subsonic cruising and manoeuvring. Aerodynamic flow around wings at supersonic manoeuvring flight conditions can exhibit a complex variety of structures and patterns, presenting a unique challenge for aerodynamic design methods. This work aims to seek an understanding of the effect of these complex flow features on aerodynamic efficiency as well as develop optimisation methods to help find the most efficient geometries which balance these flow features to their benefit.

A lift-constrained adjoint optimisation strategy for supersonic manoeuvring wings has been presented and used to produce a minimum pressure-drag conical camber design for a 57 degree delta wing. The computational efficiency of this strategy has been compared with a similar strategy for the same optimisation problem, and the resulting designs from each process have been interrogated. The optimised conical wing design has been evaluated using RANS analysis and compared with a wing designed using an analytical method and a wing with zero camber.

The lift-constrained adjoint optimisation strategy has been applied to the camber design of two supersonic manoeuvre wing concepts and the resulting minimum pressure drag designs have been evaluated and compared using RANS analysis. Supersonic and transonic pitching moment constraints were then included in the optimisation problem in a novel design methodology, in an attempt to minimise pitch trim requirements at two design points whilst improving efficiency at the supersonic manoeuvring condition. The resulting designs were then evaluated using RANS at both supersonic and transonic speeds and compared with the minimum pressure drag design examples. The most favourable wing design was found to exhibit novel and desirable flight characteristics across a range of flight conditions.

Acknowledgements

I would like to thank my academic supervisor Prof. Ning Qin for his support throughout this four-year PhD project. I also want to thank my industrial supervisor Dr Joe Coppin from DSTL for his guidance, technical insight and generosity in allowing me to extensively use DSTL HPC facilities. Dr Raj Nangia contributed to this project through frequent discussions which gave me inspiration and imparted detailed engineering knowledge, which I would like to thank him for. I wish to acknowledge Prof William Mason for inspiring and supportive words during brief correspondence at the beginning of this project.

I appreciate the enormous and continuous support of my parents, family and partner throughout this project and beyond, I could not have done it without them.

This project was funded by DSTL through an industrial scholarship.

Table of Contents

List of Figures

List of Tables

List of Symbols

α, AOA	Angle of incidence
ac, Xac	Aerodynamic centre, ac location
α_N	Flow incidence normal to the leading edge
Λ	Leading edge sweep angle
C, X/C	Chord, fraction of chord
CDp, CDf	Coefficients of pressure drag and friction drag
CL, CD, CMy, CFx	Coefficients of Lift, Drag, Pitching moment and Axial force
Cp	Coefficient of pressure
Csf	Coefficient of skin friction
DV	Design variable vector
E	Energy
ETA	Conical coordinate
F	Cell face fluxes
Fx, Fz	Axial and perpendicular forces

G	Constraint function
I	Objective function
I J K	Structured grid coordinates
K-factor	Induced drag factor
M, M_∞	Freestream mach number
M_N	Mach number normal to the leading edge
N/m, N/m²	Newtons per metre, Newtons per square metre
P	Pressure
Pr	Prandtl number
R(U)	Flow residual
Re, Re/m	Reynolds number, Reynolds number per metre
S	Surface shape
t	Time
τ	Shear stress
U	Flow variables
u v w	Velocity components
ν_t	Turbulent kinematic viscosity
x y z	Cartesian coordinates, always given in metres
Xcp	Centre of pressure location
Y+	Dimensionless wall distance
ρ	Density

List of Abbreviations

3D, 2D	3-Dimensional, 2-Dimensional
AR	Aspect ratio

CFD	Computational fluid dynamics
CFL	Courant-Freidrichs-Lewy condition
CPU	Central processing unit
DNS	Direct numerical simulation
DV	Design variable
FD	Finite differences
FFD	Free form deformation
GMRES	Generalised minimum residual method
HPC	High performance computing
HS, LS	High-speed, Low-speed
JST	Jameson-Schmidt-Turkel numerical scheme
LE	Leading edge
LERX	Leading edge root extension
LES	Large eddy simulation
MUSCL	Monotone upwind scheme for convection laws
NACA	National Advisory Committee for Aeronautics
NASA	National Aeronautics and Space Administration
PDE	Partial differential equation
RANS, URANS	Steady, unsteady Reynolds-averaged Navier-Stokes equations
SA	Spalart-Allmaras turbulence model
SLSQP	Sequential least-squares quadratic programming
SST	Shear-stress transformation turbulence model
SU2	Stanford unstructured 2 open-source code
T-Rex	Tetrahedral mesh extrusion method

Chapter 1 Introduction

This thesis will present a simplified optimisation strategy for adjoint-based aerodynamic shape design and test it using a simple conical wing design problem. Results of these optimisations will be compared with results from historical methods for the same design problem.
The simplified optimisation strategy will then be applied to some supersonic full 3D camber design concepts which are more similar to real aircraft wings, both with and without extra constraints on pitching moment, and the resulting designs will be analysed using high-fidelity CFD.
The test cases used in this project are part of a family of wings referred to as supersonic manoeuvre wings - a type of wing which is designed principally with the aim of efficiently producing large amounts of lift at supersonic speeds. This is because most aircraft manoeuvres (turning, climbing, aerobatics etc) require more lift than is produced by the wing in level flight.

1.1 Motivation

The use of computer codes for the design and optimisation of aircraft is by no means a new idea, having been developed over the last 30 years. However, the improvements in these methods have been relatively slow due to the limited nature of computers and high-performance-computing in this time. More recent improvements in computer power and CFD codes are allowing advances to be made in the field of CFD and automated design optimisation at an ever increasing rate. It is important, then, to establish the potential benefits and shortfalls of any emerging design methods, along with finding novel ways of maximising the benefit which can be attained by using this emerging technology.

1.2 Research Aim

The overall aim of this work is to present and evaluate strategies for the constrained aerodynamic adjoint optimisation of supersonic manoeuvre wings. Various methods of employing flow-based constraints will be evaluated using both validated test-cases and generalised 6th generation fighter jet wing concepts. The flow regimes featured in this study have not previously been evaluated using the adjoint method. This means that finding the most effective strategy for employing these adjoint gradients to design supersonic manoeuvre wings is of paramount importance to supersonic aircraft designers of the future.

1.3 Objectives

Objective 1: To determine the most effective and most efficient adjoint optimisation strategy for the conical camber inviscid drag minimisation problem.

This study compares two ways of posing the same optimisation problem. The first way involves the solution of both lift and drag gradients at each design step and the inclusion of angle of attack as an

optimisation design variable. This way, Lift will be conserved by all design variables during the design process. This strategy will be referred to hereafter as “hard constrained optimisation”.
In this manner of setting up the problem, design variable step length and direction are calculated using the SLSQP algorithm by D.Kraft (1988)[1].

The second way of posing the same design problem is to only solve for the drag gradient at each design step - requiring significantly less computational expense per design iteration. In order to ensure that the lift of the wing is still maintained throughout the whole design process, angle of attack is separated out from the design variables and instead is independently altered during each CFD flow simulation in order to guarantee that each flow solution is exactly at the design lift coefficient - regardless of the values of each of the shape design variables. Design variable step length and direction are also calculated using the SLSQP algorithm, however this method reduces to Newton’s method when no hard constraints are used.
This strategy will be referred to hereafter as “soft constrained optimisation”.

In order to compare these methods, this study explores how much computational effort is required in order to reach an optimum design - and if there is any difference in the optimum wing design found by each process.
It is hypothesized that if each process returns the same final design in the same number of design iterations, then the second method would be approximately 33% more efficient in terms of cost of design. This is due to the fact that the second method requires 1/3rd less expensive processes per design iteration than the first.

Objective 2: To optimise and determine the performance and characteristics of two supersonic wing concepts (trapezoidal and cranked wings).

Two wing concepts for a 6th generation supersonic stealth fighter jet have been optimised for minimum drag at CL = 0.25 and Mach number = 1.6. One wing is a trapezoidal planform with 50 degrees leading edge sweep, the other is a cranked wing with 50-75-50 degree leading edges. The aerofoil of both wings before optimisation is NACA 64A004, with thickness variations around the root to ensure surface smoothness. Their optimised design has been generated using the soft constrained adjoint-Euler method and corresponding flow features and performance have been compared using RANS solutions for a range of incidence angles and Mach numbers in order to determine their eligibility as concepts.

Objective 3: To determine the effects of various pitching moment constraints on the results of the supersonic trapezoidal and cranked wing adjoint optimisation process.

A new wing concept is presented which has been designed using the Euler-adjoint method. The objective function for the design of this wing is supersonic pressure drag, but constraints have been placed on both supersonic and transonic pitching moments using a combination of the fixed-CL and hard constraint methods.
The design process is presented and the resulting wing designs are analysed using RANS solutions in the same manner as the wings which are optimised for drag alone - providing a means of comparison for the designs. The pitch-constrained designs have been compared directly with the minimum drag wing designs created in objective 2.

1.4 Thesis Outline

This thesis begins with a statement of the motivation, aims and objectives of the research. There is then a review of literature relating to the physics of supersonic manoeuvre wings, design methods for these wings and numerical aerodynamic analysis and optimisation methods more generally.
Each component of the computational optimisation method is then presented and described; along with the algorithms which tie these components together.
In the results section, the optimisation problems are posed and their results are displayed, discussed, interrogated and analysed. The results of each optimisation are then summarised and conclusions are presented.

Chapter 2 Background and Literature Review

2.1 Background Overview

The design method used in this thesis uses adjoint sensitivity analysis and gradient based optimisation methods (as developed by Jameson *et al.* [2–11], Hicks and Henne[12] and Qin *et al.* [13–25] amongst many others) to exploit the design space efficiently for the purposes of lift constrained drag minimisation. Reuther *et al*.[26], Alonso *et al.* [27–29], Kim *et al.*[30], and Jameson *et al.* [31,32] have successfully applied the inviscid adjoint method to supersonic aerofoil, wing-body and transport aircraft optimisation at cruising CL values, including multi-objective sonic boom and drag reduction. The present study focuses on higher lifting coefficients than previously studied using this method, and aims to simplify the method in order to reduce design cost and allow an increased number of independent flow-based constraints with low added expense.

The first case investigated was originally studied by Mason *et al* [33] in the 1980s. It is a conical 57° swept delta wing and is interesting due to it's design point; close to the stanbrook-squire boundary [34,35] - which predicts whether the wing leading edge flow will be attached (low drag) or separated (high drag). In their research, Mason *et al.* used a conical full potential flow code to evaluate the wing and parametrically altered it's spanwise camber, thickness distribution and leading edge radius to design a wing with supercritical shock-free conical crossflow. The present study aims to extend their work by use of the 3D adjoint method and conical free-form deformation. Flow phenomena such as embedded cross flow shocks, separation, vortical flow and oblique shockwaves (as described by Miller and Wood[36], Squire[37] and Ghorai *et al.*[38]) are potentially present, leading to a non-linear design space and creating a unique challenge for the gradient-based design methods utilised throughout this study.

The open-source analysis and design software SU2 [39] has been used in conjunction with Pointwise grid generator in order to calculate flow and adjoint solutions based on the compressible inviscid Euler equations and viscous Navier-Stokes equations for sensitivity analysis. Modules from SU2 have been utilised by a custom python optimisation programme written by the author.

2.2 Supersonic Manoeuvre Wing Applications

Supersonic manoeuvre wings are designed to be efficient at higher lift coefficients than regular supersonic cruising wings. Typically, these wings or aerodynamic control surfaces might be designed for a loading factor of 2-4 indicating that they are intended for performing tight turns or manoeuvres at speeds above Mach 1, where loading factor is defined simply as the amount of lift in newtons divided by the weight of the aircraft in newtons.

Fig 2.1 X-37B gliding re-entry vehicle, Boeing[40] and UK Tempest fighter concept, BAe Systems[41].

Figure 2.1 shows two possible applications for the supersonic manoeuvre wings; in high-performance, highly manoeuvrable jet aircraft and fixed-wing re-entry vehicles which undergo significant loadings and perform various manoeuvres through a wide range of supersonic and transonic speeds. Drag reduction is essential to the design of such aircraft, and lift-induced drag must be considered if the aircraft is to undergo significant loadings throughout its mission. For this reason it is important to optimise with high-lift situations taken into account. Lowering drag leads to longer glide slopes, reduced fuel burn, better acceleration and higher top speeds, as well as higher sustainable G-loads for tighter sustained turns. It is also important to note that neither of the aircraft pictured above have horizontal tail surfaces, meaning that pitching moment is of great significance to the feasibility of any of these wing designs.

2.3 Supersonic Manoeuvre Wing Flow Physics

The supersonic manoeuvre wing is designed for performing high-G manoeuvres or producing large lift coefficients at speeds above the speed of sound. The flow physics required in order to perform these manoeuvres can be quite complex and highly nonlinear in nature; as categorised rigorously by Stallings[42], Stanbrook and Squire[34], Miller and Wood [43–45] amongst other notable researchers. At low incidence angles (as required for efficient cruising flight) and high Mach numbers, the flow around supersonic wings is almost entirely attached and behaves in accordance with linear physical laws. This makes it cheap and easy to predict forces and flow structures for this type and also to design optimum geometries based on algebraic theory. However, as the incidence of the swept wing increases; or indeed Mach number decreases; as is concurrent with high-G manoeuvres, the flow on the lee side of the wing can become separated (either partially or totally) and can contain various combinations of different cross-flow shockwave systems which themselves can induce further separations and nonlinear flow effects.

As the Mach number of the wing is increased, the flow at the leading edge of the wing has a stronger tendency to remain attached, as characterised by the Stanbrook-Squire boundary [34]. This means that crossflow shockwaves can form. As the flow accelerates around the wing leading edge, its crossflow velocity becomes sonic; however since in the case of a symmetric flow field, the crossflow velocity must return to zero at the wing root. This required deceleration, allowing the flow to turn back in a streamwise direction, can produce a shockwave. When the upstream normal Mach number of this

shock exceeds around 1.3, the resulting adverse pressure gradients cause flow separation, leading to a pair of vortices above the wings.

The multitudes of possible flow fields over slender delta wings at supersonic speeds has been characterised by Stallings[42], and presented very well in Figures 5, 6 and 7 of [42]; where delta wing flows are given as a function of αn and Mn, calculated as follows:

$$\alpha_N = tan^{-1}\frac{tan\alpha}{cos\Lambda} \qquad \text{Equation 2.1}$$

And (modified for use with hand calculator):

$$M_N = M_\infty\sqrt{1-\left(\tfrac{1}{2}(1+\cos(2\alpha))\right)*\left(\tfrac{1}{2}(1-\cos(2\Lambda))\right)} \qquad \text{Equation 2.2}$$

Using plots of αn vs Mn, flows are categorized into various regions. The Mason wing, within the boundaries of Masons experiments[33] is shown to lie on or near the boundary of several interesting regions; the most significant of which is the Stanbrook-Squire boundary[34] which distinguishes between separated or attached flow at the leading edge. This means that not only will both flow fields be possible with variations in wing geometry, but also the CFD flow solver must be accurate in its prediction of this separation. Squire[35] categorized the flow for the ranges of An and Mn shown in this study as having a detached shock below the upwind surface, supersonic expansion around the leading edge, with possible crossflow shock and shock-induced separation. However, lying on the Stanbrook-squire boundary, it is also possible that the flow be separated at the leading edge with a conical vortex. It will be of some interest how the adjoint optimiser deals with possible large changes in flow field across this significant boundary with small changes in geometry.

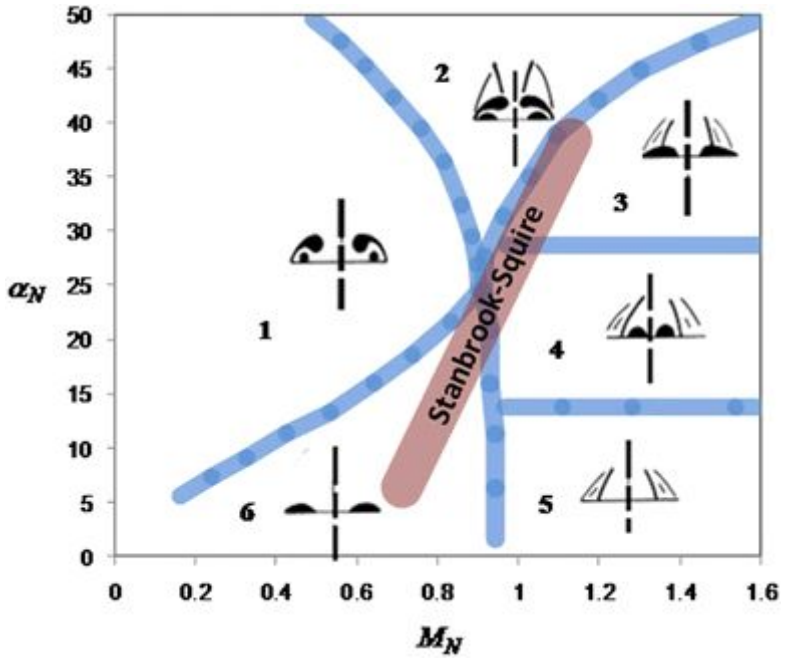

Fig 2.2 Stanbrook-Squire boundary for blunt-LE delta wings. Image from [46]

Figure 2.2 demonstrates the boundary between separated and attached LE flows for blunt leading edge delta wings, and illustrates an approximation of the expected flow fields. This figure features sketches adapted from Stallings[42] which describe the spanwise flow-field of a delta wing with various combinations of αn and Mn. This thesis will focus on wing designs which are at the boundaries of zones 3, 4, 5 and 6 detailed in figure 2.2.

Zones 6 and 3 both feature separated flow at the wing leading edge, reattaching to the upper surface towards the wing root. Separated leading-edge flow in the conical sense means strong vortices above the leading edge; increasing both lift and drag. Zones 4 and 5 both have attached flow at the leading edge and embedded cross-flow shockwaves above the upper surface of the wing. The difference between zone 4 and 5 is that in zone 4, the cross-flow shockwave is strong enough to cause boundary layer separation towards the wing root; resulting in a tight vortex which sits above the mid-span of the wing. This increases both lift and drag. It is also possible; as will be demonstrated later in the thesis; for a wing from zone 5 to not produce any crossflow shockwave - but only if the camber of the wing is carefully designed.

So, designing a wing which is optimised to fly in a velocity and alpha range which could produce both separated, attached, supercritical and crossflow shockwave flow structures will be a very interesting challenge and the optimisation method must reflect the significantly different possible flows.

2.4 Supersonic Manoeuvre Wing Design Methods

2.4.1 Mason's Design Method

Mason et al[33] utilised linear theoretical calculations to predict the flow and forces on a manoeuvre wing with fully attached flow and a single cross-flow shockwave, similar to those experienced by transonic aerofoil sections. Starting from a flat, thick, conical 59 degree delta wing, they added circular-arc camber to both upper and lower surfaces in order to produce a relatively flat pressure distribution on the upper surface; eliminating the crossflow shockwave by providing supercritical expansion and shock-free recompression in a similar manner to the Whitcomb transonic supercritical aerofoil. When compared in a wind tunnel, the introduction of this simple wing camber produced a 9.5% reduction in drag for the same lift coefficient as the flat datum wing.
This design method is not an iterative numerical optimisation procedure, the amount of camber was simply chosen to result in a leading edge which met the incoming normal flow direction, and the difference in flows was characterised both theoretically and experimentally.

Figure 2.3 Oil flow Photograph by Mason of cambered wing at M=1.62, α=12 during testing for[33]. Kindly scanned from the original Polaroid, courtesy of Mason[47].

Figure 2.3 shows clearly the lee-side surface flow field of Mason's conical cambered wing at M=1.62, α=12, Re/m=6.6x10^6 in a NASA supersonic wind tunnel. Oil applied to the wing surface shows surface shear force direction. Leading edge roughness causes fixed transition on left side of the wing, with visible streaks along the left wing surface, however on the right side of the wing there is no fixed transition and therefore streaks do not form until closer to the free transition point, with the exception of one streak due to leading edge contamination. Figure 2.3 actually demonstrates that on the right hand side of the wing, the flow transitions from laminar to turbulent just downstream of the cross-flow shockwave. Whilst the pressure coefficient distributions around each side of the wing are similar; it follows that due to the boundary layer transition location the skin friction distribution would be different on each side.

Mason later applied this shockwave reduction method to a cranked fighter wing concept[48] similar to those studied in the later sections of this thesis and tested it in NASA supersonic wind tunnels with good results.

2.4.2 Aerodynamic Shape Design Optimisation

First pioneered by Jameson[2], aerodynamic shape design through numerical optimisation is currently rarely used to its full potential by aeroplane designers, who generally prefer to create designs using low-fidelity theoretical methods due to their relative simplicity, cheapness and robustness of design. However, in recent years these newer design methods are becoming much more attractive to designers due to their ability to take real high-fidelity physics into account and creating designs with better performance than those designed through more conventional processes.

Optimisation can also be applied to aircraft and components which have already been designed through conventional means - helping to extract the last few percent of additional performance from the geometry.
In reality, aircraft designers should use a combination of conventional design processes and numerical optimisation to ensure they create the best design for a specific mission or range of missions.

2.5 Supersonic Aerodynamic Optimisation

Supersonic wing design has previously been derived from supersonic linear theory, assuming that flow perturbations propagate at the 'Mach angle' (μ), found from the relation:

$$\sin \mu = 1/M \qquad \text{Equation 2.3}$$

Where the Mach angle denotes the downstream zone of influence of geometrical perturbations of the surface geometry at supersonic speeds on the flow field.

Cp, in linear theory, can be calculated from the local angle of the body to the freestream and freestream Mach number alone. This, integrated around the aircraft, provides estimated forces, and the local body angles can therefore be optimised or designed in order to produce desired force distributions or total forces. This is the basis of traditional supersonic wing design.

A numerical optimisation method for supersonic wings utilising computers to solve integral linear theory equations was presented by Middleton and Carlson in 1965[49], and was extended to include various force and geometrical constraints, and allow for the effects of other aircraft components such as fuselage with the help of Miller [50]. Cenko [51] extended the method further to use linearized panel method codes (Woodward 1 and 2) for design optimisation, including the ability to prescribe a specific loading to any area of the wing, and allow the optimisation process to design the rest of the wing to provide minimum drag whilst constrained by the user-specified panel loading.

This type of optimisation was extended again to include full potential flow by Pittman[52], who used the NCOREL nonlinear flow solver as a basis for their optimisation method (this is the same flow solver used by Mason[33] in his supersonic manoeuvre wing design).

Carlson et al [53–57] presented various methods for the design of cambered supersonic wings for the maximisation of leading edge thrust and minimisation of lift-induced drag whilst Mason and Miller[58] focused their design efforts on controlled supercritical crossflows.

Burgreen and Baysal [59] presented the AeSOP3D optimisation procedure in 1994, featuring 3D Bezier-Bernstein surface parameterisation in order to optimise the shape of a symmetric clipped wing at Mach 1.62, a very similar case to that used by Mason for the conical camber delta wing. They use 'discrete aerodynamic sensitivity analysis' to generate gradients to drive their optimisation, essentially this is using finite differences with a sometimes very large number of flow solutions required in order to drive the solution to an optima.

More recently, the adjoint method has been used with Euler simulations to optimise aerofoils, planforms, 3D wing shapes, and even whole aircraft geometries; as shown by Reuther et al [26] (figure 2.4).

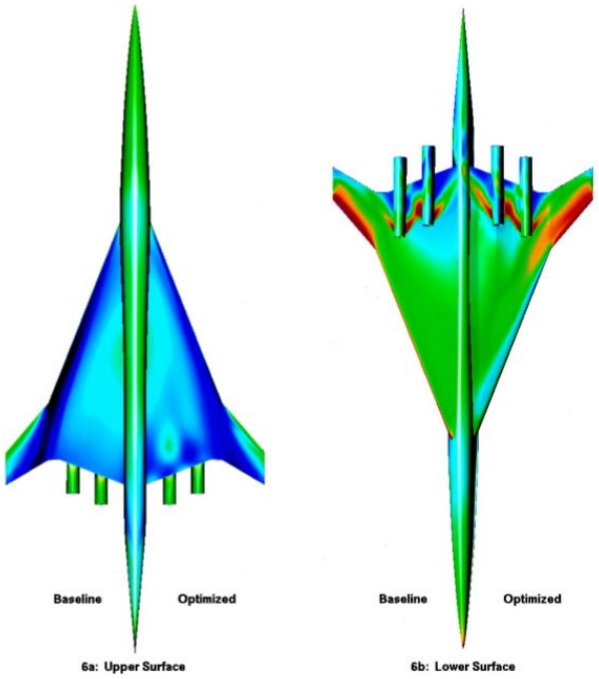

Figure 2.4 shows a generic supersonic transport design at M=2.2, Cl=0.105 with baseline and optimised Cp distributions from [26]

This is currently the highest-fidelity, most complete automatic adjoint aerodynamic optimisation of a full supersonic aircraft with a highly swept wing that is openly published and known by the author. Further advancements may have been made by private businesses or defence companies but nothing further has been openly published. This is due to the highly secretive nature of most supersonic aircraft development programmes. The geometry was parametrized by basic FFD boxes, a method which will be used during this project, Euler equations are solved as the governing equations of flow and the adjoint-Euler equations were used to generate gradients for the design process. Improvements on this process could include the solution of Navier-Stokes equations to check how realistic the design improvements actually are. The addition of off-design flow-based constraints might allow a design with desirable characteristics across the intended flight envelope. Improved geometry parameterization schemes (instead of basic FFD boxes) might yield better design optima and novel geometry shapes, and are implementable thanks to the enormous increase in available design variables provided by the adjoint method.

Chapter 3 Computational Methodology

In this chapter, the numerical methods and computer codes which have been used as the foundations of the design optimisation method used in this thesis are presented and described. First, the numerical methods used for generating flow solutions are presented, then the algorithms which define the optimisation cycle, then the adjoint CFD method used for generating surface sensitivities is described and finally the parameterisation and mesh movement methods which define the movement of surface points and volume points with geometrical perturbations are presented.

3.1 Flow Simulation

In the introductory paper[60] by the makers of SU2, several highly different validation and test cases for the software are presented. It is shown that steady and unsteady subsonic and supersonic cases can be solved accurately with both SA and SST turbulence models and a variety of first and second order methods for unstructured mesh of arbitrary topology type.

Some 2D and 3D transonic cases are also presented in [60], with varying degrees of accuracy.

In order to evaluate the flow-based function values which are required by the optimiser, the SU2_CFD flow solver is used. This section will outline the methods used by this program in order to generate a flow solution.

3.1.1 Governing Equations

There are two main sets of equations most commonly used in modern CFD simulations, both of which include conservation of energy, conservation of mass and conservation of momentum equations, ensuring that the solution satisfies the fundamental laws of thermodynamics and motion. The equations governing the flows used for optimisation in this project will be the inviscid Euler equations:

Mass continuity:

$$\frac{\partial \rho}{\partial t} + \frac{\partial(\rho u)}{\partial x} + \frac{\partial(\rho v)}{\partial y} + \frac{\partial(\rho w)}{\partial z} = 0 \qquad \text{Equation 3.1}$$

X-Momentum:

$$\frac{\partial(\rho u)}{\partial t} + \frac{\partial(\rho u^2)}{\partial x} + \frac{\partial(\rho uv)}{\partial y} + \frac{\partial(\rho uw)}{\partial z} = -\frac{\partial p}{\partial x} \qquad \text{Equation 3.2}$$

The Euler equations describe compressible, inviscid fluid flows. No energy is dissipated through viscosity, therefore these equations cannot accurately describe boundary layer development, however they can describe flows accurately if viscosity does not strongly influence the flow field, and force results can be augmented using a Csf equation (there are many to choose from), three examples of which are found in[61], such as the Schultz-Godunov formula:

$$Csf = 0.427(\log Re_L - 0.407)^{-2.64} \qquad \text{Equation 3.3}$$

Where Re_L is the local Reynolds number at the point on the aerodynamic surface which is being evaluated.

Although, these formulae are only truly applicable in very low pressure gradients. In order to properly model the boundary layer and other viscous effects in strong adverse pressure gradients such as

shock-boundary-layer interactions; without relying on experimentally-calibrated flat-plate assumptions; the Navier-Stokes equations must be used.

The viscous Navier-Stokes equations have been used for final analysis of the wing designs created by the optimiser:

X-Momentum:

$$\frac{\partial(\rho u)}{\partial t}+\frac{\partial(\rho u^2)}{\partial x}+\frac{\partial(\rho uv)}{\partial y}+\frac{\partial(\rho uw)}{\partial z}=-\frac{\partial p}{\partial x}+\frac{1}{Re}\left(\frac{\partial \tau_{xx}}{\partial x}+\frac{\partial \tau_{xy}}{\partial y}+\frac{\partial \tau_{xz}}{\partial z}\right) \quad \text{Equation 3.4}$$

Energy:

$$\frac{\partial(E_T)}{\partial t}+\frac{\partial(uE_T)}{\partial x}+\frac{\partial(vE_T)}{\partial y}+\frac{\partial(wE_T)}{\partial z}=-\frac{\partial(up)}{\partial x}-\frac{\partial(vp)}{\partial y}-\frac{\partial(wp)}{\partial z}-\frac{1}{RePr}\left(\frac{\partial q_x}{\partial x}+\frac{\partial q_y}{\partial y}+\frac{\partial q_z}{\partial z}\right)$$

$$+\frac{1}{Re}\left(\frac{\partial}{\partial x}(u\tau_{xx}+v\tau_{xy}+w\tau_{xz})+\frac{\partial}{\partial y}(u\tau_{xy}+v\tau_{yy}+w\tau_{yz})+\frac{\partial}{\partial z}(u\tau_{xz}+v\tau_{yz}+w\tau_{zz})\right) \quad \text{Equation 3.5}$$

The Navier-Stokes equations are essentially an extension of the Euler equations, and can properly model boundary layers, however in order to close them for efficient modelling (DNS is possible but requires enormous grid dimensions, since turbulent eddies must be resolved right down to the kolmogorov scale - the point at which kinetic energy is dissipated as heat), turbulence models must be used. The added physical detail of viscosity makes the Navier-Stokes equations more accurate than the Euler equations, particularly in boundary layer regions and wakes where fluid shear stresses affect the flow field.

3.1.2 Turbulence Model

Over time, there have been many different attempts at producing an accurate closure model for the Navier-Stokes equations. This ranges from the one-equation Baldwin-Lomax[62] model through to the three-equation SST model[63]. Unfortunately, there is no model which is perfectly suited to all flow cases, with some performing better than others in different situations, resulting in the requirement to conduct or refer to detailed analysis into these differences; such as that performed by Menter[64].

Due to the expected flow physics involved and after some 2D RANS investigations at the beginning of the project, only one of these turbulence models was selected to be used within this project - the widely used Spalart-Allmaras[65] one-equation model.

The SA model is a one-equation turbulence model as derived by Spalart and Allmaras [65] which is very widely used for a large variety of flows, and is considered a robust approach to the majority of slightly separated flows and boundary layers with adverse pressure gradients. This model approximates the quantity eddy viscosity (υ_t), which is used in the calculation of Reynolds stresses $-\overline{uv}=\upsilon_t\left(\frac{\partial u}{\partial y}+\frac{\partial v}{\partial x}\right)$ which then produce a model for closing the governing RANS equations. Near walls, the SA model introduces the transported quantity $\tilde{\upsilon}$, which is equal to υ_t in the freestream, however behaves linearly in the viscous region (following the notation of [65]):

$$X=ky^+ \quad \text{Equation 3.6}$$

$$f_{\upsilon 1}=\frac{X^3}{X^3+C_{\upsilon 1}{}^3} \quad \text{Equation 3.7}$$

$$\upsilon_t=\tilde{\upsilon}f_{\upsilon 1} \quad \text{Equation 3.8}$$

Where $f_{\upsilon 1}$ is a near-wall damping function from Mellor and Herring[66] using $C_{\upsilon 1}=7.1$

It has been found that using the SA-neg[67] Implementation is useful for restarting flow solutions with deformed grids. The reason it is so useful in stabilising these restarted solutions is that when the variable $\tilde{\upsilon}$ is positive or zero, there is no change to the formulation, but if it becomes negative then the absolute value of this variable is used in its place. This artificially increases the stability of the flow solution and avoids divergence through nonphysical states.

3.1.3 Discretisation

3.1.3.1 Time integration

The Euler-implicit method for time integration is used with the GMRES linear solver[68] Contained within SU2. All flow solutions in this thesis are Reynolds-averaged, meaning that they are entirely time-averaged and no fluctuating flow properties are taken into account.

3.1.3.2 Spatial integration

The Governing Equations cannot be solved continuously across the CFD domain, and require discretization across a grid within the flow domain in order to be solved accurately - in the case of SU2 the grids are always saved in unstructured format regardless of topology. In order to do this, the governing equations must be discretized at each grid point using the finite-volume method. Versteeg and Malalasekera [69] describe this method in detail. The following equation describes how the flow variables are passed from one cell face to another:

$$U_i^{n+1} = U_i^n - \frac{1}{\Delta x}\int_t^{t^{n+1}} (F_{i+\frac{1}{2}} - F_{i-\frac{1}{2}})dt \qquad \text{Equation 3.9}$$

Where U denotes flow variables. Now, it is essential that flow variables are passed between grid points in a physically correct manner. This equation, described in more detail by [70], shows this problem in one dimension - i, however this is extendable to 3 dimensions. The fluxes Fi+1/2 and Fi-1/2 need to be calculated, and can vary significantly between points in a solution. For example, in supersonic flows, information cannot be passed upstream, but in subsonic regions, information can be passed both upstream and downstream. This is where flux splitting methods play an important role. Godunov [71] suggested that since the domain is now made up of discrete cells, these fluxes could be found by a solution to the Riemann problem with the cell faces as discontinuities. Thus, most flux splitting methods employ Riemann solvers.

The main Flux splitting method used in this project will be the Jameson-Schmidtt-Turkel scheme; as described in modern terms by Jameson in [72]; however the Roe scheme [73] as implemented in SU2 has also been evaluated for this flow problem.

Following the notation of [72], the JST scheme evaluates numerical flux as:

$$F_{i+\frac{1}{2}} = \frac{1}{2}(f_{i+1} + f_i) - d_{i+\frac{1}{2}} \qquad \text{Equation 3.10}$$

Where $f = \left[\rho u \;\; \rho u^2 + p \;\; \rho uH\right]$ Equation 3.11

And the dissipative flux $d_{i+\frac{1}{2}} = \varepsilon^{(2)}_{i+\frac{1}{2}}\Delta w_{i+\frac{1}{2}} - \varepsilon^{(4)}_{i+\frac{1}{2}}(\Delta w_{i+\frac{3}{2}} - 2\Delta w_{i+\frac{1}{2}} + \Delta w_{i-\frac{1}{2}})$ Equation 3.12

Where $\Delta w_{i+\frac{1}{2}} = \left[\rho_{i+1} - \rho_i \;\; (\rho u)_{i+1} - (\rho u)_i \;\; (\rho uH)_{i+1} - (\rho uH)_i\right]$ Equation 3.13

And $H = E + \frac{p}{\rho}$ Equation 3.14

The dissipative coefficients $\varepsilon^{(2)}_{i+\frac{1}{2}}$ and $\varepsilon^{(4)}_{i+\frac{1}{2}}$ can be switched on or off by a pressure sensor, described in further detail in [72].

The Roe scheme solves the linearized approximate Riemann problem through calculation of the eigenvalues of the governing equations, giving the relative speeds of an entropy wave (corresponding to the fluid motion) and two acoustic waves (one upstream and one downstream) – however the 'upstream' wave would in fact point downstream for supersonic flow, reflecting the natural zone of influence. A significant benefit to this method is that shockwaves are allowed as a solution without any modification to the scheme. However, so are expansion shocks, which are not a physical phenomenon and must be corrected by introducing an entropy correction method.

An Edge-based dual-grid scheme is used with the JST method for computing the fluxes at each cell face. The decision to use the JST method was made after comparing flow solutions with ones generated using Roe's flux splitting scheme, shown in figure 3.1. It was found that the JST scheme, as implemented in SU2, provided far better shockwave resolution and correspondingly more accurate surface pressure distributions. This greatly affected the result of the optimisation process since shockwaves - a major source of drag - were not sharply captured during any of the design iterations by SU2 with Roe's scheme.

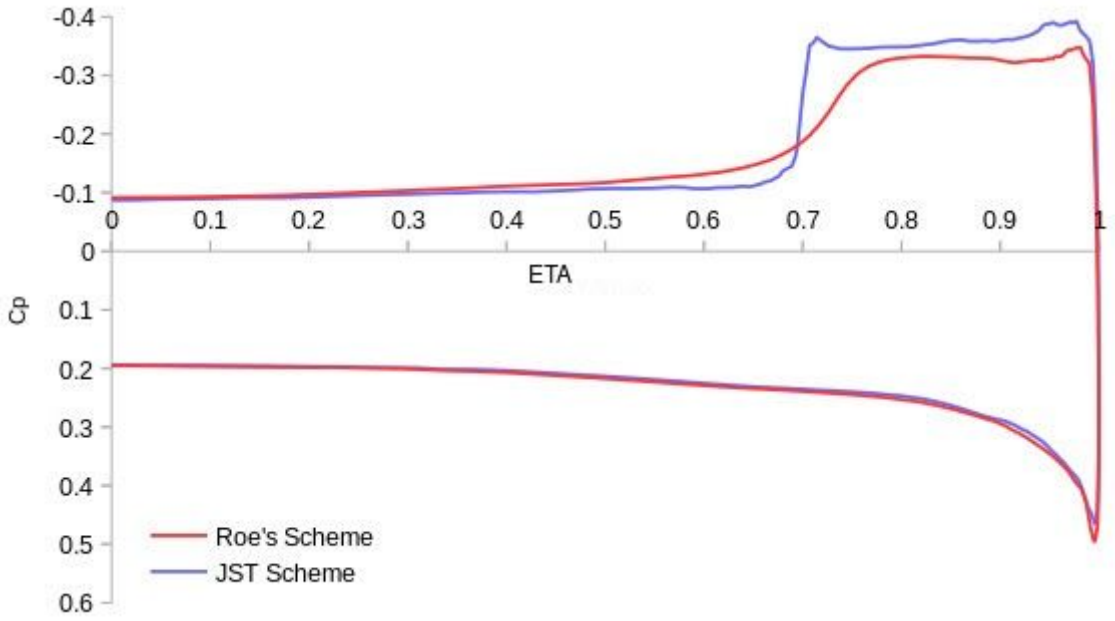

Fig 3.1 Inviscid spanwise pressure distribution of the flat conical wing, M=1.62, CL=0.4; as calculated by Roe's scheme and the JST scheme as implemented by SU2 V6.0.

It is clear from figure 3.1 that the shockwave resolution provided by the JST scheme is sharper than the shockwave calculated by the Roe scheme, when calculated on the same grid with all other parameters and boundary conditions being identical, except that the Venkatakrishnan slope limiter[74] and high entropy correction coefficients required for good convergence of Roe's scheme had the effect of decreasing shockwave resolution. This was an unexpected result as Roe's scheme is fully compatible with shockwaves; however the author suspects that the requirement for entropy correction and possibility for expansion shocks may be the cause of the smeared shockwave.

All CFD simulations included in this thesis utilise the MUSCL scheme by Van Leer [75] in order to guarantee second-order accuracy of the solution. This is now fairly common practice within CFD for aerodynamics; as the 2nd order cell face flux values which the MUSCL scheme calculates can be used to initialise the JST (or Roe) scheme.

3.1.4 CFD Grids

In order to resolve the discretized governing equations properly, a suitable 3D mesh must be used, being composed of surface grids linked by volume meshes. For the inviscid Euler equations, a fully tetrahedral mesh can be used with no constraint on surface grid spacing other than what is necessary to resolve dominant flow and geometrical features e.g. shockwaves and leading edges. For brevity in this section, only the grids used in the conical wing study will be used for illustrative purposes. In order to generate all grids used throughout this thesis, the software Pointwise V18.0 was used.
For Euler solutions, a fully unstructured mesh is used, shown below:

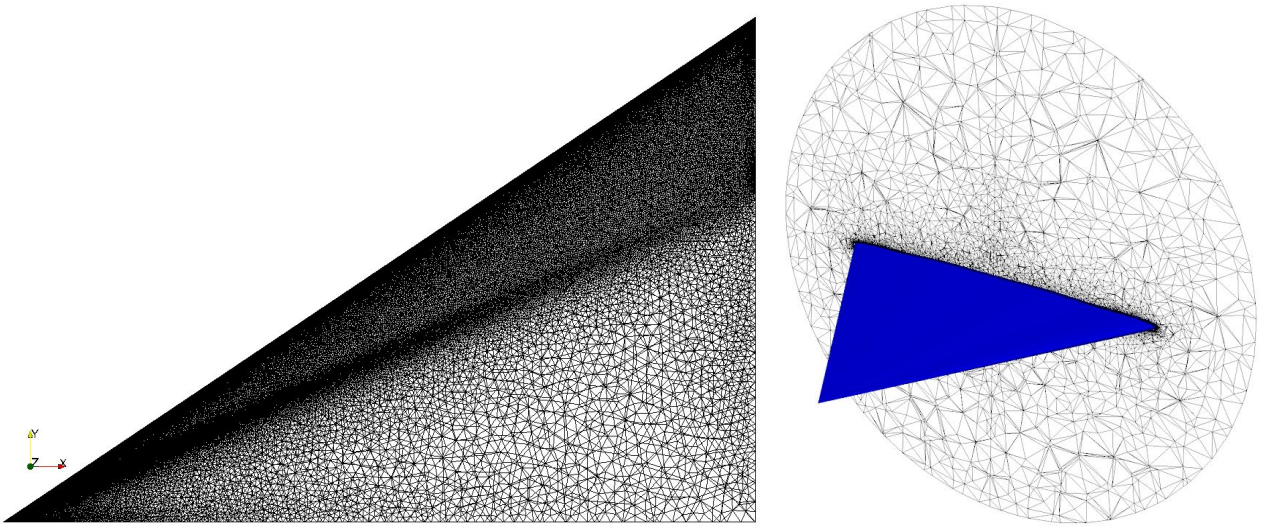

Fig 3.2 Euler unstructured surface grid (left) and volume grid slice (right)

Figure 3.2 indicates the topology and cell distribution of the unstructured CFD grids used to simulate the supersonic conical delta wing. The surface grid is made from 137,000 triangular elements and the unstructured volume mesh made from 200,000 points with 900,000 tetrahedral elements. A 1-2 level V-cycle multigrid method was utilised in order to reduce the time required to generate each flow solution, and an adaptive CFL number between 0.75 and 100 was used in order to improve solution stability and speed. Points are clustered around areas of high gradient in the flow, in order to clearly resolve any features which occur over a small distance in these regions. This grid was made using pointwise grid generator and refined based on the results of previous simulations on coarse grids. A grid convergence study was performed and it was found that the aerodynamic force coefficients could be resolved with a coarser grid with only 100,000 surface elements; however the shockwave was found to be slightly smeared and therefore more surface elements were added in order to better resolve the discontinuity.

For RANS solutions, a conical hexahedral mesh is used:

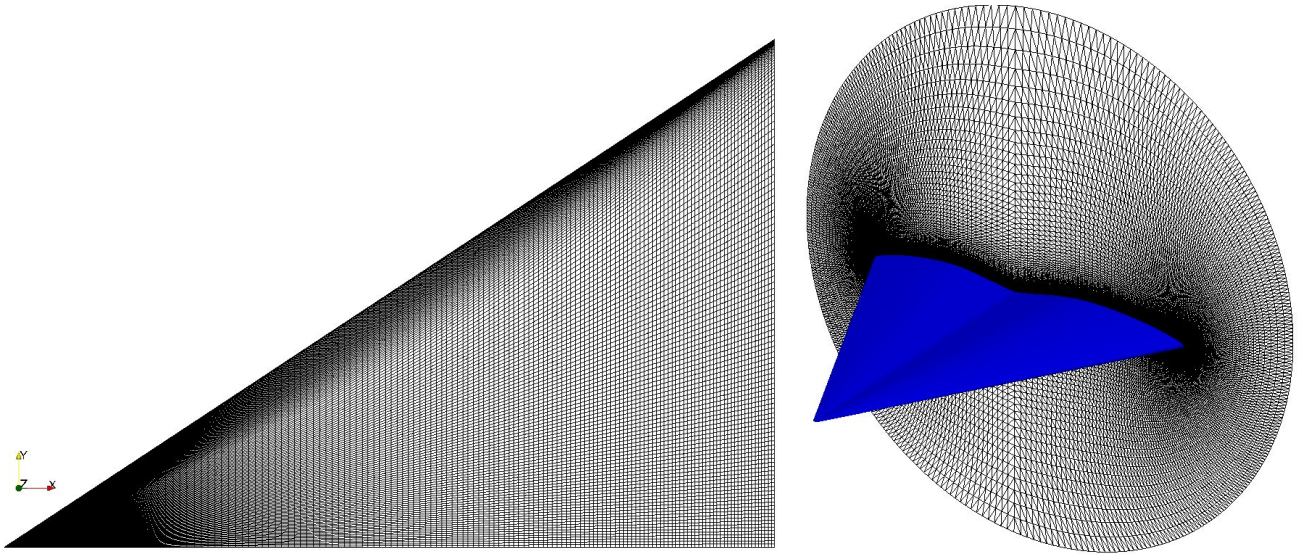

Fig 3.3 RANS conical structured surface grid (left) and volume grid slice (right)

The structured conical surface grid is made from 100x200 trapezoidal cells, with 100x100 cells on each of the upper and lower surfaces respectively. The conical volume grid consists of 100x100x200 hexahedral cells with a surface spacing of 5e-6m and an initial growth rate of 1.15. This initial grid spacing guarantees that with a Re/m of 6.6×10^6, the Y+ value will be less than 2 over the entire wing surface. A grid convergence study was undertaken and it was found that the grid with 100x100x200 cells was necessary to properly capture the effects of shock-induced separation for the uncambered wing, which increases the effective frontal area of the wing and therefore has an impact on the predicted drag value.

3.1.5 Boundary Conditions

Boundary conditions define how the CFD solver treats cell faces at the edges of the control volume. This is critical to the realism of any given CFD problem as it defines how the flow behaves both at the solid surfaces and at the inlets and outlets of the control volume. The boundary conditions used throughout this study are the far-field, symmetry plane, adiabatic slip wall (Euler) and adiabatic non-slip wall (RANS).

Symmetry planes are modelled as:

- Tangential flow only
- Zero flux across face
- 'Halo' cells used to preserve 2nd order accuracy

Far-field boundaries are modelled as:

- Supersonic or subsonic inlet or outlet based on local flow angle
- Based on work by Bayliss and Turkel[76]
- Turbulent kinematic viscosity variable $0.21\nu_\infty < \nu_t < 1.29\nu_\infty$ in the SA model for RANS solutions

In the inviscid Euler cases, solid walls are modelled as:

- Tangential flow only
- No friction
- No heat transfer

For the viscous RANS cases, solid walls are modelled as:

- Zero flow velocity
- No heat transfer
- Turbulent kinematic viscosity variable $\nu_t = 0$ in the SA model

These are all standard boundary conditions which are used in the majority of external flow CFD applications and are implemented with the SU2_CFD flow solver.

3.1.6 Convergence of the Flow Solver

In order to decide whether or not a CFD solution is stable and the solver is finished iterating, engineers observe the convergence or divergence of the flow variables and the residuals of the governing equations. For a steady-state solution to be considered converged, the flow variables must have reached a steady state (e.g. not fluctuating with more solver iterations) and the residuals of the governing equations must have reduced by a number of orders when observed on a logarithmic scale. In this thesis, the density residual is displayed since in all cases this was the last residual to reach convergence. For the results in this thesis, 6 orders of residual convergence and steady flow variables were the limits used in simulations to determine when a solution is converged.

Convergence of the Euler equations for the conical flat wing only are shown for illustrative purposes below as the convergence of RANS solutions is explored later in the results section.

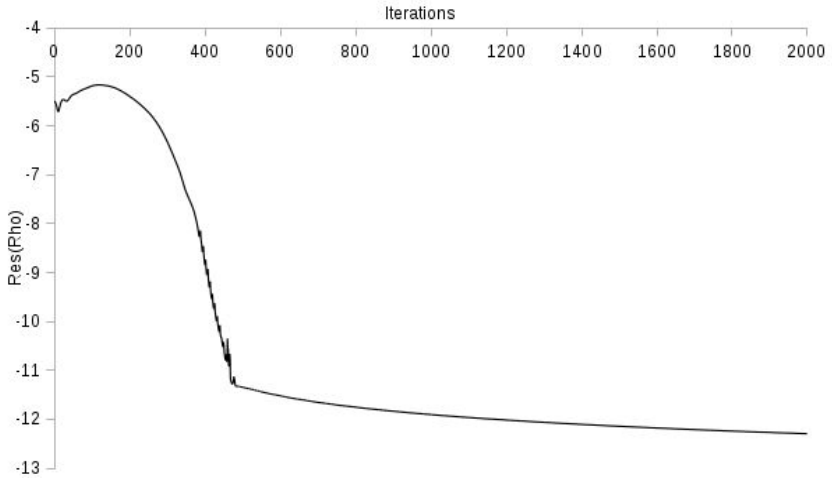

Fig 3.4 Convergence of Euler density residual in fixed alpha mode

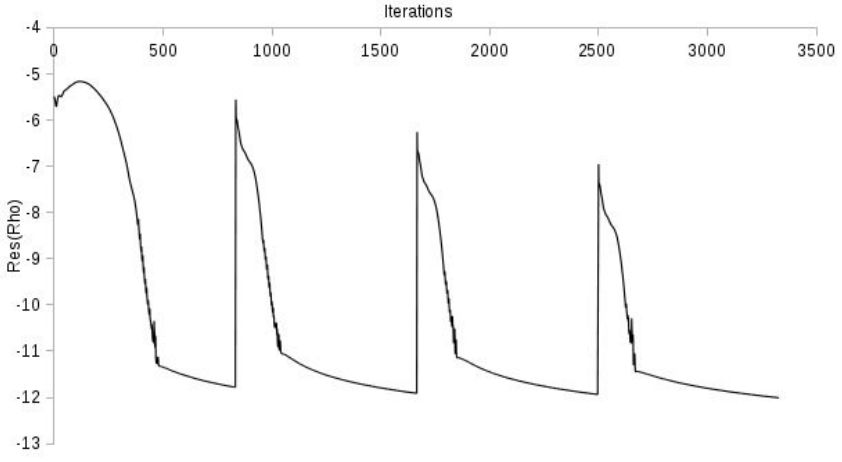

Fig 3.5 Convergence of Euler density residual in fixed CL mode

The residuals of the Euler equations are converged by 6 orders in about 1000 iterations of the flow solver with the JST scheme on the unstructured grid, and for the fixed alpha case a further 1000 iterations yields only marginal further reduction in density residual. For the fixed CL case, the value of alpha is updated 3 times in the space of 2500 iterations at regular intervals and finally converges on a result after 3400 iterations. Each time the value of alpha is changed, the density residual increases sharply by over 5 orders but then converges again over the space of around 830 iterations.
These convergence rates are accomplished using an adaptive CFL number between 1-100 (average value of about 12).
In SU2, it is possible to set convergence targets which dictate when the flow solver will stop iterating and export a solution.

3.1.7 Flow Solution Validation

In order to validate the flow solutions, spanwise pressure distributions from the conical RANS solution have been compared with wind tunnel pressure tapping data from Mason *et.al.[33]*. The RANS solutions were generated using the JST scheme with MUSCL and the SA-neg turbulence model as outlined previously in the thesis, on the 100x100x200 structured conical grid shown in figure 3.3. This similarity gives confidence in the results of computational models used during the design and analysis process within this report.

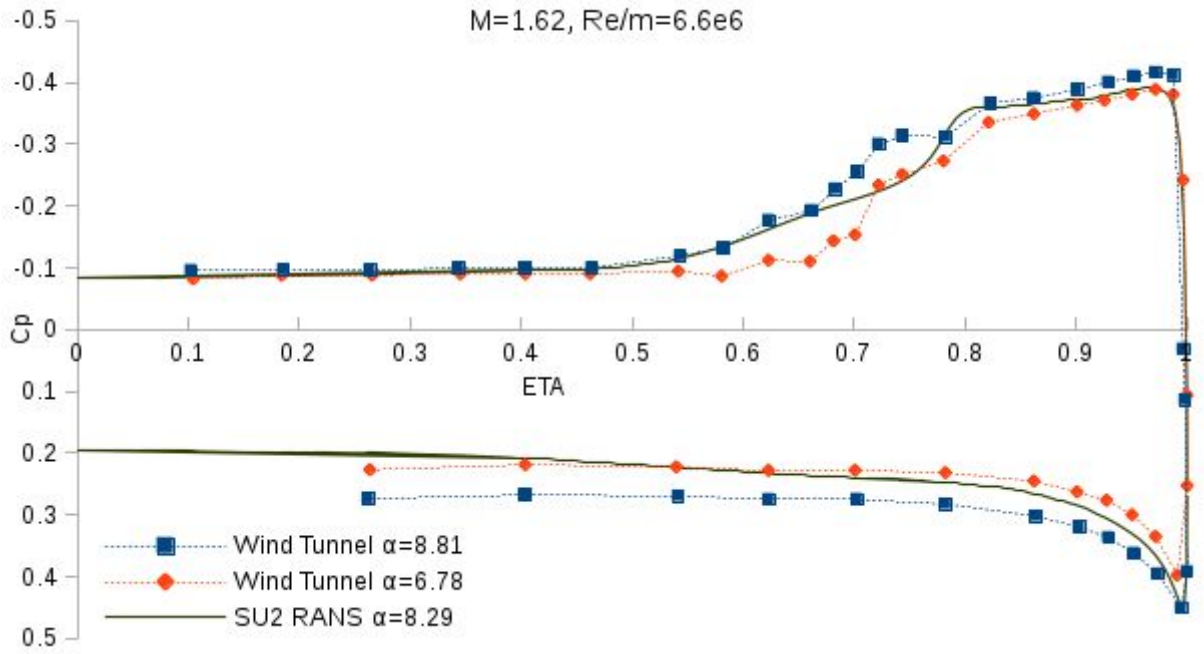

Fig 3.6 Comparison of SU2 RANS conical pressure coefficient with NASA wind tunnel data for the uncambered conical wing geometry.

The wing geometries used for this verification are identical, however the wind tunnel model included a faired body housing for the force balance on the lower surface - leading to differences in lower surface pressures near the root and increasing the CL value at any given α. This must be taken into account when observing any lower surface pressures at ETA<~0.6

Despite these small differences, there is largely good agreement between the wind tunnel and RANS results, including upper surface shockwave location and intensity, shock-induced separation reattachment point, leading edge stagnation pressure value and leading edge suction peak value. The only appreciable discrepancy is on the upper surface at 0.7<ETA<0.75, where the embedded cross-flow shock wave induced flow separation. This could be the result of a phenomena called secondary roll-up vortex in the wind tunnel experiments; however there is no further evidence to support this hypothesis.
Overall, it can be said that the CFD data is generally in good agreement with measured and trusted wind tunnel data; lending credibility to the CFD results shown throughout this thesis.

3.2 Optimisation Algorithm

A custom python programme has been written for the purposes of this project. This python code utilises both the numpy optimisation library and also custom optimisation algorithms and can locally minimise any function when given accurate function values and gradients at each design step. Thanks to the adjoint method this function minimisation can be achieved for an arbitrary number of design variables.

The python optimisation code is able to pass configuration options to and run SU2_CFD, SU2_CFD_AD, SU2_DOT, SU2_DOT_AD, SU2_SOL and SU2_DEF as individual elements from SU2 v6.2.0.

SU2_CFD – This is primarily a flow solver, capable of solving Euler, RANS, and URANS bounded PDE systems to a good degree of accuracy [drives flow solution towards R(U) ~ 0]. This module is also responsible for solving the continuous-adjoint equations (subject to R(U) ~ 0) as these are derived as PDE systems. This module has the largest computational requirement.

SU2_CFD_AD - This is a solver for the discrete adjoint. It receives the converged flow solution and outputs the discrete adjoint solution and the sensitivity of the surface grid to whichever objective function is specified. It generally requires a similar amount of CPU time as SU2_CFD.

SU2_DOT – This module uses geometrical parameters and computed surface sensitivities to project the sensitivity gradients from the surface to each design variable. This provides the crucial sensitivity gradient (dI/dD) where I is the chosen objective function to be minimised and D denotes the geometrical design variables. This computed design sensitivity gradient drives the optimisation process.

SU2_SOL - Writes out the results of SU2_CFD and SU2_CFD_AD into files which can be read by post-processing software such as Paraview or TecPlot. It also writes out a file containing a breakdown of integrated forces as calculated by the flow solver, which is read by the optimiser to return the values of objective and constraint functions.

SU2_DEF – This module deforms the surface and volume meshes for each design iteration. This is an absolutely critical module to a stable and precise optimisation process, as it directly affects the ability of SU2_CFD to converge on a flow and adjoint solution for each consecutive design step. If a change in geometry results in a poor mesh quality, the next set of solutions may not converge accurately and an inaccurate gradient for an inaccurate flow solution will be produced, possibly driving the optimiser in the wrong direction or even crashing the algorithm altogether. A linear elasticity method is used by SU2 for mesh deformation, as it is simple and robust.

These elements, when configured correctly, are able to provide accurate estimations of the objective function, constraint function, their sensitivities with respect to the wing surface grid, the design velocities of the surface grid, and also deform the volume grid for each design step.

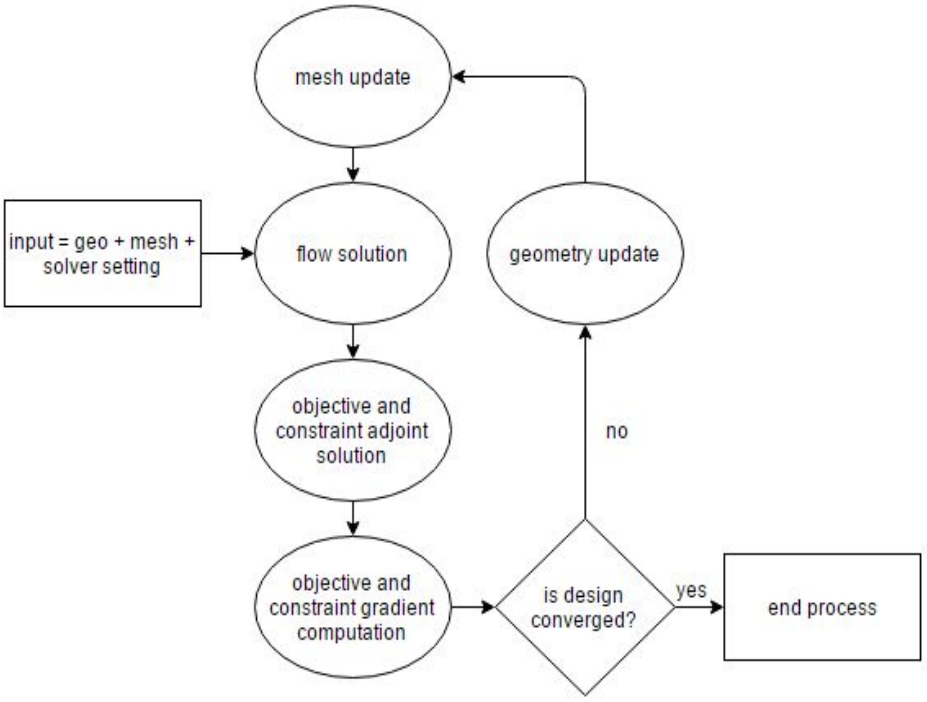

Fig 3.7 Gradient-based design loop

Figure 3.7 shows the optimisation loop used by the custom python design code. The variables which are controlled by the optimiser and change at every design iteration are a set of shape variables which describe the geometry of the wing. Generally, they have a value of zero, or a good initial guess at the beginning of an optimisation, but they can equally be started from any reasonable value.
Every time the optimiser makes a new approximation of the optimum values for the design variables, the wing geometry is updated to these specifications and the CFD mesh is deformed to match the new wing surface.

3.3 Objective and Constraint Function

The objective function of the optimisation problem is what defines the main goal of the design; generally in aerodynamic optimisation this value would be the drag, pitching moment or noise produced by a body.
In the case of this project, drag will be used as an objective function - meaning that the optimiser will seek to reduce the drag coefficient of the design.
This objective function can be expressed mathematically as:

$$I = C_D = C_{Fx} Cos\ \alpha + C_{Fz} Sin\ \alpha \qquad \text{Equation 3.15}$$

The SLSQP optimiser used during this project approximates a quadratic curve for the relationship between the objective function and each design variable, using this quadratic relationship to identify a potential optima. This approximation can be expressed in simple terms mathematically as:

$$I = AD^2 + C \qquad \text{Equation 3.16}$$

$$\frac{dI}{dD} = 2DX \qquad \text{Equation 3.17}$$

Where D denotes the design variables and A and C are constants which are updated at each design step based on values computed by the flow and adjoint solutions.
This forms the basis of the quadratic subproblem which is solved at each design step to calculate step length and search direction for the optimiser.

Constraint functions in the optimisation problem are what defines the requirements of the design, and can be based on performance values like lift and pitching moment; or geometrical functions like thickness and L.E. radius.

The constraint can be posed in two ways:
Equality -

$$G = 0$$

Inequality -

$$G > 0$$
$$G < 0$$

During this project, when constraint functions are presented directly to the optimiser e.g. ‘Hard constrained strategy’ detailed later on, they will be in the form of inequality constraints. This presents the optimiser with a larger area of feasibility in the design space. Examples of the flow-based constraints used in this project are shown below:

$$G_1 = C_L - C_{L_{Target}} = (C_{Fz} Cos\ \alpha\ - C_{Fx} Sin\ \alpha) - C_{L_{Target}} > 0 \qquad \text{Equation 3.18}$$

$$G_2 = C_{My} = \Sigma[C_P(x - x_{ac}) + C_P z] < 0 \qquad \text{Equation 3.19}$$

Constraints are not just limited to functions which are passed to the optimiser such as those shown above; for example, one of the constraints of every CFD based optimisation is that R(U)~0 e.g. the CFD flow solution at every design evaluation is converged. If this condition is not met then the design is said to be infeasible.

3.4 SLSQP Algorithm

The algorithm used in this study for gradient-based optimisation procedures is sequential quadratic programming, first used by Kraft and then implemented into the python SciPy library, it is now widely used by engineers, scientists and programmers around the world. This method works somewhat like

Newton's method; in that it takes the function of the objective and constraints and their respective derivatives in order to inform a decision on how to evolve the geometry. Where it differs, however, is in how it decides upon which step length to take in the direction indicated to it by the gradient.
SQP gathers together the values of the objective and its derivative at each subsequent design step and uses them to fit a quadratic curve which represents the design space. Following design steps can then make a much better guess at the step length required in order to drive the design to a local minima. This reduces the number of overall steps which are required to find an optimum design.
Reduction in the number of required design steps is highly attractive to aerodynamic designers due to the large expense incurred in generating flow solutions and gradient calculations - especially for very large and complex design cases such as aircraft configurations and formula 1 cars.
Hard constraints are treated as linear functions, where the value and derivative of each constraint are evaluated at each design step.

Armijo-Goldstein condition

The Armijo-Goldstein condition[77] is somewhat critical to the robustness of the SLSQP algorithm. It is a condition of sufficient decrease in the objective function and again is a tool which helps to reduce the number of gradient calculations necessary to reach an optimum design.
It means that if, once a particular change is made to the design variables, the objective function has not reduced by a large enough margin then a line-search is conducted using gradients derived in the previous design step. The line-search can reduce computational expenditure dramatically for large and complex design problems because it does not require any further gradient evaluations until the objective function has changed by a sufficient amount.

3.5 Custom Python Algorithms

The following flowcharts show, in detail, the algorithms used in the custom python script which was used for optimisation in this project. In all cases, the initial inputs to the optimiser will be:
Initial design variable values, bounds for each design variable, definition of the objective and constraint functions and their respective gradients and the optimisation method (SLSQP being used throughout this study).
The master directory will contain the python script, an SU2 configuration file, an SU2 mesh containing details of the design variables and an HPC submission script. The python program will create a ‘designs’ directory and ‘history’ directory automatically upon starting. Within the designs directory, a new directory will be created for each new design iteration; within which sub-directories will be created to contain constraint evaluations.

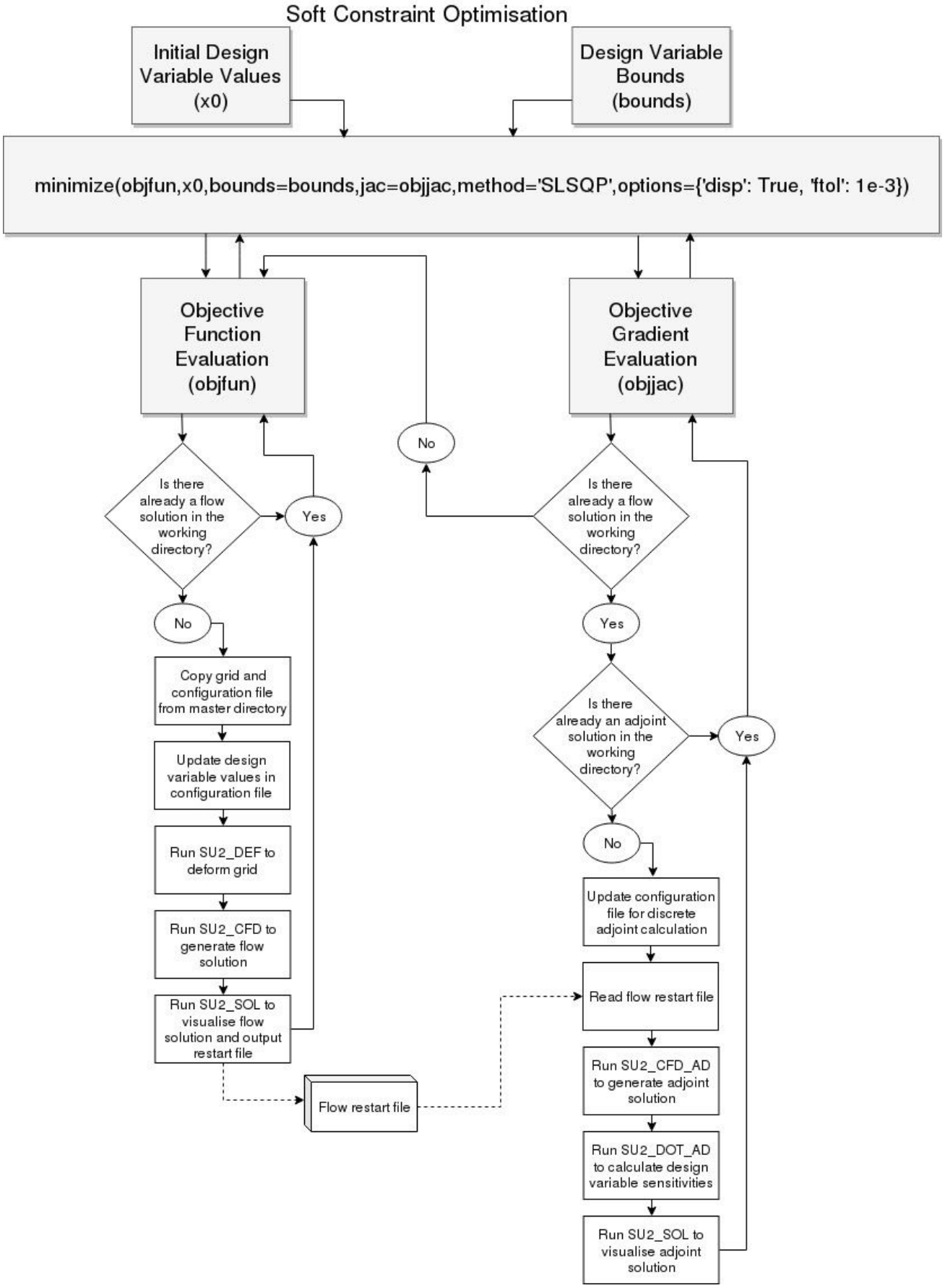

Fig 3.8 Optimisation algorithm flowchart without hard constraints

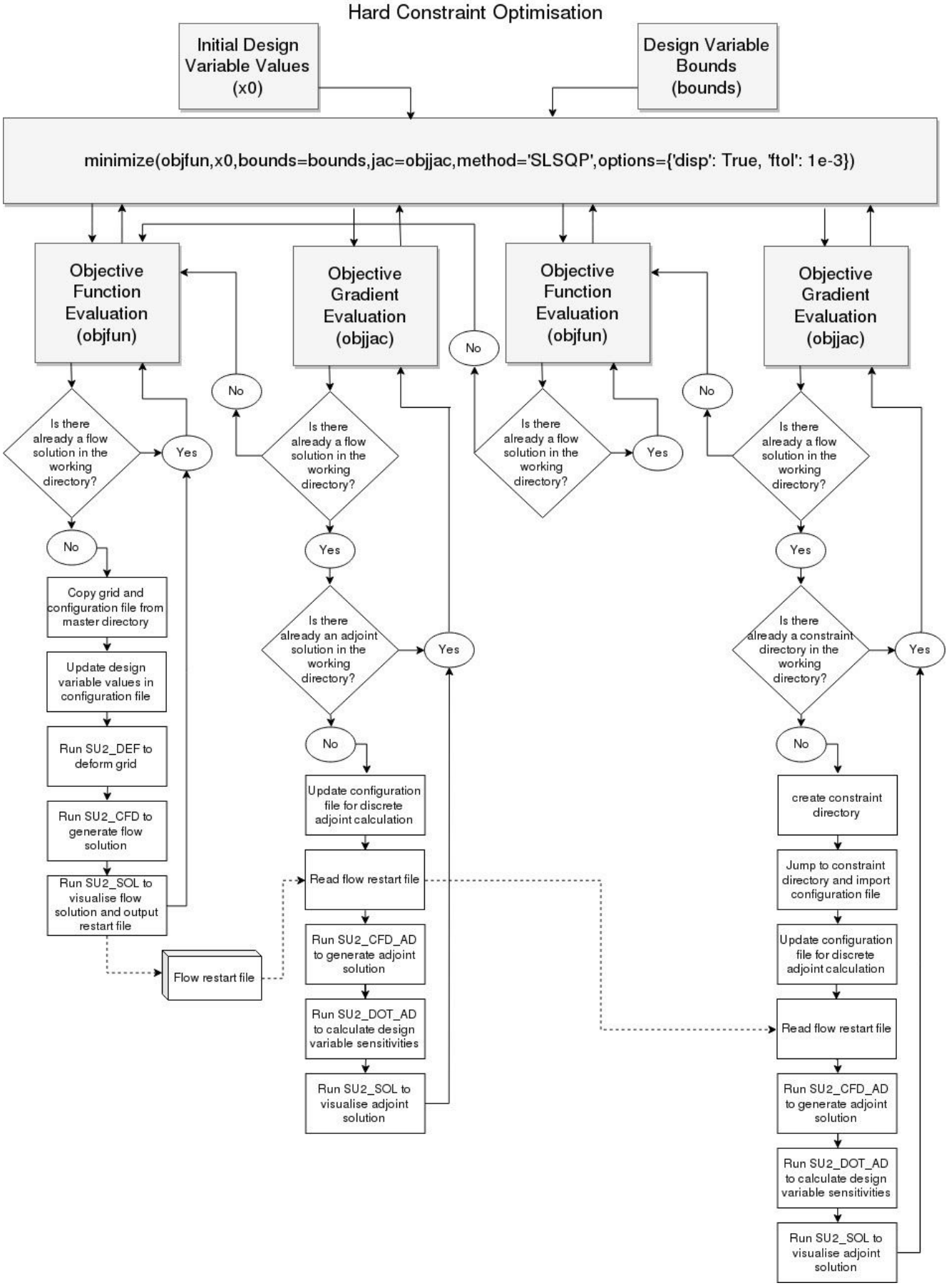

Fig 3.9 Optimisation algorithm flowchart with hard constraints

Figure 3.8 shows the algorithm used by the 'soft optimisation strategy'. What this means is that no hard constraints are presented to the optimiser. It is clear from this flowchart that the grid update (changing the shape of the wing and surrounding mesh) happens at the beginning of each flow function evaluation. This ensures that the deformed grid will always be used by the flow and adjoint solvers, avoiding the potential issue of mistaken grid identities.
At the beginning of each gradient evaluation, a check is made to ensure that there is already a flow solution for the current design, since the flow restart file is required for initialisation of the adjoint solution. In both figures 3.8 and 3.9, the decision for continuation or termination of the loop is made in the block at the top which contains the minimize function. In this function, a value is given as 'ftol' which determines the convergence tolerance for the optimisation - and hence also defines when the optimisation will be terminated.

Figure 3.9 shows the algorithm used by the 'hard optimisation strategy', meaning that a hard constraint is presented to the optimiser in the form of a linearised function. In the case of this algorithm, the aerodynamic constraint function is based on the same flow solution as the objective function, meaning that they are two values at the same flight condition e.g. same Mach number, same α, same geometry. Due to this, the constraint function evaluation is a simple call to the objective function evaluation, as the same flow restart file and force breakdown files can be used.

3.6 Adjoint Gradient Computation

The major benefit to adjoint gradient-based optimisation is that cost is reduced and the limitation of number of design variables is removed; meaning that geometries of arbitrary complexity with an arbitrary number of variables can be evaluated and optimised. The adjoint solution contains the sensitivity of every surface grid point to whichever objective or constraint function is selected, meaning that the objective gradient at any type of design variable can be evaluated quickly and easily.

The method works by first solving a flow solution for the desired case – converging the solution to R(U)~0, and then computing the adjoint of whichever governing equations are to be used, using the converged flow solution to initialize the adjoint solution. In order to find the derivative dI/dD (gradient of objective function w.r.t. design variable D), the adjoint equation uses a LaGrange multiplier λ^T which is introduced into the objective function:

$$I(U,\ D) = J(U,\ D) - \lambda^T\ N(U,\ D) \qquad \text{Equation 3.20}$$

And since R(U)~0, the multiplier can be chosen freely to satisfy:

$$\frac{\partial J}{\partial U} - \lambda^T \frac{\partial N}{\partial U} = 0 \qquad \text{Equation 3.21}$$

This means that the perturbed objective function, previously:

$$dI = \left(\frac{\partial J}{\partial U} - \lambda^T \frac{\partial N}{\partial U}\right) dU + \left(\frac{\partial J}{\partial D} - \lambda^T \frac{\partial N}{\partial D}\right) dD \qquad \text{Equation 3.22}$$

Can now be written as:

$$dI = \left(\frac{\partial J}{\partial D} - \lambda^T \frac{\partial N}{\partial D} \right) dD \qquad \text{Equation 3.23}$$

Now it is possible to find dI/dD without having to directly solve the costly dI/dU or dU/dD.

The Adjoint governing equations can be solved in two different manners: continuously and discretely. A study into the differences between these two methods and the derivation of each form was presented by Nadarajah and Jameson[78], who concluded that there is very little difference in the results of optimisation processes utilising either method, although discrete adjoints showed a very marginal improvement in gradient accuracy.

A study was performed by the author into continuous and discrete gradients vs finite difference calculations with step sizes of both 1e-3m and 1e-4m, results are presented in table 3.1. This study found that the discrete method provided a considerable improvement in accuracy over the continuous. For this reason, only the discrete adjoint formulation will be utilised for the purposes of this project.

Table 3.1 Comparison/verification of design variable drag sensitivities

Drag Sensitivity dCD/dD at FFD Design Variables for Conical Wing				
Control point	Continuous Adjoint	Discrete Adjoint	FD 1e-3m	FD 1e-4m
3	-0.007	-0.312	-0.300	-0.295
4	-0.066	-0.174	-0.162	-0.155
5	0.165	0.137	0.134	0.136
6	0.158	0.283	0.266	0.272

The design variables chosen for this comparison define the mid-span camber (3,4) and leading edge droop (5,6) of the conical delta wing. They are displayed because they are the most highly sensitive design variables and dominate the progress of the optimisation, therefore accuracy of their value is of greatest importance to the optimisation.

For all design methods used during this thesis, the inviscid adjoint Euler method has been used. Here, the convergence of the adjoint-Euler equations is shown for the conical wing case at CL=0.4 M=1.62.

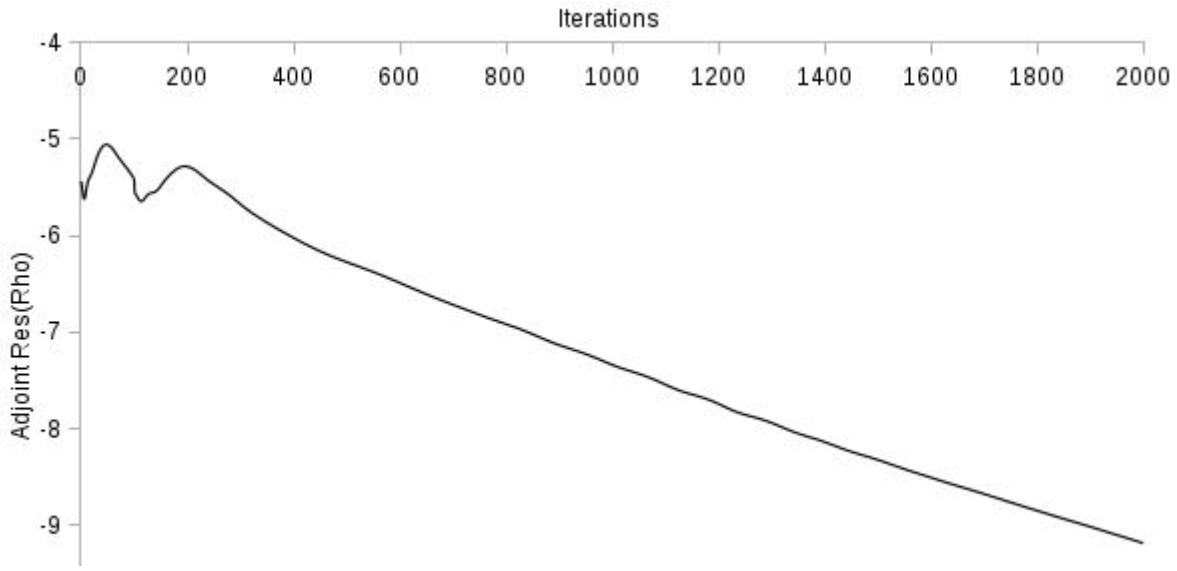

Fig 3.10 Convergence of Adjoint-Euler equations for inviscid sensitivity analysis (Log scale)

The adjoint-Euler calculations appear to converge linearly when residuals are plotted on a log scale in figure 3.10, after a few oscillations in the first 350 iterations of the solver. From the 350th iteration, the adjoint density residual converges by a further 3.5 orders in 2500 iterations. After this time the integrated gradients dCD/dS have stabilised and the solution is considered to be converged.

3.7 Surface Shape Parameterisation

Parameterisation is the practice of defining some surface shape by a discrete set of variables which either directly or indirectly determine the shape of the object to be designed. For the purposes of design optimisation, this means that the code needs to know the value of dZ/dD for every surface point with respect to every design variable for camber optimisations.

For the purposes of all studies in this thesis, a 3D free-form deformation method is used[79]. This method creates a virtual bounding box around the wing geometry and assigns every surface point within it a local set of coordinates. The FFD box is split into discrete sections in I,J,K co-ordinates where each vertex on the exterior of the box is defined as a control point. The faces of the FFD box are treated as a bezier-surface using the De Casteljau algorithm[80] to ensure smoothness.

This way, when the control points are moved and the box is deformed, the global coordinates of the surface will change in a smooth manner - i.e. the surface will move.

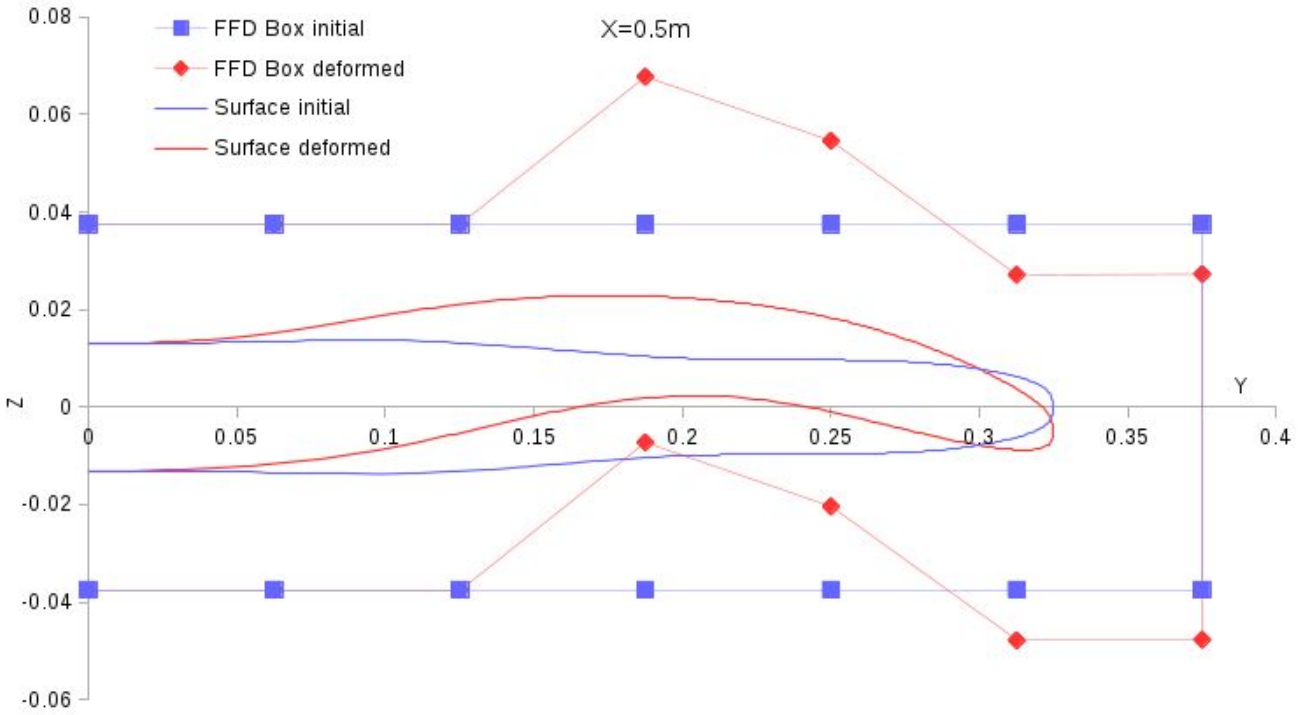

Fig 3.11 2D representation of initial and arbitrarily deformed wing geometry and bounding FFD boxes.

It is clear from figure 3.11 that the deformed surface shape, shown in red, is smooth despite dramatic changes in camber design variable, between the 4th and 5th control points from the wing root at the left.

For the design studies in this thesis, an FFD camber method is used extensively; meaning that the control points on the upper and lower surface both move in unison; effectively controlling only the mean camber line of the wing in question. This conserves the thickness distribution of any wing to be designed; meaning that within the context of aircraft design, no interior structures, mechanical components or fuel tank will necessarily need to change in size or layout. More importantly, this also means that any conical optimisation results can be compared with Mason *et al's* [33] wing designs with the same spanwise thickness distributions.

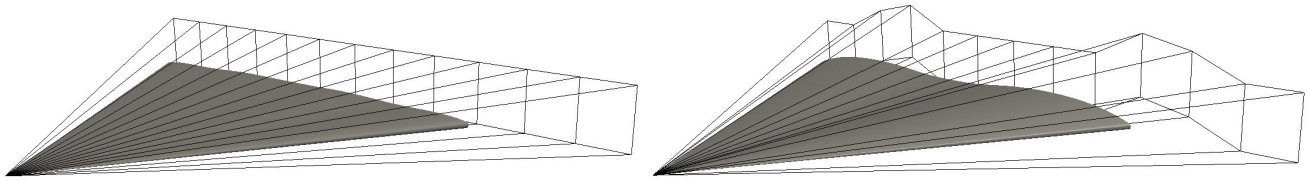

Fig 3.12 3D representation of initial and deformed wing geometry and bounding conical FFD box.

Figure 3.12 shows a 3D representation of the conical FFD box and its effect on the conical surface geometry. Variation of control points results in a purely conical deformed wing geometry, which is completely smooth and has an identical thickness distribution to the uncambered wing at every point on the planform.

3.8 Volume Grid Deformation

The GMRES[68] linear elasticity method is used in order to deform the volume mesh after each deformation of the wing surface grid. The stiffness of each cell can be scaled by either it's distance from the wing surface or the inverse of it's volume - this way the structure of the grid can be preserved more strongly near the wing surface and more weakly towards far-field boundaries. Each grid deformation step requires about 300 iterations of the GMRES linear elasticity solver contained within SU2_DEF, reducing the residual by 17 orders in this time.

The grid deformation method used in the following optimisation studies took approximately 5-10 minutes to conduct the ~300 iterations necessary to achieve a smooth CFD grid.

For the purposes of the design processes used in this study, the stiffness of each cell (K) is scaled by the inverse of the volume of the cell.

$$K = 1/\text{volume} \qquad \text{Equation 3.24}$$

It has been found during the making of this thesis that the volumetric grid deformation methods used here are robust and accurate for inviscid grids with no boundary layer mesh; however can behave poorly in the presence of very high aspect ratio and very small volume cells associated with high-Re viscous grids with wall spacings in the order of $<1x10^{-5}$m.

Chapter 4 Supersonic Manoeuvre Wing Design Optimisation

In this chapter, a variety of supersonic manoeuvre wing aerodynamic optimisation problems will be presented and solved using the methodology outlined in chapter 3. The results of these optimisations will then be presented, interrogated, analysed and compared.

4.1 Conical Supersonic Manoeuvre Wing Optimisation

Objective 1: To determine the most effective and most efficient optimisation strategy for this pressure drag minimisation problem

Two strategies for solving the lift-constrained drag minimisation problem are presented and compared. The main difference between the two strategies concerns the manner in which lift is maintained during the design process. The first strategy, referred to as hard constrained optimisation, utilises the gradients of both lift and drag for each design variable at every design iteration; conserving lift by means of both camber and angle of incidence. The second strategy, referred to as soft constrained optimisation, utilises only the drag gradient to drive the camber design of the wing, and conserves lift by means of altering the angle of attack during each function evaluation (flow solution). The second strategy requires less computational effort per design iteration than the first.

Minimise objective function: I = CDp

Subject to constraint functions: G_1 = CL > 0.4
G_2 = R(U) ~ 0

Design Variables: 7 Conical free-form deformation camber points and α

Both optimisation strategies analysed below conform to the same pressure drag minimisation problem, as outlined above.

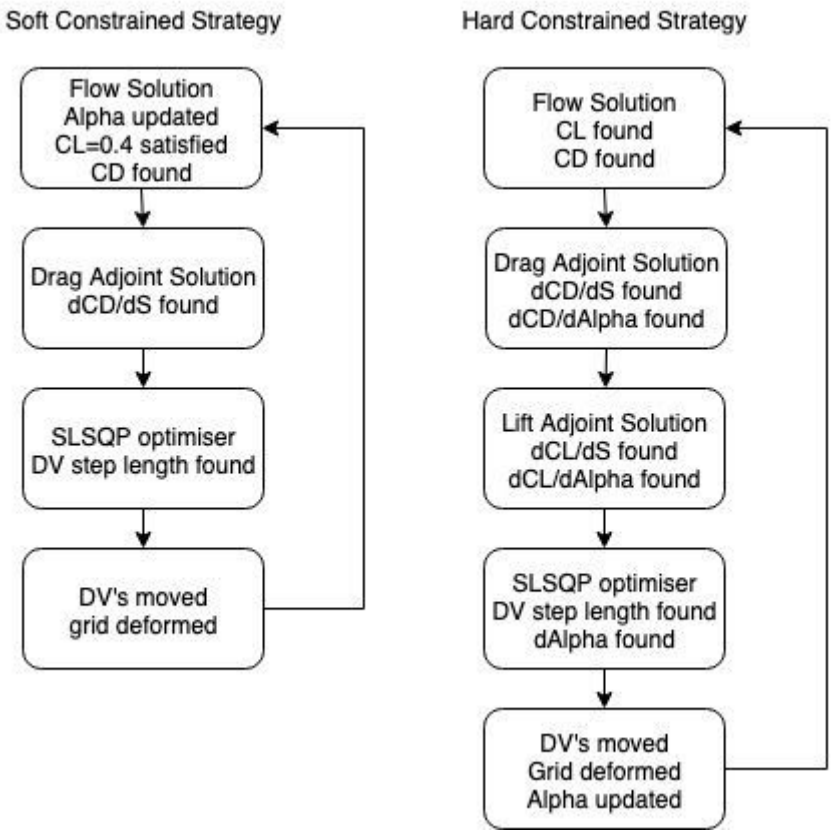

Fig 4.1 Comparison of constraint strategies flow chart

Figure 4.1 shows details of the differences in how each constraint strategy works. It is clear from this flow diagram that the soft constrained strategy requires one fewer step per design iteration than the hard constrained strategy. This is due to the way that the soft strategy satisfies it's lift constraint during the flow solution with an α which is separate from the design variables. The hard strategy requires that α is treated as a design variable and calculates the gradient dCL/dS for every point on the surface; the value of which is given to the SLSQP optimiser where the step length of each design variable for the next design is calculated using the differentiable augmented lagrange function introduced by Schittkowski [81].

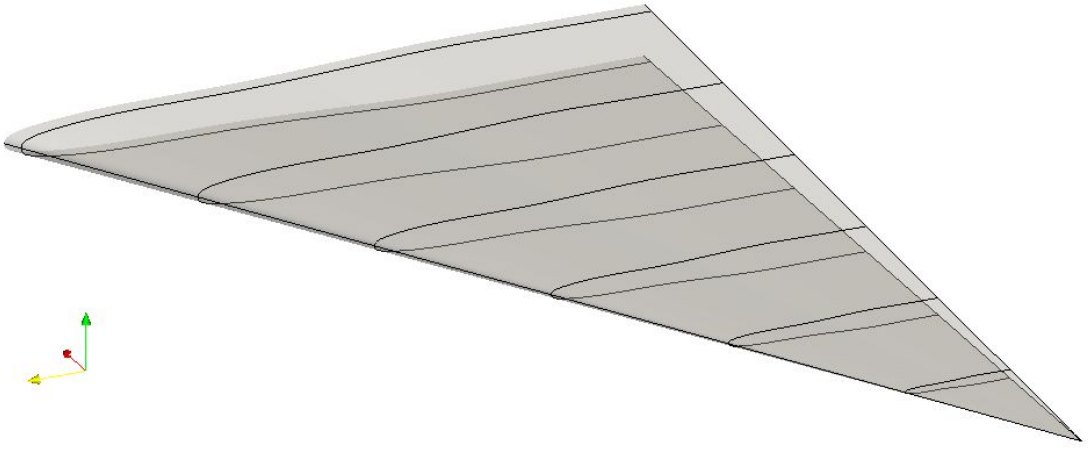

Fig 4.2 3D view of the initial conical wing semi-span geometry with spanwise slices at 0.1m intervals.

Figure 4.2 shows a 3D elevated view of the initial conical flat delta wing shape. Spanwise slices have been added at 10 cm intervals from the apex, giving a sense of the conicity of the wing and of it's scale. The surface has a level of transparency allowing the lower half of the wing to be visible, reinforcing that the initial shape is symmetrical about the XY plane and therefore has no camber. The red arrow on the axes symbol in the lower left corner denotes the X-axis, which is the freestream flow direction at α=0. Lift and Drag forces are calculated by pressure integration over the conical surface shown here only, and therefore excludes the effect of base drag on the design process.

Fig 4.3 Perspective Views of the initial conical wing semi-span geometry

Figure 4.3 is a 3-view diagram of the initial wing geometry, further clarifying the spanwise cross-section of the wing and the conicity of the surface. The chord length of the wing at the root is 60.96cm and the leading edge angle is 57 degrees. The local thickness/span ratio at every chordwise location along the wing root is 0.04. During optimisation, the wing geometry will be constrained through parameterisation so that it's planform when projected as in figure 2 does not change; also the thickness distribution as seen on the right hand side of figure 2 will not change due to camber-only deformation.

The conicity of the surface cannot be changed during the optimisation thanks to the conical FFD parameterisation method. This means that any design produced will have a surface which can be expressed as an infinite series of straight lines connecting the wing apex and base (or trailing edge).

4.1.1 Initial Flat Wing Inviscid Surface Pressure, Drag Sensitivity and Flowfield.

The results of the flow and adjoint simulations used to initiate the first step of each design process are shown below. Since both the flow solution and adjoint surface sensitivity are conical in nature, it is sufficient and accurate to display the surface pressure and sensitivity distributions as 2D spanwise slices. It can be stated that these distributions are true at any chordwise location chosen for the slice.

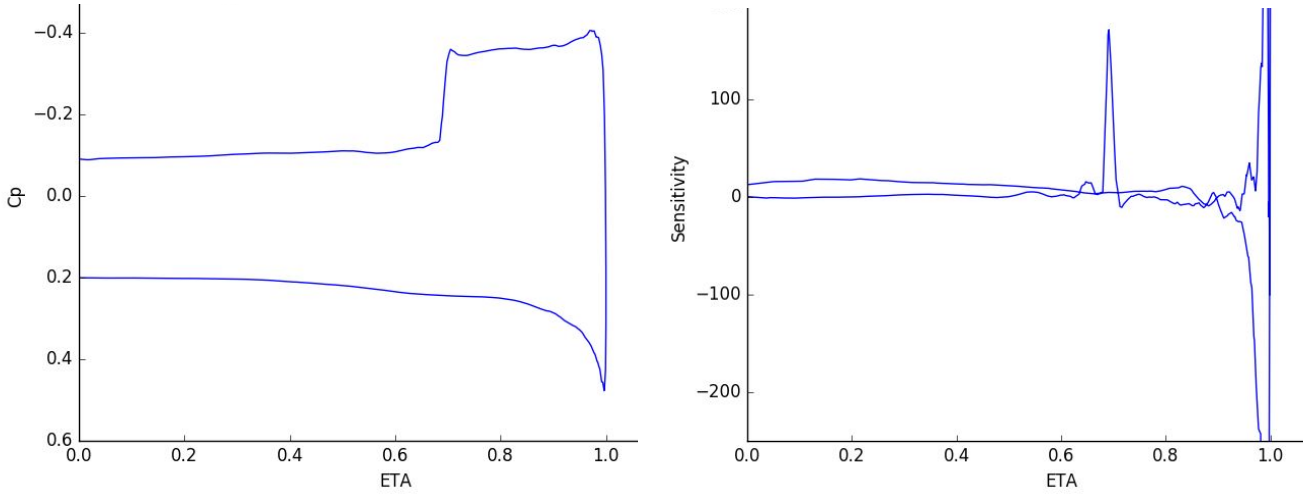

Fig 4.4 Spanwise pressure coefficient and drag sensitivity (dCD/dS) taken at a slice at X=0.3m for the initial flat wing.

On the left of figure 4.4 the plot shows the pressure coefficient distribution of the uncambered delta wing at M=1.62, CL=0.4 as calculated by the inviscid Euler equations. The starting wing shape - a zero-camber thick conical delta wing with round leading edge - clearly produces an embedded cross-flow shockwave at 0.65 ETA, with a pressure coefficient of -0.37 on the upwind side and -0.1 on the downwind side.

On the right of figure 4.4 the plot shows the adjoint drag sensitivity dCD/dS distribution of the uncambered delta wing using the flow solution on the left to initialise the adjoint solver. The drag sensitivity plot shows that the embedded crossflow shock is a major source of drag - along with the attachment line and subsequent expansion region at the leading edge. Overall, the surface sensitivity suggests that raising the upper surface at 0.7 ETA and lowering the leading edge should result in a reduction in pressure drag.

This starting point for the optimisation is where the value of each camber design variable is zero, and the angle of attack is 8.45 degrees. These values will be allowed to change during each optimisation strategy.

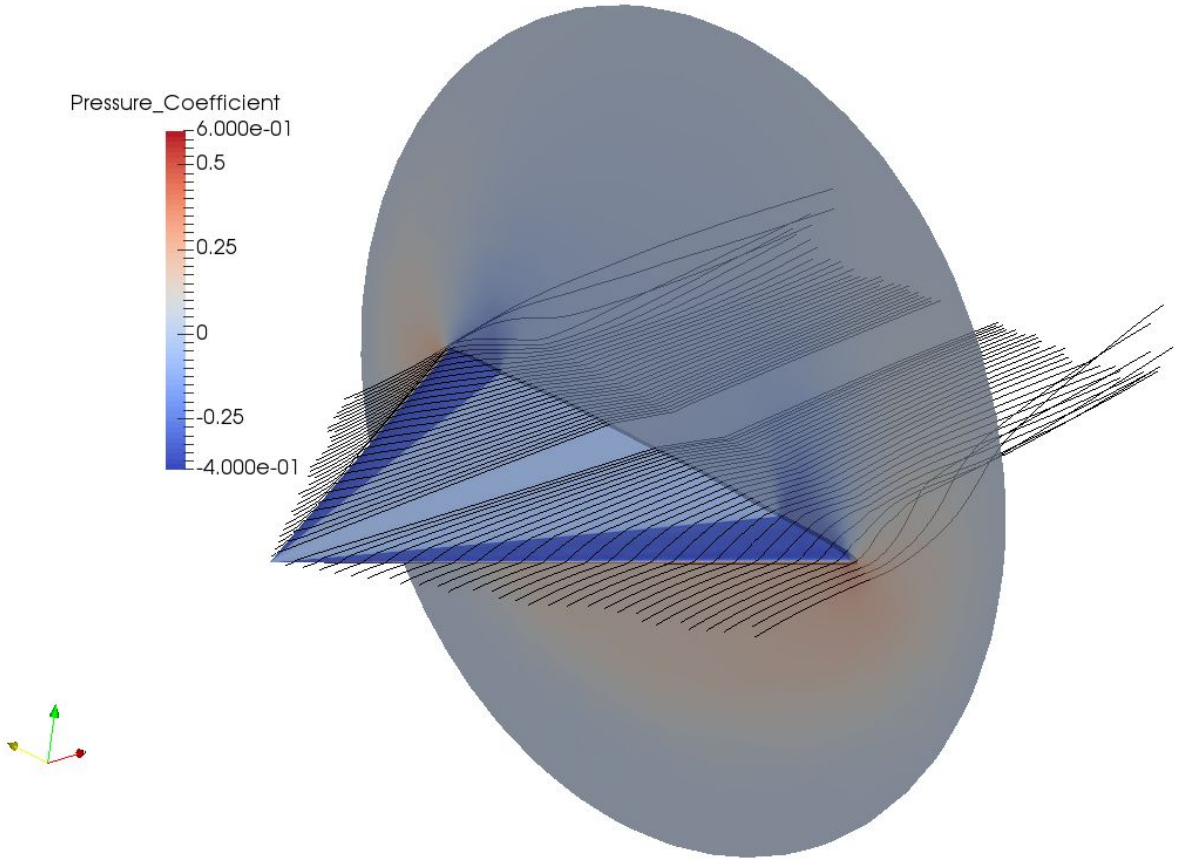

Fig 4.5 3D inviscid flowfield of the flat conical wing at M=1.6, CL=0.4

Figure 4.5 shows the surface pressure and 3D flowfield of the flat conical wing at the design condition. A 2D slice through the solution domain at X=0.6m shows the pressure distribution of the conical flowfield; highlighting the bow shock located under the lower surface and the embedded cross flow shock located above the upper surface of the wing. 3D streamlines show the flow approaching the wing at a positive incidence angle and expanding around the leading edge with no sign of flow separation, and then turning quickly through a small angle as the air passes through the cross flow shockwave. At the wing tips, the flow visibly curls up and forms a strong pair of wingtip vortices. This flow field corresponds with zone 5 in the stanbrook-squire diagram from [46].

4.1.2 Design History

Design histories are used to show how the values of aerodynamic forces and design variables evolve during each step in the optimisation process. Iteration number one is the initial wing design; whose shape, flow characteristics and surface sensitivity are presented and discussed above. Each subsequent iteration is the result of a perturbation in the design variables dictated by the SLSQP optimiser. The following figures compare the histories of both optimisation strategies over 8 design iterations.

Figure 4.6 shows the history of CD over 8 iterations of both optimisation strategies. For the first 3 iterations, the hard constrained strategy produces lower drag designs than the soft constrained method, however during these iterations the CL is lower than 0.4. From the 4th design onwards, the soft constrained strategy yields lower drag values than the hard constrained strategy. The 4th iteration of the hard constrained history has a higher CD value than the 3rd, due to the optimiser increasing the

CL in order to satisfy the constraint. Both strategies converge after 8 iterations, with the soft constrained method achieving the lowest CD value.

Figure 4.7 shows the history of CL over 8 iterations of both optimisation strategies. For the first 2 iterations, the hard constrained strategy produces lower lift designs than the soft constrained method, meaning that this method has not satisfied the lift constraint during these iterations. From the 4th design onwards, the hard constrained strategy has a CL value very slightly higher than the specified constraint (1 lift count). Some of the difference in drag between the two final designs is attributable to the small difference in lift. The soft constrained strategy only results in designs which do not vary from the constraint lift coefficient and are therefore all feasible.

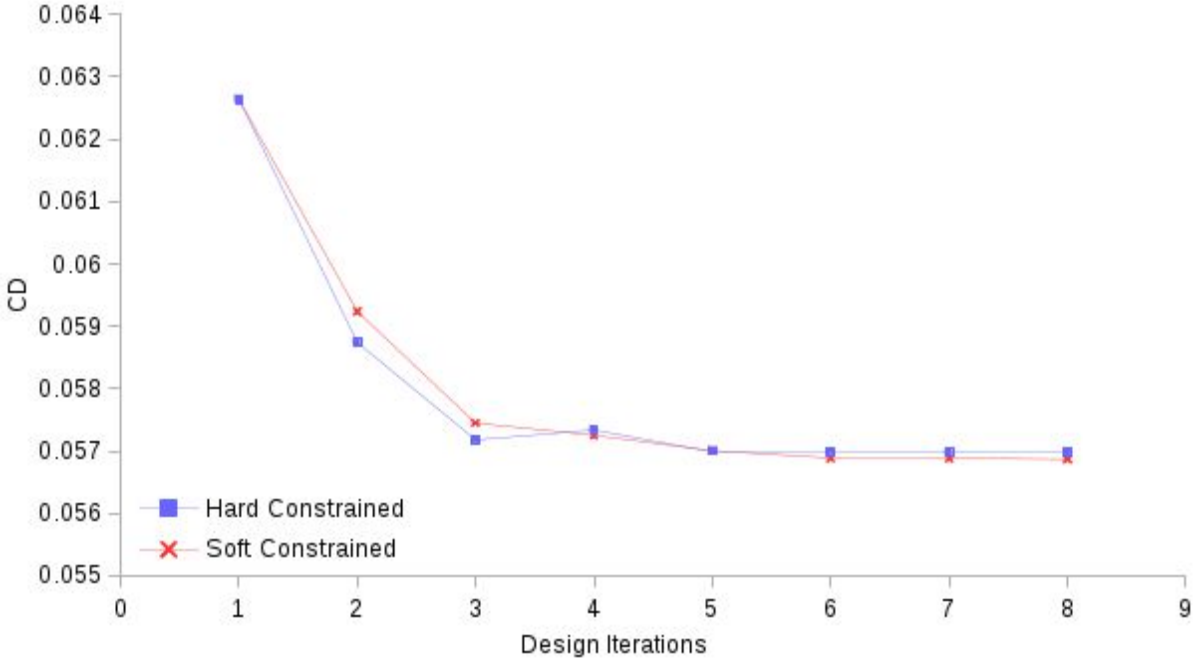

Fig 4.6 history of CD for each optimisation strategy

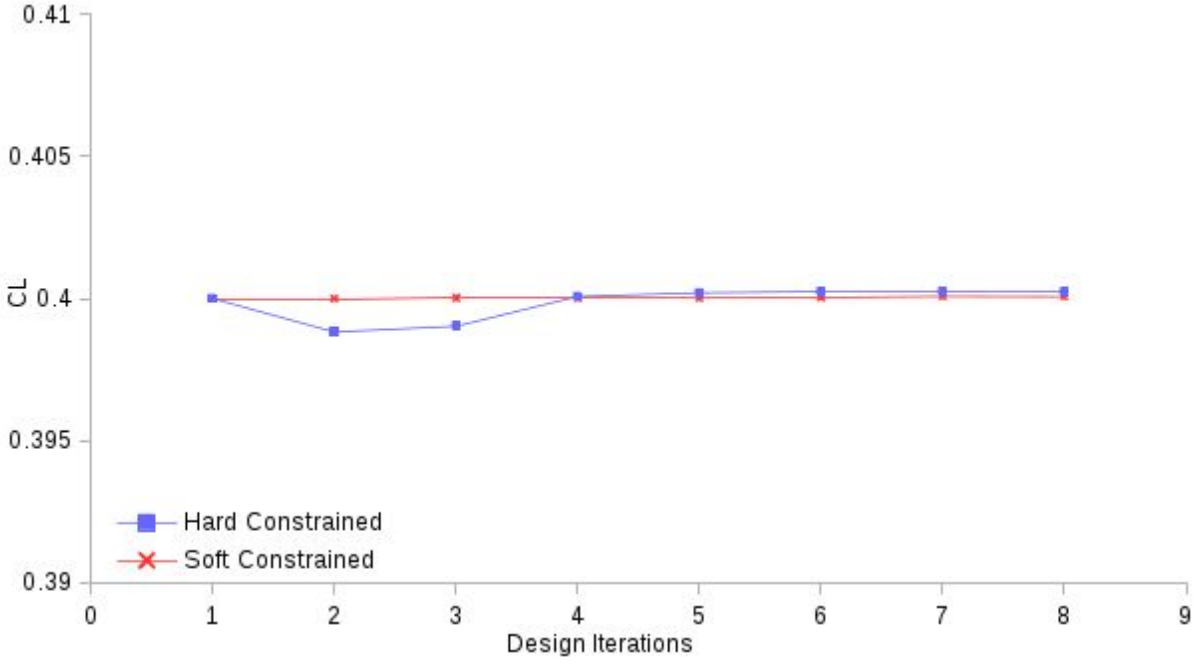

Fig 4.7 history of CL for each optimisation strategy

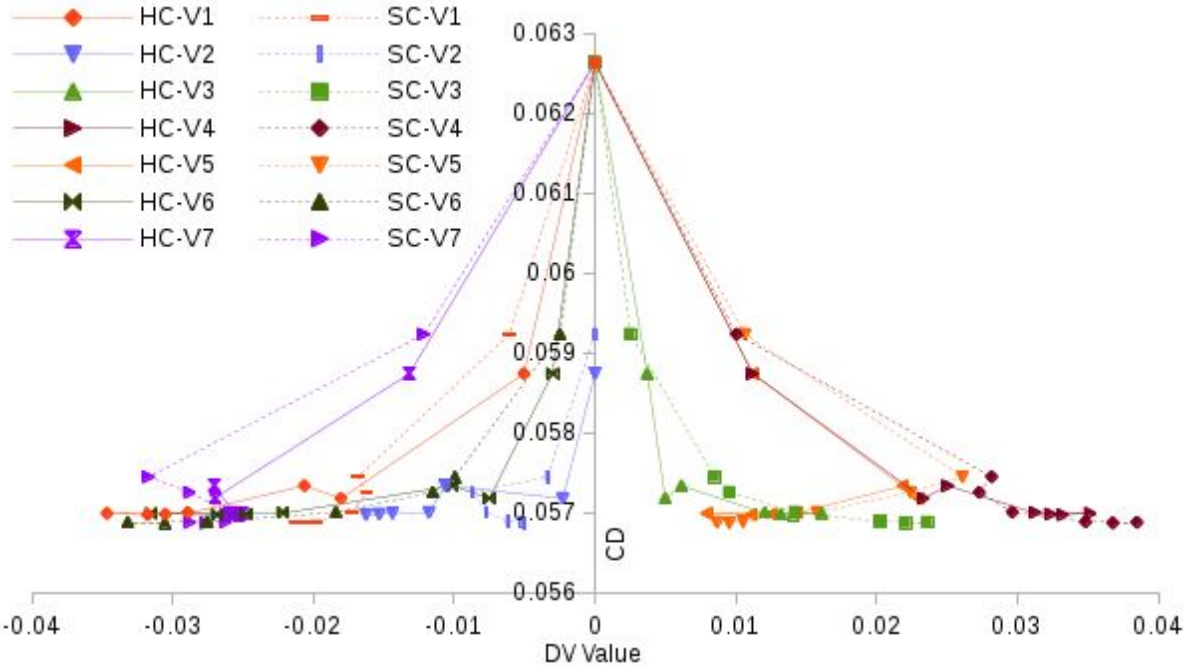

Fig 4.8 comparison of design space exploration for each design variable during both optimisation strategies

The design space is analysed in figure 4.8 by plotting the histories of design variable value against drag coefficient. Each design variable shows a roughly quadratic relationship with objective function (CD), with variables 5 and 7 both clearly forming ‘buckets’ with both sides of the optima having been explored, whereas the other variables; 1,2,3,4 and 6; have only explored the design space on one side of the optimum solution. Comparing histories between the hard and soft method one sees that there is broadly similar design space exploration and optimum values, especially for mid-span and tip camber variables. However, root camber variables 1 and 2 do show different optimum solutions, since these have an effect on the incidence angle of the wing root; which is of less significance in the soft optimisation since incidence is continuously varied during the flow solution.

It must be noted that since these variables have not been independently varied; the visible design space is a result of concurrent deformation of each design variable together. To get a better idea of the influence of each design variable on the optimum solution; it is important to take into account the design variable sensitivities shown in table 3.1 and the surface sensitivities shown in Figure 4.4.

Figure 4.9 shows how selected design variables have varied throughout the optimisation process and demonstrates a highly sensitive relationship for design variable 7, which dictates mid-span camber and shock control; and a relatively flat sensitivity for design variable 1, which dictates root incidence and conical dihedral angle. The conclusion that can be drawn from this plot is that some design variables can have a much stronger influence on drag than others. It will be seen later in this thesis that multiple design methods result in ‘minimum drag’ designs which have highly different geometries near the wing root - further indicating that in this conical case, the wing root has less influence on drag than the rest of the wing surface. This reflects the differences in surface sensitivities shown previously in figure 4.4.

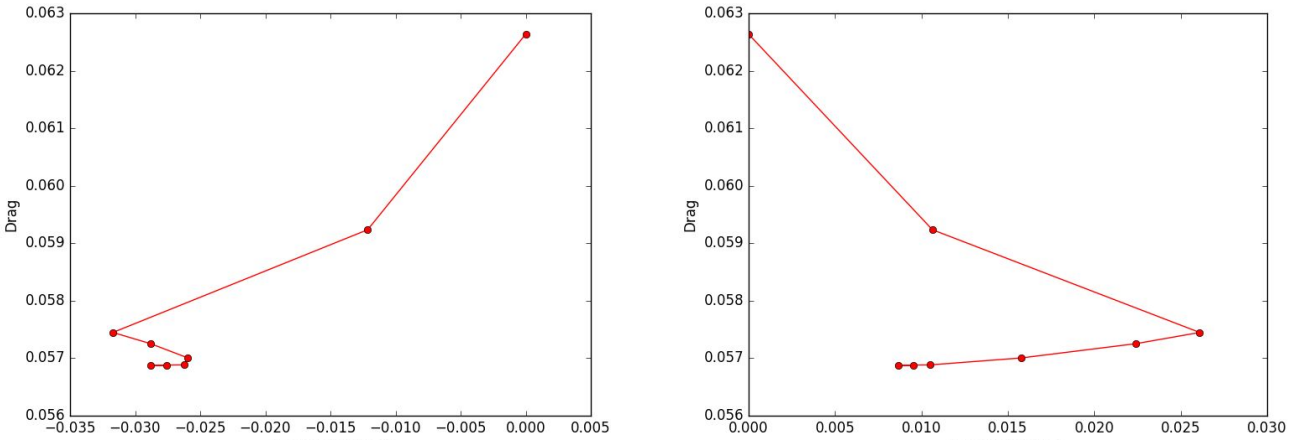

Fig 4.9 Drag vs design variable value in the soft constrained optimisation procedure, DV7 (left) and DV5 (right).

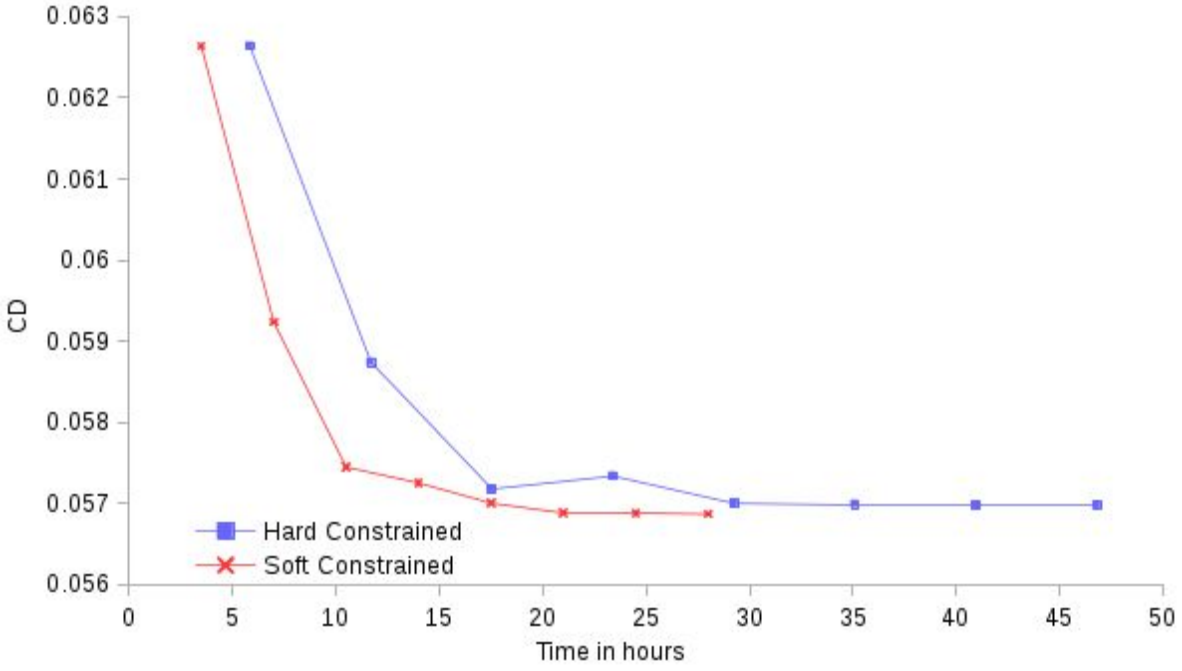

Fig 4.10 comparison of design time and drag history in the optimisation process.

The total number of hours required has been used here as a direct measure of computational cost. These optimisations were carried out using Machines with 32 Intel pentium CPUs at 2GHz and 24GB of RAM. Figure 4.10 demonstrates the major benefit of the soft constrained strategy - reduction in time required to produce an optimum design. The soft constrained strategy returns a converged optimum design in 28 hours with 16 flow and adjoint solutions, however the hard constrained strategy returns a converged optimum design in 47 hours with 24 flow and adjoint solutions. This proves a very substantial saving in the cost of generating a design for the soft constrained optimisation strategy.

4.1.3 Comparison of Optimum Design Solutions

Here, the inviscid flow solutions from the optimum designs of each optimisation strategy are compared with each other. Any differences in optimum design shapes and flow characteristics are solely a result of the different strategies of optimisation studied. The SLSQP constrained minimisation algorithm was used in both cases for calculation of step length and direction, based on gradients provided by the adjoint method and function estimations provided by Euler CFD calculations.

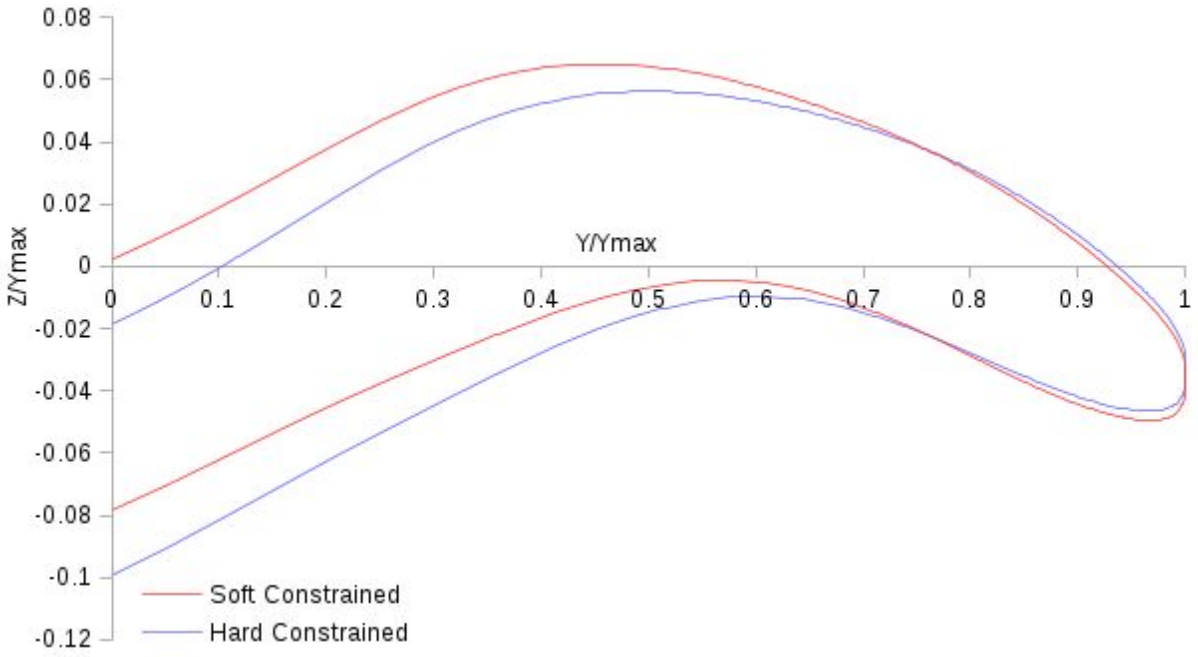

Fig 4.11 Comparison of optimised spanwise cross-sections for each strategy

Figure 4.11 shows the cross-sectional geometry of each optimum wing design, taken at X=0.3m with dimensions in meters. Both optimisation strategies have resulted in a similar M-shaped conical cross section, with leading edges drooped towards the flow direction and root sections lowered to increase local AOA. The mid-span has been moved upwards in the vicinity of the shockwave in both cases, providing a cross-flow camber profile which reduces the strength of shockwaves on the leeside of the wing.

The major differences between these designs are that the root of the wing designed using the soft constrained method is less drooped than the root of the wing designed with a hard lift constraint. This reiterates the finding that wing root spanwise camber in this supersonic conical case has very little effect on pressure drag within quite a wide range of shapes.

Figure 4.12 shows the inviscid conical Cp distribution of each optimum conical wing design. Both optimisation strategies have resulted in designs which produce similar conical pressure distributions, showing that the loading at the leading edges of both wings has been reduced, whilst the loading at the midspan and root have been increased. This results in significantly reduced shockwave strength on the leeside of the wing, but also more desirable lift distribution across the wing span - shown later in figure 4.28 - reducing drag through reduction in wingtip vortices. The conical camber M-shape has the effect of creating a wash-out effect across the span of the wing. It is observed here that the optimiser has found a balance between drag due to shockwaves and drag due to wingtip effects.

This balance means that if the shockwave drag was reduced, the lift-induced drag would increase by a larger amount than was gained by reducing the shock; additionally if the lift-induced drag was

reduced then the shockwave drag would increase by a larger amount than was gained by improving the lift distribution. Reduction in shockwave drag would necessitate an increase in lift loading towards the wing root, causing the lift distribution to become more triangular. Reduction in lift-induced drag would necessitate an increase in lift loading towards the wing tip, requiring a larger pressure differential on the outboard section of the wing which would increase the strength of the shockwave.

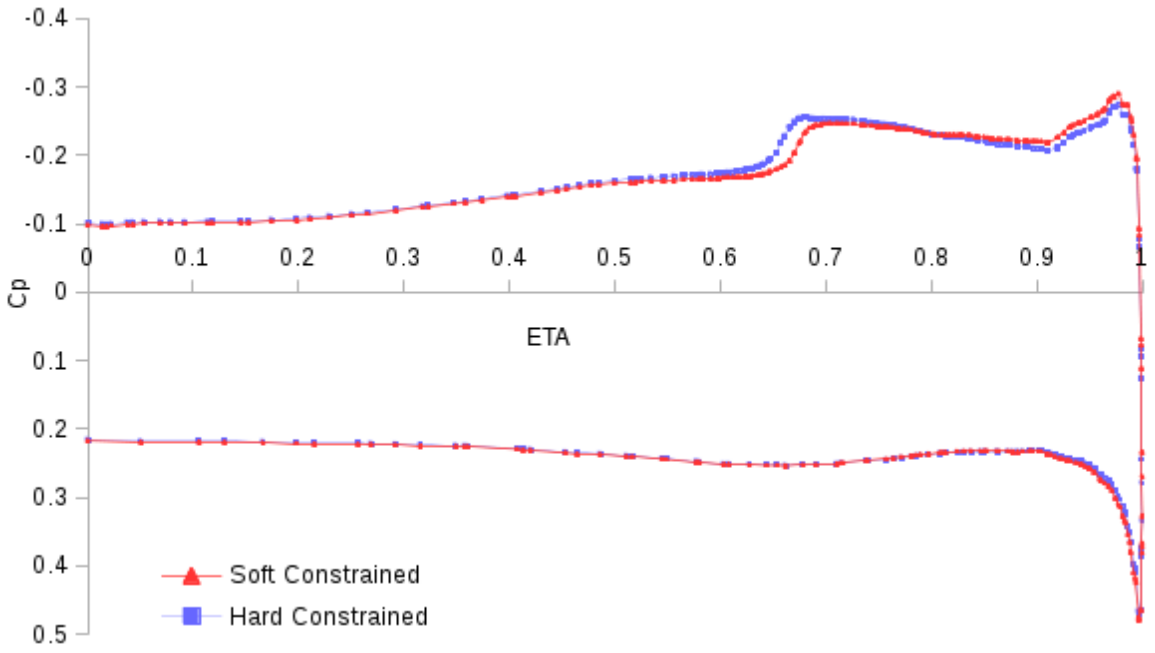

Fig 4.12 Comparison of optimised spanwise Cp distributions for each strategy

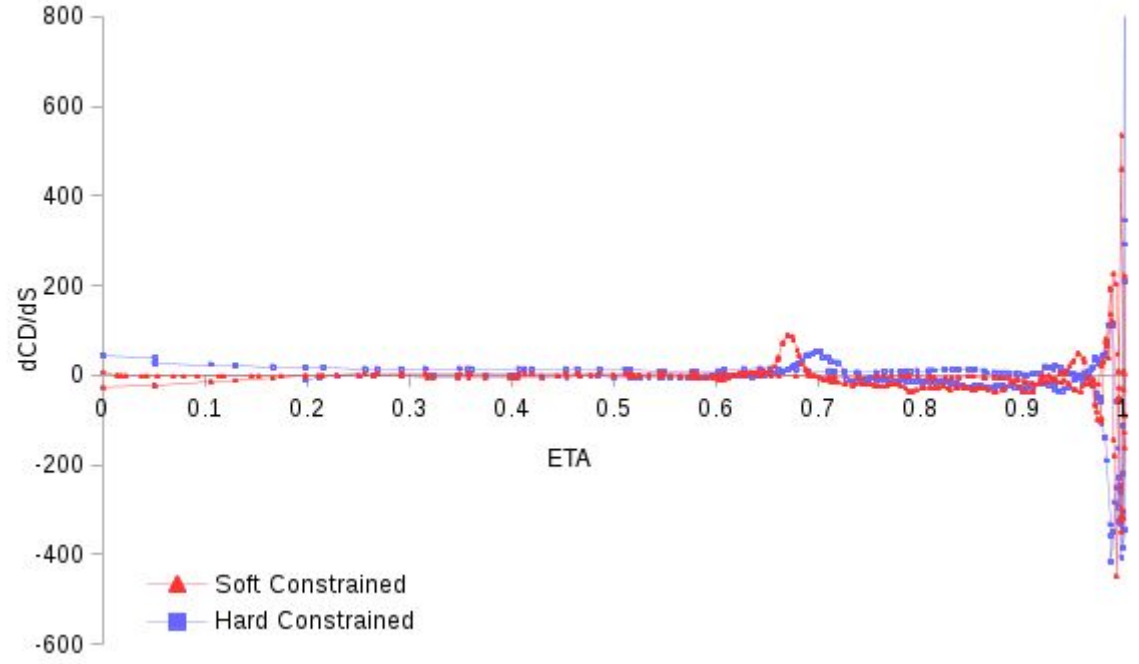

Fig 4.13 comparison of optimised surface sensitivities for each optimisation strategy

Figure 4.13 shows the drag sensitivities dCD/dS at a spanwise slice of each optimum wing design. The objective function gradient is calculated at every design step, including the final one. There remains some spikes in surface sensitivity around the small shockwave which exists in both optimised wings, however, the hard constrained optimum wing shows a smaller shockwave spike-but higher distributed sensitivity across the lower surface. Conversely, the soft constrained strategy has a larger sensitivity spike at the shockwave but near-zero sensitivity on the root and mid-section inboard of the shock.

4.1.4 Comparison of Optimum Designs from Local Optima Checking Study

The results of both strategies have been compared not only with each other but also with cases intended to test the design space for local minima. This test is performed for the hard constrained strategy by starting with an initial design which has a higher angle of attack, and thus higher CL. For the soft constrained strategy, the test is performed by starting with an initial design which has some camber already applied, in the form of leading edge droop towards the incoming flow direction.

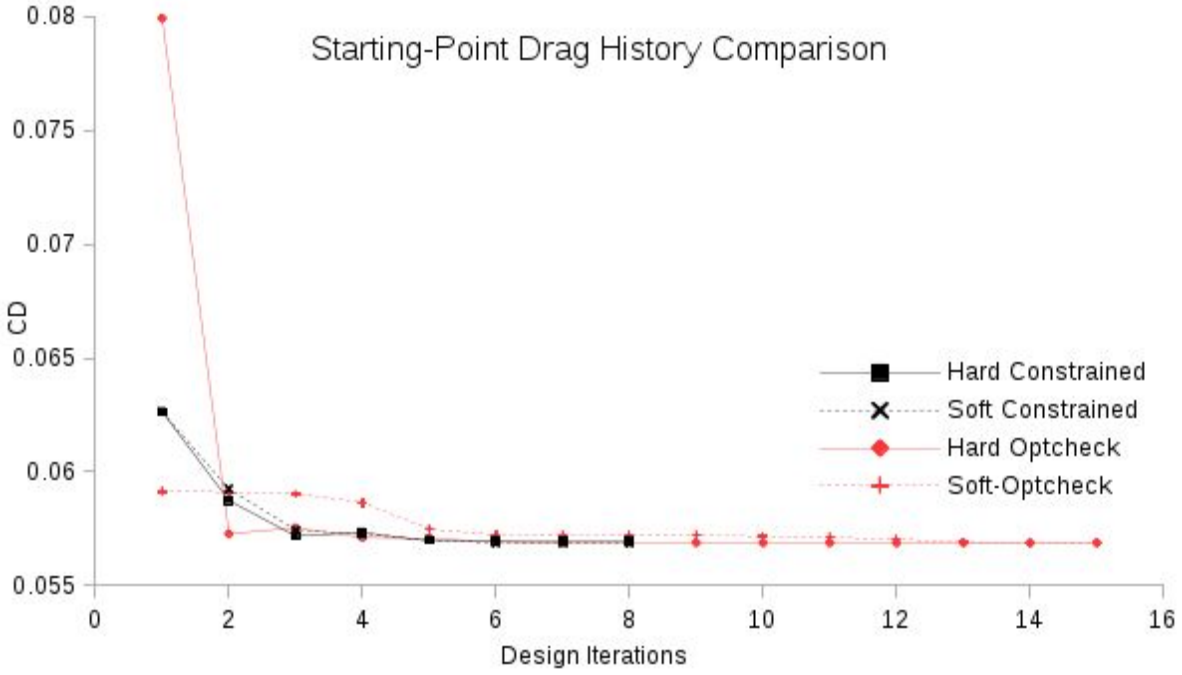

Fig 4.14 comparison of drag histories for both design strategies and checking for local optima

The drag histories of the hard and soft constrained optima-checking studies are quite different to the original optimisations, with the hard optima checking routine reducing drag very quickly after the first design step and the soft optima checking routine requiring 5 design steps to achieve any significant improvement. Both are converged within 15 design iterations.

In checking for the presence of local minima in the design space, the hard constrained strategy starting from a high AOA converges to the same final resulting drag value as both of the strategies described previously, however the soft constrained strategy starting from a pre-cambered design actually finds a final design with a slightly lower drag value than the other strategies. This indicates that the design space contains both local and global optima; and that both strategies found either a local optima or an inflexion point. However, the difference in drag between these optimum states is very small, leading to the question of whether the relationship between CD and design variable values is very flat in the region of the optimum solutions which have been found - as was investigated in figure 4.9.

Table 4.1 shows that the soft constrained strategy achieved an improvement of 1 drag count over the hard constrained strategy, in the same number of design iterations. This suggests that the soft constrained strategy has the potential to be more efficient in finding a good design than the hard constrained strategy, however this improvement is quite insignificant when taken as a fraction of the total drag.

In checking the optima, it can be seen that the hard constrained optimisation drew some benefit from having a high-CL starting point in that it's optimised drag coefficient was 1 point lower than when the starting point was at the design CL. The lowest drag value of any of the strategies was for the soft constrained method starting from a wing geometry with a leading edge drooped into the flow direction.

Table 4.1 comparison of starting and optimised performance values

Optimisation Strategy	Initial Performance	Optimised Performance
Hard constrained	CL=0.400 CD=0.0626	CL=0.400 CD=0.0570 Iteration: 8
Soft constrained	CL=0.400 CD=0.0626	CL=0.400 CD=0.0569 Iteration: 8
Hard constrained optima check	CL=0.453 CD=0.0799	CL=0.400 CD=0.0569 Iteration: 27
Soft constrained optima check	CL=0.400 CD=0.0591	CL=0.400 CD=0.0568 Iteration: 23

Figure 4.15 shows the initial starting geometries for the global optima check, using a spanwise slice taken from X=0.3m. The geometry for the hard constrained optima check is identical to the flat wing. However, is initially set at a high incidence angle in order to attain a high CL value. In contrast the starting geometry for the constrained optima check has been deformed and 'drooped' at the leading edge and mid-span, in order to place the leading edge design variables in a previously unexplored region of the design space. This is done because it was identified as the part of the unexplored design space most likely to contain further optimum solutions; due to a combination of high surface sensitivities and similarity to Mason et al's design.

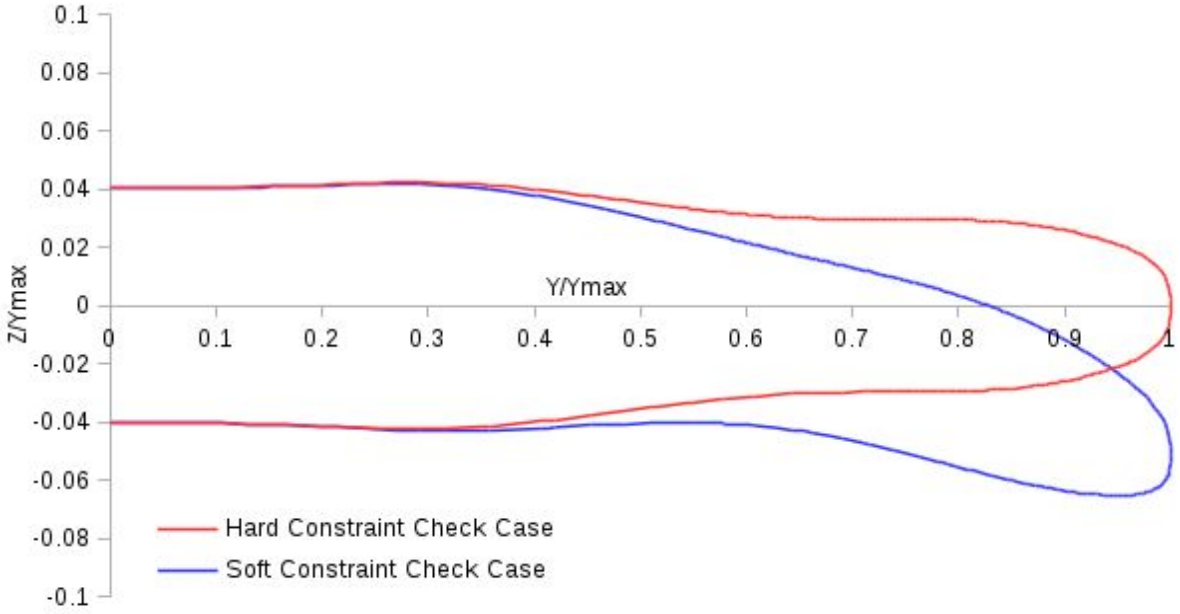

Fig 4.15 comparison of initial geometries for hard and soft constrained optima checking study.

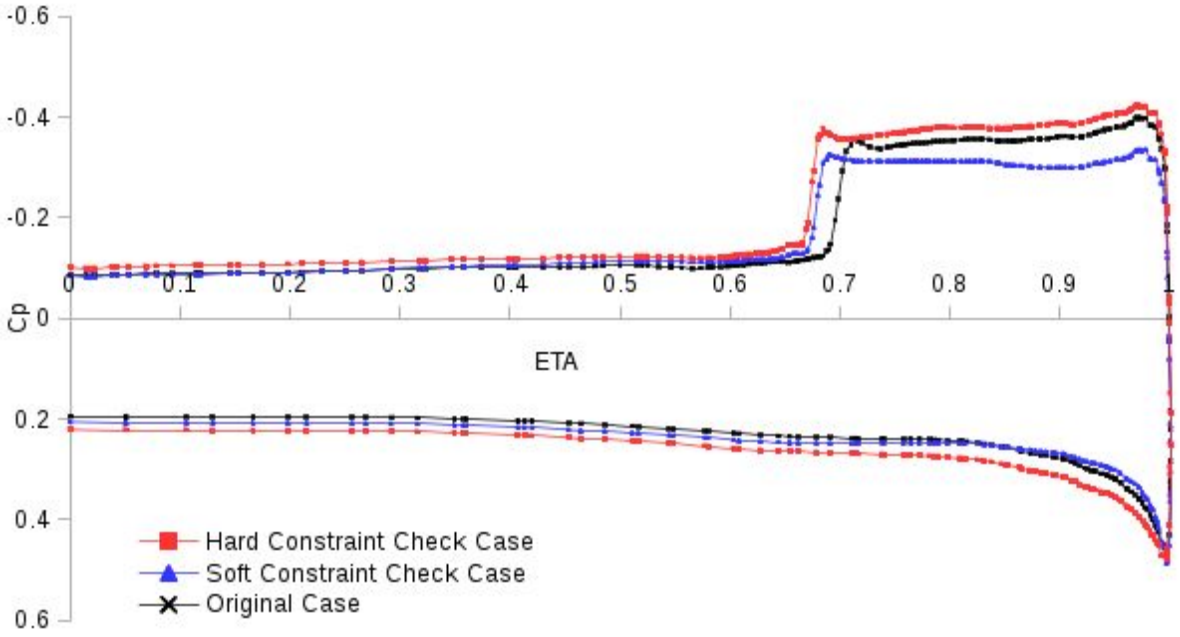

Fig 4.16 comparison of initial Cp distributions for hard and soft constrained optima checking study and original case.

Figure 4.16 shows the initial conical Cp distributions for the global optima check. The hard constrained flat wing at a high CL exhibits a strong cross-flow shock with suction peak at the leading edge. The soft constrained drooped initial wing at CL=0.4 shows a reduced but still strong cross-flow shock with equal suction peaks between leading edge and upstream of the shock. Lower surface pressure distributions are similar between these starting points with the high-CL flat wing having a slightly higher pressure coefficient near the wing root.

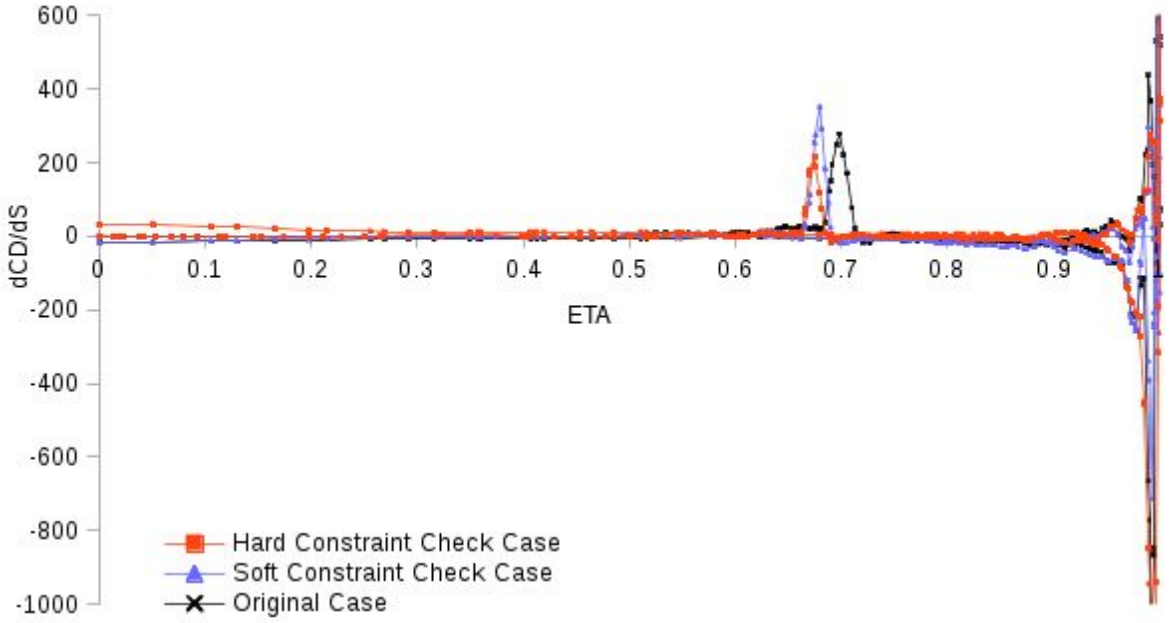

Fig 4.17 comparison of initial drag sensitivity distributions for hard and soft constrained optima checking study and original case.

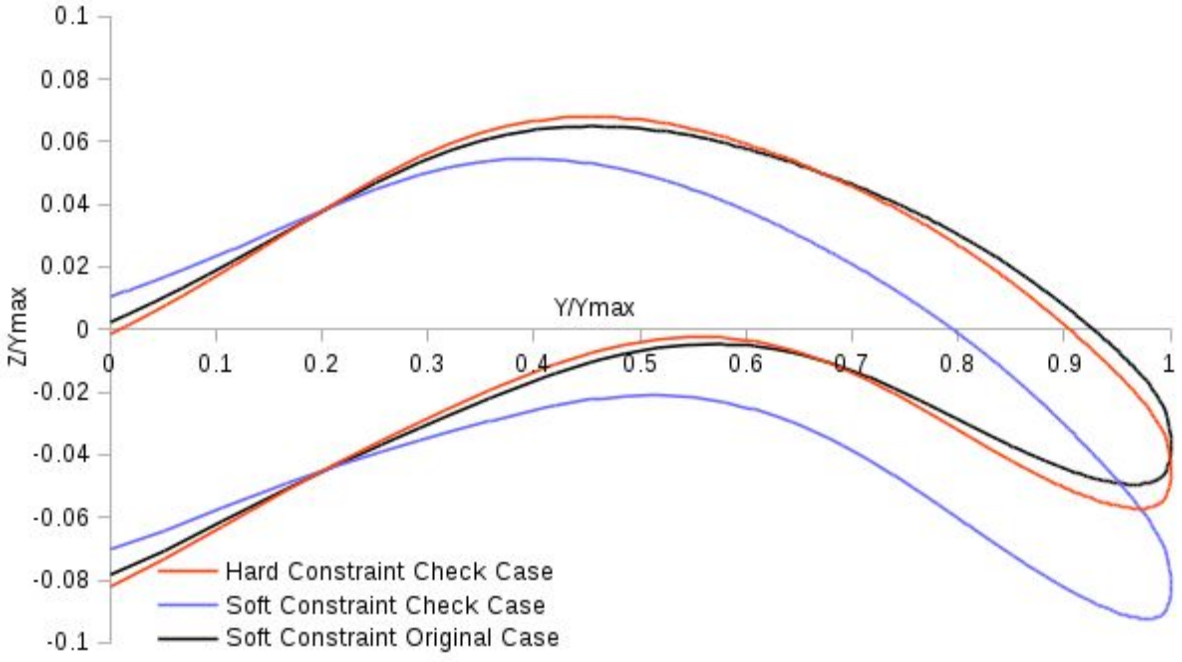

Fig 4.18 comparison of optimised conical camber shapes for hard and soft constrained optima checking study and original soft constrained case.

It is interesting to note that in figure 4.17, the pre-cambered design has a much larger sensitivity around the crossflow shock than the high-CL flat wing, even though the shockwave size is larger in the high-CL case. This indicates that the surface in this region will always rise when following the adjoint sensitivity gradient - unlike in William Mason et al's design. However, the pre-cambered starting design shows a more strongly negative sensitivity between the shock and leading edge on the

upper surface, meaning that the leading edge has even more tendency to droop down than the flat wing.

There is some visible difference in camber and droop between the resulting conical wing shapes produced by each optima checking study, as shown in figure 4.18. The hard constrained optimisation starting from a high initial angle of incidence has resulted in a slightly more cambered mid-span than the previous optimisations but similar leading edge and root positions. The soft constrained optimisation starting from a cambered initial shape resulted in an optimum shape with similar mid-span camber and leading edge droop, but a lower dihedral angle at the root, resulting in a much lower leading edge position.

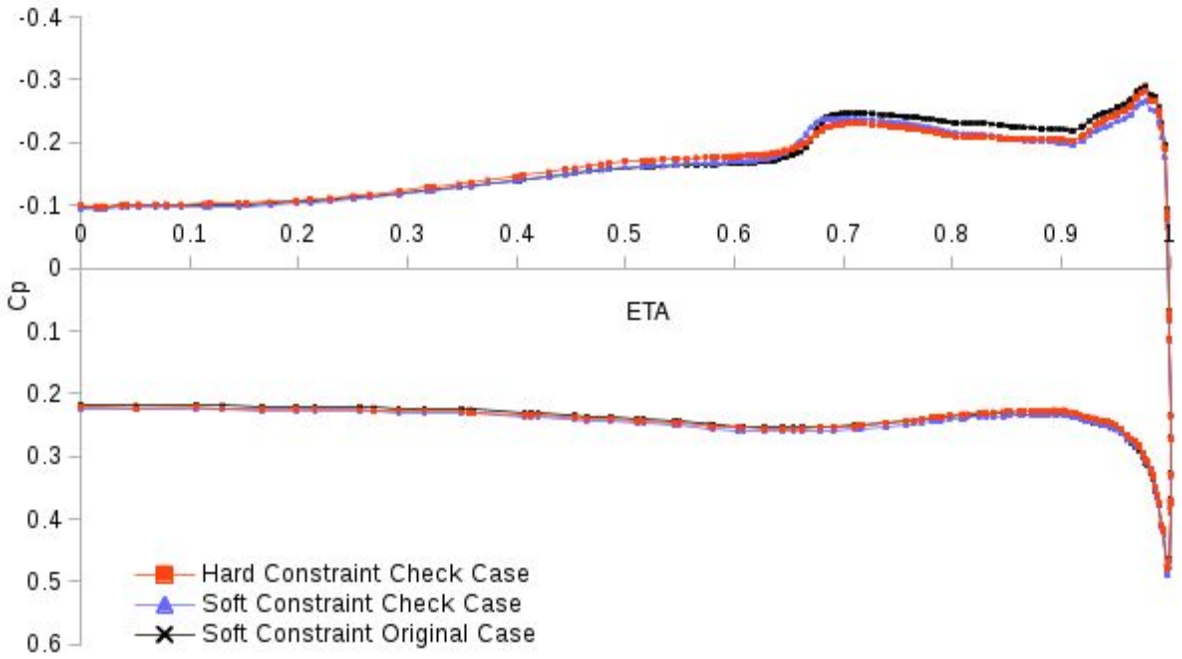

Fig 4.19 comparison of optimised Cp distributions for hard and soft constrained optima checking study and original soft constrained case.

The effect of the increased mid-span camber produced by the hard constrained optima checking study is a further reduction in shockwave strength as indicated by figure 4.19. The soft constrained optima check still has a similar shockwave strength to the previous optimisation, and very little difference in loading at the root. This shows that the conical dihedral angle at the root has a negligible effect on spanwise pressure distribution, compared to the other conical camber variations.

4.1.5 RANS Analysis of Optimum Design

In this section, both SU2 and Cobalt RANS solvers have been used in order to compare the performance of the optimum wing design shown in the previous section with Mason et.al's minimum drag wing design and the datum flat wing. Lift and drag polars will be analysed along with surface pressures and flow features at CL=0.4.

A conical structured grid comprising 100x100x200 hexahedral cells is used for all wing geometries in the comparison, having boundary layer cells with a surface spacing to satisfy Y+=1 ($Re/m=6.6x10^6$) and growth rate of 1.15.

The most meaningful comparison to make is the performance of each wing at the design point; since this is the main objective of the study. Values of 3D drag coefficient, broken down into friction and

pressure components are shown for each wing geometry, with M=1.62, Re/m=6.6x10^6, CL=0.4; as calculated by both SU2 and Cobalt solvers.

Table 4.2 comparison of drag coefficients at the design condition for various wing geometries

Geometry	CDtotal		CDfriction		CDpressure	
Solver	SU2	Cobalt	SU2	Cobalt	SU2	Cobalt
Flat Wing	0.06840	0.06932	0.005803	0.007566	0.06260	0.06175
Mason *et.al.*	0.06361	0.06500	0.005592	0.007622	0.05801	0.05738
Adjoint Optimised	0.06226	0.06387	0.005303	0.007615	0.05696	0.05626

It is clear from table 4.2 that the adjoint optimised wing design has the best performance at the design condition, improving upon the flat wing drag by 8.98% or 61 drag counts and Mason *et.al*'s minimum drag design by 2.12% or 13.5 drag counts. This result shows a clear advantage of the adjoint method for this design problem, it's ability to efficiently optimise large numbers of design variables means that it has more geometrical freedom to find an optima and thus generated a better design. It is interesting to note that both adjoint optimisation strategies resulted in designs with better performance at the design condition than the other design methods.

The largest contributing factor to the total drag reduction is pressure drag, which is comprised of CDwave+CDinduced. In order to explore these factors further, pressure distribution, flow-field and lift distribution will be analysed in greater detail.

4.1.5.1 Flow-field visualisation

The following images show each of the wing surfaces with streamlines denoting local surface shear force direction and coloured by local pressure coefficient. The local surface shear force direction informs us further on the flowfield of each respective wing, revealing the presence of separation, vortical flows and surface-impinging shockwaves (if present). The pressure coefficient colour scale helps to identify these flow features and also to illustrate that each flow field is conical in nature.
Figure 4.20 shows the upper surface of the uncambered conical wing at M=1.62, CL=0.4 and Re/m=6.6x10^6. Surface coloring denotes local pressure coefficient and the black lines on the surface denote local shear direction. This figure clearly visualises the embedded crossflow shockwave and demonstrates the shock-induced separation region. The flow at the leading edge is attached, with flow separation line just upstream of the shockwave. There is a gradual increase in pressure coefficient across the separated flow region and is constant in the subsequent attached flow region. The separation region with reattachment indicates the presence of a vortex above the wing at around 0.6<ETA<0.8.
Figure 4.21 shows the 3D viscous flowfield of the flat conical wing at the design condition. A 2D slice through the solution domain at X=0.6m shows pressure distribution and streamlines using the Y and Z components of momentum of the conical flowfield; highlighting the bow shock located under the lower surface and the embedded cross flow shock located above the upper surface of the wing, with associated shock-induced separation. The symmetry plane shows pressure distribution and streamlines using the X and Z components of momentum, highlighting the bow shockwave below the wing and the expansion fan above the wing. 3D streamlines coloured by Mach number show the flow approaching the wing at a positive incidence angle and expanding around the leading edge with no leading edge flow separation, and then turning quickly through a large angle as the air passes through the cross flow shockwave and then forms a tight vortex of separated flow. This vortex crosses through

the X=0.6m 2D slice just downstream of the crossflow shockwave, further illuminating how this vortex is formed. This flow field corresponds with zone 4 in the stanbrook-squire diagram from [46].

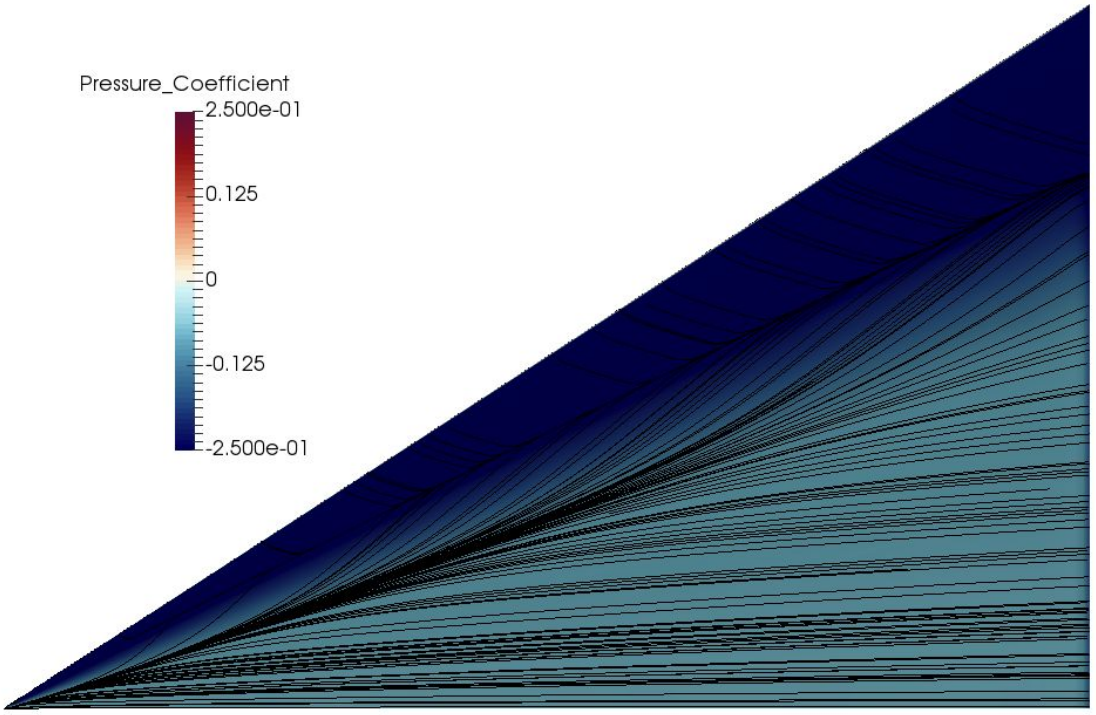

Fig 4.20 surface streamlines and CP flat conical wing

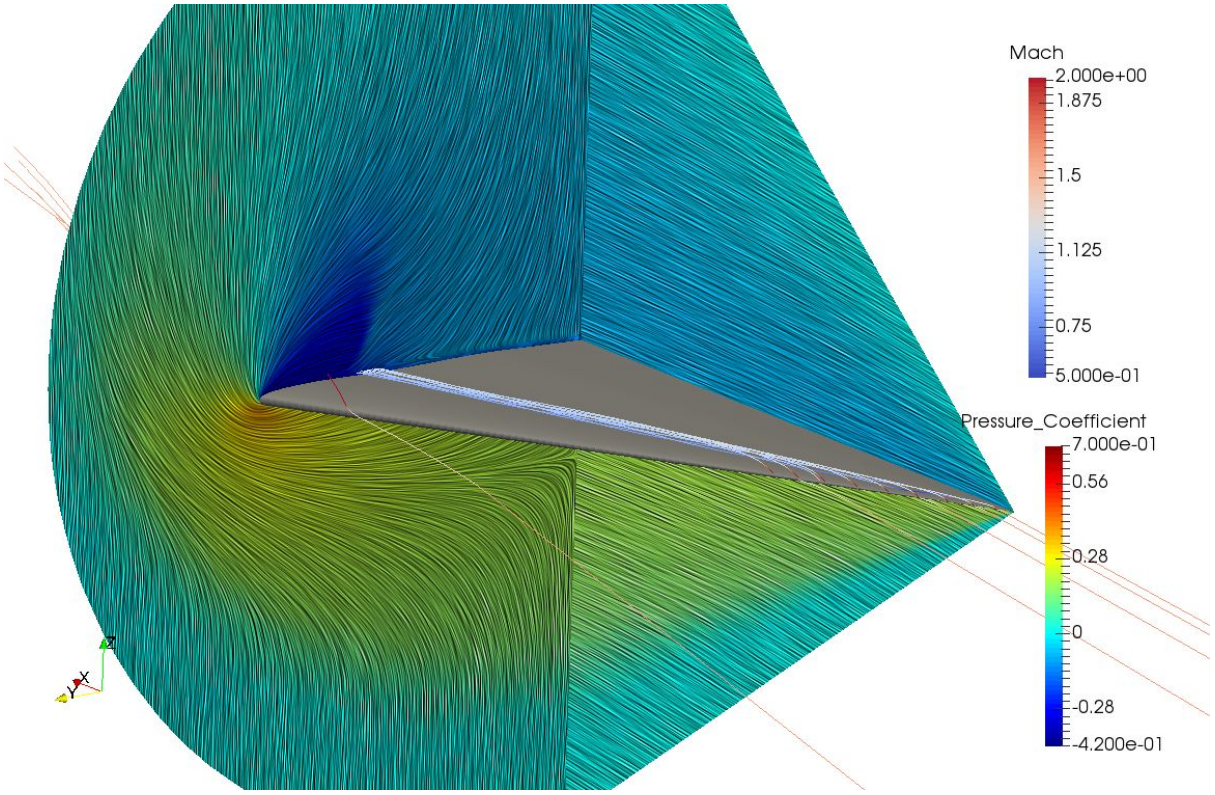

Fig 4.21 3D flowfield of the flat conical wing

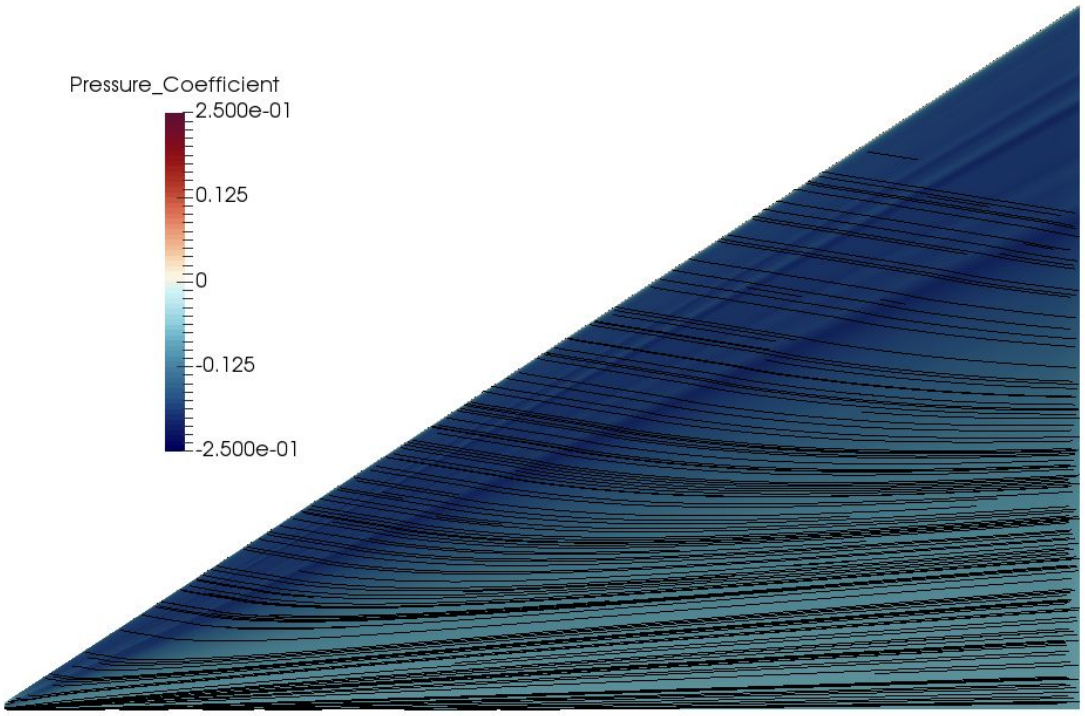

Fig 4.22 surface streamlines and CP Mason conical wing

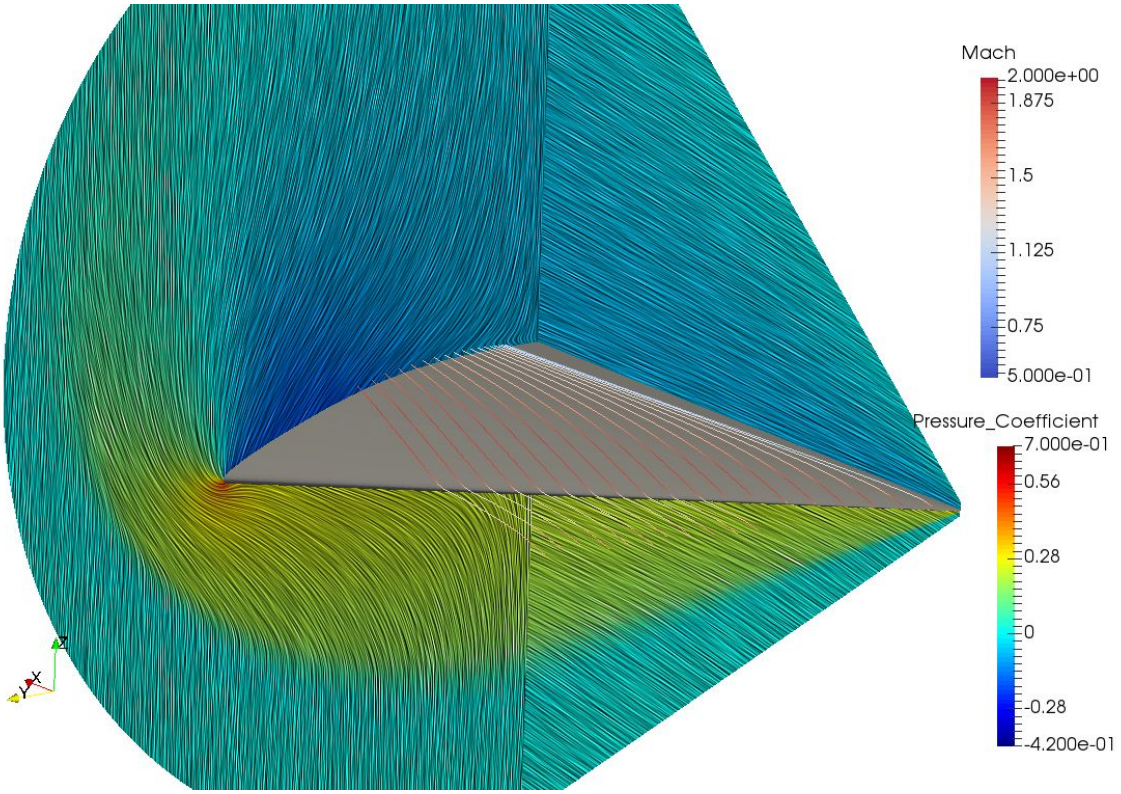

Fig 4.23 3D flowfield of Mason et al's conical wing

Figure 4.22 shows the upper surface of the Mason's conical cambered wing at M=1.62, CL=0.4 and Re/m=6.6x10^{6}. The flow is completely attached over the upper surface and does not feature a crossflow shockwave, rather a smooth shock free recompression where the flow is gradually turned

through a small angle. The pressure distribution in the previously shockwave-dominated region is quite smooth. The wing suction peak is located at around 0.8ETA.

Figure 4.23 shows the 3D viscous flowfield of Mason et al's conical wing at the design condition. A 2D slice in the X plane shows pressure distribution and streamlines; highlighting the bow shock located under the lower surface and smooth expansion around the leading edge, with shock-free recompression towards the wing root. 3D streamlines coloured by Mach number show the flow approaching the wing at a positive incidence angle and expanding around the leading edge with no flow separation. The flow reaches Mach 2 before it gradually turns back towards the trailing edge and recompresses with no shock. This flow field does not correspond with any zone in the stanbrook-squire diagram from [46], due to the lack of any shockwave or separation on the upper surface of the wing.

Figure 4.24 shows the upper surface of the adjoint optimised conical wing at M=1.62, CL=0.4 and Re/m=6.6x10^{6}. There is a weak embedded crossflow shockwave which turns the surface flow through a small angle, and there is a further slight recompression downstream of the shockwave which causes the flow to gradually turn through another small angle. The suction peak of the wing is at the leading edge.

Figure 4.25 shows the 3D viscous flowfield of the adjoint optimised conical wing at the design condition. A 2D slice in the X plane shows pressure distribution and streamlines; highlighting the smooth expansion around the leading edge, with weak cross-flow shock without any induced separation. 3D streamlines coloured by Mach number show the flow approaching the wing at a positive incidence angle and expanding around the leading edge with no flow separation. The flow reaches Mach 2 before it sharply turns through a small angle as the air passes through the crossflow shock and then gradually continues to turn back towards the trailing edge and compresses further. The flow is slowest at the wing root, where the streamlines visibly turn white. This flow field corresponds with zone 5 in the stanbrook-squire diagram from [46].

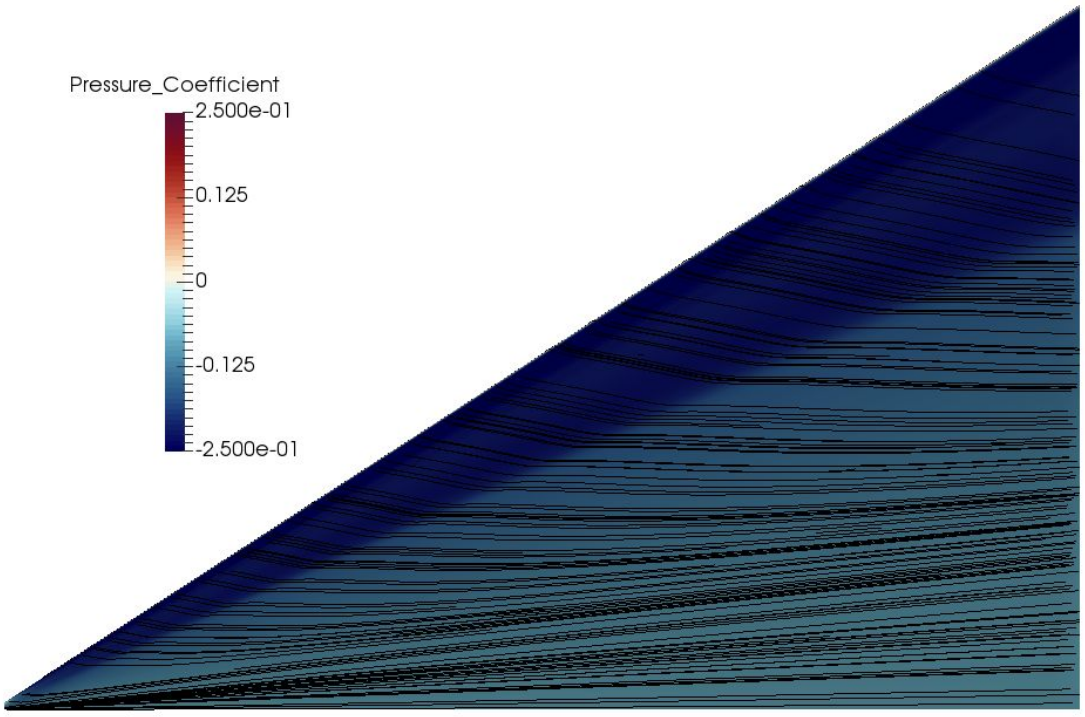

Fig 4.24 surface streamlines and CP adjoint conical wing

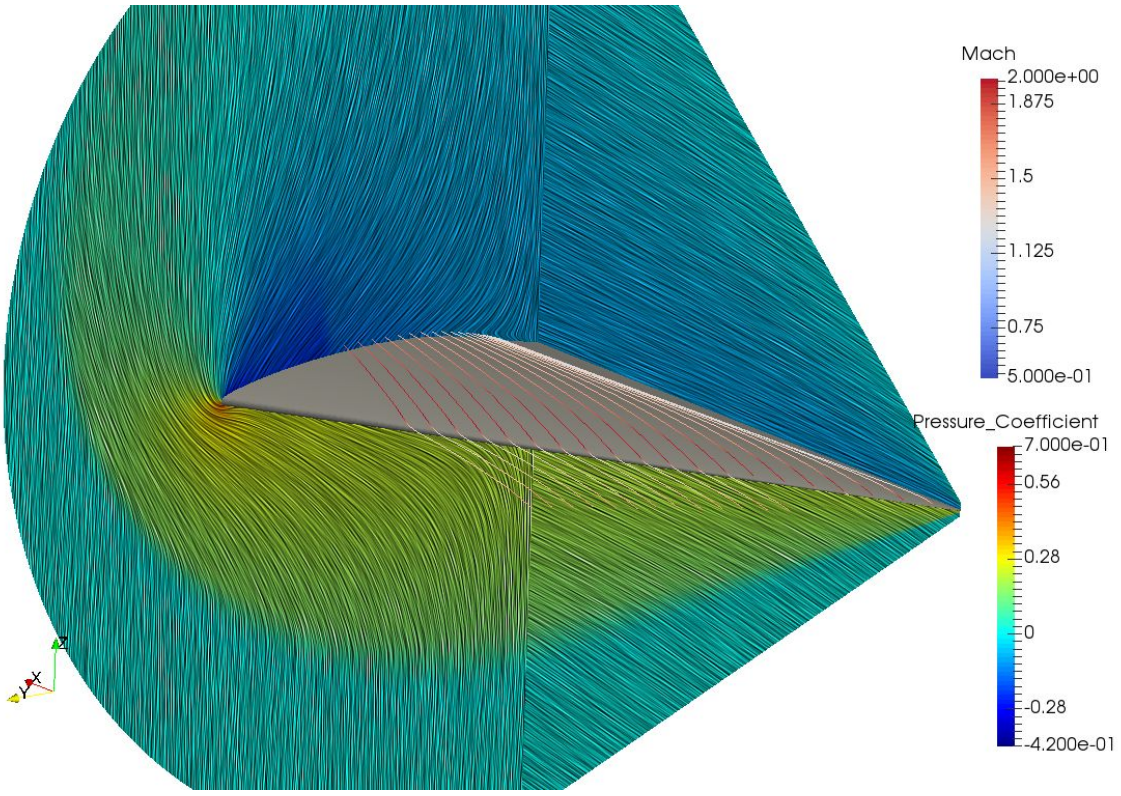

Fig 4.25 3D flowfield of the adjoint optimised conical wing

4.1.5.2 2D Spanwise Shape and Pressure Distributions

A standard comparison method for conical wings with conical flow-fields is to plot camber and surface pressure against Y/Ymax. This has been done in this section in order to compare the uncambered initial wing, mason's conical wing design and the adjoint optimised design.

Figure 4.26 shows a direct comparison between the conical spanwise geometries generated by each design method. The flat wing starting point is shown as a solid black line. Mason et al's conical camber design is entirely drooped downwards. In contrast, the adjoint optimised design is only deformed in the upwards direction with a characteristic M shape and leading edge at almost exactly the same location as the flat wing, as if a dihedral angle was added to Mason's design.

Figure 4.27 shows a direct comparison between the conical spanwise pressure distributions at X=0.3m generated by each design method at the design condition. The solution for the flat wing is shown as a solid black line for reference.

Rather interestingly, the adjoint optimum and Mason's design have the most similar pressure distributions; despite the fact that Mason's design has a very different conical cross section. Mason's design features the flattest pressure distribution on the upper surface, with no significant cross-flow shockwave; in agreement with Mason et al's wind tunnel experiments.

The adjoint optimum design features a suction peak of Cp=-0.28 at the leading edge, followed by a very weak cross-flow shockwave which does not induce separation. At the wing root, there is more suction on the upper surface than the other designs, however the lower surface has a lower pressure than Mason's design.

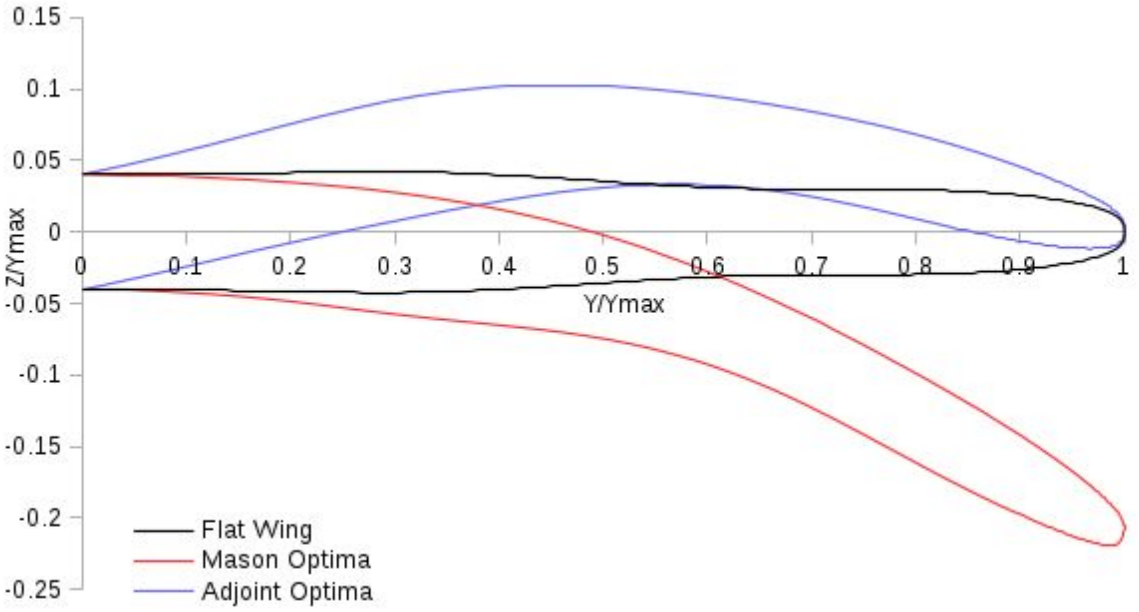

Fig 4.26 comparison of spanwise shapes from each design method

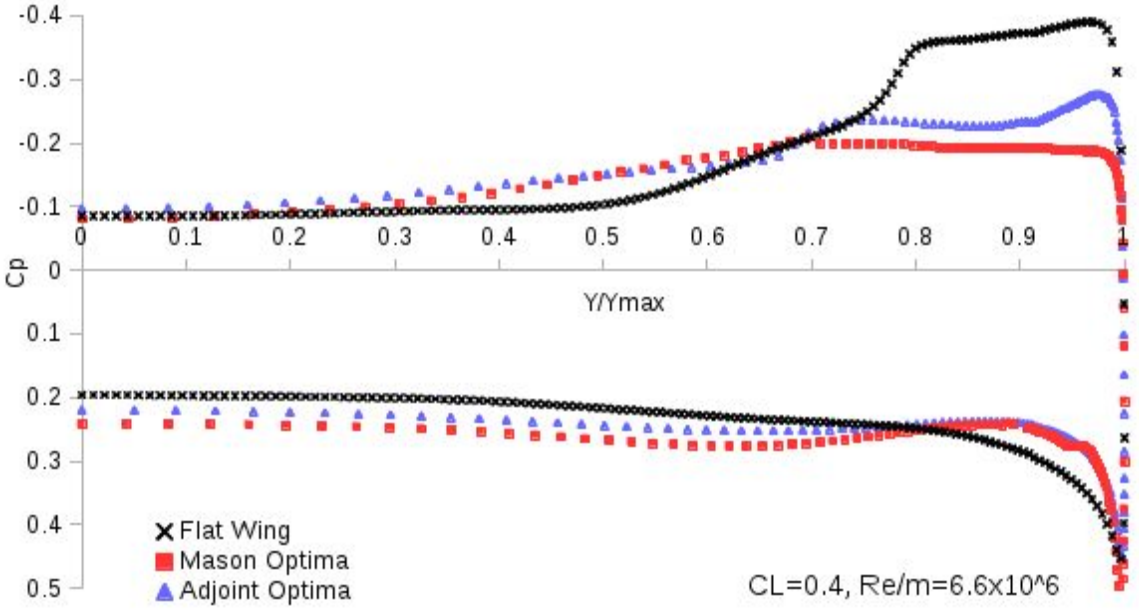

Fig 4.27 comparison of spanwise RANS Cp distributions from each design method

4.1.5.3 Integrated Spanwise Force Distributions

Here, a series of chordwise cuts have been made at spanwise stations along the wing span, then forces have been integrated around each chordwise cut and resolved into local lift, drag and axial force.

These forces on each aerofoil section have been plotted against the spanwise coordinate of the section, providing a visualisation of the spanwise force distributions on each wing design.

Figure 4.28 shows a comparison between spanwise lift distributions for each design. A purely elliptical lift distribution is shown as a solid black line for reference. The flat wing has the closest lift distribution to elliptical, with the designed wings both having more triangular distributions. Mason's design has the highest lift loading at the root, but the lowest in the outer-span 0.17m<Y<0.39m. The adjoint optimum wing has the lowest root lift loading out of the two designed wings, but the highest tip loading - making it slightly closer to the flat-wing and elliptical lift loadings.

Figure 4.29 shows a comparison between spanwise drag distributions for each design. The flat wing has a nearly elliptical drag distribution, whereas each of the designed wings have fairly similar bell-shaped distributions. The adjoint design has the lowest wingtip drag from 0.295m<Y<0.395m, however the highest mid-span drag of either designed wing due to it's cross-flow shockwave. The adjoint optimum design has the lowest average drag loading, but generally is quite similar in distribution and magnitude to Mason et al's designed wing. It can clearly be seen in this figure that a trade-off has been made: slightly increased shockwave drag for reduced wingtip and wing root drag.

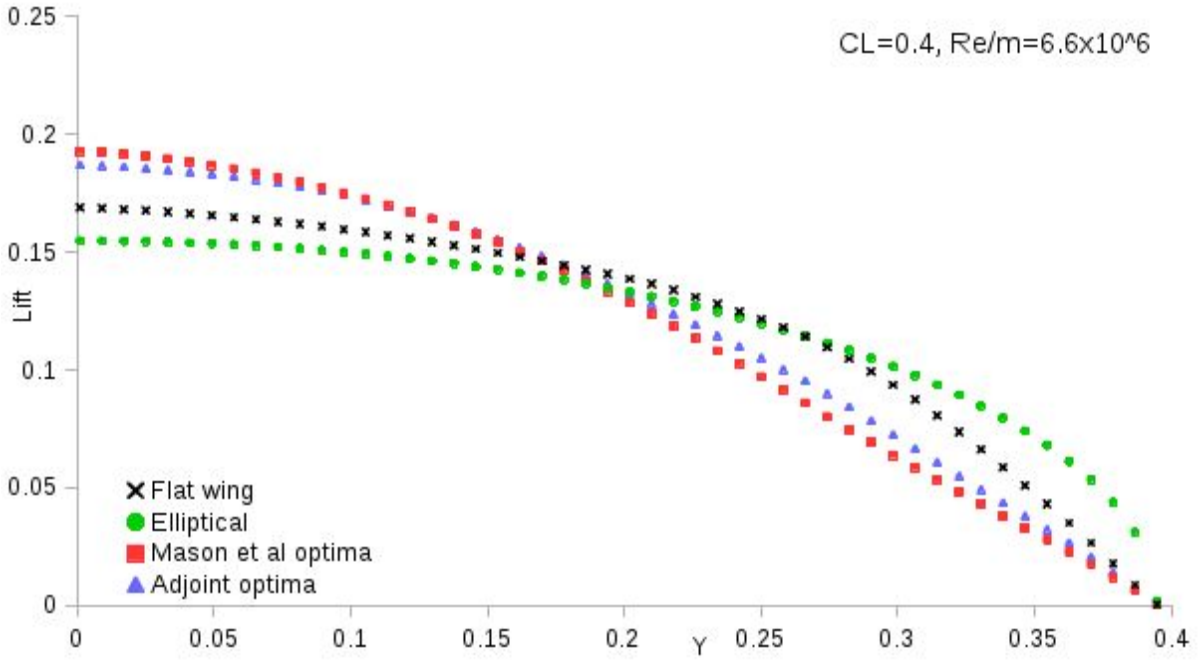

Fig 4.28 comparison of spanwise lift distribution for each wing design

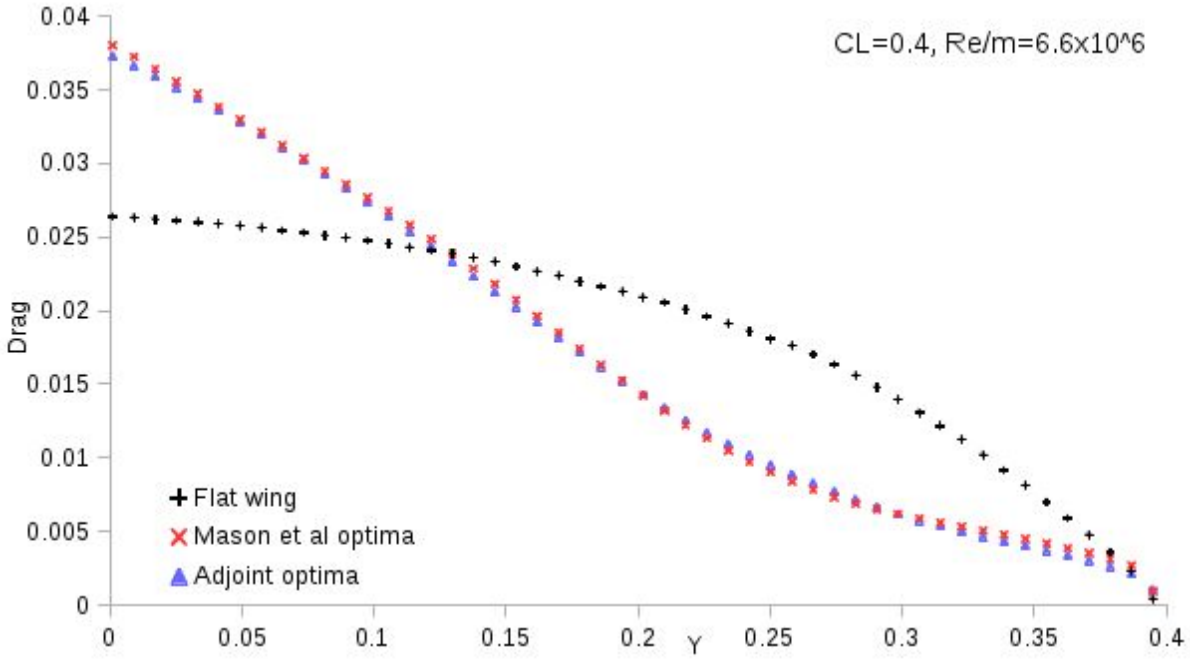

Fig 4.29 comparison of spanwise drag distribution for each wing design

4.1.5.4 Force Polar Study

In this section, the fast and robust flow solver Cobalt was used with the 100x100x200 RANS grids to generate flow solutions for each conical wing design at a wide range of incidence angles to give an indication of each wing's performance throughout the flight envelope in viscous flow.

Figure 4.30 shows lift polars for both of the designed conical wings and flat datum wing. The flat uncambered wing has a slightly nonlinear lift curve, with dCL/dα gradually reducing as α increases. Mason's design has a linear lift slope at least up until the 16 degrees included in this analysis, and produces zero-lift at 2.5 degrees α. The adjoint optima design has a similarly nonlinear lift curve to the flat wing, however it produces zero lift at 2.55 degrees, the highest α of either of the designs.

Figure 4.31 shows CL vs CD for each of the conical wing designs for the α range 0-16 degrees. The flat wing has the lowest zero-lift drag of any design by some margin, followed by adjoint optima and finally the Mason's design with the highest zero-lift drag. The flat wing has the lowest drag value up to a CL of about 0.3, above which the drag value rises significantly over the other designs. At this scale, it is difficult to discern the differences between either of the designed wings, except above CL=0.6 where mason's design has the lowest drag value. This is why a magnified version from 0.3>CL>0.5 is also presented here.

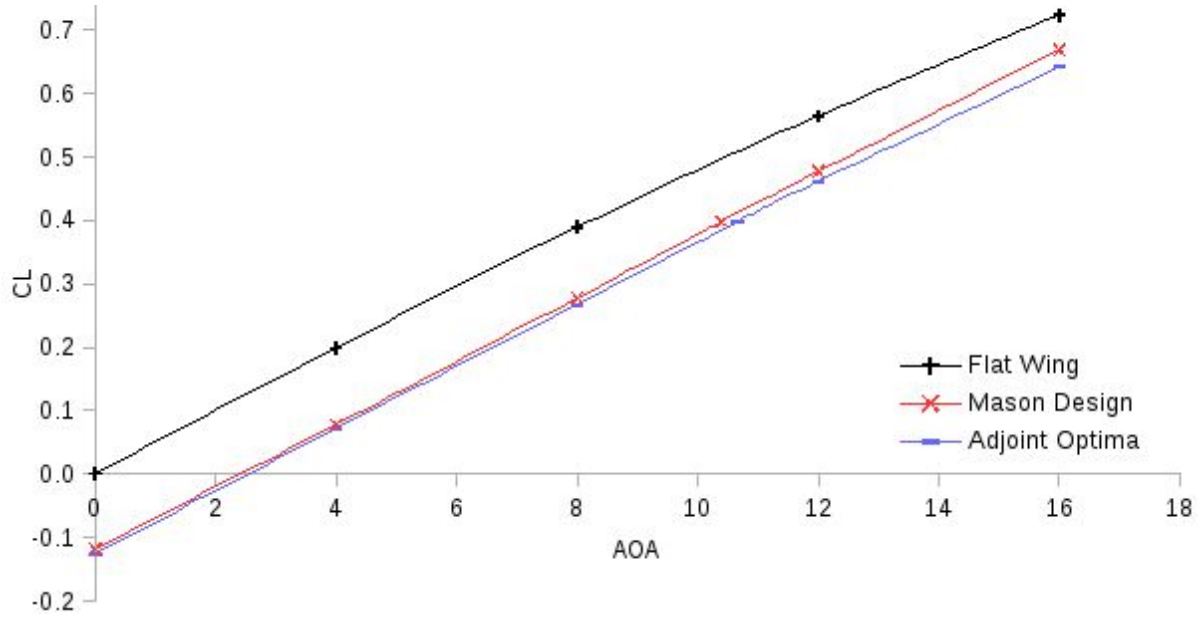

Fig 4.30 comparison of Cobalt RANS lift polars for each design method

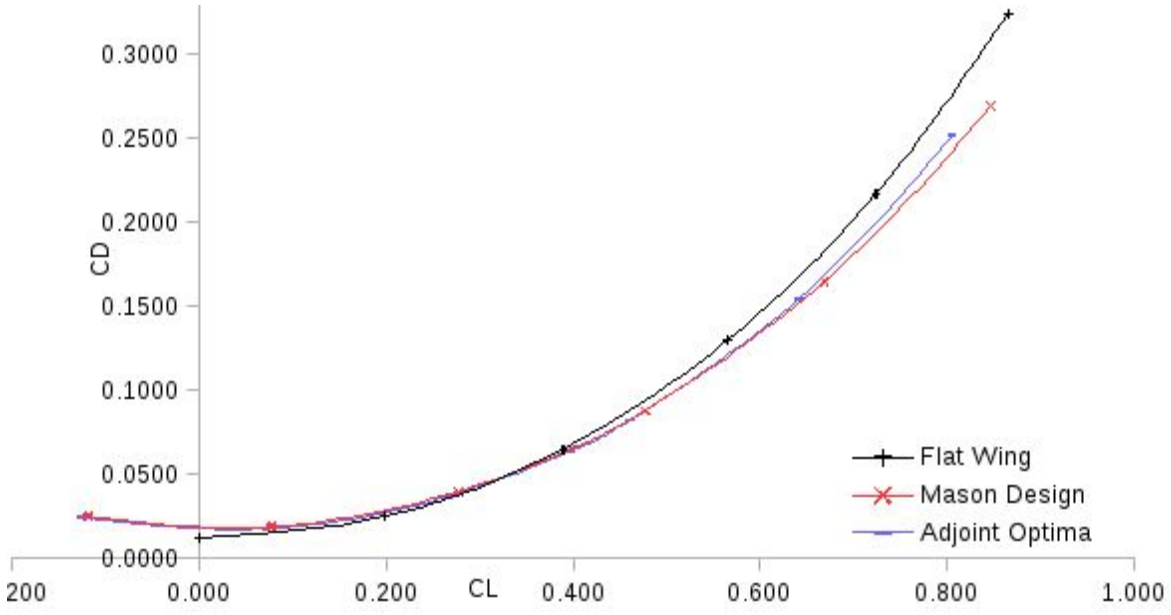

Fig 4.31 Comparison of Cobalt RANS drag polars for each design method

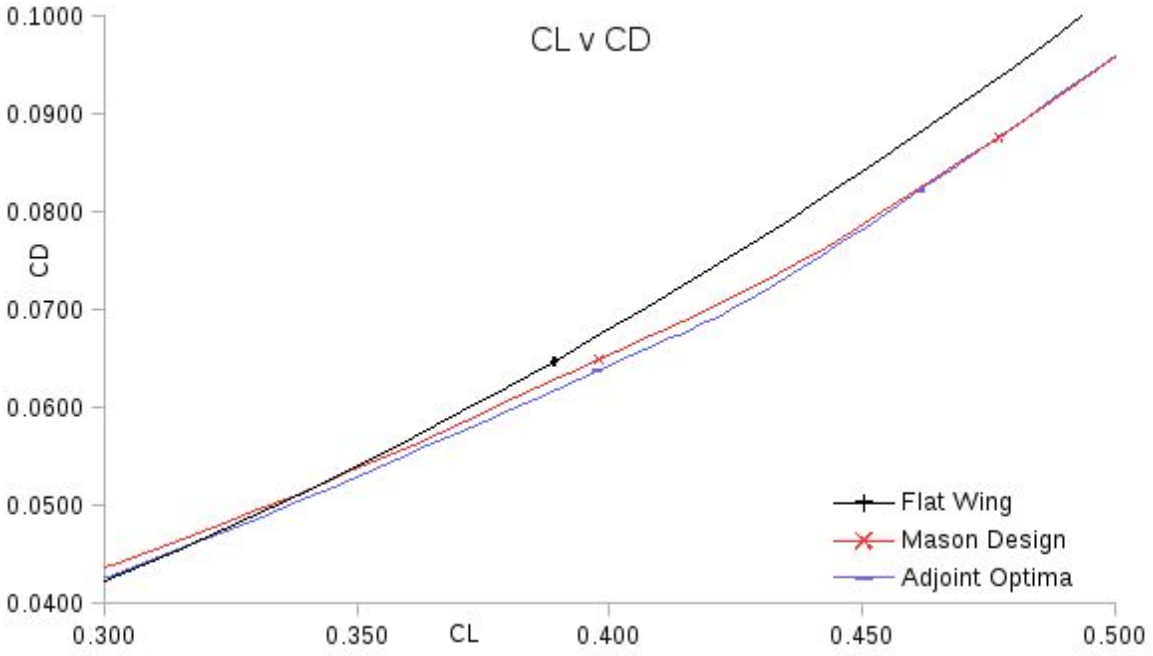

Fig 4.32 comparison of Cobalt RANS drag polars for each design method, 0.3<CL<0.5

Figure 4.32 shows CL vs CD for each of the conical wing designs for the CL range 0.3-0.5. The flat wing has the lowest drag value at CL=0.3, however from this point until CL=0.45 the adjoint optima has the lowest drag. From CL=0.475 onwards, Mason's design has the lowest total drag value. It is important to note that the trend lines on this chart are illustrative only; and are there for visualisation since this plot contains a relatively small selection of data points.

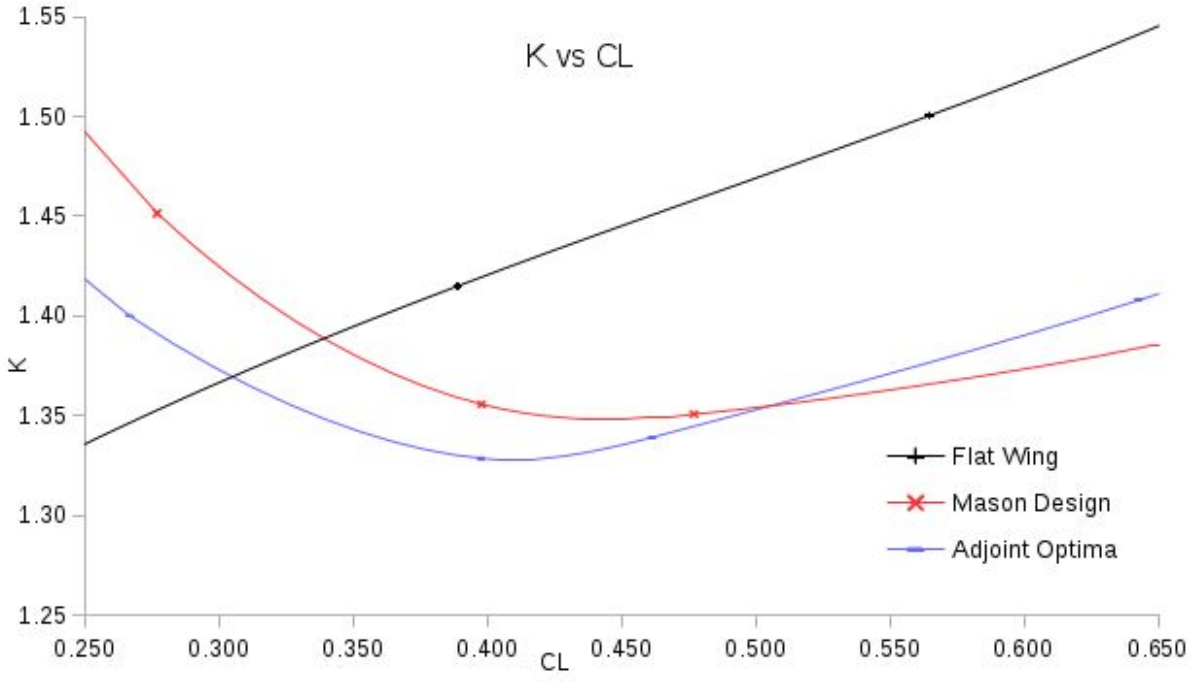

Fig 4.33 comparison of K-factor polars for each design method

Figure 4.33 shows K factor, which is a term used by aerodynamicists to measure lift-induced drag. For a theoretically ideal subsonic or transonic wing with elliptical lift distribution, K would be equal to or just larger than one. In the case of supersonic wings, this does not always appear to be the case since shockwaves become a dominant source of drag.

K factor here has been calculated as:

$$K = ((CD - CD_0) * Pi * AR)/CL^2 \qquad \text{Equation 4.1}$$

Where CD_0 is the zero-lift drag of the flat datum wing.

Figure 4.33 shows a comparison of K-factors vs CL for each of the conical wing designs in the region 0.25<CL<0.65. As expected, the flat wing has a low K value at low CL values. The adjoint optima design has the lowest K factor from CL=0.3 up to CL=0.5, however mason's design has the lowest K factor from CL=0.5 onwards. The adjoint optima design has the lowest K factor at the design CL=0.4; followed by Mason's design and the flat wing.

4.1.6 Conclusions of Conical Lift-Constrained Drag Minimisation Study

A simple lift constrained optimisation strategy has been presented and compared with another widely used constrained optimisation strategy, using Mason *et al*'s supersonic conical cambered wing as a test case. The soft-constrained strategy utilised fixed-CL (variable α) Euler flow solutions in order to constrain it's designs to a specified lift coefficient whilst adjoint-drag solutions provided the SLSQP optimiser with drag sensitivities at each design variable, which drove the shape of the wing towards minimum pressure drag. This means that it only required one adjoint solution per design iteration.
The widely-used hard-constrained strategy utilised fixed-α Euler flow solutions and discrete adjoint-lift solutions which are provided to the SLSQP optimiser as linear inequality constraints in addition to the discrete adjoint-drag solutions which are again used to drive the shape towards a minimum drag design. This means that two adjoint solutions are required per design iteration.
Therefore, if the soft-constrained strategy could generate a similar or better design within the same number of design iterations then it would clearly be a preferable method over the hard constrained strategy. The soft constrained optimisation strategy used less computational time than the hard constrained strategy; 28 hours instead of 46.8 hours - a substantial saving of 39.25% and produced a very slightly better design with similar characteristics, therefore confirming that it is the most efficient method for imposing a lift constraint in supersonic adjoint optimisation studied in this thesis.
For this reason, the soft method for imposing lift constraints was used for the remainder of the wing designs in the thesis. This method produced a wing with CDp=0.0569 in inviscid flow compared with CDp=0.0626 for the flat wing at the same lifting coefficient, providing a 9.1% reduction in pressure drag.

RANS was used to evaluate the performance of the soft-constrained optimised wing, the initial flat wing and wing generated by Mason et al[33]. Only the soft constrained adjoint design has been analysed here since both optimisation strategies produced similar designs, with the soft-constrained design having marginally better performance.

The adjoint optimum design had a higher performance than either of the other wing designs investigated using RANS, with CD=0.06226 - improving upon the flat wing drag by 8.98% or 61 drag counts and Mason *et.al*'s minimum drag design by 2.12% or 13.5 drag counts. This demonstrated one advantage of the adjoint numerical optimisation method over other wing design methods.

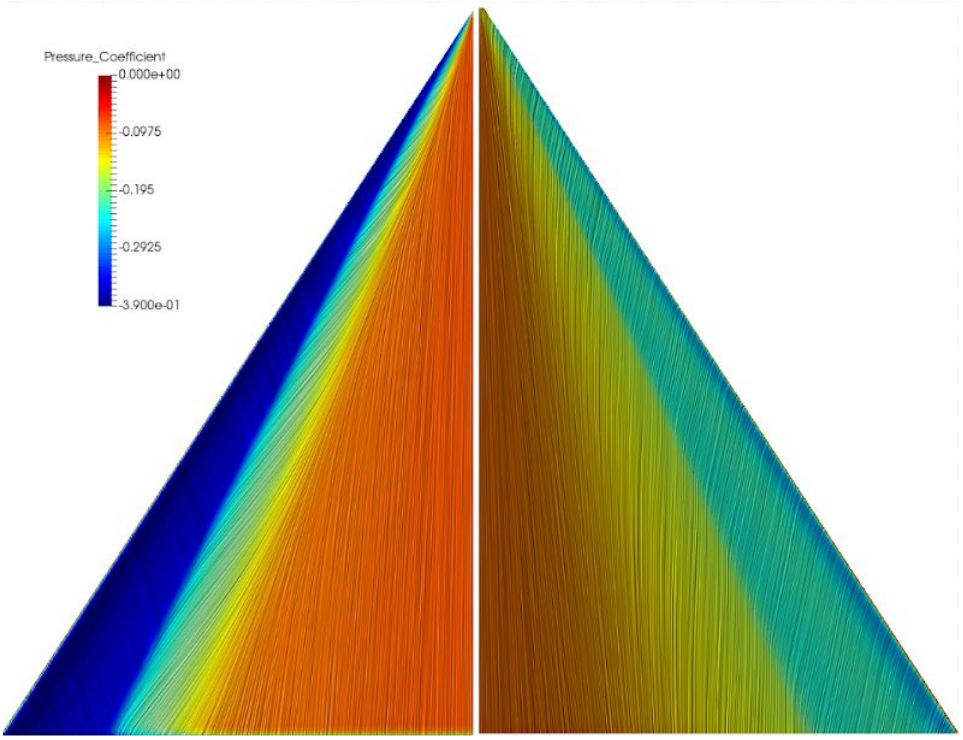

Fig 4.34 RANS surface flows of the flat conical wing (left) and adjoint optimised conical wing (right)

Figure 4.34 shows the difference in lee-side surface flows for the flat and adjoint optimised conical wings. Color denotes local Cp and surface streaks denote local shear force direction. On the left, the flat wing shows a strong cross-flow shockwave with associated shock-induced flow separation. The separated flow reattaches, indicating the presence of a vortex above the surface of the wing. At the wing leading edge there is a suction peak of Cp=-0.39.
On the right, the adjoint optimised wing shows a weak cross-flow shockwave which is located further inboard than the shock exhibited by the flat wing, which instantaneously turns the surface flow through a small angle. Downstream of this weak shockwave there is a gradual recompression from Cp=-0.15 to -0.05 at the root, with gradual turning of the surface flow through a small angle. At the wing leading edge, there is a suction peak of Cp=-0.3.

It can be concluded that the soft lift constraint strategy, as outlined in chapter 3.4, provided a 39.25% reduction in design cost when compared with a conventional lift constraint strategy, and that the adjoint pressure drag minimisation method produced a better wing design than the other method included in this study, with 2.12% less drag than the second best method when compared using RANS solutions.

4.2 Pressure Drag Minimisation of two Non-conical Supersonic Wing Concepts

The initial wings used for this study are concepts for future supersonic manoeuvring aircraft, having planforms which are designed to reduce radar signature return angles. The two planform shapes being tested are a trapezoid wing and a cranked wing, and are sized for a generalised 6th-generation fighter jet concept. A NACA 64-A004 aerofoil will be applied as an initial datum point for the designs for two reasons; firstly the leading edge radius and thickness distribution is beneficial for low-speed handling qualities and performance; and this thickness distribution is sufficient to allow sensibly sized structures, tanks, actuators and ordnance. Because the thickness distributions have already been specified and should not be altered, they will be maintained throughout the design process by only deforming the camber of the wing. The concept wings are parameterised using the same free-form camber deformation method as is used in the conical wing study, however in this case the bounding box is trapezoidal enclosing the wing and has 10 control points in the I direction meaning that deformations will not be only conical.

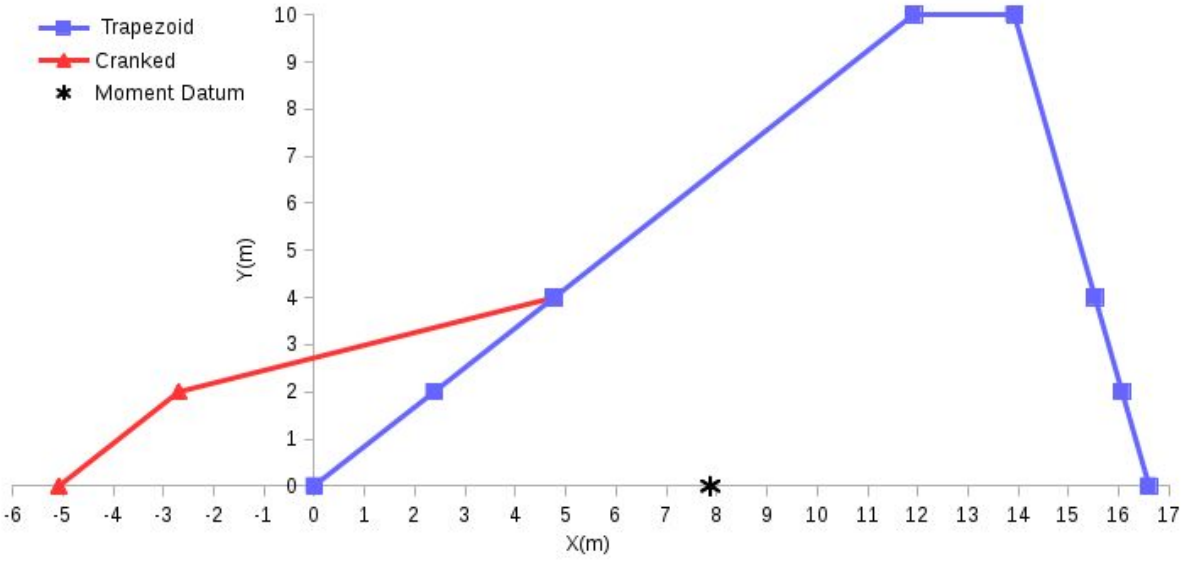

Fig 4.35 Comparison of supersonic manoeuvre wing concept planforms

Figure 4.35 shows both of the planform shapes used in this section of the thesis. Dimensions are in meters. The 50 degree leading edge sweep angle is 7 degrees less than the conical case presented previously in this thesis, however a similar flow structure should be present at the design point (CL=0.25, M=1.6).

For the cranked planform, the outer 6m of the wing semi span and trailing edge are identical to that of the trapezoid wing. The difference being a leading edge root extension (LERX), making the leading edge into a 50-75-50 degree cranked shape. The crank locations are located at 2m intervals from the wing root and have the effect of increasing the root chord by 5.1m. In order for the results to remain comparable, the area of the trapezoid wing in blue will be used as a reference value in both cases in

order to ensure that actual lift values were the same; not just coefficients. For example, both wings would be supporting the same weight; not the same weight/area.
The aerofoils for the LERX section of the cranked wing have been slightly thinned relative to their larger chord, in order to maintain the same total thickness and frontal area for both wings.

4.2.1 Design Problem Description

The formulation for the design process is as follows:

Minimise objective function: I = CDp

Subject to constraint functions: G_1 = CL = 0.25
G_2 = R(U) ~ 0

Design Variables: 99 free-form deformation box camber variables and α

At the design Mach number: M = 1.6

Initially, pitching moment will be left unconstrained during the optimisation process, allowing the computer to find the solution with minimum drag without any consideration for aircraft stability. It is expected that the minimum drag designs will be statically unstable in the pitch axis at supersonic flight conditions without the addition of some trim surface - incurring some trim drag penalty.

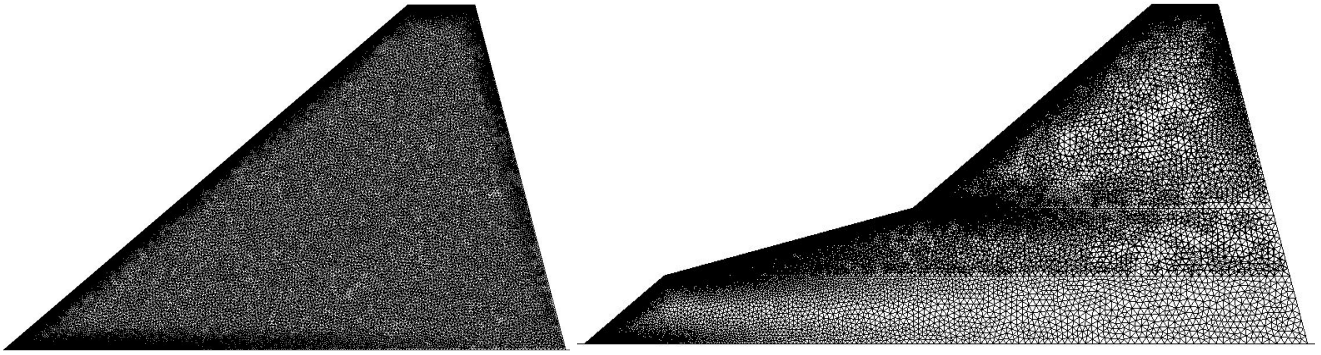

Fig 4.36 unstructured surface grids for each wing geometry

Figure 4.36 shows the unstructured surface grids for each wing planform. These grids are composed of 290,000 triangular elements which are clustered around sharp edges and the leading edge. These can be considered ‘engineering grids’, they are globally refined enough to capture features of interest but not refined to resolve any specific flow features in extra detail. Some further coarsening and grid adaptation could have increased the efficiency of the grid; however these were perfectly sufficient for the optimisation problem.

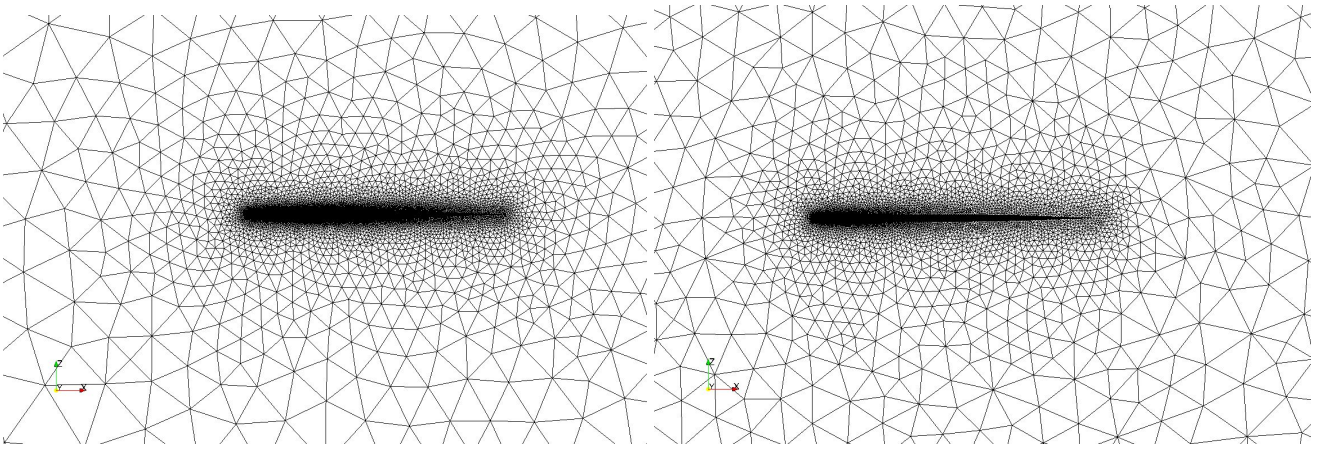

Fig 4.37 unstructured symmetry plane grids for each wing geometry

Figure 4.37 shows the symmetry plane of each unstructured grid in order to provide a visual representation of what the volumetric grid is like. Once again, it is clear that this is an inviscid engineering grid - intended to be robust for a range of Mach numbers, incidence angles and wing geometries. Nothing about the flow has been taken for granted and so the grid is globally refined enough to capture any features of interest but not aligned to any particular flow feature (as one might expect with a grid for a single supersonic Mach number, which might be aligned to the Mach or local shock angles).

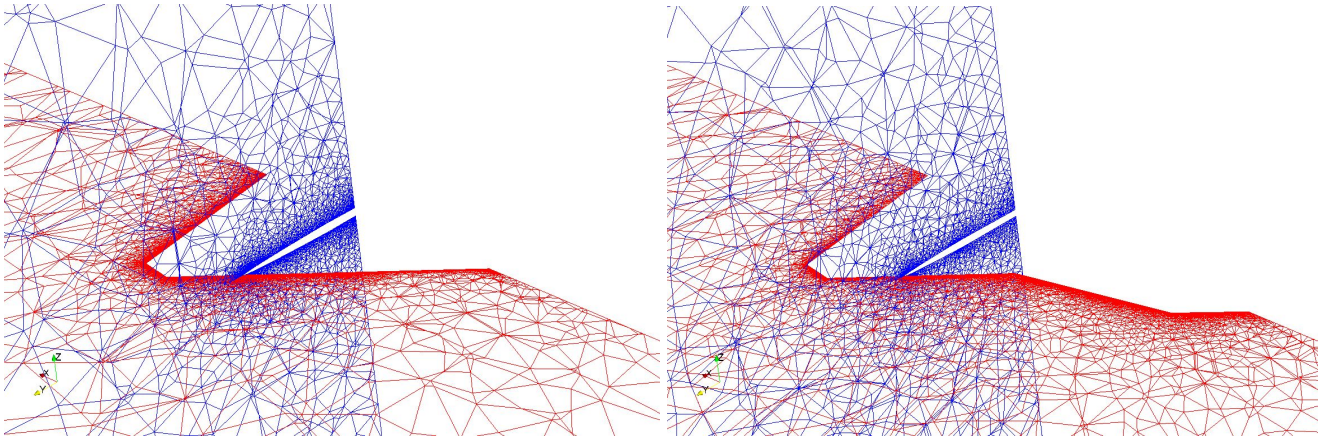

Fig 4.38 unstructured volume grid slices for each wing geometry

Figure 4.38 shows planar slices of the unstructured volume grids for each geometry. The planes Z=0m are shown in red and the planes X=15m are shown in blue. These planes demonstrate how the volumetric grid points are distributed away from the wing surface. These grids have been created in order to resolve flow features in both supersonic and transonic conditions; and figure 4.38 demonstrates further how the grid is globally refined. The volume grids are composed of 6.6 million elements.

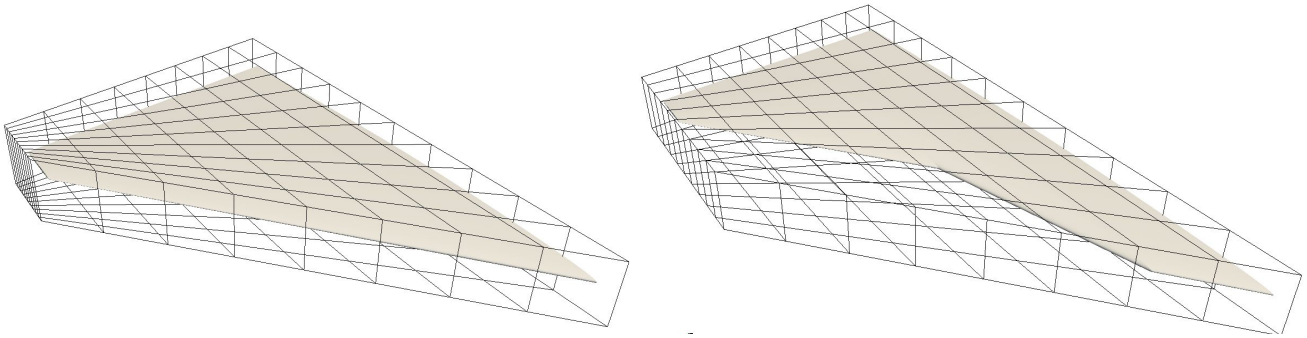

Fig 4.39 3D perspective view of the FFD boxes used for shape parameterisation. Trapezoid (left) Cranked (right).

Figure 4.39 shows the FFD boxes in 3D with their corresponding wing geometries. Both boxes are 10x8x1 structured grids with their J=0 plane lying on the symmetry plane. Since each face of the FFD box must be a quadrilateral, the planform angles of the cranked wing cannot be matched by the box. This means that at the wing tip and the outer span of the wing, there are multiple control point locations ahead of the leading edge of the wing; leading to some redundant control points. Despite this, there is still significant design freedom to allow detailed camber design for the cranked wing.
Both boxes have the same leading and trailing edge angles and the same thickness in the K direction. For the purposes of camber optimisation, control points with equal I and J values are coupled so that upper and lower surfaces move in unison. Movement is only allowed in the Z direction, preserving both planform and thickness distribution.

4.2.2 Initial Aerofoil Sections, Inviscid Pressure Distributions and Surface Sensitivities

In this section, the 3D shape, inviscid pressure distribution and surface drag sensitivity of both of the initial uncambered supersonic wing concepts are presented and discussed. These shapes and solutions are what dictate the subsequent behaviour of the optimiser, and each is influenced by the other; the geometry affects the pressure distribution, which in turn affects the drag sensitivity.

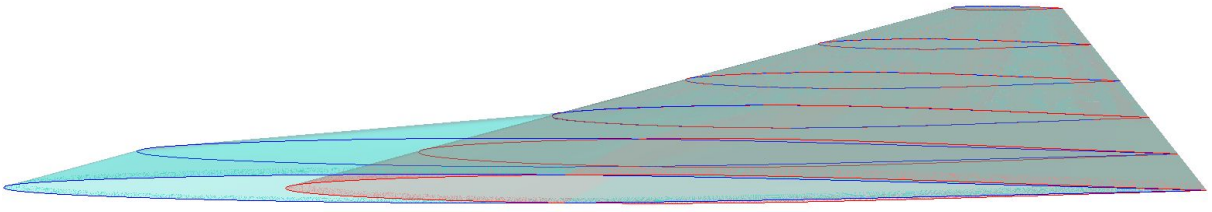

Fig 4.40 Geometrical comparison of trapezoid and cranked wing sections

Figure 4.40 shows the trapezoid (red) and cranked (blue) wing 3D shapes with highlighted aerofoil sections at 2m intervals along their span. The aerofoil sections are NACA 64A004 with slightly reduced thickness near the wing root. This image highlights that the maximum thickness of the aerofoil is the same at any spanwise location regardless of planform shape, meaning that the frontal area of each wing is identical.

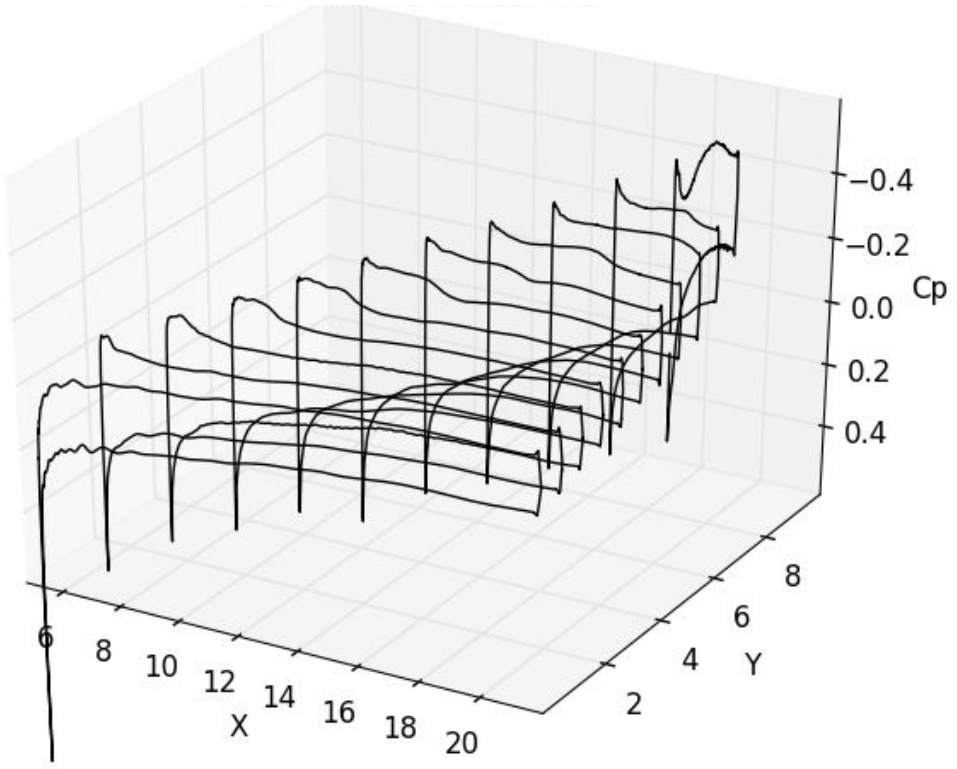

Fig 4.41 Inviscid chordwise Cp distributions of the initial trapezoid wing at the supersonic design condition

Figure 4.41 shows inviscid chordwise Cp distributions at 1m intervals along the span of the flat trapezoid wing at the supersonic design condition; M=1.6, CL=0.3. This plot can be used for both reference and basic verification of the flow solution. For example; the stagnation pressures at the leading edge of the wing can be compared with analytical solutions using the same Mach number and angle. These solutions provide Cp=0.559 at the attachment line on the leading edge; which is very close to the values shown in figure 4.41. This comparison provides extra confidence in the validity of the Euler CFD calculations which are to be used by the optimiser. The upper surface pressure distribution shows evidence of an embedded crossflow shockwave. There is an expansion at the wingtip; with the flow continuously expanding from leading to trailing edge on both upper and lower surfaces - with the exception of a suction peak at the leading edge.

Figure 4.42 shows the surface pressure distribution of the first concept wing - the trapezoid planform - at the supersonic design condition of M=1.6 and CL=0.25 as calculated by the Euler equations. The upper surface is shown on the left side of the figure facing left and the lower surface is shown on the right side of the figure facing right. This figure configuration is utilised throughout the remainder of this thesis. It is clear that on the upper surface there is an embedded crossflow shockwave as with the conical design case. There is also a surface-impinging shock caused by the wingtip which coalesces with the crossflow shock at the trailing edge. The lower surface has a flat pressure distribution except along the leading edge where there is a uniform band of high pressure from the root to the tip.

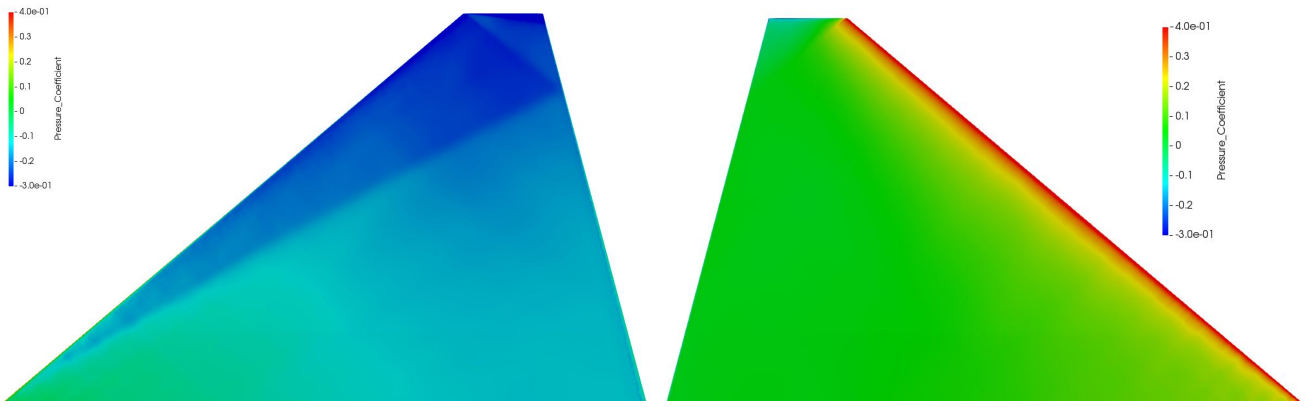

Fig 4.42 Upper (left) and lower (right) surface pressure coefficient color maps of the trapezoid wing at the supersonic design condition.

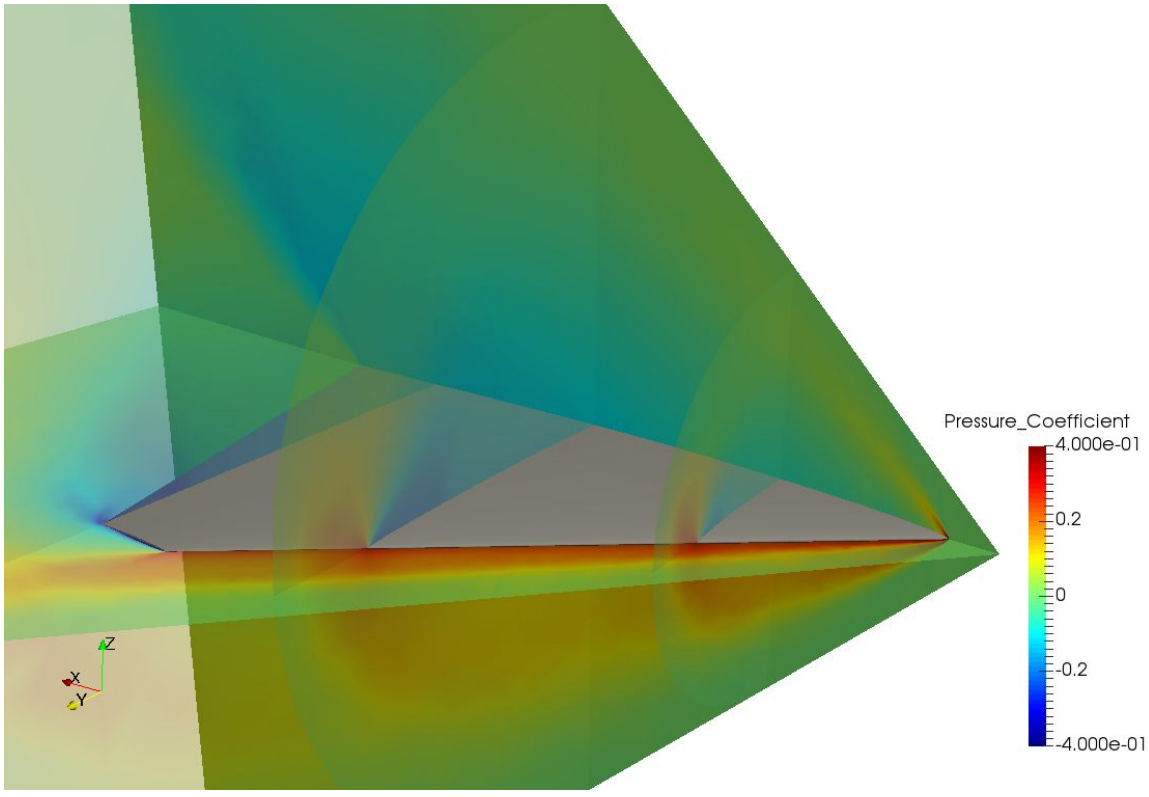

Fig 4.43 Inviscid flow solution slices of initial trapezoid wing at the supersonic design condition

Figure 4.43 shows the volumetric pressure distribution in the flowfield around the initial uncambered trapezoid wing at the supersonic design condition. Transparent slices are located on the Y=0m, Z=0m, X=10m, X=15m and X=20m planes. On the symmetry plane, the bow shockwave is clearly visible - extending both above and below the wing due to the round leading edge at the wing apex. Above the upper surface on the symmetry plane, there is an expansion fan just downstream of the bow shock, caused by flow acceleration around the leading edge and resulting in a weakening of the bow shockwave away from the upper wing surface. On the Z=0m plane, the strong bow shock is clearly shown to lie just ahead of the wing leading edge - denoting that the wing has a subsonic leading edge at this flight condition. At the wing tip, the flow expands rapidly around the sharp corners and results in an expansion fan which lies just downstream of the bow shockwave.

On the constant-X planes, the bow shockwave is visible and it's conical shape is evident. These planes also serve to highlight the flow expansion around the lee-side of the wing leading edge and subsequent cross-flow shockwave above the wing. The cross-flow shockwave is clearly planar and near-conical from figures 4.42 and 4.43, and when viewed on the crossflow plane it is inclined very slightly so that the wave slopes towards the symmetry plane away from the wing surface.
At the wing trailing edge, especially at the symmetry plane and wing tip, there are strong shock waves where the flow turns quickly back towards the free-stream direction. This shockwave is very clearly visible on the symmetry plane extending above the wing surface from the trailing edge downstream, eventually coalescing with the broad expansion fan which is located above the wing surface.

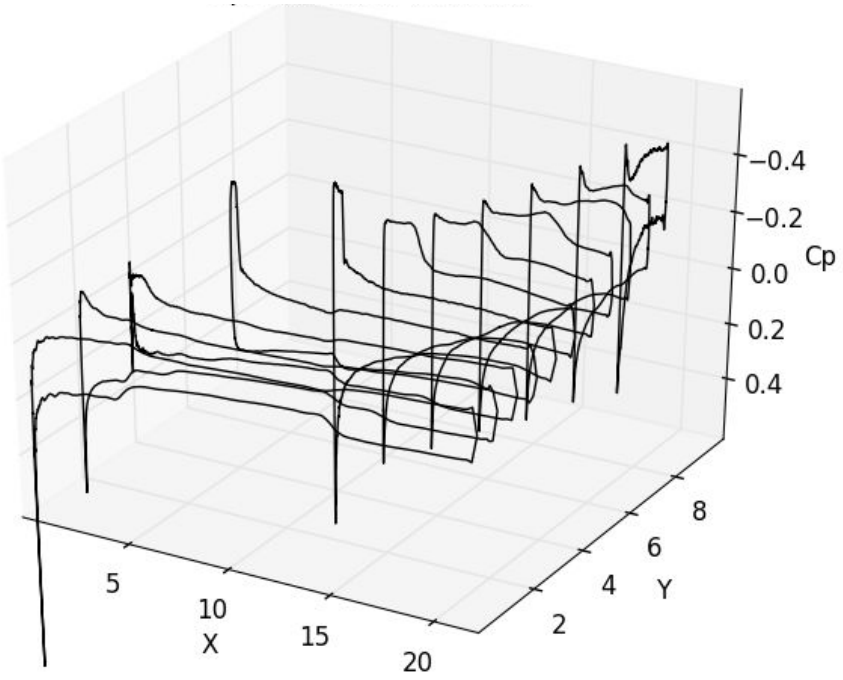

Fig 4.44 Inviscid chordwise Cp distributions of the initial cranked wing at the supersonic design condition

Figure 4.44 shows inviscid chordwise Cp distributions at 1m intervals along the span of the flat cranked wing at the supersonic design condition; M=1.6, CL=0.3. The upper surface shows evidence of two embedded crossflow shockwaves; one directly downstream of the suction peak at the cranked leading edge and another on the outer span of the wing. As with the trapezoid wing, there is an expansion at the wingtip. On the lower surface, there is an expansion wave coming from the convex leading edge crank which reflects from or crosses over the symmetry plane and extends out back towards the leading edge. Conversely at the convex leading edge crank there is a corresponding shockwave which emanates towards the wing root and crosses over the symmetry plane in the same manner as the expansion mentioned previously.

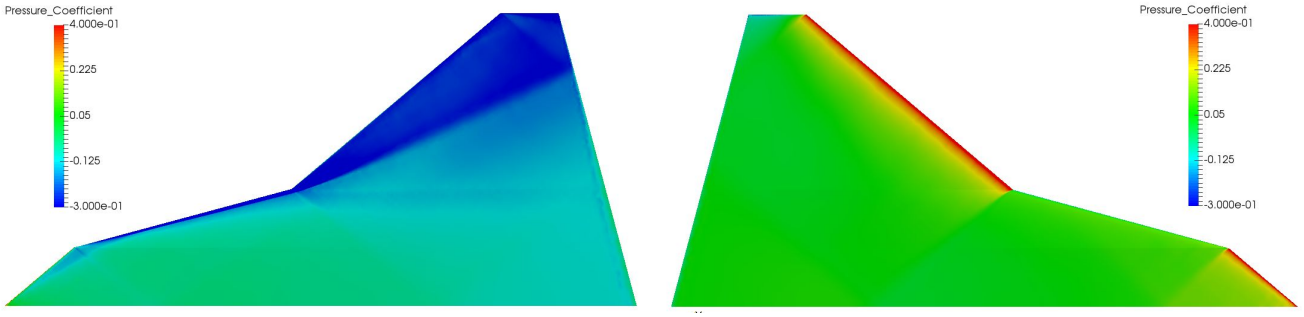

Fig 4.45 Upper (left) and lower (right) surface pressure coefficient color maps of the cranked wing at the supersonic design condition.

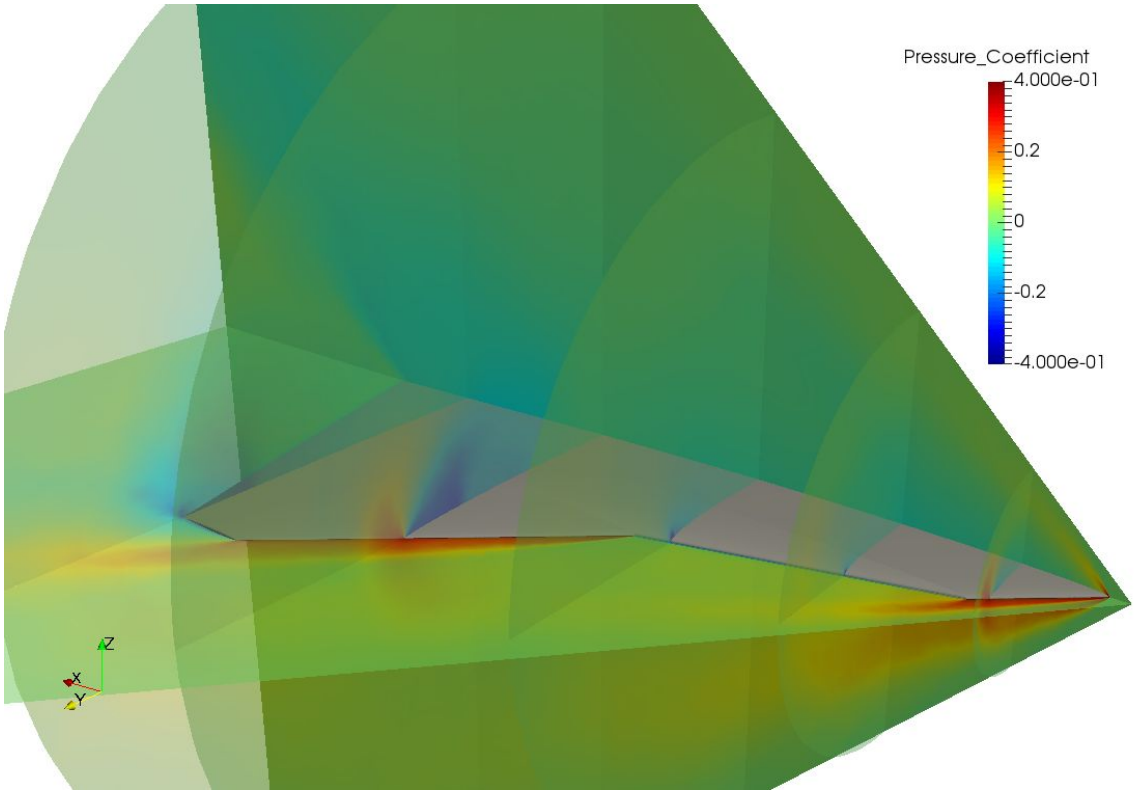

Fig 4.46 Inviscid flow solution slices of initial cranked wing at design condition

Figure 4.45 shows the surface pressure distribution of the second concept wing - the cranked planform - at the supersonic design condition of M=1.6 and CL=0.25 as calculated by the Euler equations. It is clear that on the outer 6m span of the upper surface there is an embedded crossflow shockwave as with the conical design case and the trapezoidal wing. There is also a strong surface-impinging shock caused by the LERX at the leading edge of the 75 degree swept portion of the wing, which joins directly with the crossflow shockwave on the outboard span of the wing. This is an artefact of the inviscid flow solution since flow separation is not properly modelled. A small expansion wave emanates inwards from the concave crank location at the Mach angle; and crosses over the symmetry plane. There is a chordwise low-pressure streak beginning at concave leading edge crank where the two crossflow shockwaves touch the inboards-facing expansion wave. In viscous flows, this would cause separation and vortices which would explain the chordwise low pressure streak. Artificial dissipation in the inviscid solution can cause the same effect.

At the root of the leading edge on the upper surface there is a weak crossflow shockwave which intersects and joins with the strong crossflow shock created by the 75 degree swept portion of the leading edge. Another weak shockwave emanates inwards from the convex crank location, interacting with and weakening the inboard crossflow shockwave.
On the lower surface, there are strong bands of pressure which are uniform along the 50 degree swept leading edge segments. At the convex leading edge crank and wingtip, these pressure peaks are terminated by expansion waves which emanate inwards. At the concave leading edge crank, a shockwave emanates inboards and diminishes towards the wing root.

Figure 4.46 shows the volumetric pressure distribution in the flowfield around the initial uncambered cranked wing at the supersonic design condition. Transparent slices are located on the Y=0m, Z=0m, X=0m, X=5m, X=10m, X=15m and X=20m planes. On the symmetry plane, the bow shockwave is clearly visible - extending both above and below the wing in the same manner as it does around the trapezoid wing. Due to the presence of the convex wing crank angle, there is an expansion fan which coalesces with the bow shock from the wing apex, severely weakening this shockwave as it propagates away from the wing surface towards the ground and laterally. The highly swept leading edge section has a lower normal Mach number and higher normal incidence angle than the 50 degree swept sections, and due to the concave crank there is an expansion fan upstream of this leading edge section instead of a shockwave. At the concave crank location there is another bow-type shockwave which lies just upstream of the outer wing leading edge.
On the constant-X planes, the bow shockwaves are visible upstream of the 50 degree leading edge sections and the expansion fan is visible upstream of the 75 degree swept section. These planes also serve to highlight the extreme differences in flow structures caused by the differences in leading edge geometry. The flow structure around the outer span of the wing is highly similar to the flow structure around the trapezoid wing, due to the geometrical similarity of the wings in this region.
At the wing trailing edge, the shock waves which turn the flow back towards the free-stream direction are weaker in the cranked wing case than the trapezoid wing case. This could be due to slightly lower wing root loading (N/m in 2D or N/m² in 3D) which arises from the increased root chord length and wing area.

Figure 4.47 shows solutions to the discrete adjoint-Euler equations describing the surface drag sensitivity of the trapezoid wing. Red regions of the plot show positive gradient (i.e. drag will reduce if surface moves outwards) and blue regions show negative gradient (i.e. drag will reduce if surface moves inwards). As with previous studies, there is a strong spike in positive sensitivity around both surface-impinging shockwaves, shown here by red lines on the upper surface. There is a strong negative sensitivity along the upper leading edge, trying to droop the edge down to meet the flow direction. Rather interestingly, there is also a negative sensitivity region protruding inboards from the wingtip at the local Mach angle towards the root/apex; on both upper and lower surfaces. It is reasoned that these are the regions which directly influence wingtip vortical flow at the supersonic flight condition.
These results suggest that the major sources of drag, without taking skin friction into account, are surface-impinging shockwaves and wingtip vortices.

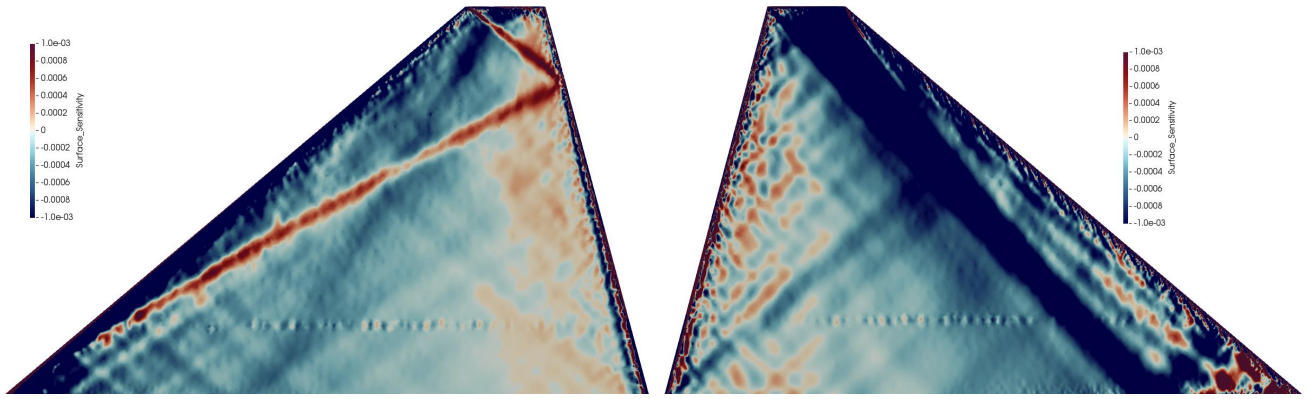

Fig 4.47 Upper (left) and lower (right) drag surface sensitivity colour maps of the trapezoid wing at the supersonic design condition.

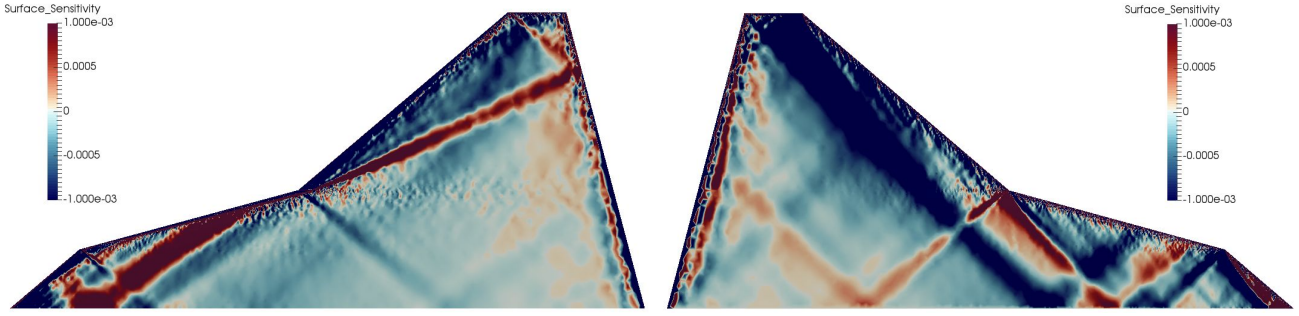

Fig 4.48 Upper (left) and lower (right) drag surface sensitivity colour maps of the cranked wing at the supersonic design condition.

Figure 4.48 shows the discrete adjoint surface drag sensitivity for the cranked wing planform. As with the flow solution, the outer 6m of the span shows a very similar surface sensitivity to the trapezoid wing surface sensitivity, due to the strong similarity of flow features in this region. Rather interestingly here, there is a strong positive/negative sensitivity band in the LERX region which is not aligned with any shockwave. It does, however, emanate inboards and upstream from the concave crank location at the Mach angle. This suggests that areas which influence the flow at the concave crank location have a very strong impact on the drag of the wing.
On the lower surface, the crank angles and the wingtip cause an interesting sensitivity pattern which is aligned with the Mach angle. In general from viewing this pattern it can be said that surface impinging shockwaves generally result in a positive drag sensitivity, whereas surface impinging expansions result in a negative drag sensitivity.

4.2.3 Design Optimisation Histories

The history of forces during the lift-constrained drag minimisation processes will be shown and discussed below. Both optimisations were performed in exactly the same manner except for the wing planform and, out of necessity, the corner points of the bounding FFD box. As a result; any differences are due only to the difference in wing planform.

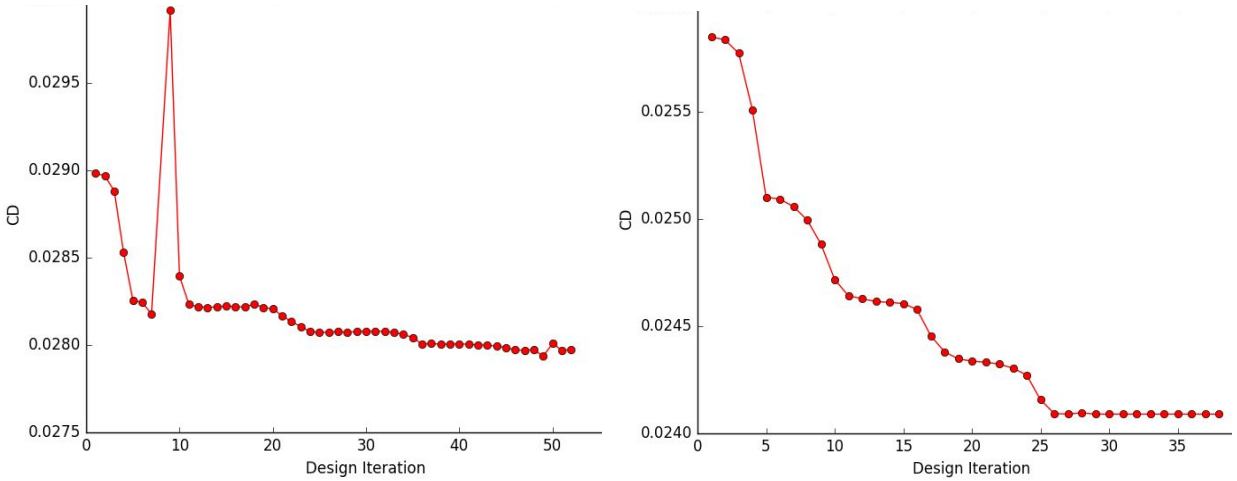

Fig 4.49 Drag history of trapezoid (left) and cranked (right) wing drag minimisation process.

Figure 4.49 shows the drag values during the design of the two wings. The trapezoid wing drag history is shown on the left, and begins with a sharp reduction in drag after the first two iterations, however on the 9th iteration there is a large increase in drag. This is part of the armijo-linesearch feature in the SLSQP algorithm. After the drag jump, there are two major steps down in drag over the course of 30 or so iterations. It is possible that during the flatter parts of these histories, there are control points with very small gradients which are at or near inflexion points in the design space. The cranked wing drag history, shown on the right, does not exhibit the same large armijo-linesearch jump as the trapezoid wing design history. The cranked wing history does however also exhibit the same stepped appearance, having a series of iterations with small changes in drag and then a large drop in drag before another few iterations with only small improvements.

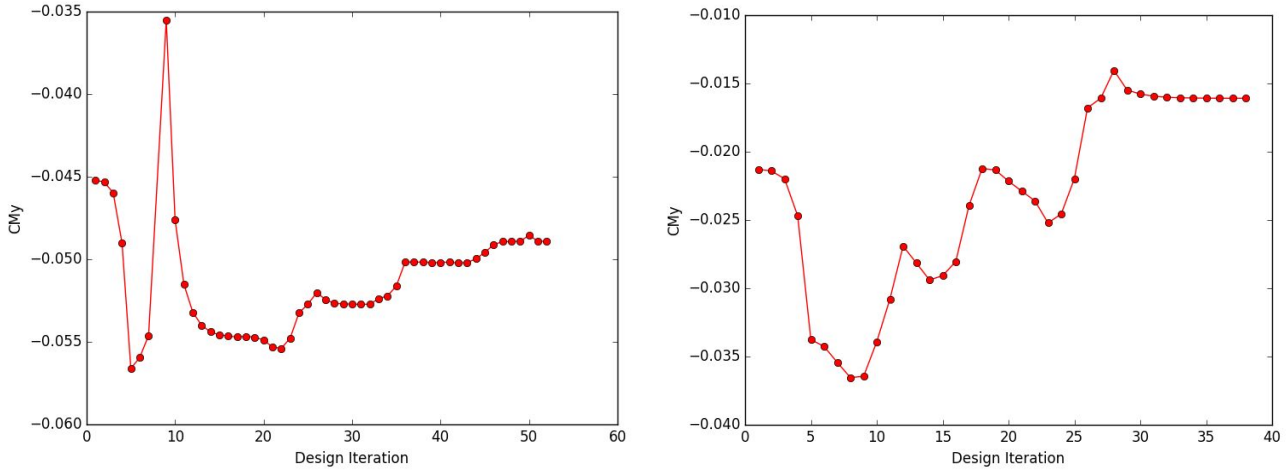

Fig 4.50 Pitching moment history of trapezoid (left) and cranked (right) wing drag minimisation process.

Figure 4.50 shows the histories of pitching moments of each wing throughout the two design processes. In both cases, the nose-down pitching moment increases by a large margin during the first 5 design iterations, in concurrence with the large drag reduction region in figure 4.49. After this, in both cases, there are decreases in nose-down pitching moment following each subsequent reduction in drag. This indicates that drag reduction is possible with both increases and decreases in pitching

moment. The optimum trapezoid wing has a larger nose-down pitching moment than the uncambered trapezoid wing, however the optimum cranked wing has a smaller nose-down pitching moment than the uncambered cranked wing. This shows a strong influence from wing planform on both pitching moment, drag, and the relationship between pitching moment and drag.

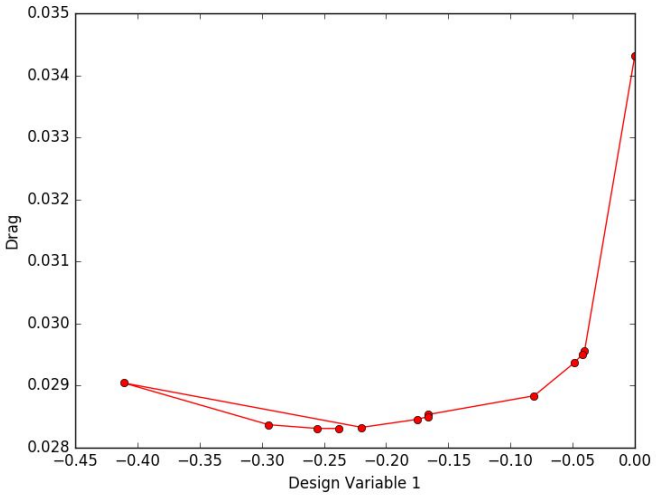

Fig 4.51 Graph of CD vs design variable value

Figure 4.51 shows the relationship between one of the FFD camber design variables at the apex point of the trapezoid wing and the drag of the wing. It is clear from this plot that this relationship forms a largely symmetrical bucket around the optimum point, with a well-defined minimum point at around -0.245m (meaning that the apex point of the wing has been drooped down by approximately 24.5cm).

4.2.4 Inviscid CFD and Geometrical Analysis of Optimum Designs

In this section, the optimised wing designs and their corresponding inviscid flow solutions will be presented, along with the integrated pressure forces on each wing. These flow solutions are what was created by SU2 and used by the optimisation algorithm in order to return the lift and drag values of the final design.

Table 4.3 Comparison of Euler forces for each wing design

Geometry	CL	CD	CMy
Trapezoid Initial	0.2500	0.02899	-0.04520
Cranked Initial	0.2500	0.02585	-0.02129
Trapezoid Adjoint Optima	0.2500	0.02794	-0.04890
Cranked Adjoint Optima	0.2500	0.02409	-0.01608

Table 4.3 shows the initial and optimised inviscid force values from the trapezoid and cranked wings. Since the soft-constrained strategy was used, the CL is exactly equal to 0.25 in all of these cases; indicating identical lift forces between each case. The drag coefficient of the trapezoid wing has been

reduced by 3.6% with a corresponding -8.2% change in pitching moment. The drag coefficient of the cranked wing has been reduced by 6.8% with a corresponding 24.5% change in pitching moment. The optimised cranked wing has the lowest drag of either design, with a 13.8% lower drag coefficient than the optimised trapezoid wing.

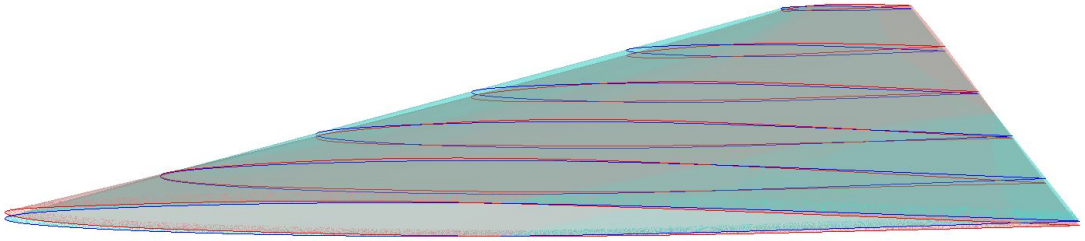

Fig 4.52 Geometrical comparison of uncambered and optimised trapezoid wing sections

Figure 4.52 shows the trapezoid uncambered (blue) and optimised (red) wing 3D shapes with highlighted aerofoil sections at 2m intervals along their span. This image demonstrates the increase in incidence at the wing root with slight reflex camber near the wing apex. The wing camber gradually increases along the span, and the max camber location moves backwards along the wing chord as span increases.

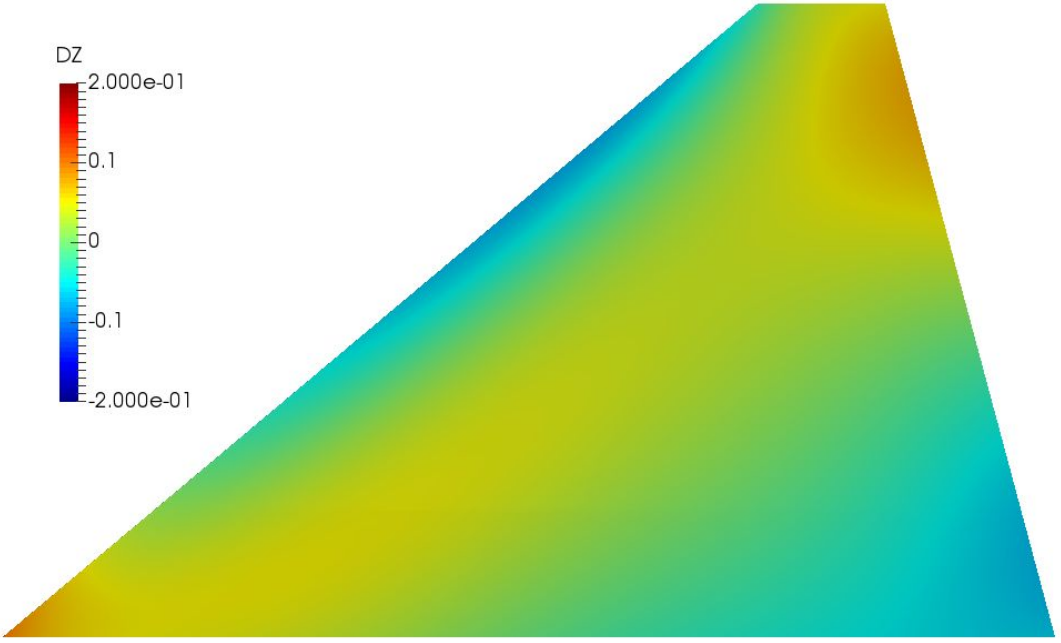

Fig 4.53 Mean camber surface of optimised trapezoid wing

Figure 4.53 shows the geometrical difference between the uncambered trapezoid wing and the minimum drag trapezoid wing. Since only the wing camber has been changed, this difference represents both upper and lower surfaces, and also accurately describes the mean camber surface of the wing. Notable effects are:

- Increased incidence at the wing root
- Increased twist or washout from root to tip
- Near-conical leading edge droop and mid-span upwards deflection as seen in the conical wing design study
- Wingtip raised by ~0.05m

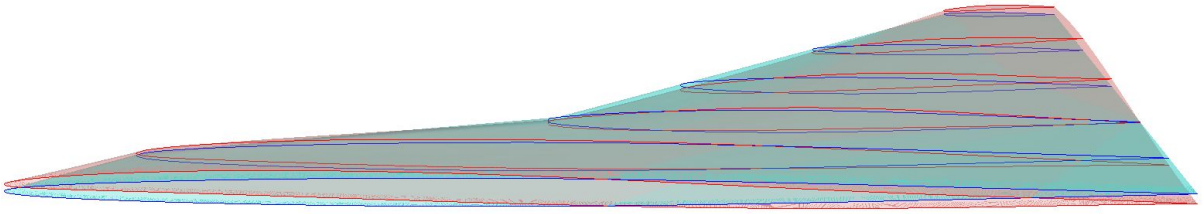

Fig 4.54 Geometrical comparison of uncambered and optimised cranked wing sections

Figure 4.54 shows the cranked uncambered (blue) and optimised (red) wing 3D shapes with highlighted aerofoil sections at 2m intervals along their span. This image demonstrates a similar increase in incidence at the wing root to the trapezoid case. As with the optimised trapezoid wing, the wing camber gradually increases along the span, and the max camber location moves backwards along the wing chord as span increases. The wing tip is raised and there is a consistent wing twist from root to tip.

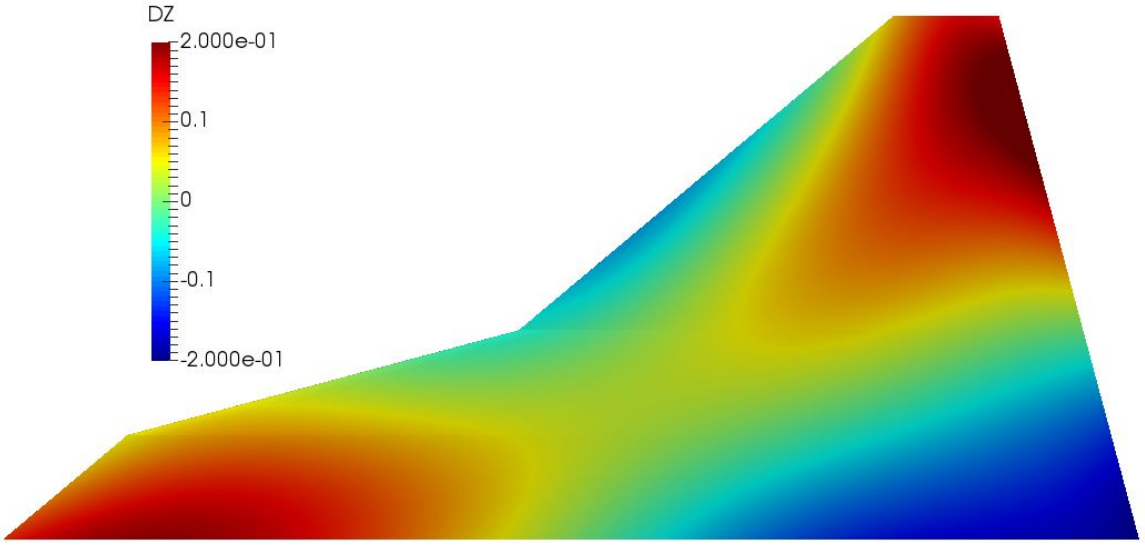

Fig 4.55 Mean camber surface of optimised cranked wing

Figure 4.55 shows the geometrical difference between the uncambered cranked wing and the minimum drag cranked wing, representing both upper and lower surfaces. Once again, this plot also represents the mean camber surface of the optimised wing; since the initial wing has a planar mean camber surface with constant Z=0. Notable effects are:

- Increased incidence at the wing root
- Increased twist or washout from root to tip
- Slight leading edge droop for the inner 50 degree swept leading edge portion
- Large leading edge droop at and outboard of the concave leading edge crank
- Wingtip raised by ~0.15m

It is interesting to note that nearly all of the changes in camber are around double the magnitude of those which were applied to the minimum drag trapezoid wing. Leading edge droop has mostly been applied to the outer 6m wing section rather than being near-conical for the whole span.

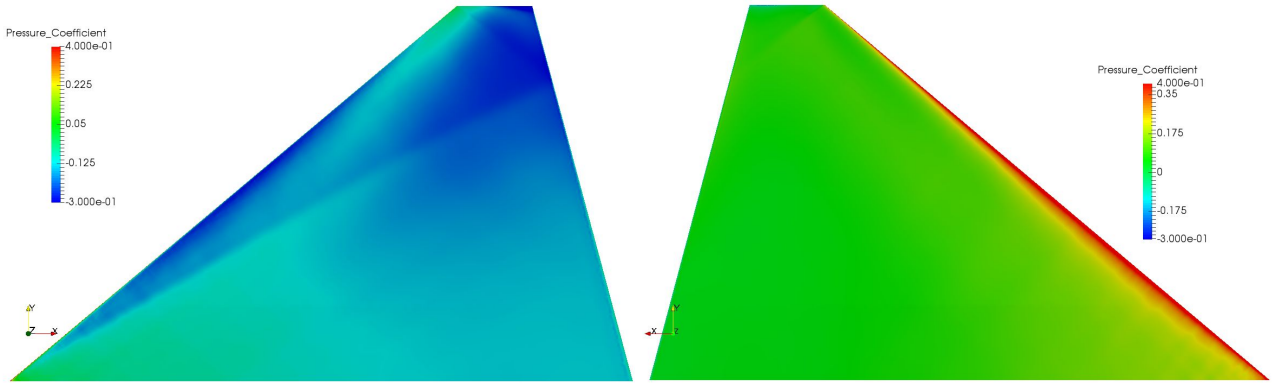

Fig 4.56 Upper (left) and lower (right) surface pressure coefficient color maps of the optimised trapezoid wing at the supersonic design condition.

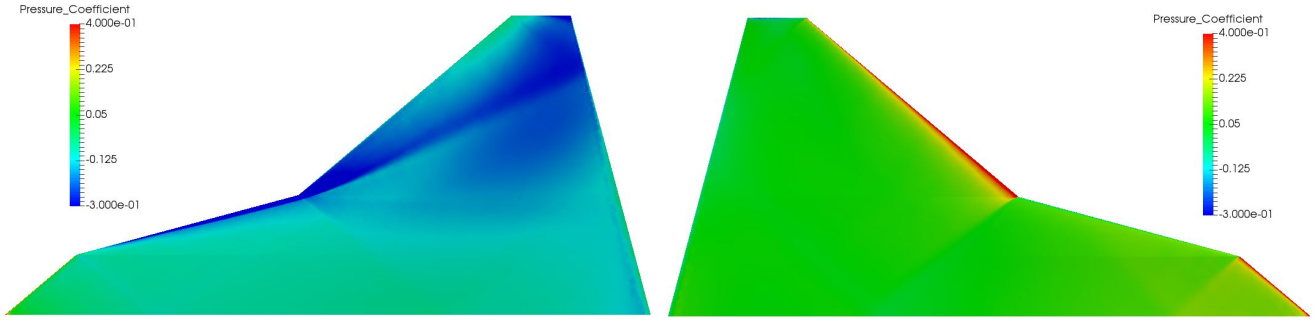

Fig 4.57 Upper (left) and lower (right) surface pressure coefficient color maps of the optimised cranked wing at the supersonic design condition.

Figure 4.56 shows the surface pressure distribution of the optimised trapezoid wing as calculated by the Euler equations. It is clear that the strength of the embedded crossflow shockwave has been reduced across the span of the wing, but not eliminated entirely and that the loading at the wingtip has been reduced dramatically in order to control vortex drag. The unloading of the wing tip has also had the effect of nearly eliminating the surface-impinging shockwave which was present between the tip and trailing edge of the initial design. The outer 4m of the span is highly aft-loaded; weakening shockwaves through favourable pressure gradient and helping to reduce wingtip drag. On the lower surface the high-pressure band which was previously uniform along the span has now been reduced dramatically towards the wing tip and smeared near the wing root due to the wing twist which has been applied.

Figure 4.57 shows the surface pressure distribution of the optimised cranked wing as calculated by the Euler equations. It is clear that the strength of the embedded crossflow shockwave on the outer span of the wing has been reduced, and that the loading at the wingtip has been reduced dramatically in order to control vortex drag. The unloading of the wing tip has also had the effect of nearly eliminating the surface-impinging shockwave at the wingtip, as in the trapezoid wing case. The crossflow shockwave has been eliminated from the innermost wing leading edge section from the apex to the convex wing crank. On the lower surface, as with the trapezoidal case, the bands of high pressure at the leading edge have been reduced.

4.2.5 Inviscid Spanwise Force Distributions

In this section, the spanwise inviscid force distributions have been analysed and presented in the same manner as was shown in the conical wing design section. 2D chordwise slices of each wing surface at ~0.1m spanwise intervals were taken from the flow solutions and the pressure forces on each slice were integrated into lift, drag etc.

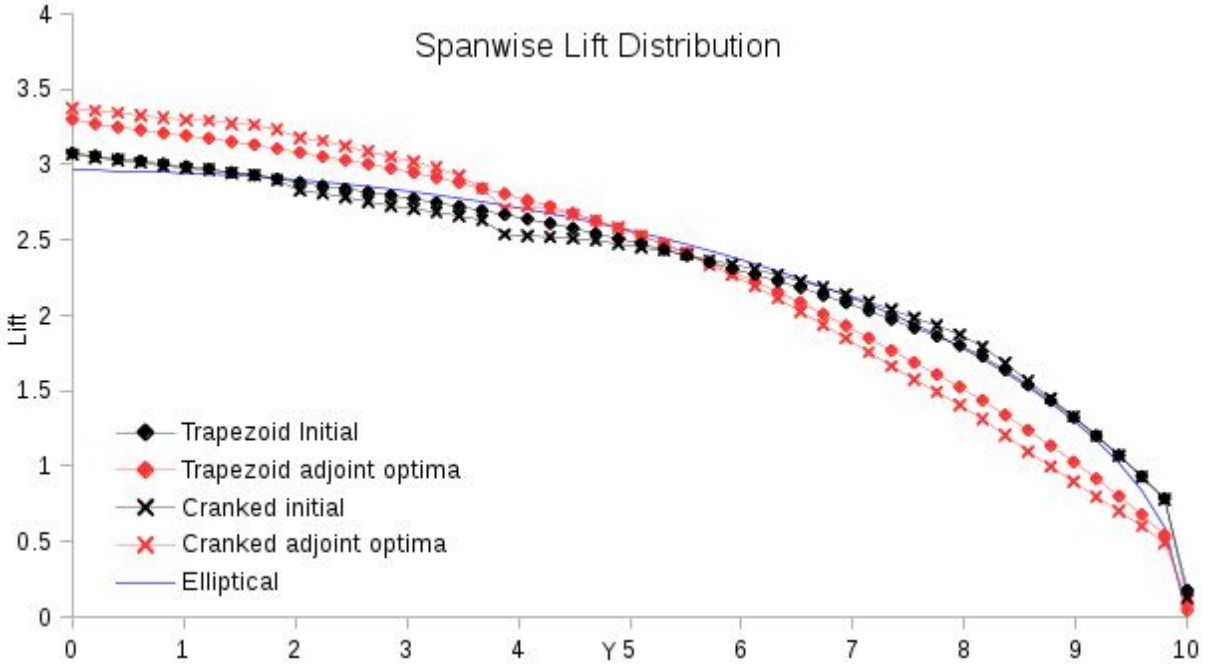

Fig 4.58 Comparison of inviscid spanwise lift distribution for initial and optimised wing concepts.

Where:

Lift = Fz(cos[α])-Fx(sin[α]) Equation 4.2

Fz = ∑(Cp*Znormal) Equation 4.3

Fx = ∑(Cp*Xnormal) Equation 4.4

With α in radians. Xnormal and Znormal represent the area of each surface mesh element when projected in the X and Z directions respectively.

Figure 4.58 shows the spanwise lift distributions of the uncambered and minimum drag wings as calculated by the inviscid Euler equations. An elliptical distribution is shown as a light blue line on the chart for reference. The minimum drag designs are displayed in red and the initial designs are displayed in black. Rather interestingly, both minimum drag wings share a similar lift distribution to each other; with some minor differences; indicating that optimum lift distribution is not particularly sensitive to differences in planform for low-AR supersonic wings. The uncambered wings both show a near-elliptical lift distribution whilst the minimum drag designs have a lift distribution which appears to be somewhere between elliptical and triangular. The minimum drag cranked wing has slightly lower wingtip loading and slightly higher root loading than the minimum drag trapezoid wing.

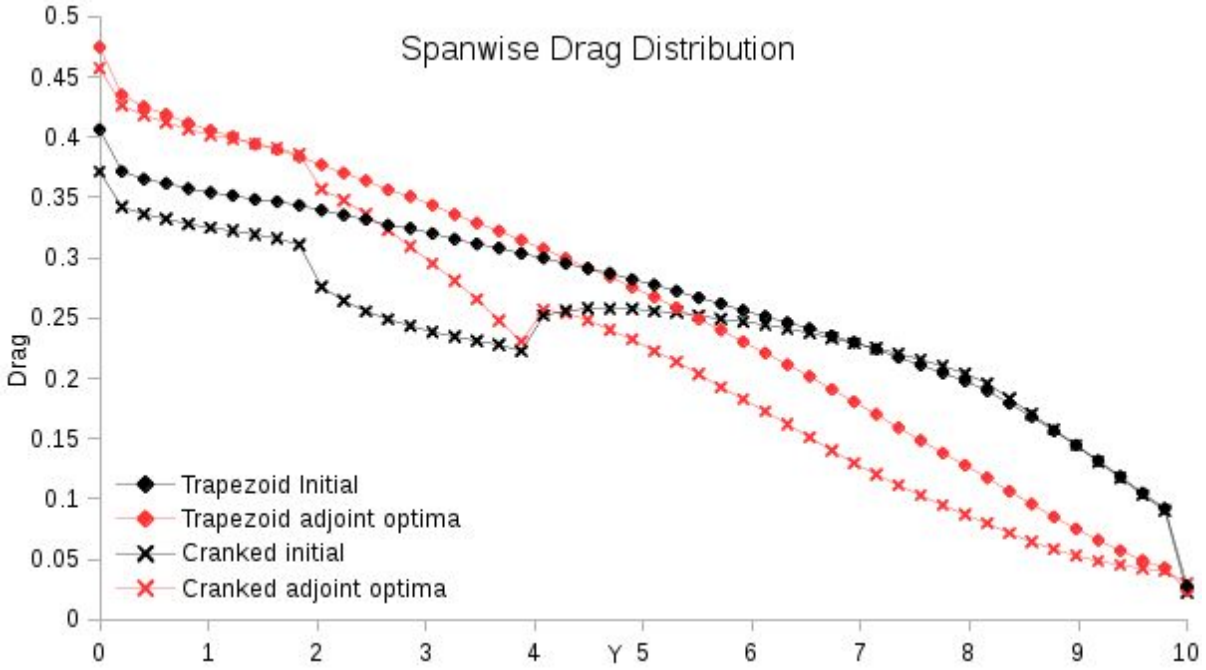

Fig 4.59 comparison of spanwise drag distribution for initial and optimised wing concepts.

Where:

Drag = Fx(cos[α])+Fz(sin[α]) Equation 4.5

Figure 4.59 shows the spanwise drag distributions of the uncambered and minimum drag wings as calculated by the inviscid Euler equations. Interestingly, both minimum drag designs have higher drag at the wing root than the uncambered wings; due to increase in local lift. The 75 degree swept leading edge portion of the cranked wing produces a notable drop in drag in both cases due to reduction in attachment line pressure, however in the optimised case this drop is less notable towards the root. Drag at the root of both optimised wings is near-identical, however from the convex leading edge crank onwards the cranked minimum drag wing has a lower drag than the minimum drag trapezoid wing. Drag at the tip of both uncambered wings is near-identical, with the uncambered cranked wing having lower drag from Y=6m inwards.

Figure 4.60 shows the spanwise axial force distributions of the uncambered and minimum drag wings as calculated by the inviscid Euler equations. Largely reminiscent of the spanwise drag distributions, the axial force distributions show the impact of leading edge suction on the 75 degree swept portion of the wing and indicate that both of the optimised wings have ‘thrust-producing’ wing tips, with forces which act in-line with the thrust direction (Fx). Clearly, these sections do actually produce drag in the literal sense when their forces are resolved into wind-axis coordinates.

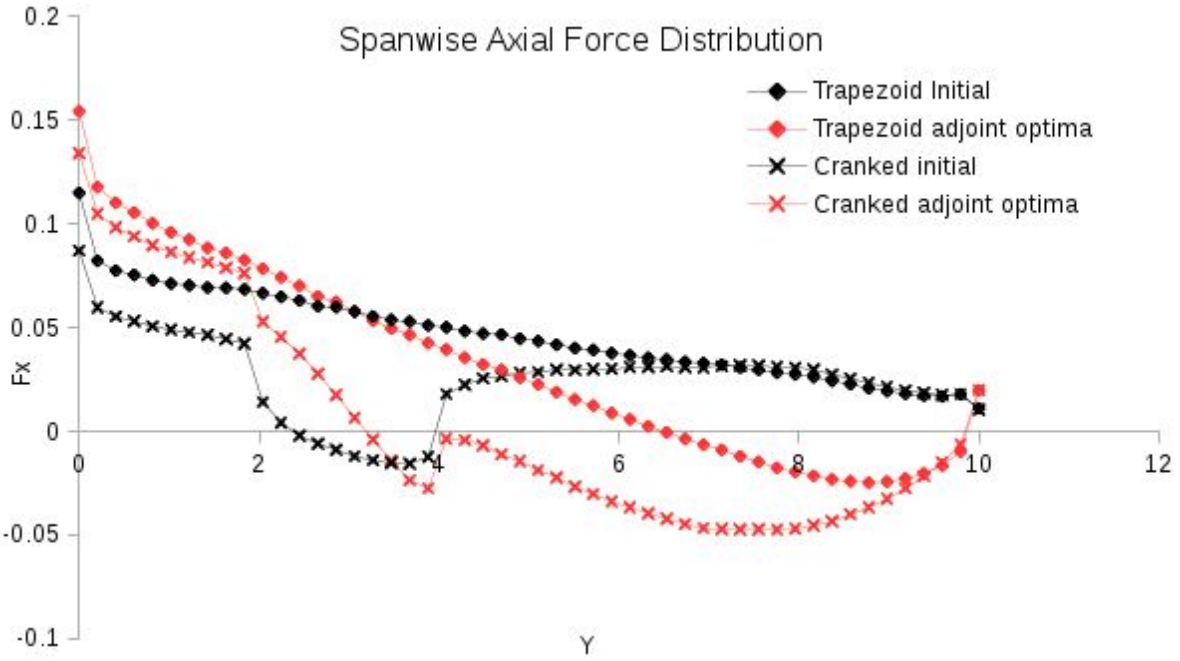

Fig 4.60 comparison of spanwise axial force distribution for initial and optimised wing concepts

4.2.6 RANS Evaluations of Minimum Pressure Drag Wings

The SU2 flow solver has been used to generate RANS solutions for both designed wings and uncambered datum wings in order to compare their performance and characteristics whilst taking the effects of viscosity into account. The Reynolds number used for these evaluations is 6.6×10^6/m in all following cases; since solutions with this Reynolds numbers have already been verified against wind tunnel data earlier in this thesis. It has already been established that boundary layers will interact with the shockwave-dominated flow structures present in these cases; potentially producing separation, vortical flow and boundary layer thickening. All of these interactions will have some effect on the performance and stability of the wing.

Hybrid RANS grids have been utilised using the T-Rex feature in pointwise; with a mix of cell types used for surfaces and the volume grid.
Figure 4.61 shows the hybrid surface grids used for RANS evaluations. Each wing design with the same planform shares the same grid topology as shown above; simply projected onto the deformed Z coordinates of the cambered wing surfaces. For the surface grids, the initial spacing at the leading edges is 0.0005m and 0.005m at the trailing edges; both having a growth rate of 1.15. The triangular elements in the surface grids are not specifically aligned or refined according to any particular flow feature but are refined enough to capture any feature of interest at multiple incidence angles and Mach numbers.

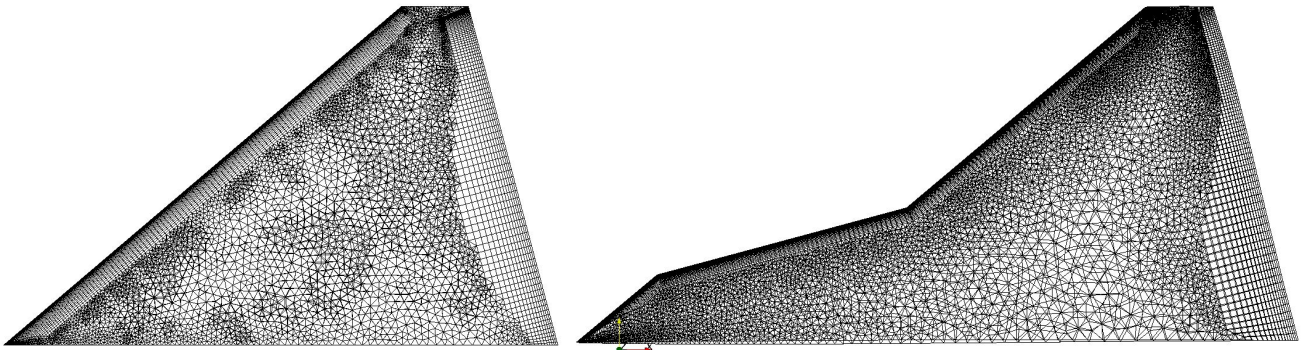

Fig 4.61 RANS Unstructured surface grids with hybrid topology

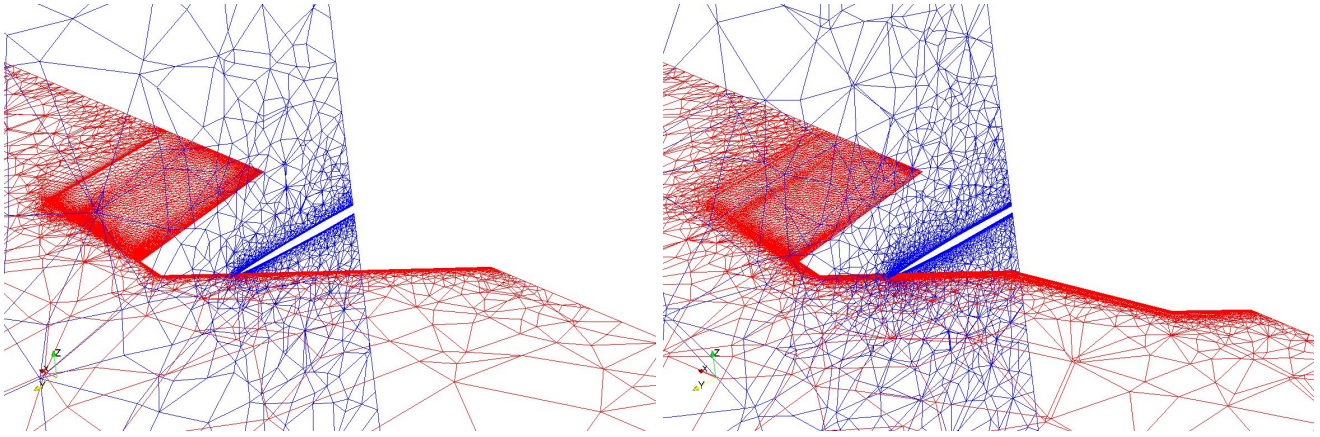

Fig 4.62 RANS unstructured volume grid slices showing hybrid topology

The volumetric grids share a similar mix of cell types as the surface grids, with hexahedral and prism layers close to the surface- grown out from the surface grid normals. After 10-35 layers of boundary layer prisms, the grid becomes unstructured tetrahedrons - joined to the prisms using pyramid cells. The tetrahedral cells then extend out to a hemispherical farfield grid with a radius of 500m. This large radius was used instead of a shock-aligned grid topology so that the grid can be used equally for both supersonic and transonic flow evaluations.

Initially, the RANS flow solver has been used in fixed-CL mode in order to investigate the designs at precisely their intended design point. Some grid refinement in the wake region is visible in figure 4.62 aft of the trailing edges of each wing. This refinement has been used in order to accurately capture wake patterns and accurately resolve flows at both supersonic and transonic flow velocities.

Figure 4.63 shows the history of various flow and solver variables during a flow simulation at CL=0.25. It can be seen in the plot on the top left that in the first 2000 flow solver iterations, the density residual converges by 3 orders of magnitude. From the plot on the bottom right, it can be seen that in the same number of iterations the CL value converges to a steady state. This is an essential part of the fixed-CL methodology, since the updated α value depends on the accuracy of the calculated CL value at this point. On the plot on the bottom left it can be seen that after the first 2000 iterations, a large jump of ~0.5 degrees is made in α. After this point, there is a corresponding divergence of the density residual whilst the flow solution goes through an abrupt change due to the new α value. The effect of this can be seen in the plot on the bottom right, where CL value begins to oscillate once again and begins to converge on a new value. As the solution progresses, the updates in α become smaller and

smaller until they have a negligible effect on the total forces calculated by the solver. On the top right, the CFL condition history is shown. The SU2 solver features an adaptive CFL number which adjusts itself to improve both solution stability and accelerate convergence. The minimum value is 0.5, which it returns to every time the α value is changed. On average, a value of 5.5<CFL<6.5 is generally selected. Convergence is said to be achieved when three conditions are met: firstly that the lift coefficient has reached the target value, secondly that the lift coefficient has reached a steady state and thirdly that the density residual has converged by 3 orders.

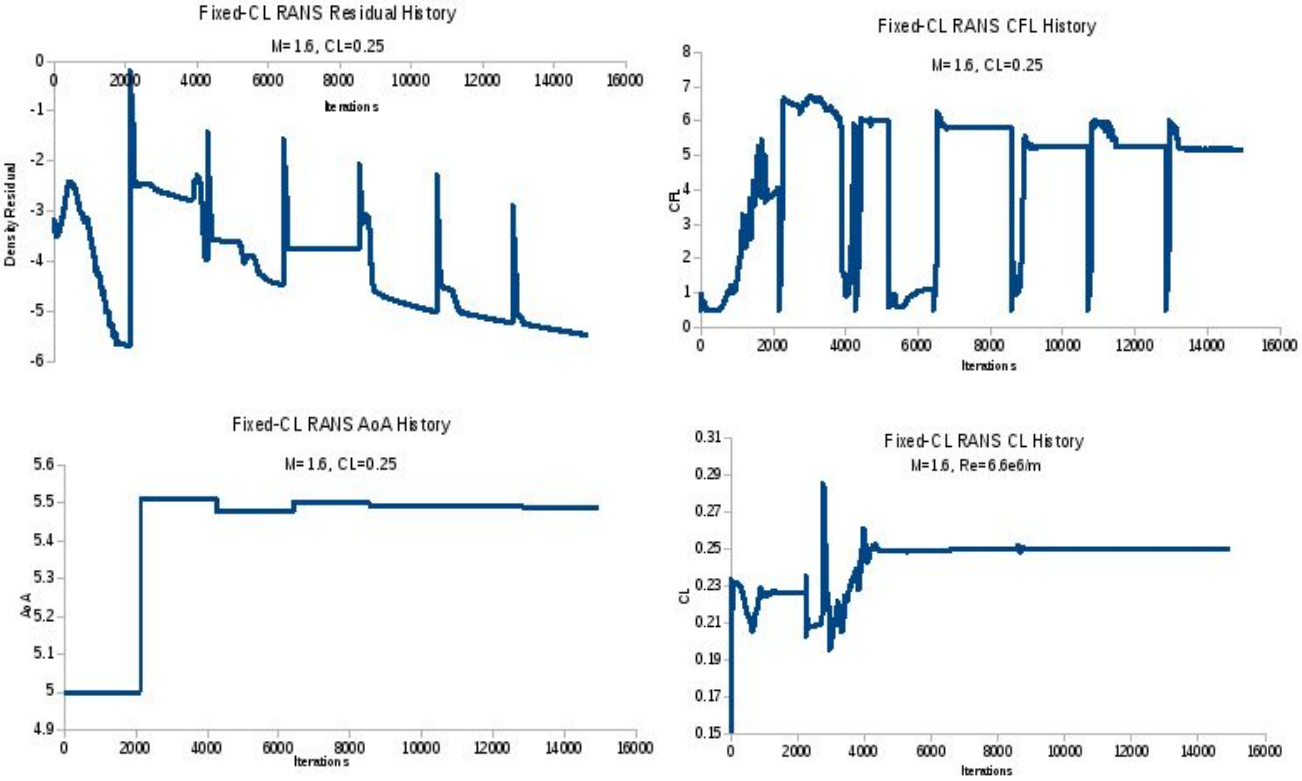

Fig 4.63 Histories during fixed-CL RANS calculation. Density residual (top left), CFL (top right), α (bottom left), CL (bottom right).

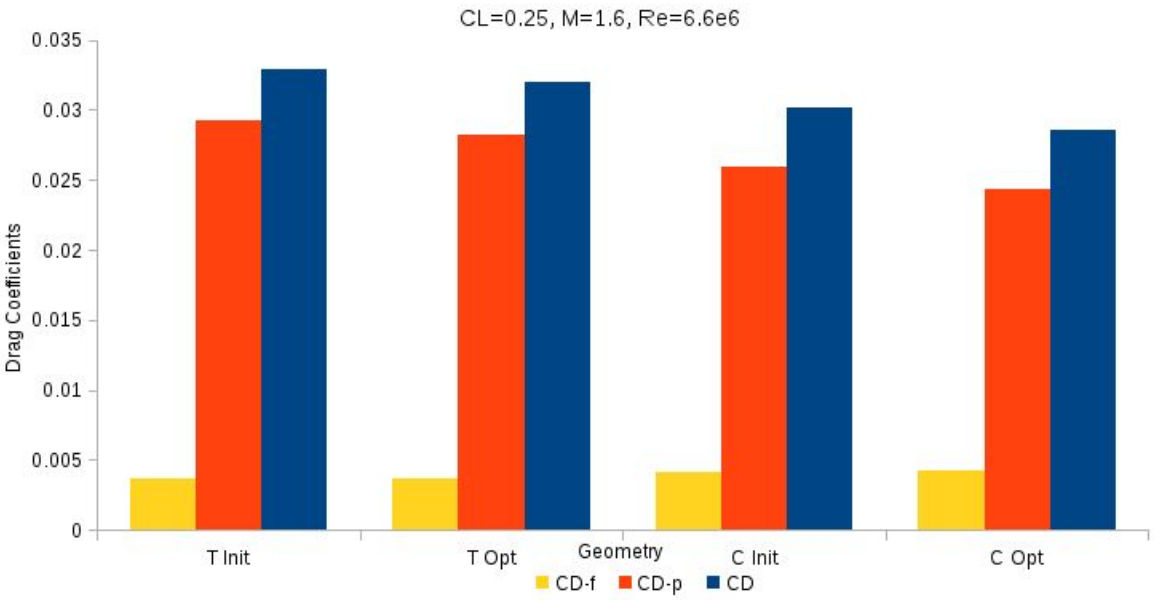

Fig 4.64 Comparison of drag components for both uncambered and optimum wings at the supersonic design condition.

Figure 4.64 helps to visualise the components of drag on both minimum drag wings and the uncambered datum wings. Friction drag is shown in yellow, pressure drag in red and total drag in blue. As expected, the optimiser has only had any significant effects on the pressure drag of the wings. This is expected since friction drag was not taken into account during the optimisation process. The cranked wing has a higher skin friction drag component than the trapezoid wing due to it's increase in wetted area, however the lower pressure drag more than makes up for this difference. Interestingly, the wing with lowest total drag also has the highest skin friction drag.

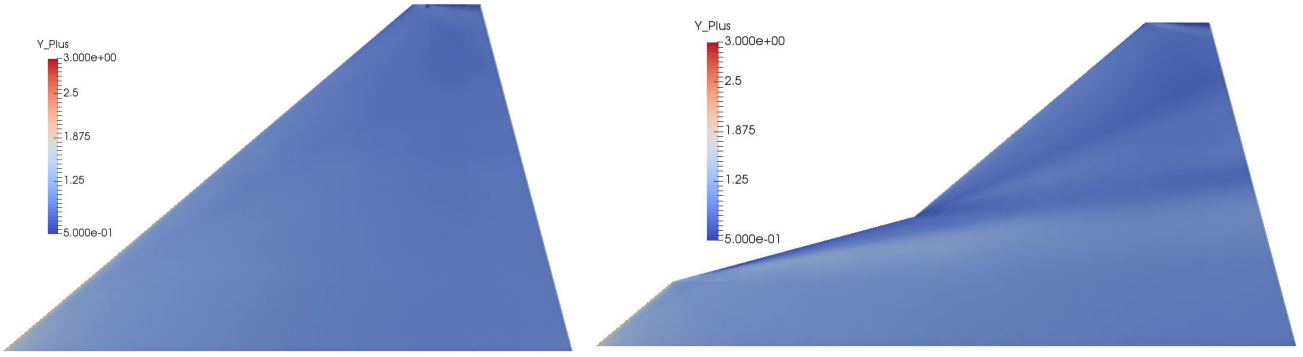

Fig 4.65 Y+ values on the upper surface of the uncambered trapezoid and cranked wings at the supersonic design condition.

Figure 4.65 demonstrates that the value of Y+ on the surface of both wing planforms at the design condition averages 1, with some zones slightly higher (near attachment lines) and some slightly lower (shockwaves). This means that there is high enough resolution near the wall to capture all boundary layer effects. This provides a high level of confidence in the accuracy of the boundary layer model.

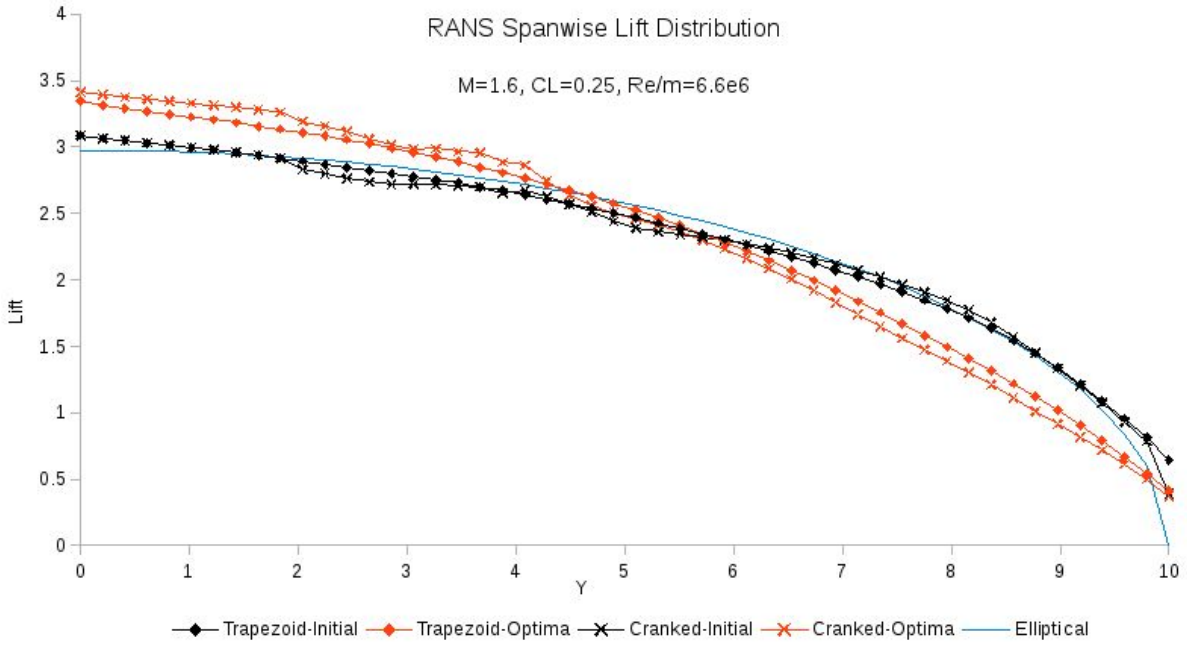

Fig 4.66 comparison of spanwise lift distribution for initial and optimised wing concepts.

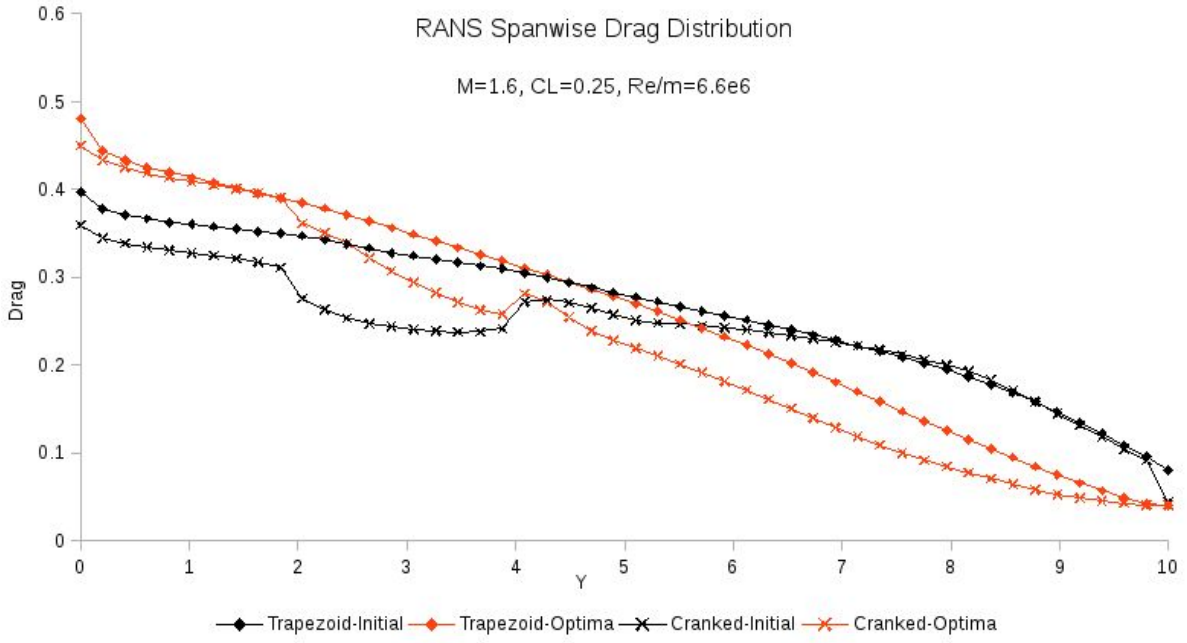

Fig 4.67 comparison of spanwise drag distribution for initial and optimised wing concepts.

Figure 4.66 shows the spanwise lift distributions of the uncambered and minimum drag wings as calculated by the viscous RANS equations. An elliptical distribution is shown as a light blue line on the chart for reference. The main difference between these results and those derived from the Euler flow solutions is at the wing tip, where the lift does not fall to near zero as it does in the inviscid case. The other difference concerns the cranked wing shape, which when simulated using RANS produces a large increase in lift in the region 3m<Y<4.5m. This difference in lift is attributable to the vortical flow

structure created by the shock-boundary interaction at the 75 degree swept portion of the leading edge.

Figure 4.67 shows the spanwise drag distributions of the uncambered and minimum drag wings as calculated by the viscous RANS equations. They are, once again, broadly similar to the drag distribution calculated by the Euler equations except for the cranked wings at Y=4m where vortical flow increases the lift and drag values.
In order to explore the characteristics of each wing in further detail, an α-sweep was conducted for each wing at 4 degree intervals in order to generate force polars.

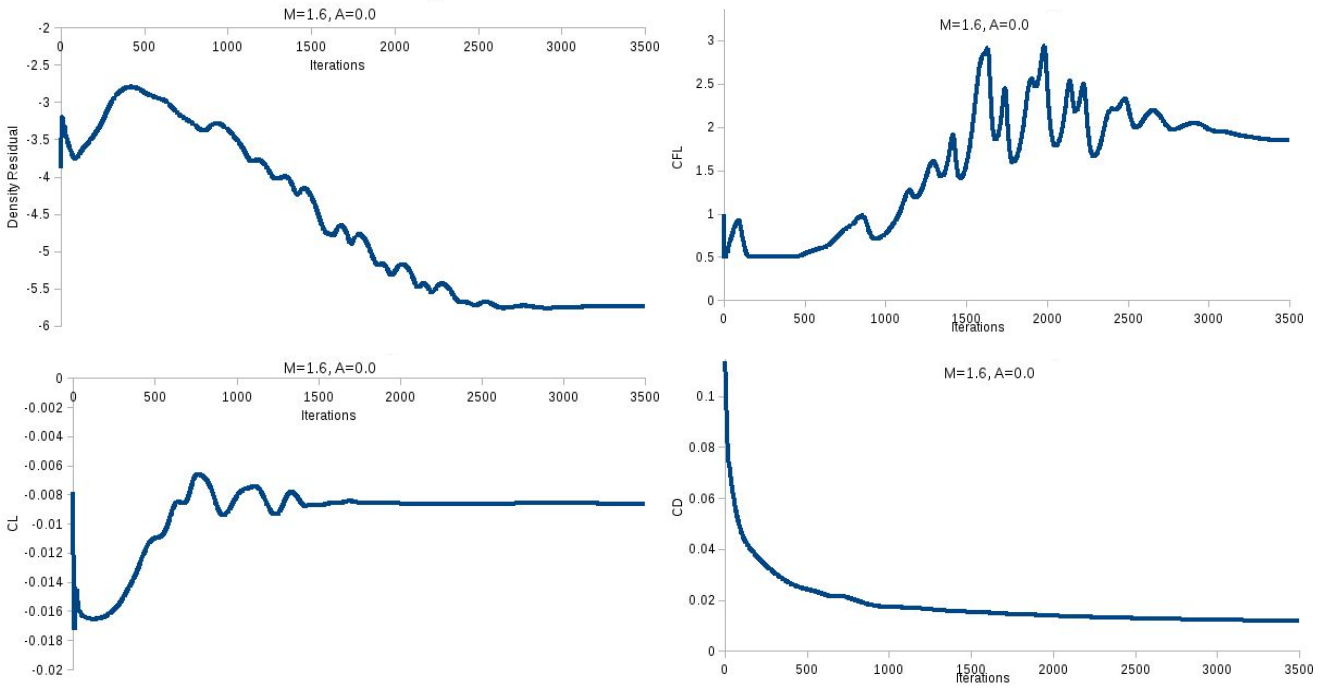

Fig 4.68 Histories during fixed-α RANS calculation. Density residual (top left), CFL (top right), CL (bottom left), CD (bottom right).

Figure 4.68 shows the histories of flow and solver variables during fixed-α studies. The density residual converges by 3 orders and then remains steady at a value of nearly 10-6 after 3000 iterations. The CL value visibly converges to a steady value after 2000 iterations however the CD does not converge until 3000 iterations. Figure 4.68 is representative of all geometries at all α values; in that forces and residuals converge in a similar manner for each case - however the data is taken directly from the flat trapezoidal zero-incidence case.

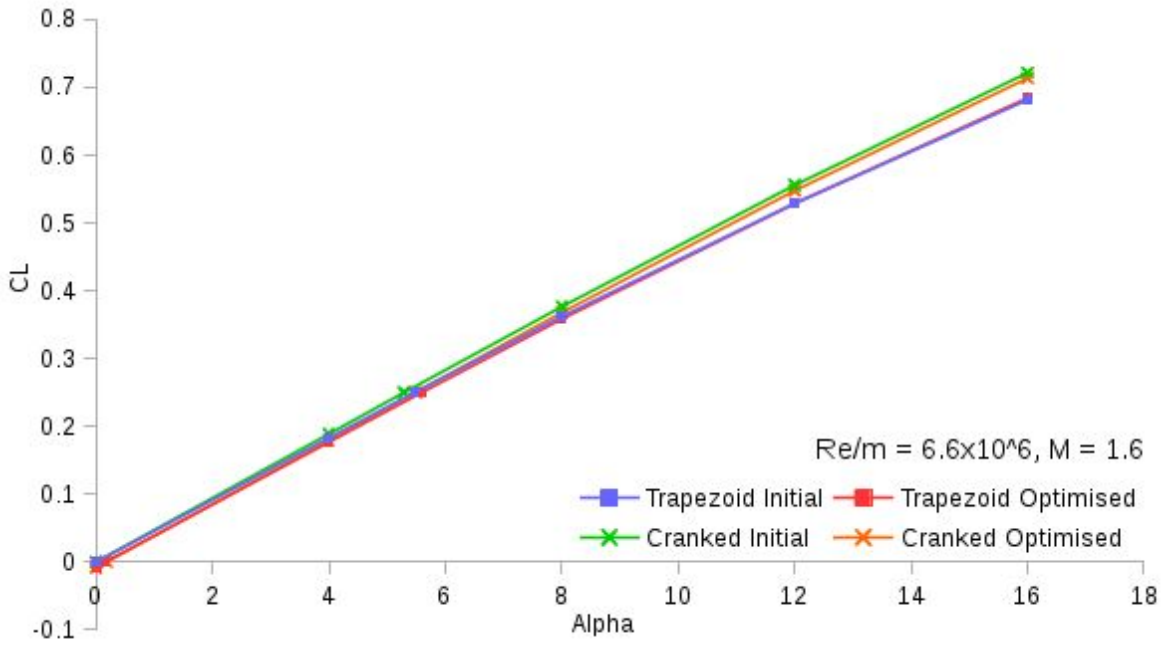

Fig 4.69 RANS CL vs α, M=1.6, Re/m=6.6x10^6

Figure 4.69 shows the lift curves of the trapezoid and cranked minimum drag designs compared with the initial uncambered wings. Both uncambered wings have zero lift at zero degrees α, however the lift slope of the cranked wing is slightly higher than the trapezoid wing. The slope of the trapezoid wing also decreases slightly with increased α, making it slightly nonlinear.
Both of the minimum drag wings have negative lift coefficients at zero degrees α and produce CL=0 at similar incidence values. The trapezoid optimised design has a more linear lift curve than the uncambered trapezoid wing, meaning that it produces more lift at α values above 12 degrees. The optimised cranked wing has a very similar lift curve slope to the flat cranked wing throughout the range of incidences tested here, simply shifted downwards by approximately 0.01.

Figure 4.70 shows the drag curves of the trapezoid and cranked minimum drag designs compared with the initial uncambered wings. The cranked uncambered wing has the lowest zero-lift drag due to its lower leading edge pressure than the trapezoid wing. At all the positive lifting coefficients tested in this study the uncambered trapezoid wing has the highest drag due to it's large lift-induced drag. The cranked minimum drag wing has the lowest drag at all positive lifting coefficients tested in this study. The trapezoid optimised wing has the highest zero-lift drag.

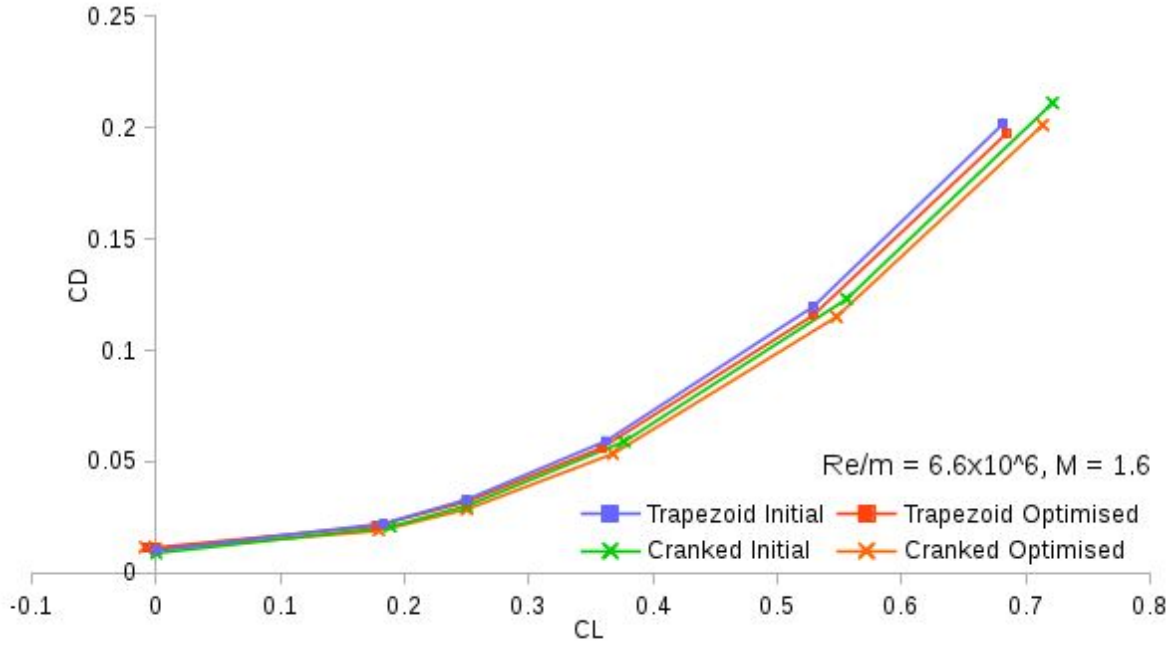

Fig 4.70 RANS CL vs CD, M=1.6, Re/m=6.6x10^6

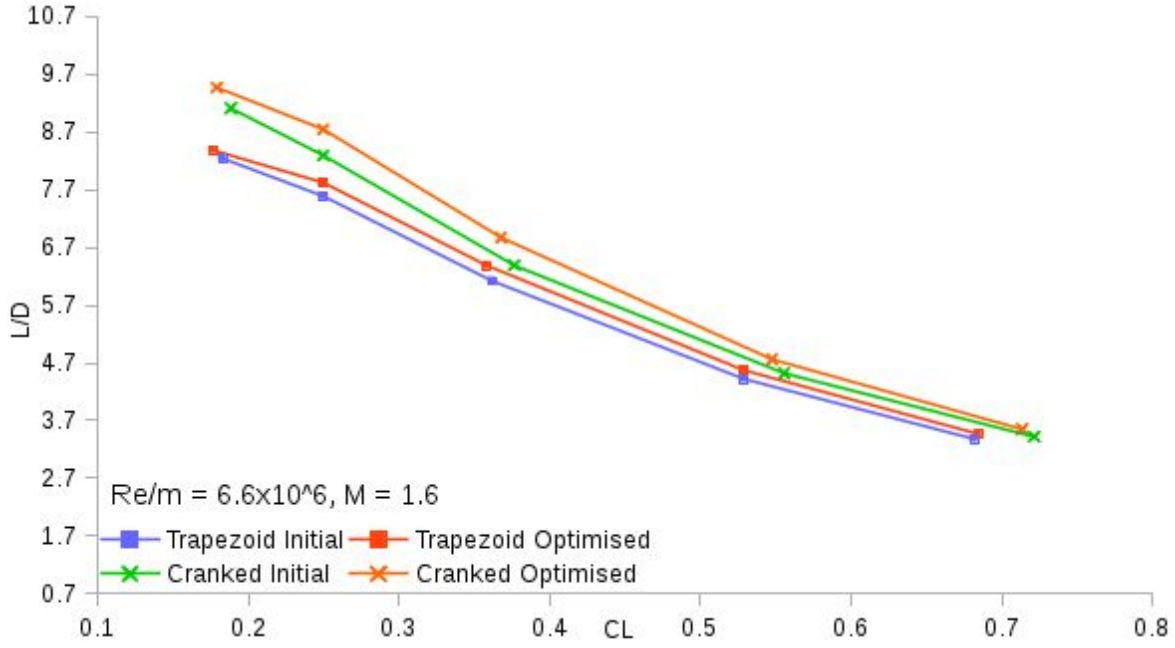

Fig 4.71 RANS CL vs L/D, M=1.6, Re/m=6.6x10^6

Figure 4.71 shows the efficiency of the trapezoid and cranked minimum drag designs compared with the initial uncambered wings, between $4<\alpha<16$. The cranked optimised wing has the highest efficiency whilst the trapezoid uncambered wing has the lowest. At CL=0.25, there is a larger difference in efficiency between optimised and uncambered cranked wings than optimised and uncambered trapezoid wings.

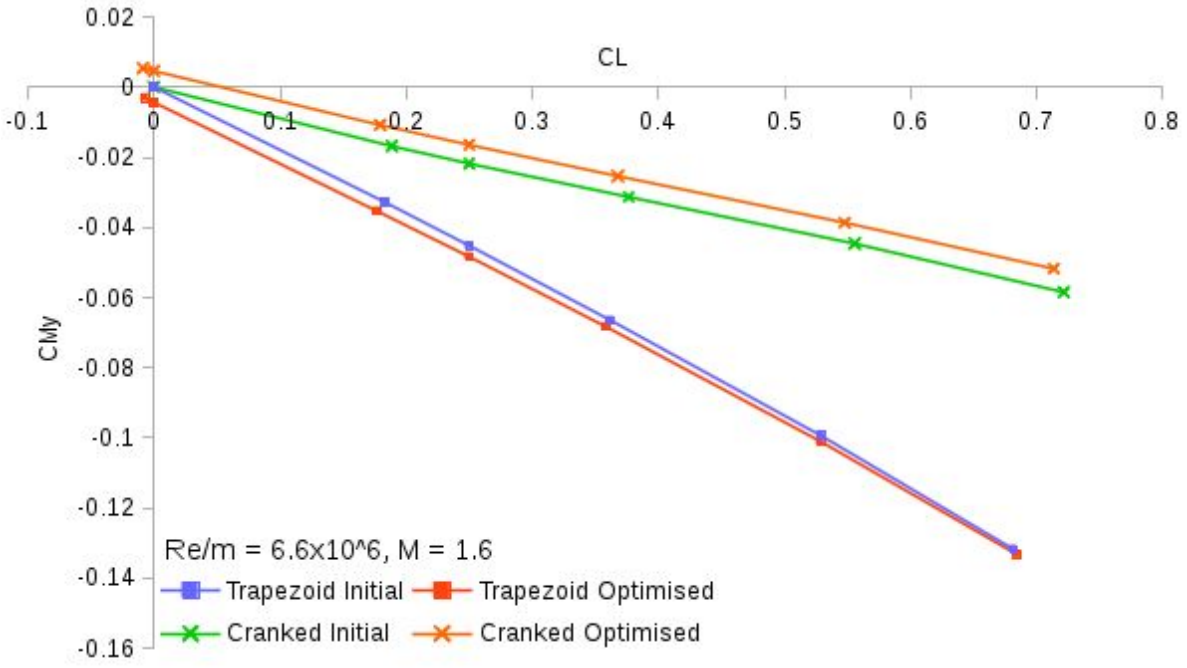

Fig 4.72 RANS CL vs CMy, M=1.6, Re/m=6.6x10^6

Figure 4.72 shows CL vs pitching moment for the designs in this study. The trapezoid wings have a larger pitching moment slope than the cranked wings, indicating higher stability in the pitch axis. Both uncambered wings have zero pitching moment at zero lift. Rather interestingly, the optimised cranked wing has a CMy curve which is shifted upwards from the uncambered wing, whilst the optimised trapezoid wing has a CMy curve which is shifted downwards from the uncambered wing.

At the supersonic design point, CL=0.25, the cranked minimum drag wing has the smallest pitching moment, meaning that it would require less pitch trim to achieve equilibrium. The optimised trapezoid wing would require the most pitch trim to achieve equilibrium at the design condition.

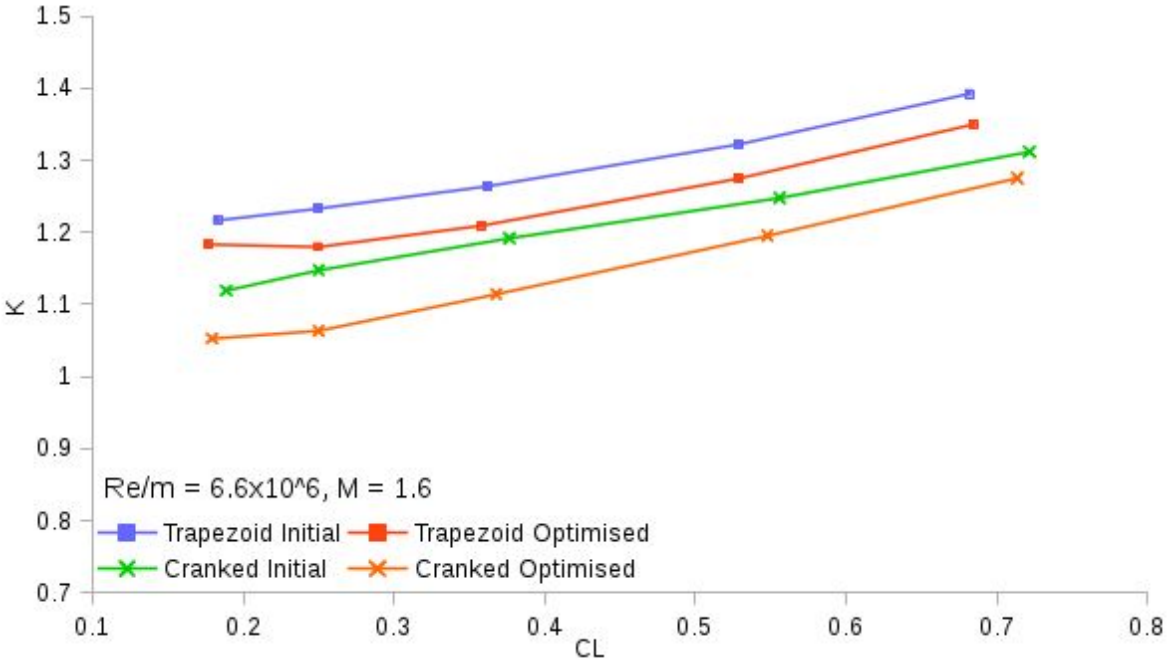

Fig 4.73 RANS CL vs K, M=1.6, Re/m=6.6x10^6

K-factor shown in figure 4.73 is calculated in the manner described previously. Both initial flat wings seem to have nearly linear CL-K relationships in the region shown, whereas both optimised wings seem to have a more nonlinear relationship. The trapezoid minimum drag wing has its lowest K-factor at the design condition, CL=0.25, whereas the cranked minimum drag wing has its lowest K-factor at a lower CL.

4.2.7 Conclusions of Concept Wing Pressure Drag Minimisation Study

The soft constrained optimisation method was utilised to produce minimum pressure-drag camber designs for two supersonic wing planforms with fixed thickness distributions, providing a significant increase in the performance of each wing. The effect of planform on wing performance at supersonic speeds is found to be substantial with an 8.5% difference in drag between each planform with uncambered aerofoil. It is also found that the difference in drag values between uncambered and minimum drag wings is greater in the case of the cranked wing planform, with the trapezoid wing achieving 3% drag reduction and the cranked wing achieving 5.2% drag reduction.

The designs produced in this section can be seen as having the minimum pressure drag for their given planform shape, aerofoil thickness distribution and lifting coefficient. They can be used as a benchmark to evaluate the performance of wings which are designed with other objectives or constraints because it can be seen how close the performance values are to these ‘ideal’ designs.

As with the conical wing drag reduction study, it has been found that a major source of drag at this Mach number was embedded crossflow shockwaves; which were reduced substantially by the adjoint optimisation process. It has also been found, however, that in a similar way to the conical wing, the minimum drag wings do indeed still feature weak crossflow shockwaves. It can be ascertained from this that other sources of pressure drag become equally as important as shockwave drag as the size of the shockwave reduces. A tradeoff has been made between embedded crossflow shock intensity and lift-induced or wingtip drag; some shockwave has been tolerated but in exchange for a reduction in drag from other sources. It is known from Mason et al’s previous experiments[33,48] that both delta and cranked supersonic manoeuvre wing designs which are free of lee-side shockwaves are indeed possible - but this thesis has proven that a shock-free solution is not necessarily the same as the minimum drag solution.

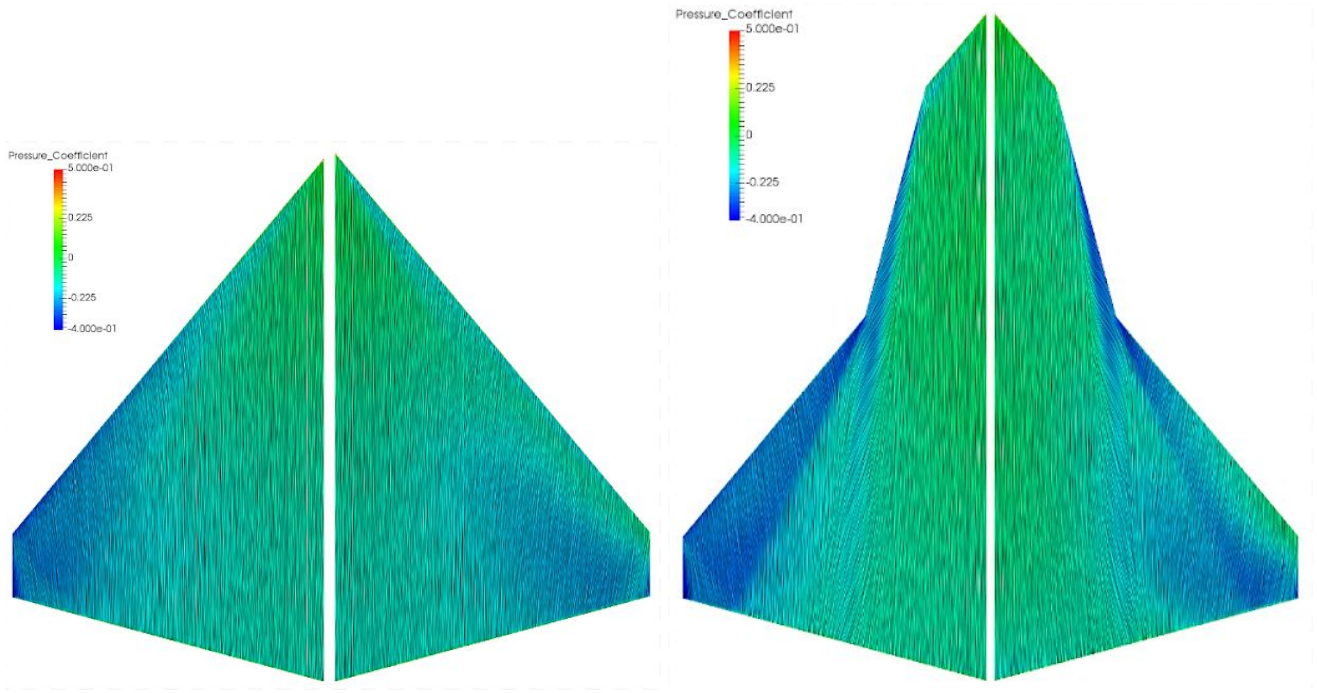

A. Uncambered B. Min. CDp C. Uncambered D. Min. CDp

Fig 4.74 RANS surface flows of the trapezoid wing (left) and cranked wing (right)

Figure 4.74 demonstrates the lee-side surface flows of the minimum pressure drag trapezoid and cranked wing at the supersonic design point and compares them with those of the uncambered wings. The minimum pressure drag trapezoid wing still features a small weak crossflow shockwave near the apex, however the shock is completely eliminated at Y/Ymax>0.45 due to wing twist and camber which cause aft-loading near the wingtip.

The minimum pressure drag cranked wing features a delayed vortical flow pattern at the 75 degree swept leading edge due to reduced leading edge loading at the inboard crank section. The delayed crossflow shockwave and vortical flow are stronger with the minimum drag camber design, providing a region of lower pressure at the outer wing crank: Cp~-0.4 compared with Cp~-0.25. The outer region of the wing is heavily aft-loaded as with the trapezoid design however a weak cross flow shockwave still remains.

This study has shown that the adjoint optimisation method is effective at reducing the drag of a design which features flow phenomena from both sides of the stanbrook-squire boundary[34,35]. Supersonic manoeuvre wings featuring these flow phenomena have never been redesigned using the adjoint method before - meaning that this thesis provides a new appreciation for the effectiveness of the adjoint method for previously unpublished applications.

4.3 Pitch-Moment Constrained Optimisation

4.3.1 Optimisation Problem Descriptions

Here, two optimisation problems are presented and compared using the wing planforms investigated in the above section.

The first optimisation problem uses supersonic drag as an objective function, with lift being constrained by means of the fixed-CL soft constraint detailed in chapter 3. Additionally, a hard constraint is implemented, specifying that the supersonic pitching moment must be positive (nose up) or zero. The pitching moment reference point for this computation is the transonic aerodynamic centre of the uncambered trapezoidal wing and was calculated using a simple panel method code using the trapezoidal wing planform and a NACA64-A004 constant aerofoil section at M=0.85.

Minimise objective function:	I = CDp	at M = 1.6
Subject to constraint functions:	G_1 = CL = 0.25	at M = 1.6
	G_2 = CMy > 0	at M = 1.6
	G_3 = R(U) = 0	at M = 1.6

Design Variables: 99 free-form deformation box camber variables and α

For the second optimisation problem, supersonic drag is used again as an objective function, with soft-constrained supersonic lift and hard-constrained supersonic pitching moment, as in the first problem. Additionally, a hard constraint is placed on the transonic pitching moment such that CMy is less than or equal to zero (nose down) at CL=0.3, M=0.85. This requires an additional flow and adjoint solution per design step at the transonic constraint point.

Minimise objective function:	I = CDp	at M = 1.6
Subject to constraint functions:	G_1 = CL = 0.25	at M = 1.6
	G_2 = CMy > 0	at M = 1.6
	G_3 = R(U) = 0	at M = 1.6
	G_4 = CL = 0.3	at M = 0.85
	G_5 = CMy < 0	at M = 0.85
	G_6 = R(U) = 0	at M = 0.85

Design Variables: 99 free-form deformation box camber variables and α

Both optimisation problems have been posed using the trapezoidal and cranked planforms; and the resulting optimised wing geometries are presented and evaluated using RANS.
The idea of these design optimisation problems is to attempt to reduce the requirement for pitch trim changes between the transonic and supersonic flight conditions. These pitch trim changes are usually

required in order to prevent ‘Mach-tuck’, a loss of aerodynamic stability due to the centre of pressure moving aft during the transition from transonic to supersonic flight. Designing a wing which requires less pitch trim change between transonic and supersonic flight could result in an aircraft with overall better performance - since there is less or no drag penalty to pay through the need for control surface movement; no requirement for auxiliary fuel tanks for mass-balancing (as in concorde), and increased control effectiveness at both flight conditions since control surface deflection is no longer limited by trim.

The flowcharts on the following pages detail the strategies which are used for each optimisation problem. In the case of the first problem, the supersonic flow solution is used to initialise all adjoint gradient computations; and so when the constraint function evaluation is called by the optimiser it simply performs a check back to the objective function evaluation and uses the flow solution generated during that step. For the second design problem, a transonic flow solution is necessary for calculation of one of the constraint functions and in order to initialise the adjoint computation of this constraint’s gradient.

The Flowchart on the first pull-out page represents the first of the two moment-constrained design optimisation algorithms and is figure 4.75.

The Flowchart on the second pull-out page represents the second of the two moment-constrained design optimisation algorithms and is figure 4.76.

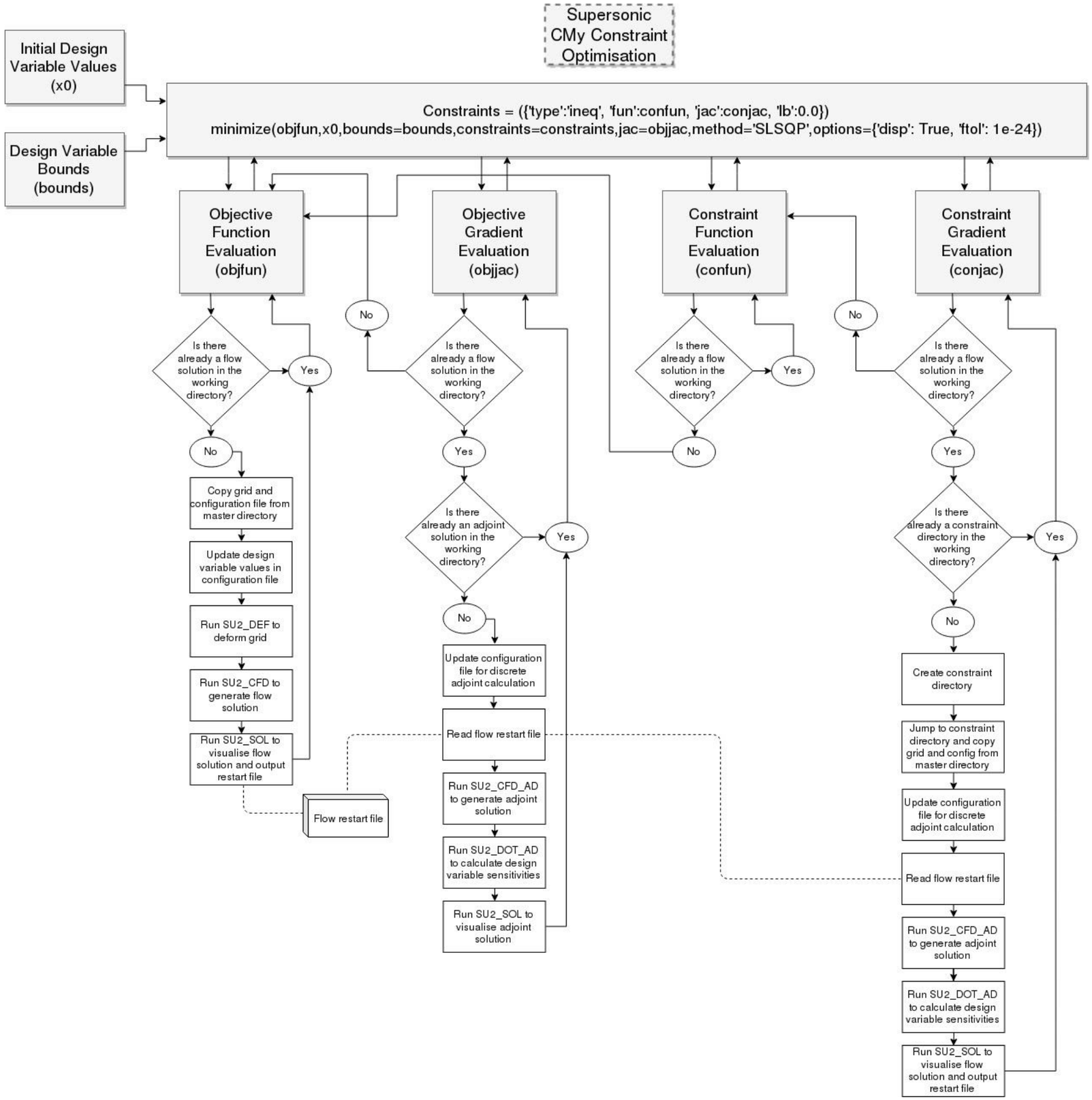
Supersonic CMy Constraint Optimisation
Initial Design Variable Values (x0)
Design Variable Bounds (bounds)
Constraints = ({'type':'ineq', 'fun':confun, 'jac':conjac, 'lb':0.0})
minimize(objfun,x0,bounds=bounds,constraints=constraints,jac=objjac,method='SLSQP',options={'disp': True, 'ftol': 1e-24})
Objective Function Evaluation (objfun)
Objective Gradient Evaluation (objjac)
Constraint Function Evaluation (confun)
Constraint Gradient Evaluation (conjac)
Is there already a flow solution in the working directory?
Yes
No
Copy grid and configuration file from master directory
Update design variable values in configuration file
Run SU2_DEF to deform grid
Run SU2_CFD to generate flow solution
Run SU2_SOL to visualise flow solution and output restart file
Flow restart file
Is there already an adjoint solution in the working directory?
Update configuration file for discrete adjoint calculation
Read flow restart file
Run SU2_CFD_AD to generate adjoint solution
Run SU2_DOT_AD to calculate design variable sensitivities
Run SU2_SOL to visualise adjoint solution
Is there already a constraint directory in the working directory?
Create constraint directory
Jump to constraint directory and copy grid and config from master directory
Update configuration file for discrete adjoint calculation
Read flow restart file
Run SU2_CFD_AD to generate adjoint solution
Run SU2_DOT_AD to calculate design variable sensitivities
Run SU2_SOL to visualise flow solution and output restart file

Fig 4.75

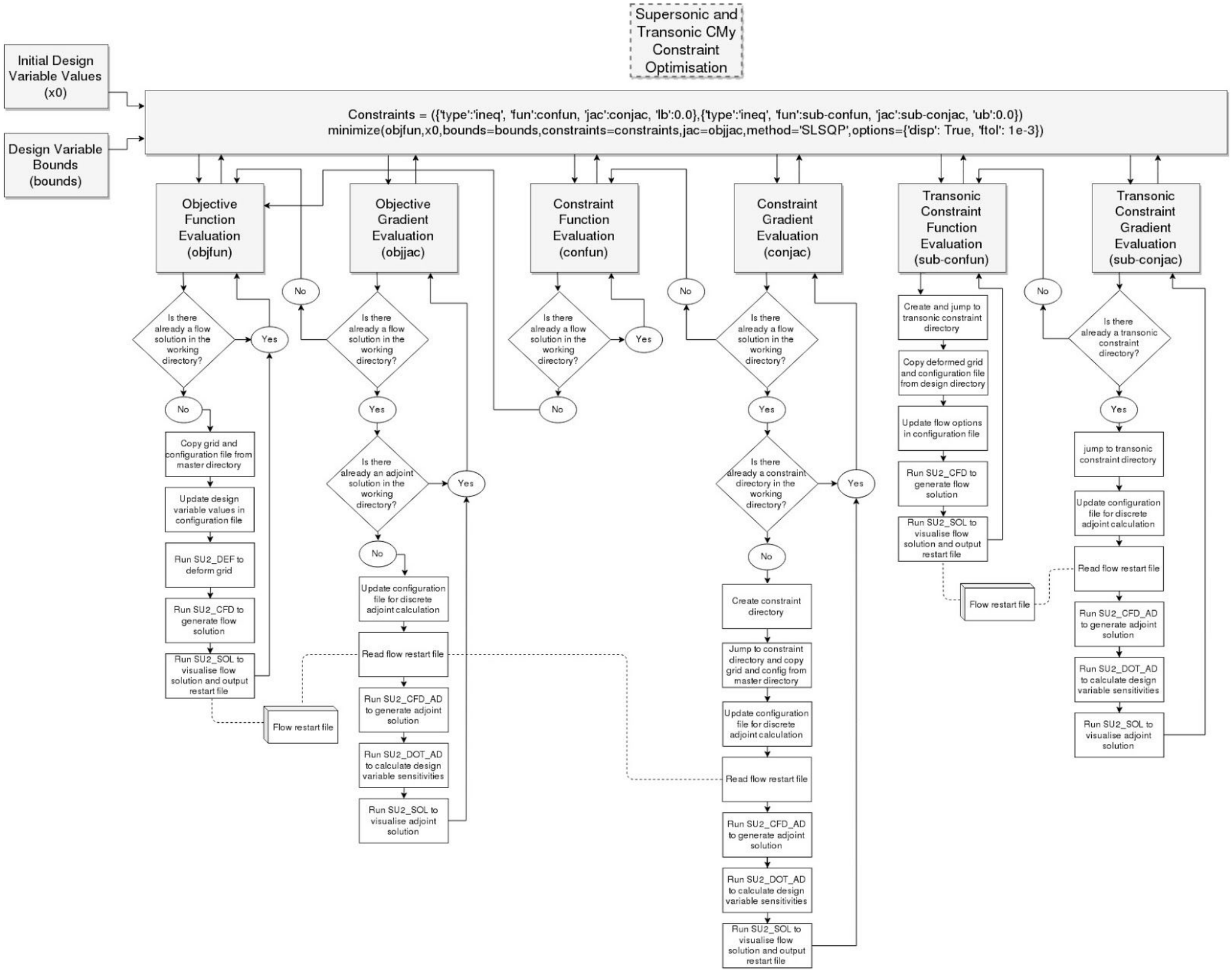
Supersonic and Transonic CMy Constraint Optimisation
Initial Design Variable Values (x0)
Design Variable Bounds (bounds)
Constraints = ({'type':'ineq', 'fun':confun, 'jac':conjac, 'lb':0.0},{'type':'ineq', 'fun':sub-confun, 'jac':sub-conjac, 'ub':0.0})
minimize(objfun,x0,bounds=bounds,constraints=constraints,jac=objjac,method='SLSQP',options={'disp': True, 'ftol': 1e-3})
Objective Function Evaluation (objfun)
Objective Gradient Evaluation (objjac)
Constraint Function Evaluation (confun)
Constraint Gradient Evaluation (conjac)
Transonic Constraint Function Evaluation (sub-confun)
Transonic Constraint Gradient Evaluation (sub-conjac)
Is there already a flow solution in the working directory?
Yes
No
Copy grid and configuration file from master directory
Update design variable values in configuration file
Run SU2_DEF to deform grid
Run SU2_CFD to generate flow solution
Run SU2_SOL to visualise flow solution and output restart file
Flow restart file
Is there already an adjoint solution in the working directory?
Update configuration file for discrete adjoint calculation
Read flow restart file
Run SU2_CFD_AD to generate adjoint solution
Run SU2_DOT_AD to calculate design variable sensitivities
Run SU2_SOL to visualise adjoint solution
Is there already a constraint directory in the working directory?
Create constraint directory
Jump to constraint directory and copy grid and config from master directory
Create and jump to transonic constraint directory
Copy deformed grid and configuration file from design directory
Update flow options in configuration file
Run SU2_CFD to generate flow solution
Run SU2_SOL to visualise flow solution and output restart file
Flow restart file
Is there already a transonic constraint directory?
jump to transonic constraint directory
Update configuration file for discrete adjoint calculation
Read flow restart file
Run SU2_CFD_AD to generate adjoint solution
Run SU2_DOT_AD to calculate design variable sensitivities
Run SU2_SOL to visualise adjoint solution

Fig 4.76

4.3.2 Optimisation Euler Histories

The histories of inviscid forces seen by the optimiser are explored below. The beginning set of design variables was not zero for these cases, the trailing edges of each starting wing were reflexed in order to provide a starting point with positive pitching moment. This helps the optimiser to establish a feasible region for the design process.

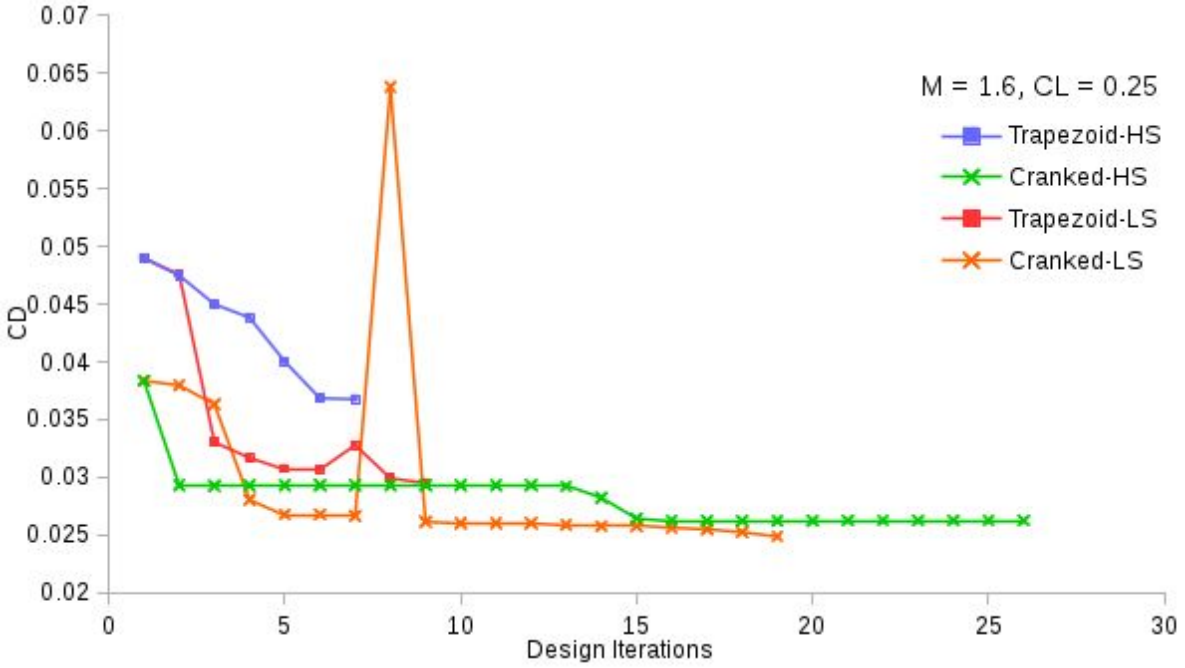

Fig 4.77 Drag coefficient histories in pitch-moment constrained optimisations

Drag coefficient values during each optimisation are shown in Figure 4.77. For the trapezoid wing cases, the best designs were both found within less than 10 design iterations. The cranked wing cases both required considerably more design iterations in order to find their best designs, however found better designs in both cases. The cranked high-speed constraint drag history shows a series of jumps down in drag separated by a large number of design iterations. This is due to a conflict between objective and constraint, and it takes the optimiser a number of iterations to find a feasible step direction which will yield a large reduction in objective function. During these seemingly flat iterations, drag is still reducing by small amounts.

Supersonic pitching moment coefficient values during each optimisation are shown in Figure 4.78. It is clear from this chart that the trapezoid wing optimisation with constraints on both transonic and supersonic pitching moment did not settle on a suitably small or positive value of supersonic CMy. The optimiser was unable to find a shape which satisfied both constraints whilst still reducing drag. The resulting design has low drag but does not meet the imposed pitch trim requirement. All of the other optimisation histories show good convergence to near-zero supersonic pitching moment. The cranked high-speed constrained case jumps straight to the limit of the constraint (CMy~0) and remains there until the design process is finished.

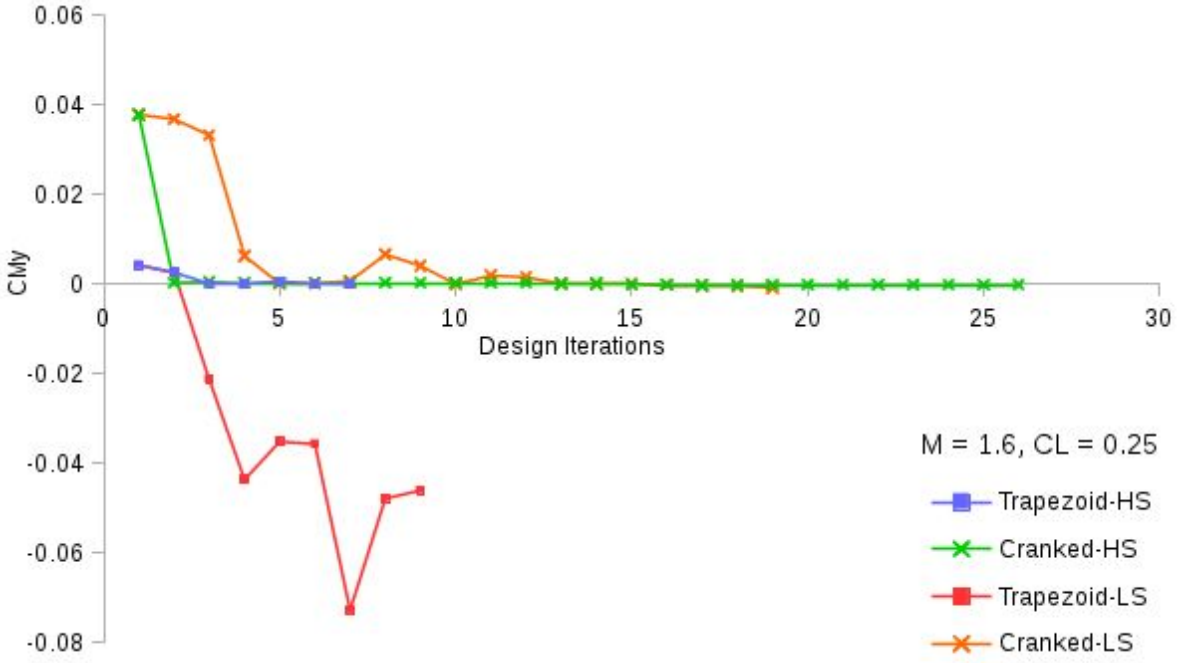

Fig 4.78 Supersonic pitch-moment coefficient histories in pitch-moment constrained optimisations

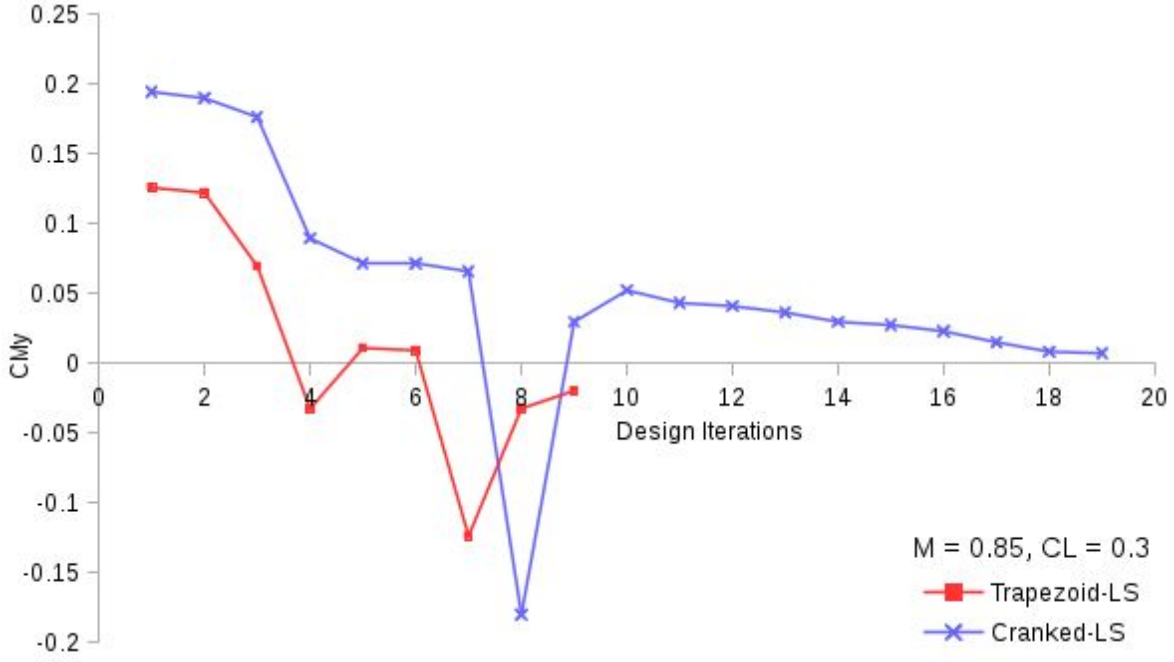

Fig 4.79 Transonic pitch-moment coefficient histories in transonic pitch-moment constrained optimisations

Figure 4.79 shows the history of transonic pitching moment coefficient during the optimisation cases with transonic constraints. Both cases are seen to converge towards, but not quite reach, the limit of the constraint (CMy~0).

All of the design processes shown above were left to continue running after the number of iterations shown above, however did not find any better designs after the points shown. Rather, after the optima

shown here each case simply jumped between points on a pareto front within a very narrow band. The requested accuracy of the optimisation could be lowered to prevent this. No penalty to the objective value is incurred when the pitching moment has not met the requested value, however in this case the design is said to be unfeasible; until the value of pitching moment gets within a small tolerance of zero.

4.3.3 Optimisation Euler Final Force Values

Here, forces derived from Euler flow solutions on each of the best designs are presented and compared with the uncambered datum wings.

Table 4.4 Comparison of Supersonic Euler forces for each wing design

M=1.60			
Geometry	CL	CD	CMy
Trapezoid Uncambered	0.2500	0.02899	-0.04520
Cranked Uncambered	0.2500	0.02585	-0.02129
Trapezoid Min. Drag	0.2500	0.02794	-0.04890
Cranked Min. Drag	0.2500	0.02409	-0.01608
Trapezoid HS CMy Constrained	0.2500	0.03677	-0.00006
Cranked HS CMy Constrained	0.2500	0.02625	-0.00017
Trapezoid LS+HS CMy Constrained	0.2500	0.03716	-0.00201
Cranked LS+HS CMy Constrained	0.2500	0.02496	-0.00108

Table 4.5 Comparison of Transonic Euler forces for low-speed constrained wing designs

M=0.85			
Geometry	CL	CD	CMy
Trapezoid LS+HS CMy Constrained	0.3000	0.03204	0.030211
Cranked LS+HS CMy Constrained	0.3000	0.01655	0.007551

Table 4.4 shows the forces of each wing design at the supersonic design point. The minimum drag wing designs are the ones presented in chapter 4.2. In this table, ‘HS CMy constrained’ denotes designs which have been constrained by pitching moment at M=1.6, CL=0.25 and ‘LS+HS CMy constrained’ denotes designs which have been constrained by pitching moment at both M=1.6, CL=0.25 and M=0.85, CL=0.3.

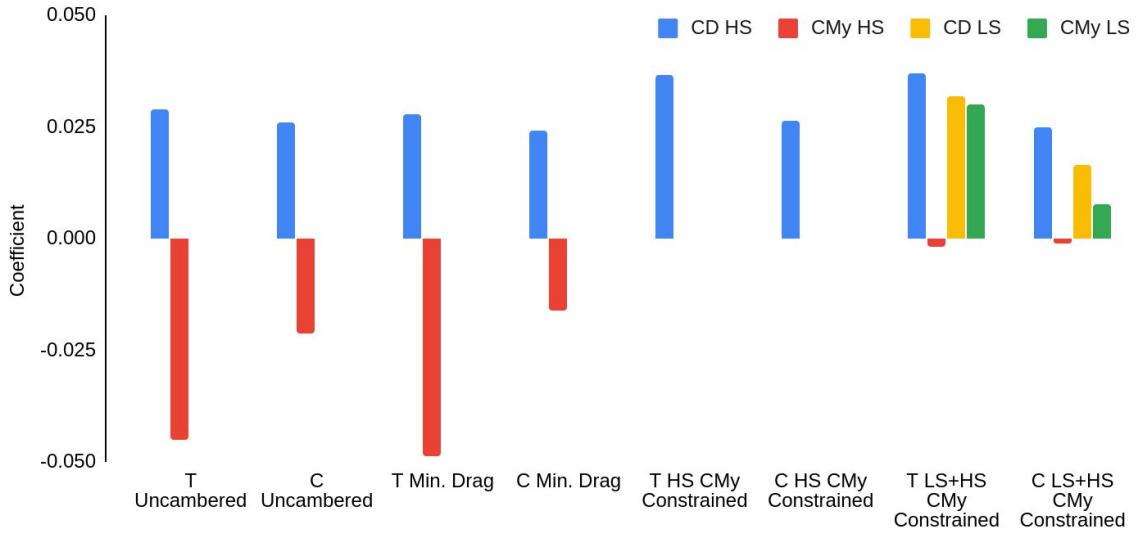

Fig 4.80 Visualisation of supersonic and transonic Euler forces on each wing design

Figure 4.80 is a visualisation of the force coefficients displayed in tables 5 and 6. Both of the HS constrained designs have a higher drag value than the uncambered datum wings, but have very small pitching moments at the design condition. These drag values can be seen as being the lowest for their respective planforms, CL and pitching moment.

The LS+HS constrained trapezoid wing has the supersonic highest drag value of any of the designs included; and whilst the supersonic pitching moment is very small compared with the uncambered or minimum drag trapezoid wings, it is still 2 orders of magnitude larger than the supersonic pitching moment of the HS constrained trapezoid wing. Table 4.5 shows the transonic forces of the LS+HS constrained designs, and it can be seen here that the trapezoid design still has a significant pitching moment; indicating that the optimiser was unable to find a design which satisfies both pitching moment constraints.

The LS+HS constrained cranked wing has a lower supersonic drag value than both uncambered and HS constrained cranked wings, and a supersonic pitching moment which is only half the value of the trapezoid LS+HS constrained design. In table 4.5 it can be seen that the cranked LS+HS constrained design has just over half the transonic drag coefficient of the trapezoid design, and a pitching moment which is under 1/3rd the value of the trapezoid design. This makes the LS+HS constrained cranked wing a highly favourable design, with good performance and low pitching moment at both supersonic and transonic speeds.

The forces shown here do not take viscosity into account, and so whilst being generally indicative of the flow characteristics and forces they do not indicate the true performance of the wing designs in real world conditions. RANS solutions will be presented later in the thesis to give a full representation of the real flow and forces of each wing in flight.

4.3.4 Final Designs Surface Pressures and Shape

In this section, the shapes and inviscid surface pressure distributions of each designed wing will be shown. Since the design process only changed the camber of each wing, the new geometries can be equally expressed in terms of both their mean camber and their distributed aerofoil shapes.

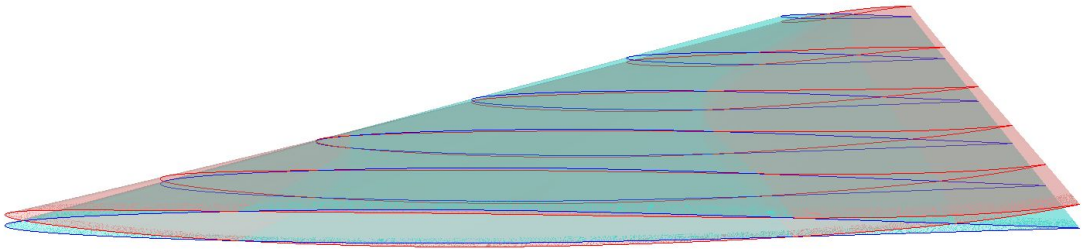

Fig 4.81 Geometrical comparison of uncambered and supersonic CMy constrained trapezoid wing sections

Figure 4.81 shows the trapezoid uncambered (blue) and supersonic CMy constrained (red) wing 3D shapes with highlighted aerofoil sections at 2m intervals along their span. There is a strong reflex camber at every point along the span of the supersonic CMy constrained wing, with the only positive camber existing near the trailing edge of the wing tip - however this is only very slight. There is also a very strong wing twist towards the tip.

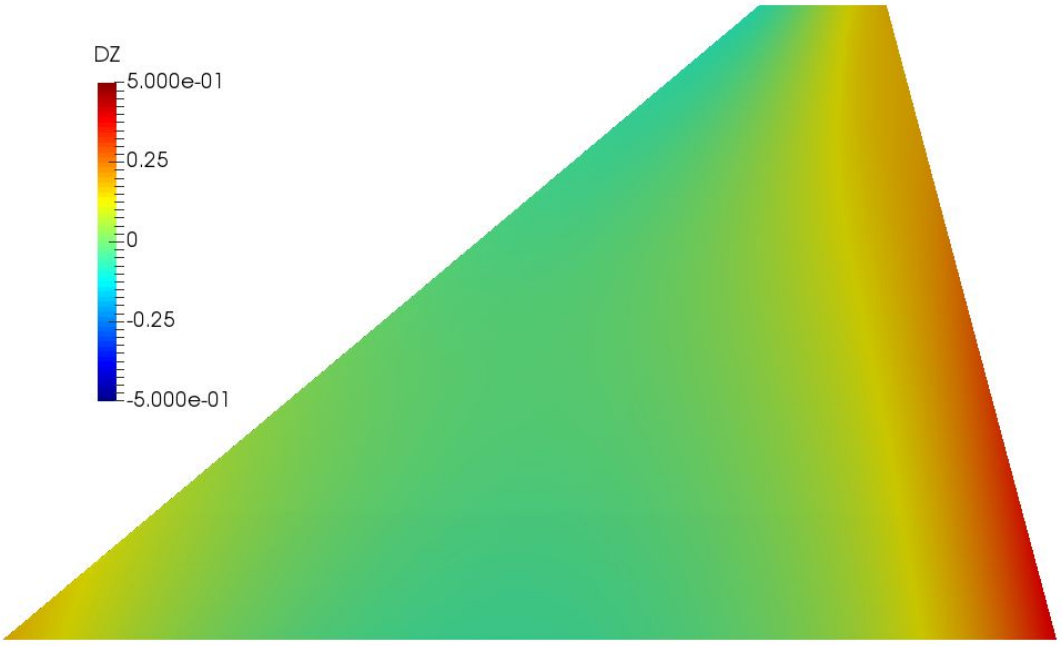

Fig 4.82 Mean camber surface of the supersonic-constrained trapezoid wing

Figure 4.82 shows the mean camber of the supersonic CMy constrained trapezoid wing, calculated as Zopt-Zflat for each point on the wing surface. It can be seen here that a strong reflex camber has been applied to the trailing edge, especially at the wing root and reducing towards the wing tip. The apex of the wing has been deflected upwards, leading to a negatively cambered wing root in this region. The leading edge has been drooped slightly towards the wingtip in a similar manner to the minimum drag case.

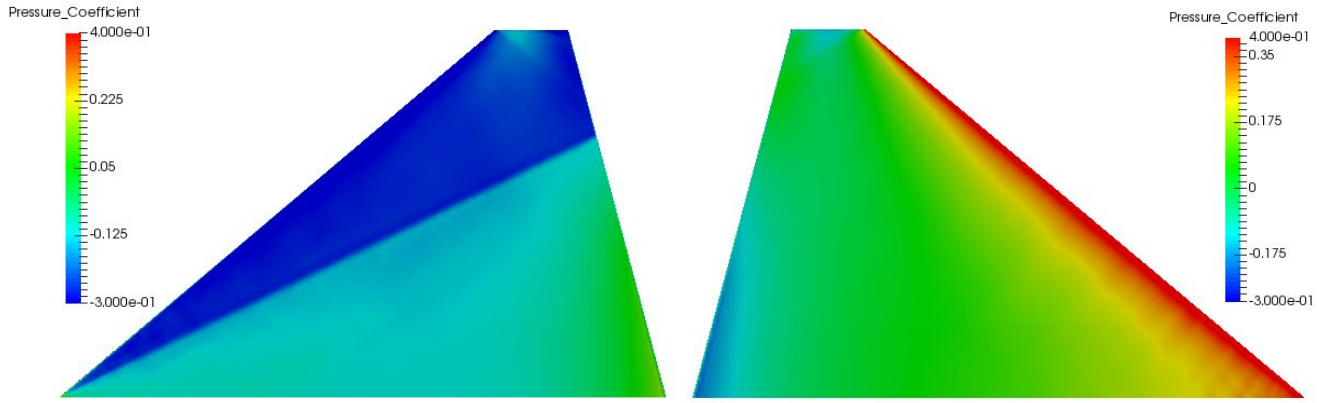

Fig 4.83 Surface Cp distribution of HS-constrained trapezoid wing M1.6 CL0.25

Figure 4.83 shows the pressure coefficient distribution on the upper and lower surfaces of the supersonic CMy constrained trapezoid wing at the supersonic design point. On the upper surface there is a very strong embedded crossflow shockwave starting at the wing apex, with suction reducing towards the wing tip where the leading edge is drooped. At the trailing edge, there is a strong suction force on the lower surface near the wing root. It is clear from this image that the optimiser has tried to shift the centre of lift as far forwards as possible, generating lots of lift at the leading edge and apex and some downforce at the trailing edge. On the lower surface at the leading edge, the negative wing camber has resulted in a smooth expansion from the leading edge downstream - increasing the average pressure coefficient on the lower surface forwards of the moment datum point.

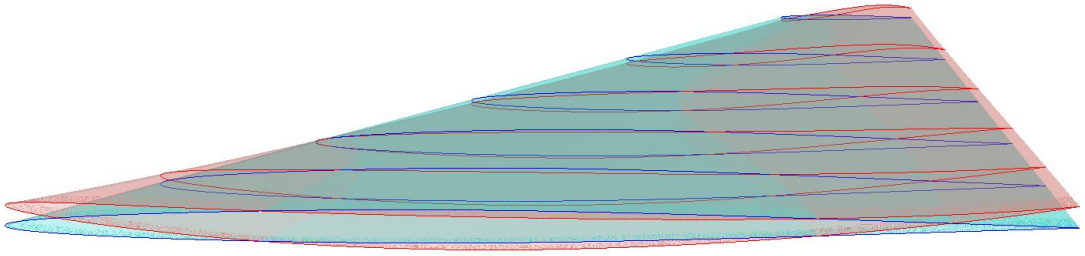

Fig 4.84 Geometrical comparison of uncambered and transonic CMy constrained trapezoid wing sections

Figure 4.84 shows the trapezoid uncambered (blue) and transonic CMy constrained (red) wing 3D shapes with highlighted aerofoil sections at 2m intervals along their span. As with the supersonic CMy constrained trapezoid wing, there is a strong reflex camber at every point along the span of the supersonic CMy constrained wing, with some moderate positive camber existing near the trailing edge at the outer 30% of the span.

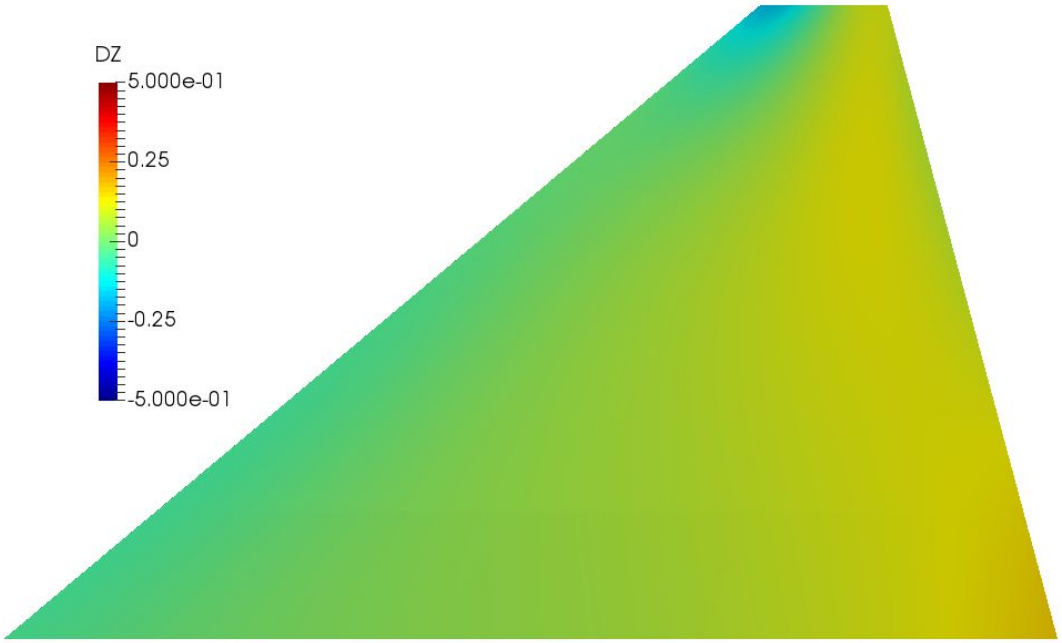

Fig 4.85 Mean camber surface of the transonic-constrained trapezoid wing

Figure 4.85 shows the mean camber of the transonic and supersonic CMy constrained trapezoid wing. The entire leading edge including the apex has been slightly drooped with a very strong droop at the wing tip. At the wing root, there is reflex camber especially towards the trailing edge. However, as the trailing edge extends outwards the reflex camber becomes positive trailing edge camber, serving to increase the loading towards the trailing edge. The maximum camber location in the mid-span region is at about 0.9X/C.

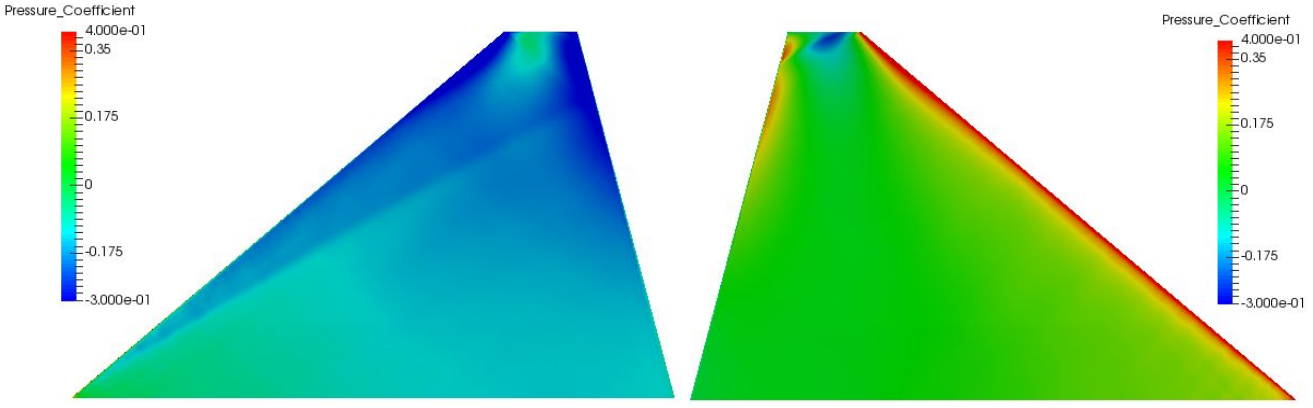

Fig 4.86 Surface Cp distribution of LS+HS-constrained trapezoid wing M1.6 CL0.25

Figure 4.86 shows the pressure coefficient distribution on the upper and lower surfaces of the transonic and supersonic CMy constrained trapezoid wing at the supersonic design point. On the upper surface there is a weak embedded crossflow shockwave starting about 1m along the leading edge from the apex. The majority of the wing appears to be aft-loaded, with upper surface pressure gradually reducing towards the trailing edge. At the wingtip, there is strong suction at both the leading and trailing edges on the upper surface accompanied by high pressures on the lower surface.

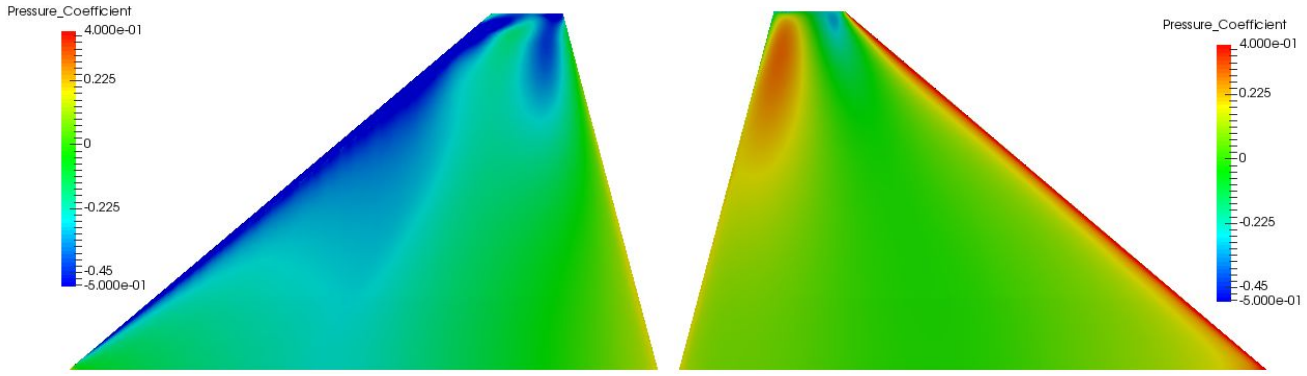

Fig 4.87 Surface Cp distribution of LS+HS-constrained trapezoid wing M0.85 CL0.3

Figure 4.87 shows the pressure coefficient distribution on the upper and lower surfaces of the transonic and supersonic CMy constrained trapezoid wing at the transonic constraint point. On the upper surface there is a lambda shockwave, with the leading shock starting at 0.5m from the wing apex extending in a straight line to the wing tip and the trailing shock starting at about 2m from the wing root at 0.4X/C extending in a curve towards the leading shock. Both shocks coalesce at 0.8Y/S. There is a strong suction region on the upper surface at the wingtip near the trailing edge, extending inwards to about 0.75Y/S. This is accompanied by a high pressure region on the lower surface at the trailing edge. There is also a very small suction region near the leading edge of the wing tip on the lower surface.

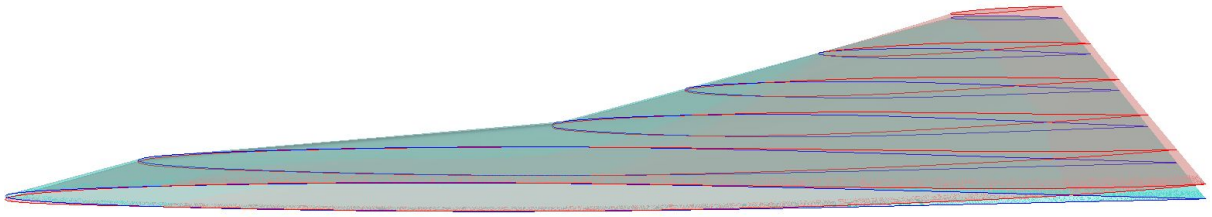

Fig 4.88 Geometrical comparison of uncambered and supersonic CMy constrained cranked wing sections

Figure 4.88 shows the cranked uncambered (blue) and supersonic CMy constrained (red) wing 3D shapes with highlighted aerofoil sections at 2m intervals along their span. There is a moderate trailing edge reflex camber at the inner 50% of the span of the supersonic CMy constrained wing. There is a slight leading edge droop near the wing apex. The wing tip is raised and twisted but not strongly cambered.

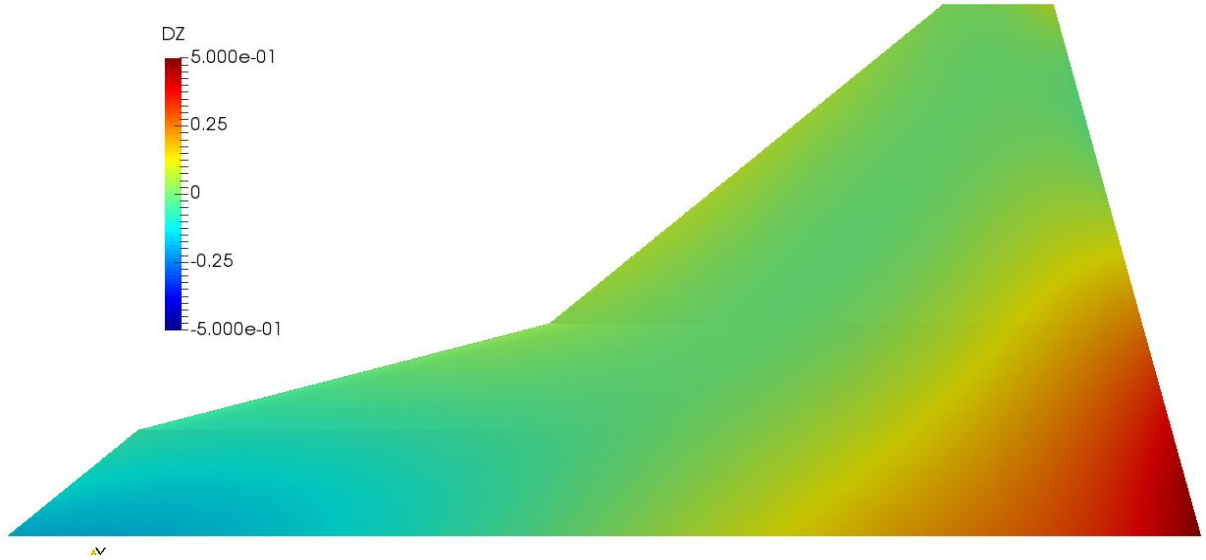

Fig 4.89 Mean camber surface of the supersonic-constrained cranked wing

Figure 4.89 shows the mean camber of the supersonic CMy constrained cranked wing. The trailing edge at the wing root is strongly reflexed in a triangular pattern; shown in figure 4.88 by a dark red triangle.

The wing apex droop extends inwards to about 0.4Y/S, however the inner 50% of the 75 degree swept section is not drooped. The outer 50% of the 75 degree swept section and the outer 50 degree swept section is actually raised, leading to a negatively cambered outer span of the wing.

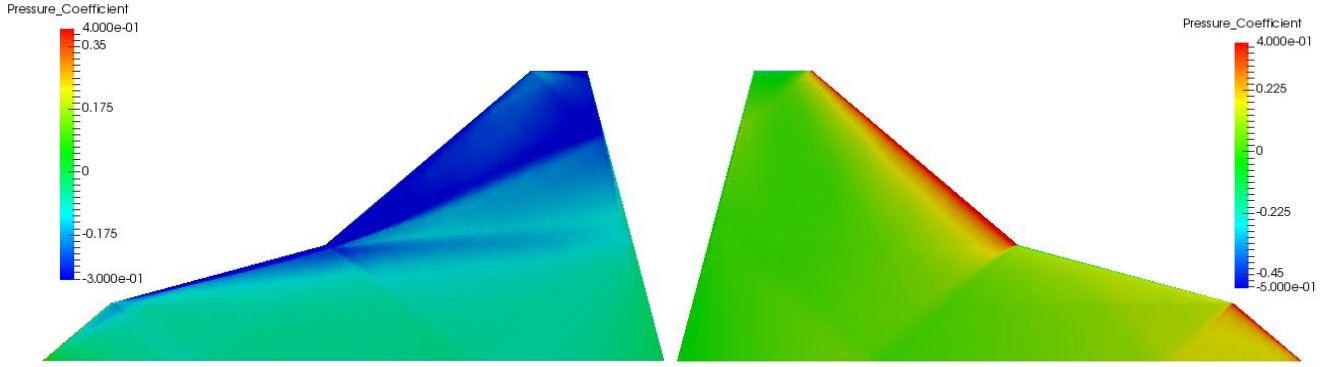

Fig 4.90 Surface Cp distribution of HS-constrained cranked wing M1.6 CL0.25

Figure 4.90 shows the pressure coefficient distribution on the upper and lower surfaces of the supersonic CMy constrained cranked wing at the supersonic design point. On the upper surface there is a very strong embedded crossflow shockwave, as with the trapezoid wing designed using the same constraints, located on the outer 60% span of the wing with suction reducing towards the wing tip where the leading edge is drooped. A small crossflow shockwave exists at the leading edge Y=1m to the convex crank, where the leading edge rises up from the drooped position at the apex. This small shockwave coalesces with the leading edge suction peak of the 75 degree swept section.

On the lower surface, at the apex of the wing out to the first crank location, there is a high pressure region forming a diamond pattern. This region has a higher average pressure than the equivalent region on the uncambered wing, significantly adding to the nose-up pitching moment. The same can be said for all 50 degree swept portions of the leading edge which are in front of the pitching moment

datum point. Behind the datum point, on the very outer span of the wing, the high pressure region visibly reduces in size due to the leading edge droop and subsequent lower surface expansion.

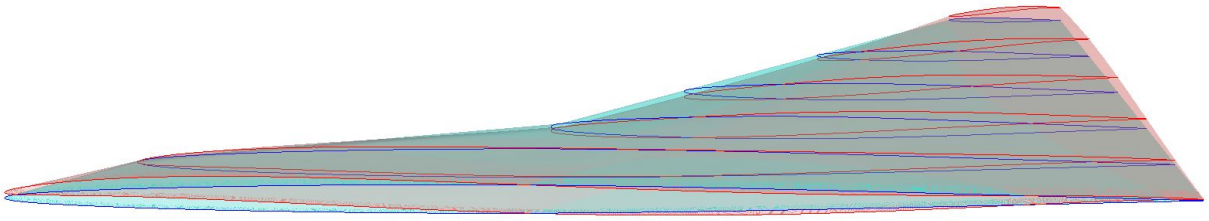

Fig 4.91 Geometrical comparison of uncambered and transonic CMy constrained cranked wing sections

Figure 4.91 shows the cranked uncambered (blue) and transonic CMy constrained (red) wing 3D shapes with highlighted aerofoil sections at 2m intervals along their span. There is a slight positive trailing edge camber along the span, gradually increasing towards the wing tip. At the wing root, near the leading edge there is a raised and positively cambered region, with a negative camber located at around 0.6X/C, resulting in an S-shaped aerofoil section. The leading edge of the outboard wing section is drooped, with a very slight negative camber near the leading edge at Y=8m.

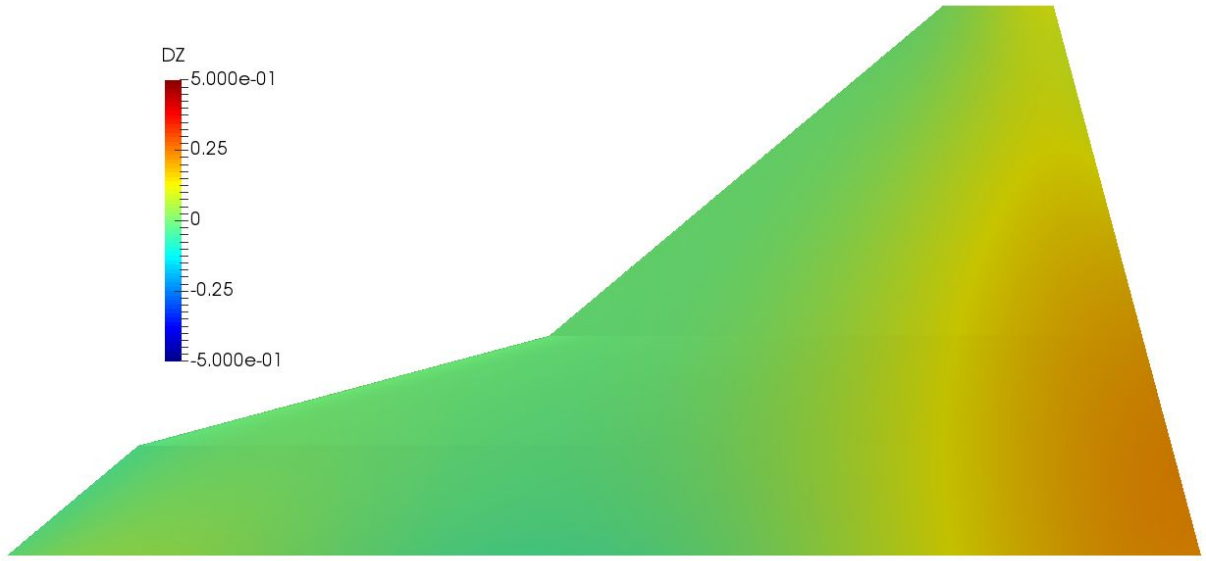

Fig 4.92 Mean camber surface of the transonic-constrained cranked wing

Figure 4.92 shows the mean camber of the transonic and supersonic CMy constrained cranked wing. The trailing 30% of the wing is moderately reflexed from 0m>Y>7.5m, however there is a small positive camber near the trailing edge. A small positive camber has been applied to the leading edge extension region, seen in figure 4.91 as a yellow area at the wing root near the leading edge.

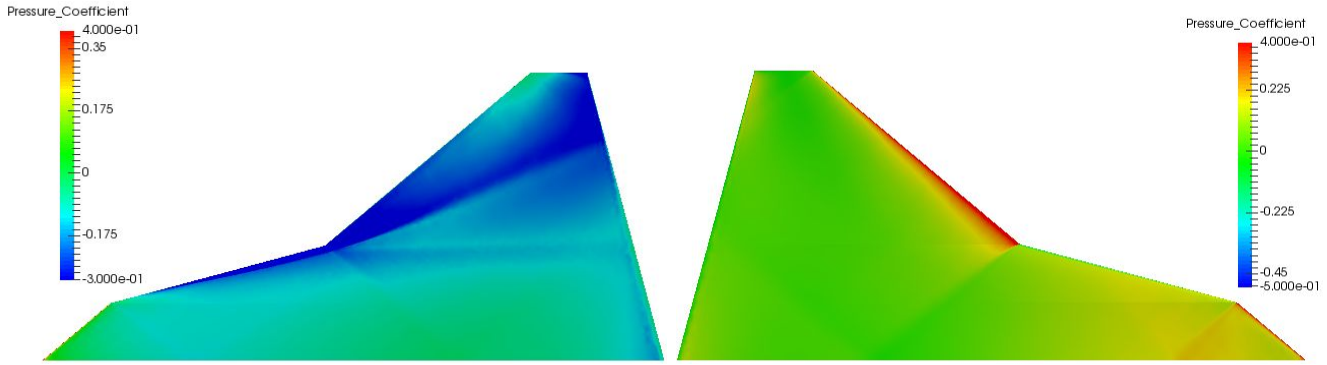

Fig 4.93 Surface Cp distribution of LS+HS-constrained cranked wing M1.6 CL0.25

Figure 4.93 shows the pressure coefficient distribution on the upper and lower surfaces of the transonic and supersonic CMy constrained cranked wing at the supersonic design point. On the upper surface there is a strong embedded crossflow shockwave located on the outer span of the wing with suction reducing substantially towards the wing tip where the leading edge is drooped. The intensity of the shockwave is reduced towards the wing trailing edge as the downstream pressure is reduced. There is no shockwave at the leading edge 0m<Y<2m due to the camber applied to the leading edge extension region. Instead, the flow expands smoothly and then recompresses with no shock around the cambered region. This cambered region also leads to a shock-free recompression of the flow around the leading edge of the 75 degree swept region. At the trailing edge there is a low pressure region stretching from wing root to Y=4m.

On the lower surface, at the apex of the wing out to the first crank location, the diamond pattern high pressure region is weaker than in other designs using this planform; with the expansion being smoothed by the positive camber. At the trailing edge, there are small high pressure regions at the root and tip.

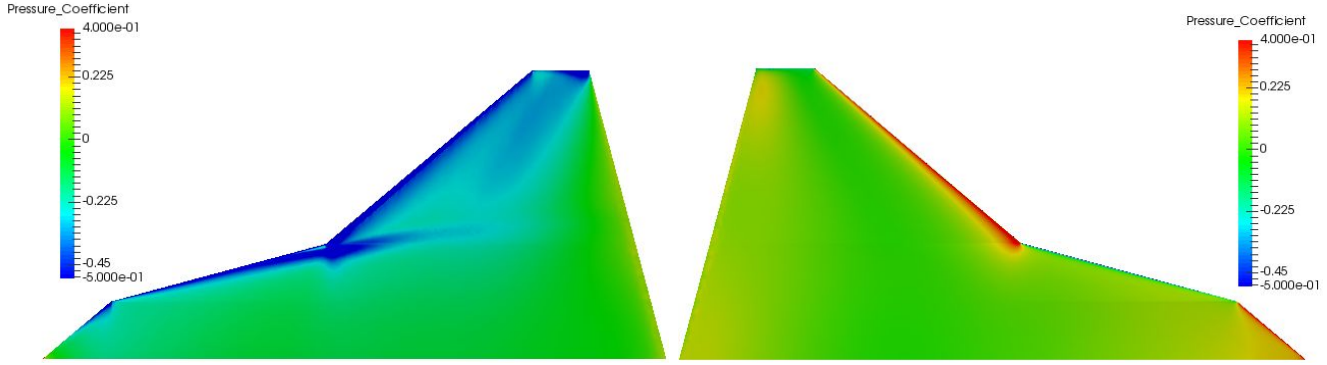

Fig 4.94 Surface Cp distribution of LS+HS-constrained cranked wing M0.85 CL0.3

Figure 4.94 shows the pressure coefficient distribution on the upper and lower surfaces of the transonic and supersonic CMy constrained cranked wing at the transonic constraint point. On the upper surface, on the leading edge at 1m<Y<2m, there is a suction peak which is terminated by a small shockwave, however no suction peak at the root. The highly swept leading edge region has a strong suction peak which extends downstream of the concave leading edge crank. On the outboard section of the wing, the leading edge is the main low pressure zone however there is a second low pressure region about 1-2m downstream of the leading edge on the outer 50% span of the wing.

On the lower surface, there are high pressure regions on both 50 degree swept leading edge sections, however there is no visible high pressure region at the 75 degree section of the leading edge. At the trailing edge, there are moderate high pressure regions at the root and at the tip.

4.3.5 RANS Forces at Transonic and Supersonic Design Points

Here, RANS modelling has been used to simulate all of the designed wings and compare them with their uncambered equivalents at both the supersonic design point and the transonic flight condition used to constrain some of the designs. In both cases, the Reynolds number is 6.6×10^6/m since this range is already verified for the SU2 RANS solver. This equates to kinematic viscosities of 11.67m²/s for the supersonic case and 6.18m²/s for the transonic case, corresponding to altitudes of 18000m (59000ft) and 13900m (45000ft) respectively. Using the same Reynolds number between cases also means that the same grids can be used since boundary layer spacing does not need to change.

Table 4.6 includes lift, drag and pitching moment information for each wing geometry at both flight conditions; as well as the difference in pitching moment coefficient between transonic and supersonic states. The difference in pitching moments between these states gives a reliable measure of the amount of pitch trim which would be required in order to maintain equilibrium; which in turn can be taken as a measure of the additional drag penalty (for aerodynamic trim used mostly in fighter jets) or weight and volume penalty (for mas-balance trim famously used by concorde). Therefore, the most favourable designs would have a combination of low drag and small trim requirement.

Table 4.6 RANS forces on each wing design at both supersonic and transonic flight states.

Geometry	Supersonic M=1.60			Transonic M=0.85			Delta
	CL	CD	CMy	CL	CD	CMy	CMyT-CMyS
Trapezoid Uncambered	0.25	0.03295	-0.04521	0.3	0.02543	-0.00831	0.03690
Cranked Uncambered	0.25	0.03015	-0.02182	0.3	0.02618	0.01159	0.03341
Trapezoid Min. Drag	0.25	0.03197	-0.04836	0.3	0.02112	-0.01142	0.03694
Cranked Min. Drag	0.25	0.02859	-0.01647	0.3	0.02220	0.01668	0.03315
Trapezoid HS CMy Constrained	0.25	0.04037	-0.00015	0.3	0.05166	0.07997	0.08012
Cranked HS CMy Constrained	0.25	0.03069	-0.00109	0.3	0.03012	0.03942	0.04051
Trapezoid LS+HS CMy Constrained	0.25	0.04042	-0.00210	0.3	0.04060	0.03328	0.03538
Cranked LS+HS CMy Constrained	0.25	0.02954	-0.00135	0.3	0.02351	0.01109	0.01244

Table 4.6 shows that CMyT-CMyS is generally larger for the trapezoid wing planform than the cranked wing planform, and that the difference between this figure for uncambered and minimum drag wings is very small. For these unconstrained designs, it is found that the trapezoid planform generally has about 7-10 drag counts less than the cranked equivalent at the transonic flight condition, but about 30-35 drag counts more at the supersonic flight condition. It is also true and noteworthy that the only wings which are stable (nose-down moment) at both supersonic and transonic conditions are the trapezoid uncambered and minimum drag designs. This trend changes dramatically when pitching moment constraints are applied to the design process.

The designs which were constrained by only supersonic pitching moment both have relatively high values of CMyT-CMyS and drag; however they do have the most favourable pitching moment at the supersonic design condition. At the transonic condition, these designs have very large nose-up pitching moments making both of them unstable.

In the Supersonic flight condition, the lowest drag design is the cranked minimum drag design, followed by the cranked LS+HS CMy constrained design. The highest drag and lowest pitching moment design at the supersonic condition is the trapezoid HS CMy constrained geometry, which also has the highest drag and pitching moment at the transonic flight condition.

The designs which were constrained by both supersonic and transonic pitching moments differ wildly in their performance - showing the great importance of planform shape on the potential design space for the wing. In order to search for a feasible design given these constraints, a large drag penalty was incurred on the trapezoid wing in both flight states. Even so, only one of the constraints was satisfied within limits - the transonic pitching moment was not able to be reduced by as much as it was with the cranked wing planform. Conversely, the design process was able to find a camber distribution for the cranked planform which provides low drag values and low pitching moments at both flight conditions - representing the wing design with most favourable all-round characteristics at the specified supersonic and transonic flight conditions. Later in this thesis, RANS α sweeps will be presented at both Mach numbers in order to explore the flight characteristics of each wing design through a wider range of flight states.

4.3.6 RANS Flow Visualisations

Here, the RANS surface flows on each wing design and the 3D flowfields of the datum wings are presented and discussed. The surfaces are shown coloured by local pressure coefficient with streak lines representing local surface shear direction. This combination provides a good representation of each of the flow features which affect the forces presented in the previous section. The colour scales representing pressure coefficient are slightly different between supersonic and transonic flow visualisations, but are constant between all simulations within each Mach number. Legends are included in each plot for reference.

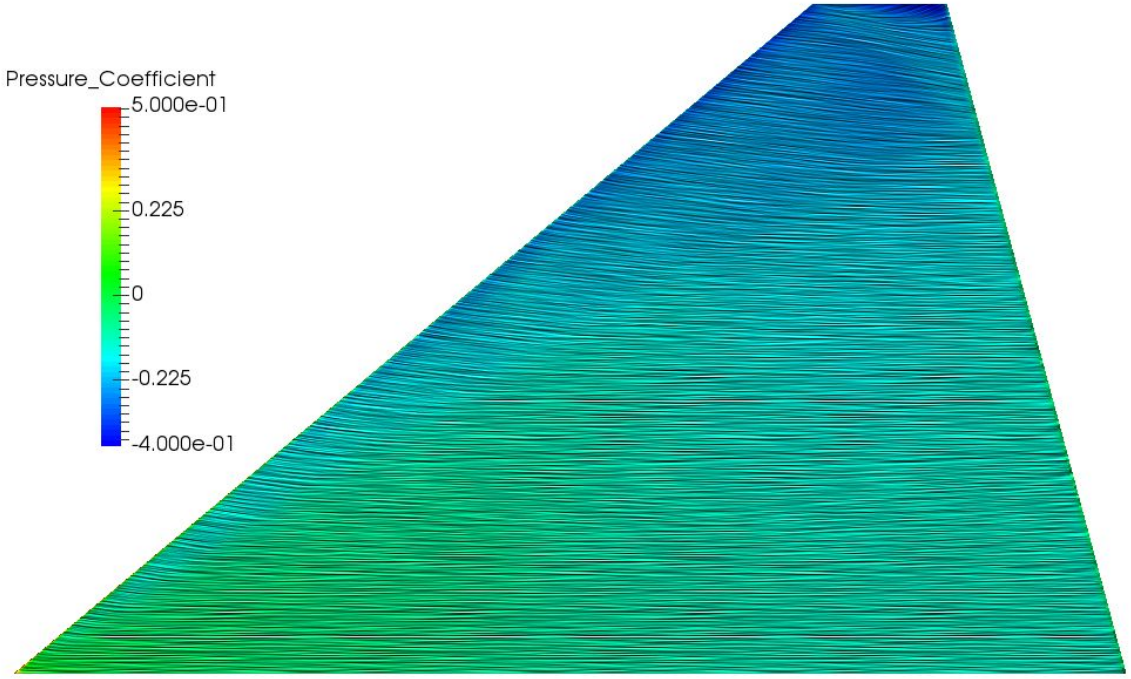

Fig 4.95 Trapezoid uncambered M=1.6, CL=0.25, Re/m=6.6x10^{6} surface flow visualisation

Figure 4.95 shows the flow on the upper surface of the uncambered trapezoid wing at the supersonic design condition. An embedded crossflow shockwave is present as also predicted by the inviscid simulations, as well as a shockwave generated at the wing tip which meets the crossflow shockwave near the trailing edge.

Suction increases gradually from the root (average Cp ~-0.1) to the tip (average Cp ~-0.3) upstream of the embedded crossflow shockwave, and increases gradually from near the leading edge to the trailing edge at the root.

Sharp changes in flow direction are seen across each surface-impinging shockwave, but the flow remains totally attached across the whole surface.

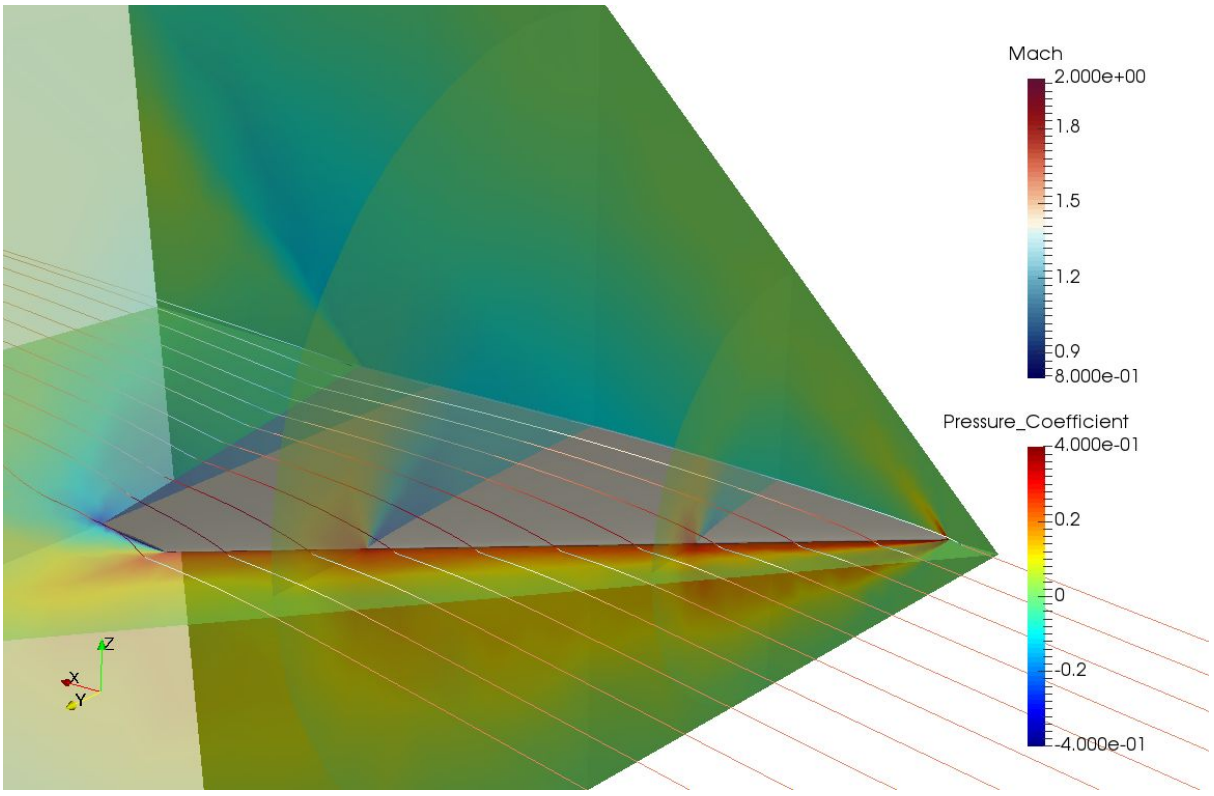

Fig 4.96 Trapezoid uncambered M=1.6, CL=0.25, Re/m=6.6x10^6 3D flow visualisation

Figure 4.96 shows the flowfield around the initial uncambered trapezoid wing at the supersonic design condition in viscous flow. Transparent slices are located on the Y=0m, Z=0m, X=10m, X=15m and X=20m planes, and streamlines have been seeded from the edge of the boundary layer on the upper wing surface and show both the local flow direction and the local Mach number. Except from the boundary layer, the dominant features of this flow structure are the same as what was predicted in the inviscid Euler solutions. The bow shockwave is clearly visible in each of the flow slices shown and is as predicted by the Euler solution. The cross-flow shockwave is once again predicted to be planar and conical, however extend out into the flow almost exactly perpendicular to the wing surface.
The flow streamlines show that the flow is attached over the entire wing surface, and detail the direction changes which occur through each shockwave as well as the changes in Mach number. At the wing tip, one of the streamlines shows a strong expansion and acceleration of the flow from lower to upper sides of the wing and subsequent formation of wingtip vortex.

Figure 4.97 shows the flow on the upper surface of the uncambered trapezoid wing at the transonic design condition. The lambda shockwave pattern predicted by Euler simulations is also present here in the RANS solution, however the pressure jump at the downstream shockwave is slightly less sharp than calculated by Euler simulations. The flow is separated at the leading edge from Y=3m outwards with the reattachment line just upstream of the leading shockwave until Y=5m where it moves downstream of the shock. In the separated region at the leading edge of the wing, the surface flow is actually perpendicular to the freestream flow.

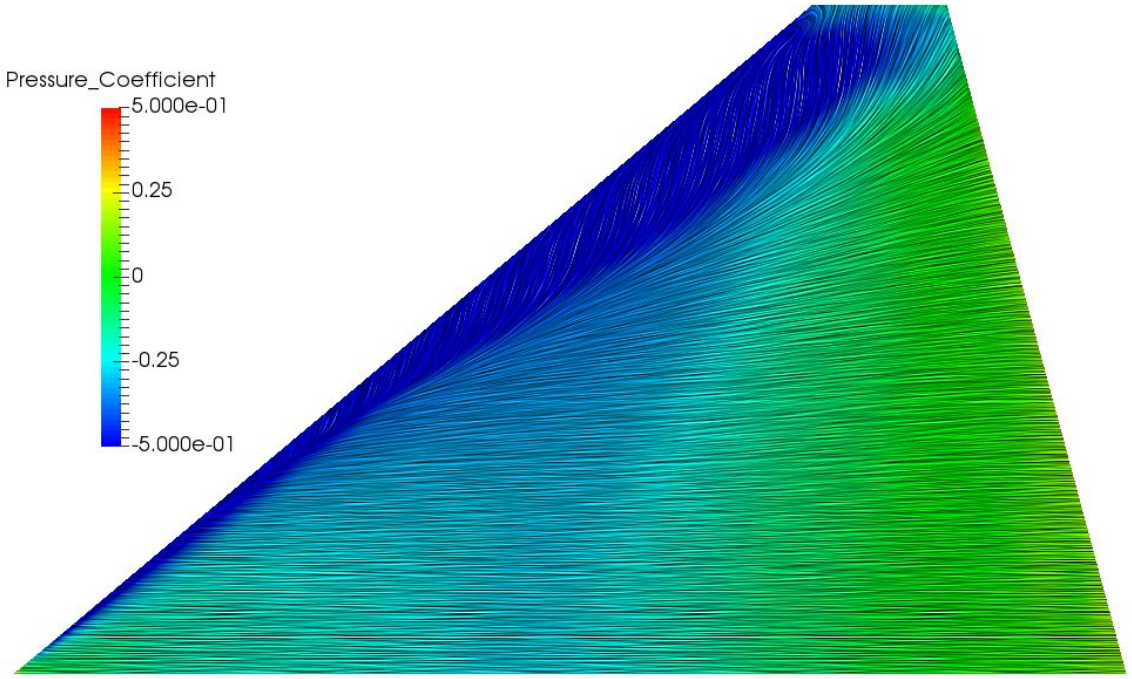

Fig 4.97 Trapezoid uncambered M=0.85, CL=0.3, Re/m=6.6x10^6 surface flow visualisation

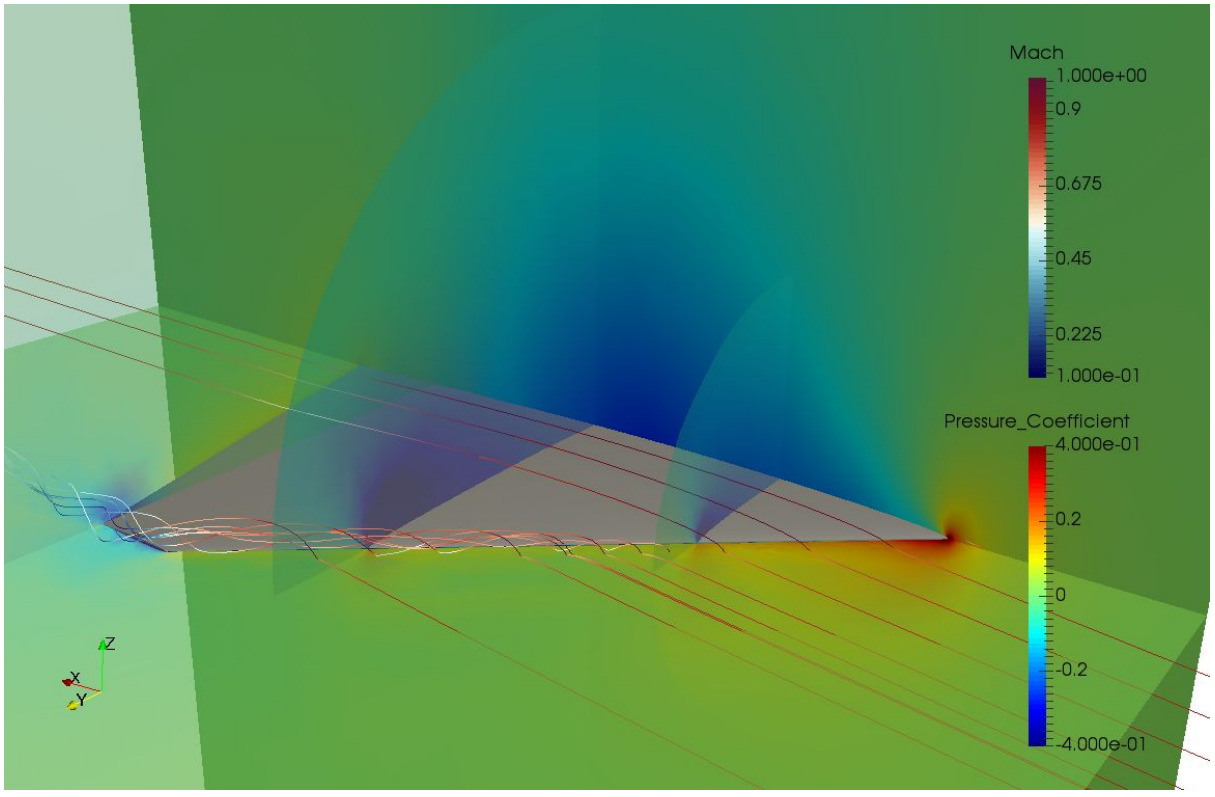

Fig 4.98 Trapezoid uncambered M=0.85, CL=0.3, Re/m=6.6x10^6 3D flow visualisation

Figure 4.98 shows the flowfield around the initial uncambered trapezoid wing at the transonic design condition in viscous flow. Transparent slices are located on the Y=0m, Z=0m, X=10m, X=15m and X=20m planes, and streamlines have been seeded from the edge of the boundary layer on the upper wing surface near the leading edge and show both the local flow direction and the local Mach number.

The flow streamlines show that the flow is separated at the leading edge over the outer 8m of the wing span, forming a strong vortical structure which extends out to the wing tip and beyond, where it coalesces with the wing tip vortex. For the inner 2m of the span, the flow is visibly attached over the whole chord length. The pressure field around the wing shows some interesting features which are indicative of transonic flow in general. For example: over the upper wing surface, the symmetry plane slice shows a high pressure stagnation region at the wing apex; followed by a gradual flow acceleration into the low pressure zone shown in blue. In this blue region the flow velocity becomes sonic - the lighter blue band can be seen as an approximation of the 'sonic line'. At about 0.75X/C on this plane there is an abrupt increase in pressure coefficient as the flow decelerates back to subsonic velocities. This pressure distribution is always associated with transonic flow around aerofoils. The region with the largest amount of suction is the leading edge vortex, which is represented on the constant-X flow slices as a dark blue region which always coincides with the leading edge vortex location.
At the wing tip there is a low pressure region due to both the dominating vortical flow and the sharp corners of the wing tip.

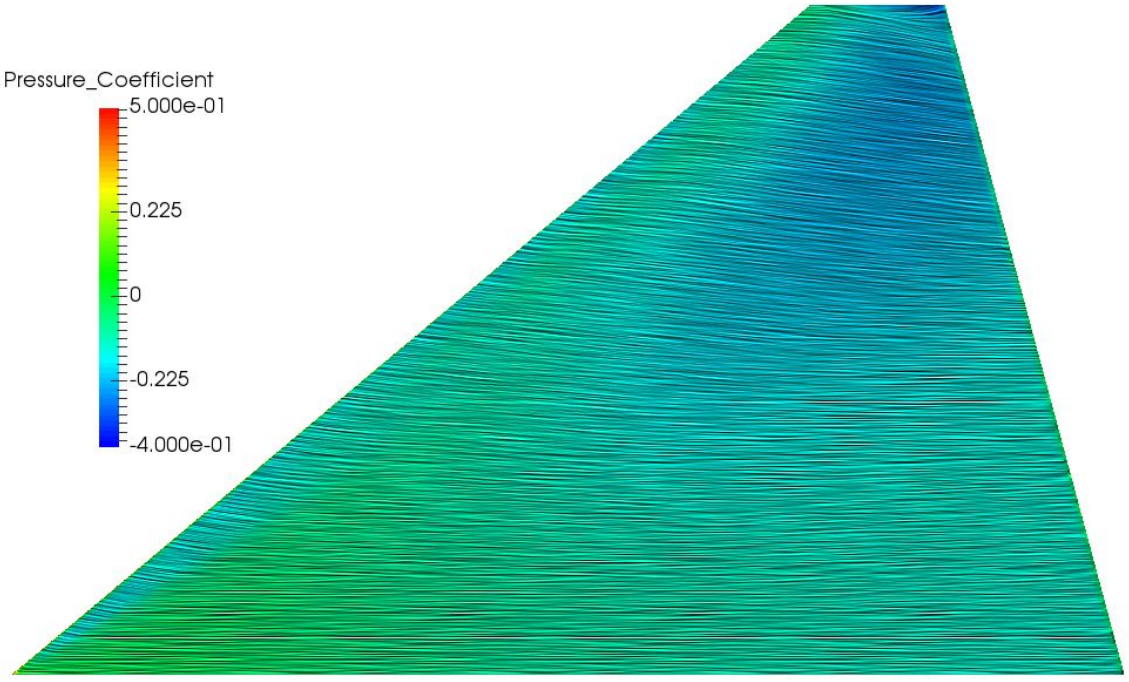

Fig 4.99 Trapezoid minimum drag M=1.6, CL=0.25, Re/m=6.6x10^6 surface flow visualisation

Figure 4.99 shows the flow on the upper surface of the minimum drag trapezoid wing at the supersonic design condition. A weak imbedded crossflow shockwave is present near the leading edge in the region 0.1m<Y<4m, however this disappears as the outer 5m span of the wing is highly aft-loaded, to the extent that the suction peak is near the trailing edge for the outer 3m of the wing.
The loading near the wingtip appears to have been reduced in comparison to the uncambered wing.

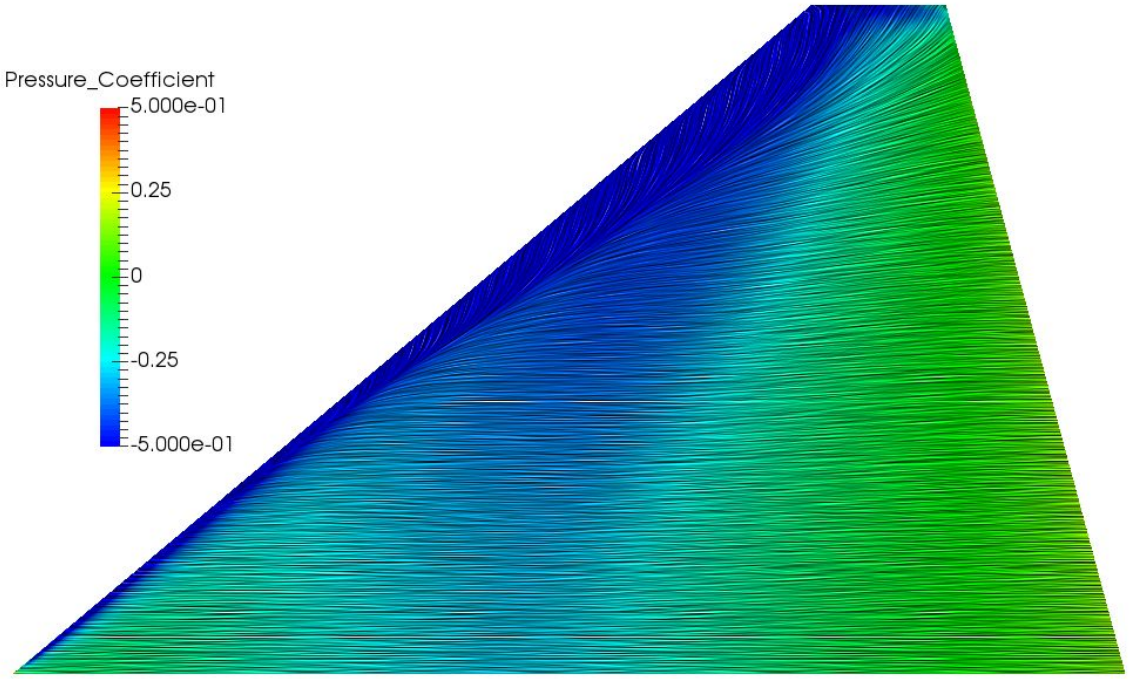

Fig 4.100 Trapezoid minimum drag M=0.85, CL=0.3, Re/m=6.6x10^{6} surface flow visualisation

Figure 4.100 shows the flow on the upper surface of the minimum drag trapezoid wing at the transonic design condition. The shockwave pattern is different from the lambda pattern on the uncambered wing in that the leading shock terminates at Y=5m because pressure upstream of the trailing shock has been reduced. This reduces the intensity of the leading shock but increases the intensity of the trailing shock. The flow separation region is reduced and the reattachment line is closer to the leading edge than the uncambered wing.
Near the wing root, the trailing shockwave smears and becomes a shock-free expansion and recompression zone.

Figure 4.101 shows the flow on the upper surface of the supersonic CMy constrained trapezoid wing at the supersonic design condition. At the wing root there is an adverse pressure gradient towards the trailing edge as a result of the negative wing camber. The embedded crossflow shockwave is stronger than the one exhibited by the uncambered wing, and has a fairly constant suction peak along the leading edge.
At the wingtip there is a reduction in loading between the leading and trailing edges due to the wing twist and S-shaped camber.

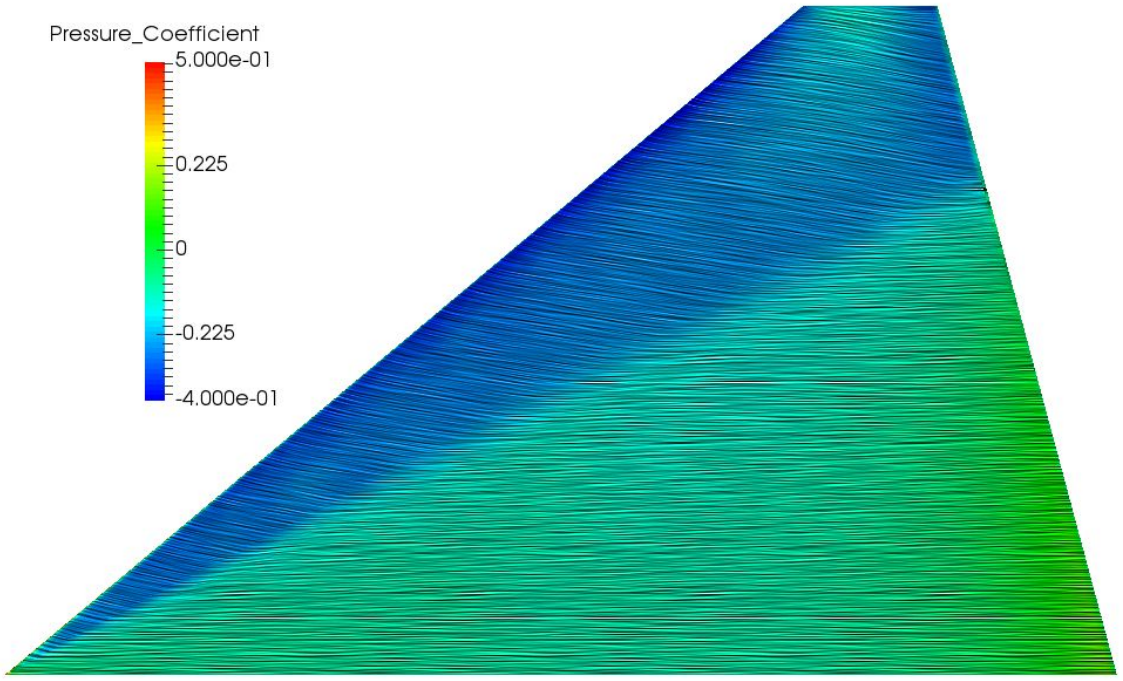

Fig 4.101 Trapezoid HS CMy Constrained M=1.6, CL=0.25, Re/m=6.6x10^6 surface flow visualisation

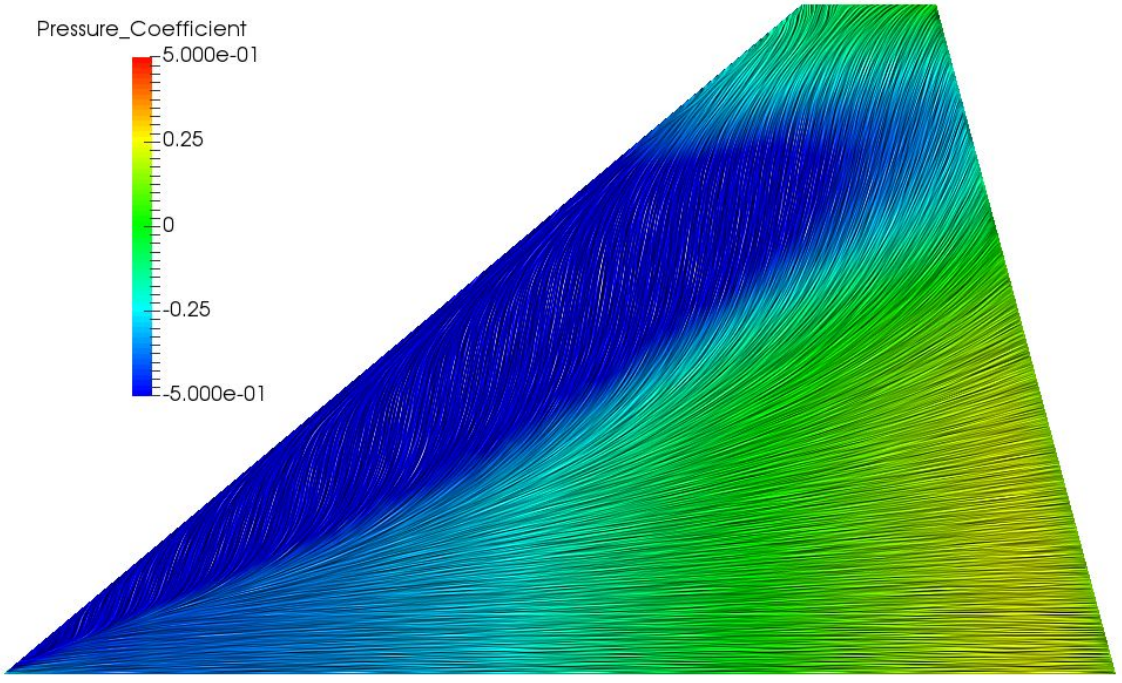

Fig 4.102 Trapezoid HS CMy Constrained M=0.85, CL=0.3, Re/m=6.6x10^6 surface flow visualisation

Figure 4.102 shows the flow on the upper surface of the supersonic CMy constrained trapezoid wing at the transonic design condition. As with the supersonic surface flow, there is an adverse pressure gradient along the wing root. There is a lambda pattern in the pressure distribution however the trailing pressure jump appears quite smeared indicating shockless compression. All of the flow on the outer 60% of the wing is separated, with spanwise flow dominating the majority of the wing surface. The outer 1m of the wing tip has a large reduction in loading.

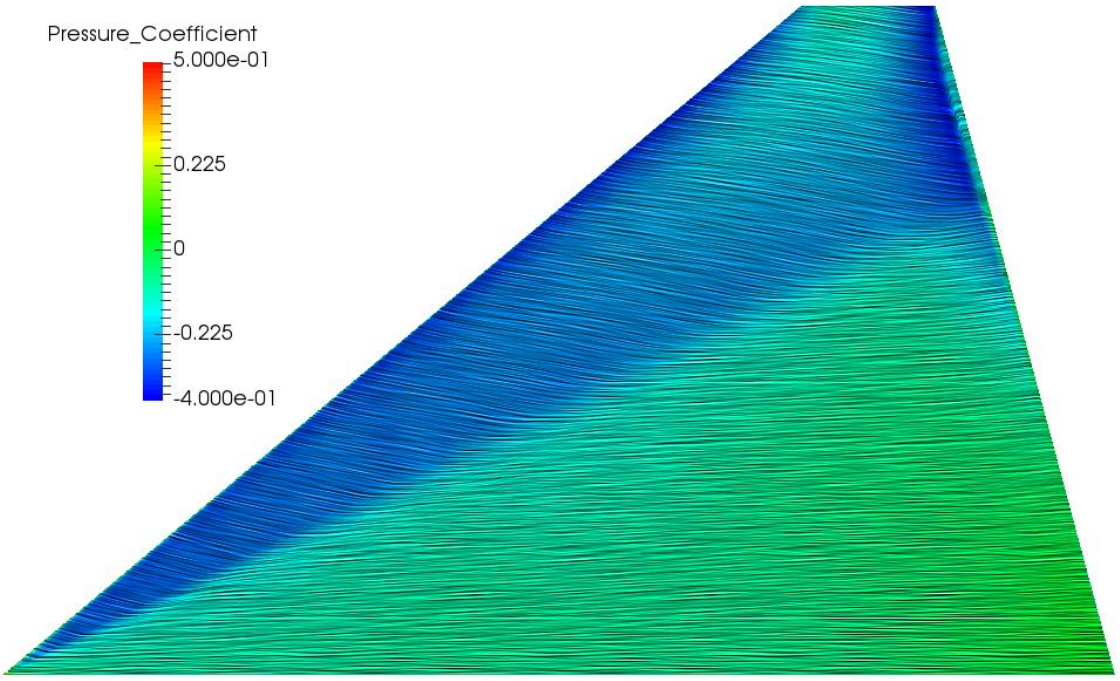

Fig 4.103 Trapezoid LS + HS CMy Constrained M=1.6, CL=0.25, Re/m=6.6x10^6 surface flow visualisation

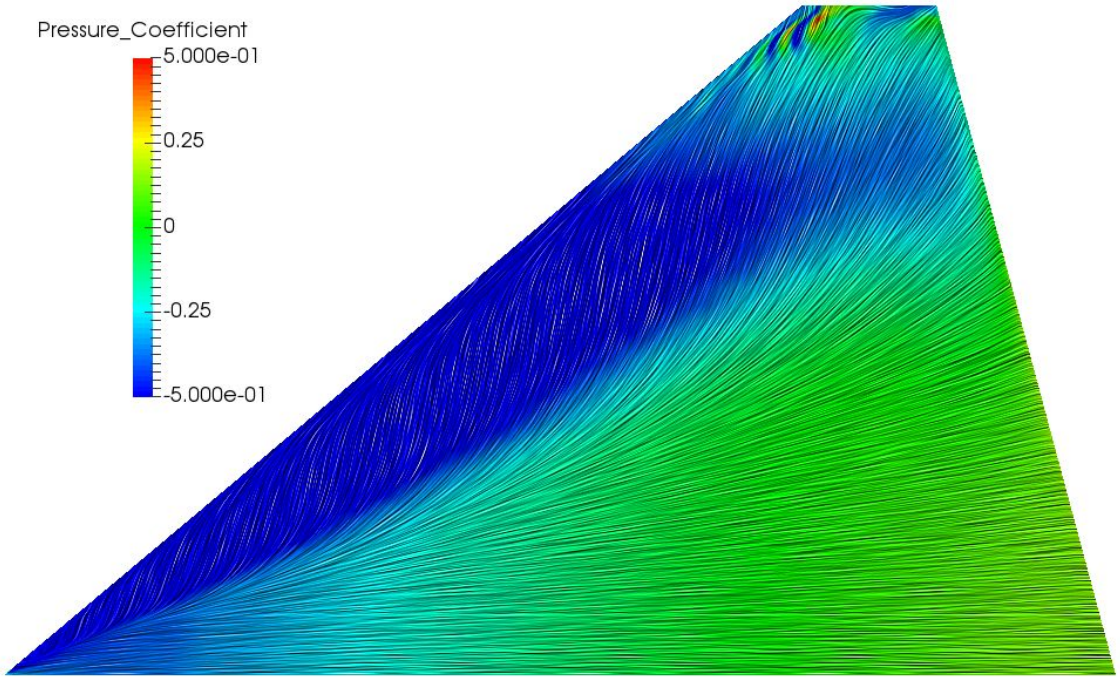

Fig 4.104 Trapezoid LS + HS CMy Constrained M=0.85, CL=0.3, Re/m=6.6x10^6 surface flow visualisation

Figure 4.103 shows the flow on the upper surface of the transonic and supersonic CMy constrained trapezoid wing at the supersonic design condition. At the wing root there is a slight adverse pressure gradient towards the trailing edge as a result of the trailing edge reflex camber. Towards the wing tip, there is a strong suction region at the trailing edge caused by positive trailing edge camber, serving to

aft-load the wing in this region. The pressure gradient at the trailing edge is so great that the flow is separated in a 0.1m band in the region 7m<Y<10m, outboards of the embedded crossflow shockwave.
The crossflow shockwave is strong, with strong suction near the wing apex and reduction in loading towards the wing tip. The leading edge suction peak is fairly uniform along the span of the wing, and there is no evidence of a shockwave at the wingtip due to reduction in loading in this region.

Figure 4.104 shows the flow on the upper surface of the transonic and supersonic CMy constrained trapezoid wing at the transonic design condition. There is an adverse pressure gradient over the first 50% of the wing root. All of the flow on the outer 60% of the wing is separated, as with the supersonic CMy constrained design, however there is less of a high pressure region at the trailing edge near the root due to the reduced reflex camber. Pressure perturbations at the wing tip are physical and are the result of the (possibly time dependent) interactions of vortices and secondary 'rollup' vortices, which are characterised by converging 'fishbone' patterns in the surface friction lines - visible very close to the leading edge. URANS or LES simulations would be required to fully understand the nature of this flow.

Figure 4.105 shows the flow on the upper surface of the uncambered cranked wing at the supersonic design condition. The pressure distribution pattern is very similar to the inviscid Euler prediction presented earlier in the thesis. A weak crossflow shockwave exists near the leading edge of the first 50 degree cranked region, which coalesces with a strong crossflow shockwave near the leading edge of the 75 degree cranked region causing flow separation. A vortical structure exists from this separation point along the leading edge of the 75 degree section and extends to the trailing edge, causing a corridor of low pressure under its core. A strong crossflow shockwave exists on the outer 50 degree swept sing section with a fairly uniform low pressure upstream of the shock; with the exception of at the concave crank location where the crossflow shockwave interacts with the vortical flow structure. At this interaction, the vortical structure increases the angle that the shock must turn the flow by; locally increasing the intensity of the shockwave. There is a weak shockwave at the wing tip which meets the crossflow shockwave at the wing trailing edge.

Figure 4.106 shows the flowfield around the initial uncambered cranked wing at the supersonic design condition in viscous flow. Transparent slices are located on the Y=0m, Z=0m, X=10m, X=15m and X=20m planes, and streamlines have been seeded from the edge of the boundary layer on the upper wing surface near the leading edge showing both the local flow direction and the local Mach number. Except from the boundary layer, leading edge separation region and subsequent vortical flow, the dominant features of this flow structure are similar to what was predicted in the inviscid Euler solutions.
On the symmetry plane and Z=0m plane, the shockwave and expansion fan patterns are exactly the same as what was predicted by the Euler solutions. The major difference in pressure field is visible on the X=15m plane, where the mid-span vortex crosses this plane there is a low-pressure region which interacts strongly with the cross-flow shockwave. This means that the cross-flow shockwave no longer has a planar shape, and visibly curves inwards towards the vortex. A complex interaction exists between the mid-span vortex, the expansion fan propagating inboards from the concave crank location and the crossflow shockwave on the outer wing section. The core of the vortex is initially drawn outboards by the low-pressure region ahead of the cross-flow shock, turning through a small

angle as it interacts with the expansion fan. The vortex core then turns through another small angle so that it continues along the wing in a chordwise direction.

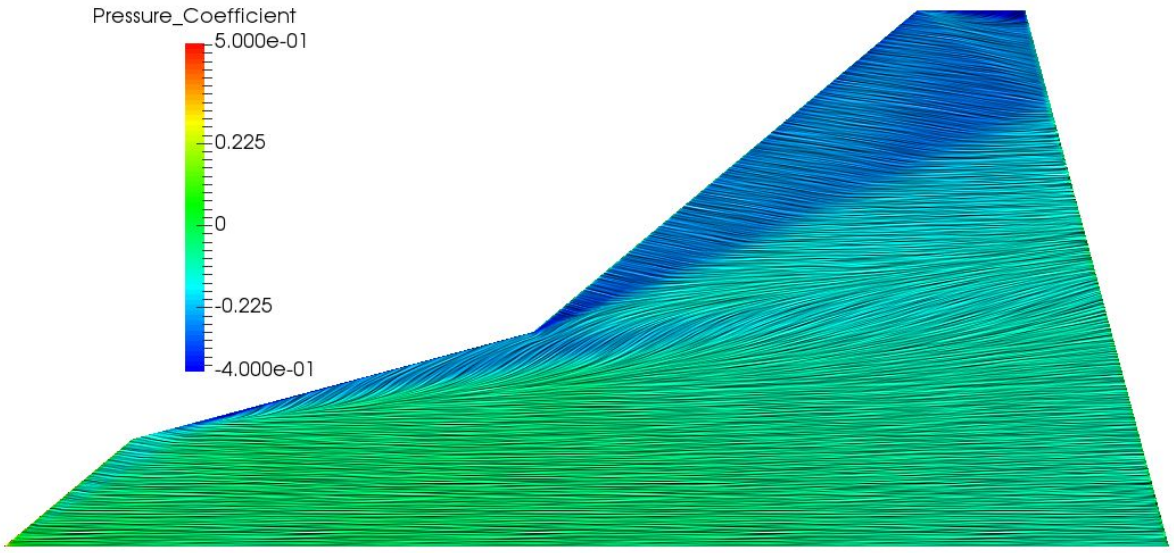

Fig 4.105 Cranked uncambered M=1.6, CL=0.25, Re/m=6.6x10^6 surface flow visualisation

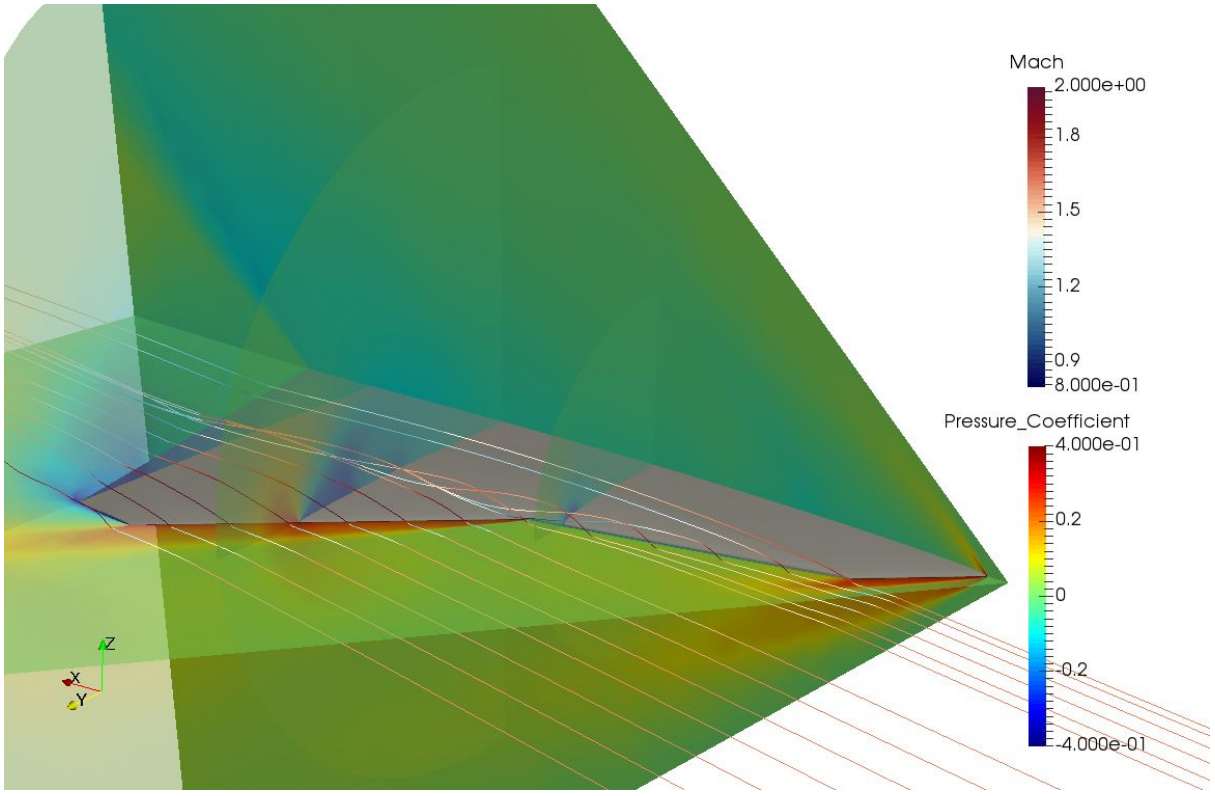

Fig 4.106 Cranked uncambered M=1.6, CL=0.25, Re/m=6.6x10^6 3D flow visualisation

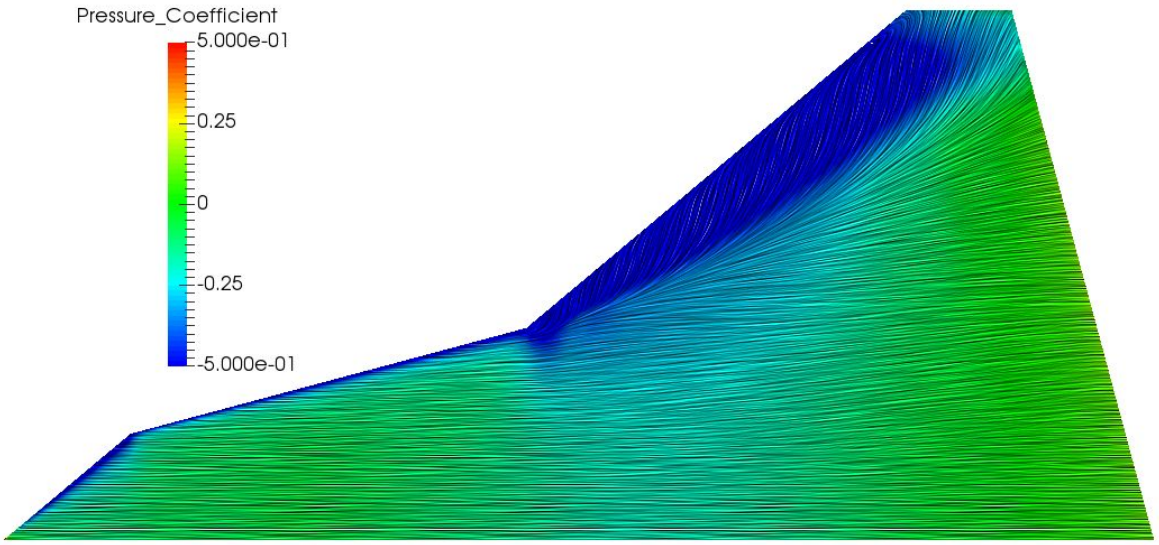

Fig 4.107 Cranked uncambered M=0.85, CL=0.3, Re/m=6.6x10^6 surface flow visualisation

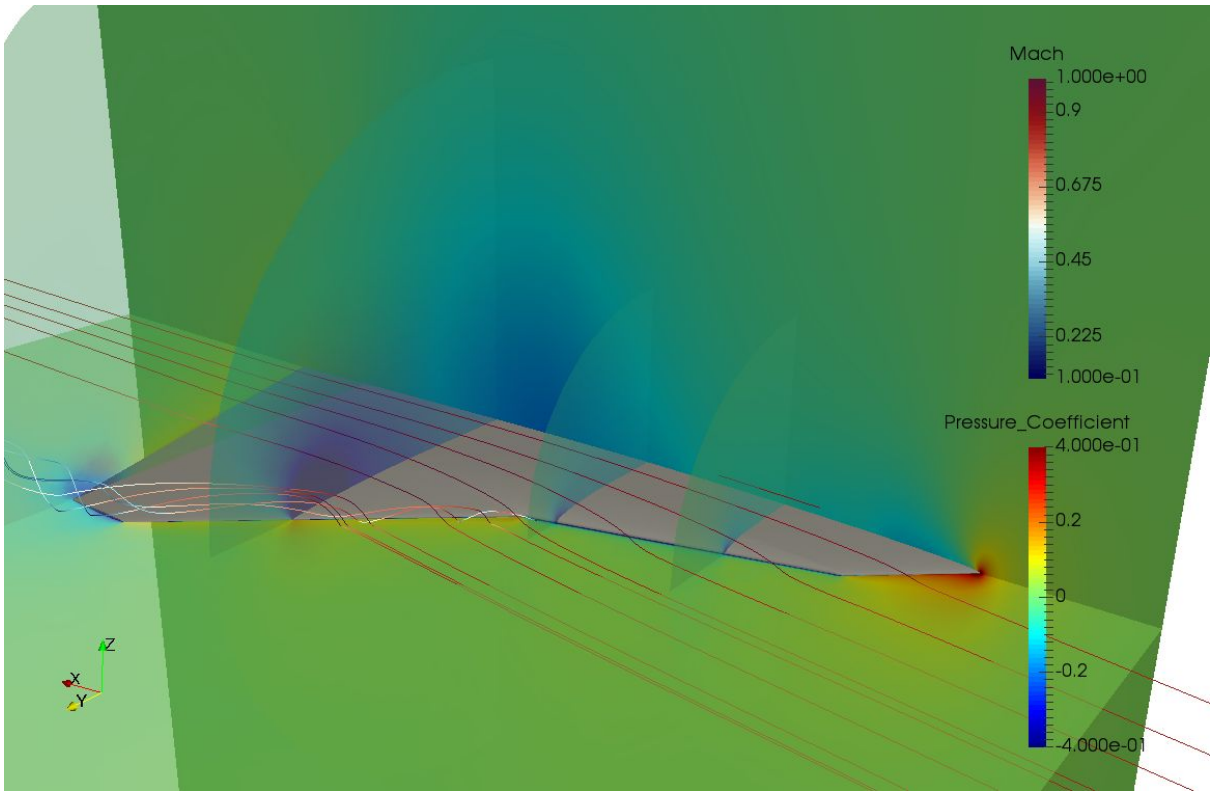

Fig 4.108 Cranked uncambered M=0.85, CL=0.3, Re/m=6.6x10^6 3D flow visualisation

Figure 4.107 shows the flow on the upper surface of the uncambered cranked wing at the transonic constraint condition. As with the supersonic simulation, the pressure distribution is very similar to what was predicted by the inviscid Euler simulation. Upstream of the shockwave pattern on the outer wing section, the flow is totally separated - with a reattachment line just downstream of the shockwave. There are strong suction peaks along the leading edges of the two inboard sections.

Figure 4.108 shows the flowfield around the initial uncambered cranked wing at the transonic design condition in viscous flow. Transparent slices show the pressure field around the wing and streamlines show both the local flow direction and the local Mach number.
The streamlines show that the flow is separated at the leading edge over the outer 6m of the wing span, forming a strong vortical structure which coalesces with the wing tip vortex. For the inner 4m of the span, the flow is visibly attached over the whole chord length. The pressure field around the wing shows that the transonic flow features have been significantly affected by the presence of the cranked leading edge. For example: over the upper wing surface, the symmetry plane slice shows two distinct and separate low pressure zones with sonic flow. The Z=0m plane shows how the pressure ahead of the leading edge changes with sweep angle; providing lower pressure and hence higher suction on the more highly swept leading edge portion. This is also reflected in the angle through which the oncoming flow is deflected around each leading edge portion - the highly swept leading edge portion turns the flow through a larger angle than the 50 degree swept portions; except very close to the surface where the flow is separated and turns through a very large angle.
Once again it can be said that the flow structure on the outer 6m section of the cranked wing is very similar to the flow structure on the outer 8m section of the trapezoid wing.

Figure 4.109 shows the flow on the upper surface of the minimum drag cranked wing at the supersonic design condition. The crossflow shock near the wing apex has been completely eliminated, and as a result the separation point has moved further outboards and the vortical structure has been reduced slightly. The intensity of the crossflow shockwave on the outer span of the wing has been reduced due to the moderate leading edge droop towards the wingtip, however it's interaction with the vortical flow structure still exists. It appears that the outer and inner portions of the wing are mostly aft-loaded, with the exception of the 75 degree swept section where the vortical flow structure exists.

Figure 4.110 shows the flow on the upper surface of the minimum drag cranked wing at the transonic constraint condition. The flow separates from the leading edge at Y=3m between the two crank locations. Forming a vortical flow structure similar to that found in the supersonic case. The flow separation at the leading edge of the outboard section of the wing has been greatly reduced, and now all flow is attached at the trailing edge. The vortical structure at the 75 degree leading edge interacts with and feeds into the separation region at the leading edge of the outboard region - serving to reduce the intensity of the vortical structure downstream of this point. The shockwave pattern on the outboard section of the wing has been moved aft and far downstream from the reattachment line.

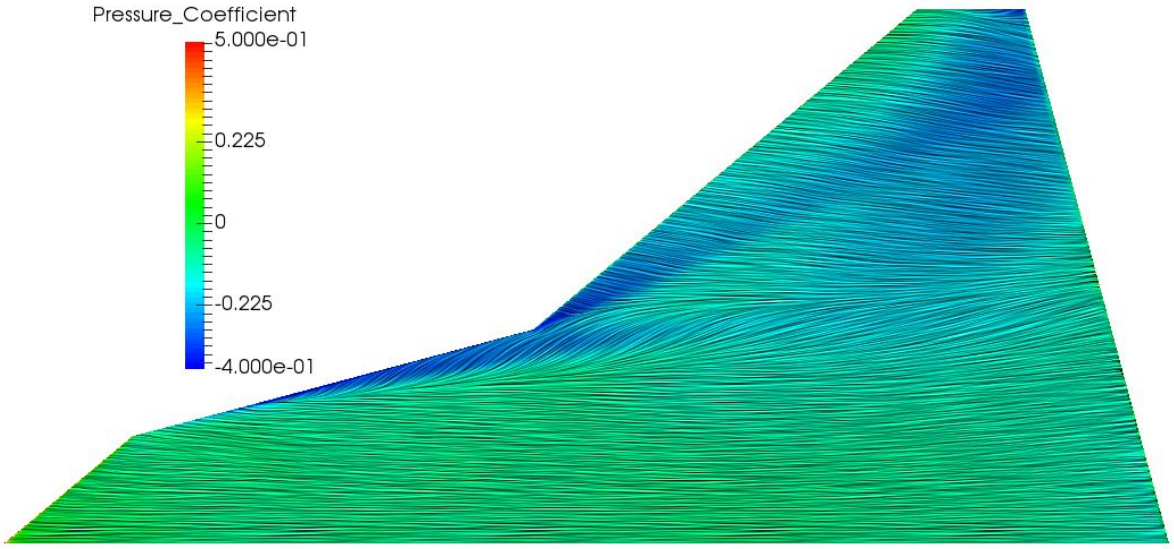

Fig 4.109 Cranked minimum drag M=1.6, CL=0.25, Re/m=6.6x10^6 surface flow visualisation

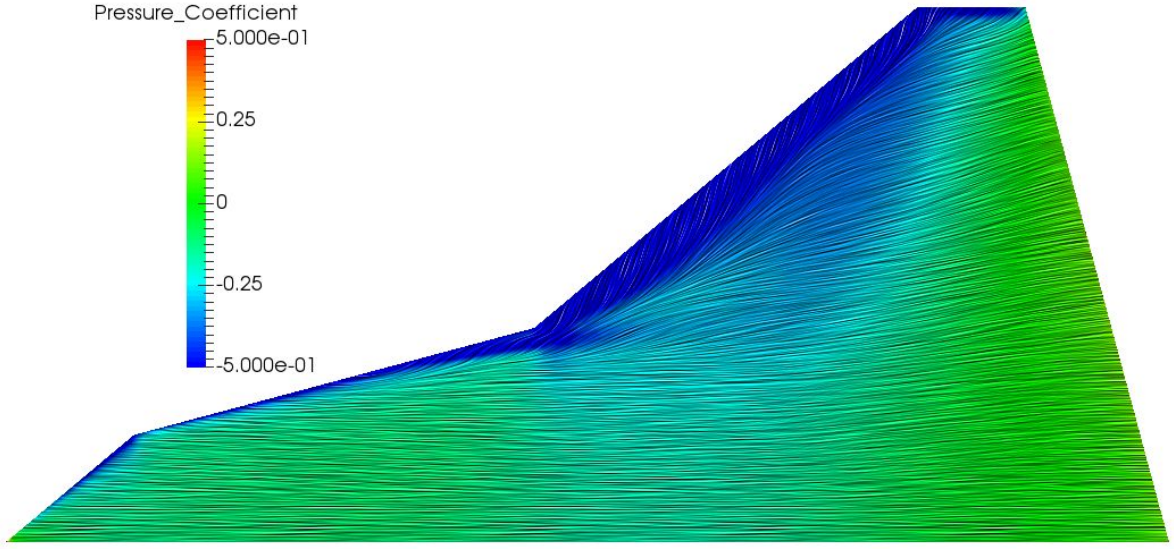

Fig 4.110 Cranked minimum drag M=0.85, CL=0.3, Re/m=6.6x10^6 surface flow visualisation

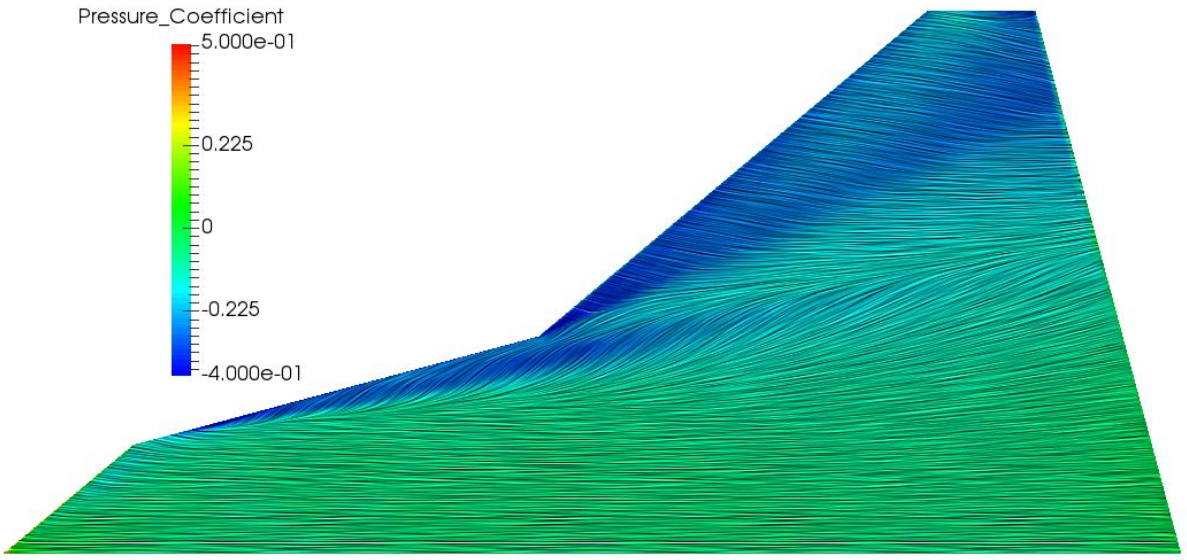

Fig 4.111 Cranked HS CMy Constrained M=1.6, CL=0.25, Re/m=6.6x10^6 surface flow visualisation

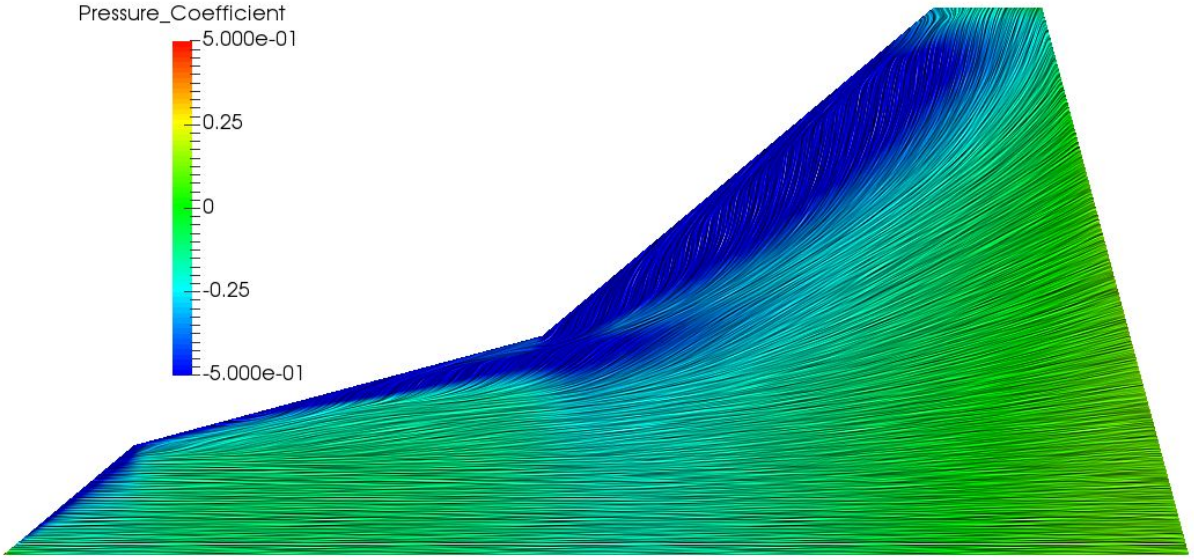

Fig 4.112 Cranked HS CMy Constrained M=0.85, CL=0.3, Re/m=6.6x10^6 surface flow visualisation

Figure 4.111 shows the flow on the upper surface of the supersonic CMy constrained cranked wing at the supersonic design condition. The crossflow shock near the wing apex has been weakened, but still interacts with the 75 degree leading edge causing flow separation at the same point as the uncambered wing. The intensity of the crossflow shockwave on the outer span of the wing has been reduced, but not by as much as the minimum drag case. It's interaction with the vortical flow structure is quite strong, however the vortex strength is not reduced as significantly as in the uncambered wing case. The wing root has an almost entirely flat pressure distribution with the exception of the stagnation point at the apex.

Figure 4.112 shows the flow on the upper surface of the minimum drag cranked wing at the transonic constraint condition. The flow separates from the leading edge at Y=2m between at the first crank location, Forming a vortical flow structure along the 75 degree leading edge. The separation line moves downstream from the leading edge before the second crank location meaning a small region of attached flow at the leading edge just ahead of the second crank. At the second crank location, the

flow separates again forming a very large vortical structure along the outer 50 degree leading edge section. This outer vortex interacts with the inboard vortex just downstream of the second crank location, first turning the inner vortex tube outwards towards the low pressure core of the outer vortex. Eventually the inner vortex merges completely with the outer vortex. Spanwise flow dominates the outer portion of the wing.

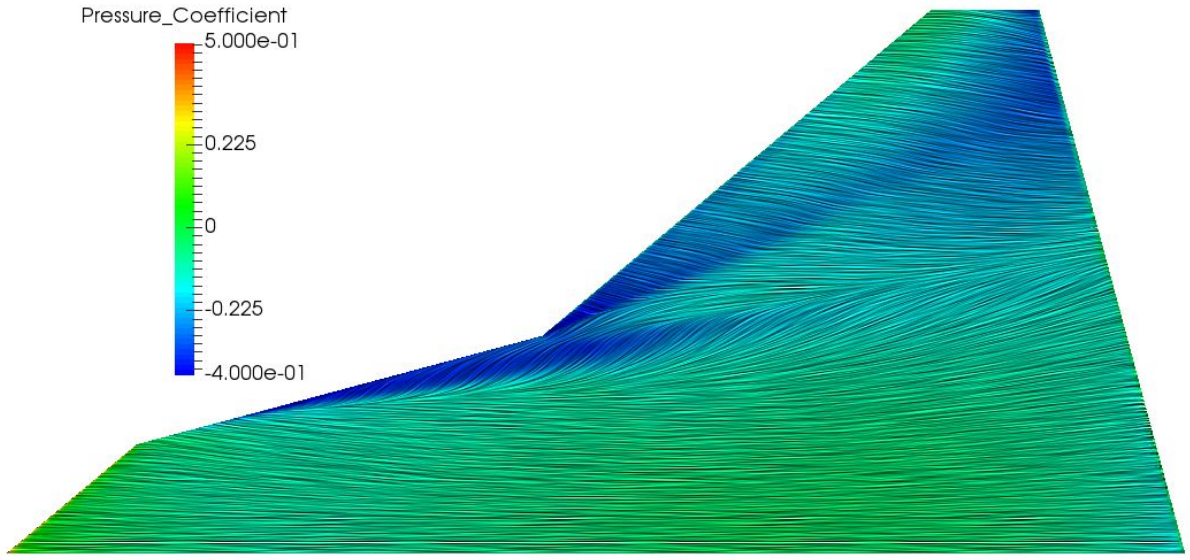

Fig 4.113 Cranked LS + HS CMy Constrained M=1.6, CL=0.25, Re/m=6.6x10^6 surface flow visualisation

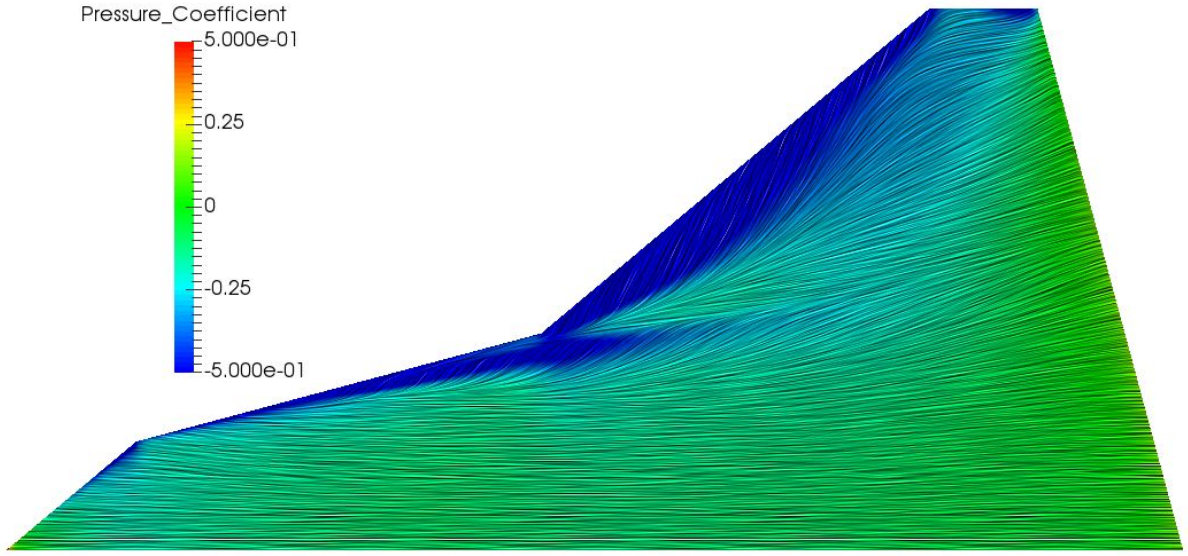

Fig 4.114 Cranked LS + HS CMy Constrained M=0.85, CL=0.3, Re/m=6.6x10^6 surface flow visualisation

Figure 4.113 shows the flow on the upper surface of the transonic and supersonic CMy constrained cranked wing at the supersonic design condition. As with the minimum drag wing, the crossflow shockwave has been eliminated from the inboard 50 degree leading edge section however the flow separates from the 75 degree section in a similar location to the uncambered wing case. The intensity

of the crossflow shockwave on the outer span of the wing has been reduced by a similar amount as the minimum drag case due to aft-loading the outer span of the wing. The wing root is also slightly aft-loaded, as in the minimum drag case - with the exception of a slight low pressure region 0.1<X/C<0.4.

Figure 4.114 shows the flow on the upper surface of the transonic and supersonic CMy constrained cranked wing at the transonic constraint condition. The flow separates from the leading edge at Y=3m in the same location as the minimum drag wing case, however there is a small attached area just ahead of the second cranked location just like in the supersonic CMy constrained case. The flow separation at the leading edge of the outboard section follows a similar pattern to the minimum drag wing case, except with a stronger interaction with the inner vortical structure. The vortical structure at the 75 degree leading edge interacts with the outboard vortex, but does not merge with it and persists to the trailing edge. The separation region on the outer span of the wing has an attachment line which follows the shockwave pattern very closely.

4.3.7 RANS Spanwise Force Distributions

In order to provide a measure of the spanwise distribution of forces on each wing geometry in viscous flow, the RANS surface solutions have been sliced at 0.2m intervals along their span. The forces on each 2D slice are then integrated and resolved into lift, drag and pitching moments. In these plots, trapezoid wing data will be displayed using a diamond shaped marker and cranked wing data will be displayed using a cross marker. Different line colours represent the design method used to create each geometry, as detailed in the legend.

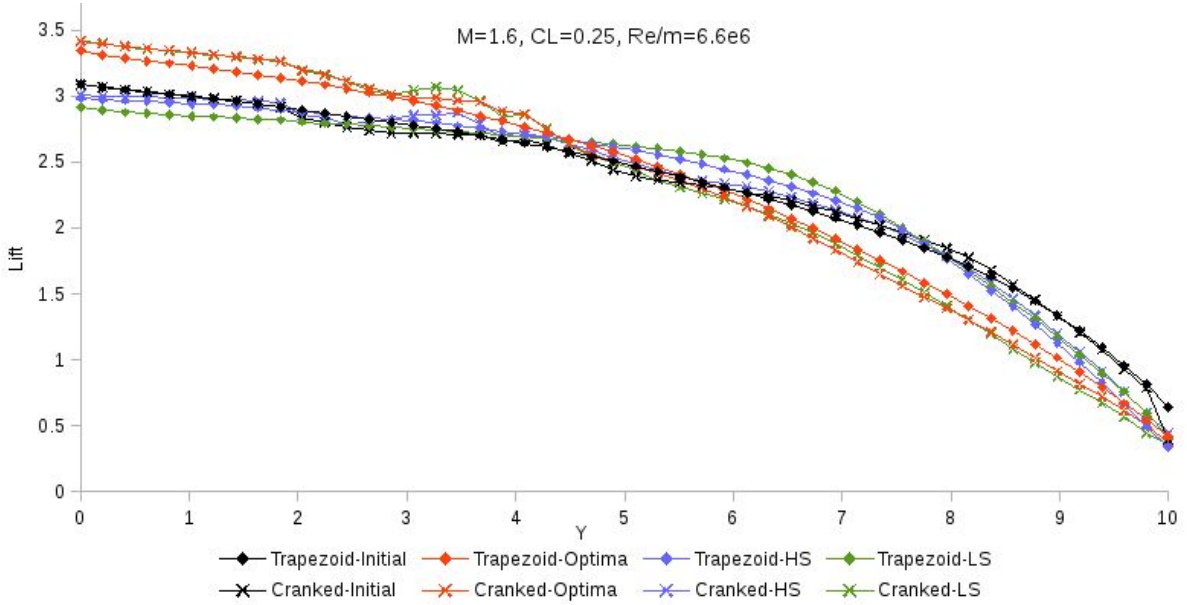

Fig 4.115 RANS spanwise lift distributions for each wing design at supersonic flight condition

Figure 4.115 shows the spanwise lift distributions of each wing design at the supersonic design point as calculated by the viscous RANS equations. In Black and red are the uncambered and minimum drag designs presented and discussed in the previous section of this thesis, with the additional blue lines representing the supersonic CMy constrained designs and the additional green lines representing the transonic and supersonic CMy constrained designs. Every designed wing has a

lower loading at the outer 2m of the span than the uncambered wing designs, however the two pitch-constrained trapezoid wings have the highest loading of any design at 4.5m<Y<7.5m, with the transonic constrained design being loaded the highest of all in this region. These two pitch constrained trapezoid wings also have the lowest loading of any design at the wing root and inner 2m of the span, with the transonic constrained design being the lowest.

The pitch moment constrained cranked wing designs do not show the same similarities that the trapezoid designs do, having largely different characteristics from one another. The supersonic pitching moment constrained cranked wing design has a nearly identical loading to the trapezoid transonic constrained design at the outer 2.2m of the span, however at this point it follows the uncambered cranked wing loading until Y=6m where its loading rises above that of the uncambered wing but follows the same general trend. At the wing root the supersonic pitching moment constrained cranked wing has a slightly lower loading than the uncambered cranked wing.

The transonic pitching moment constrained cranked wing has the lowest wingtip loading of any design until Y=8.2m, but otherwise follows the load distribution of the minimum drag cranked wing almost exactly; with the exception of at 2.8m<Y<3.8m, the outer half of the 75 degree swept region of the wing, where it has the highest loading of any of the designs.

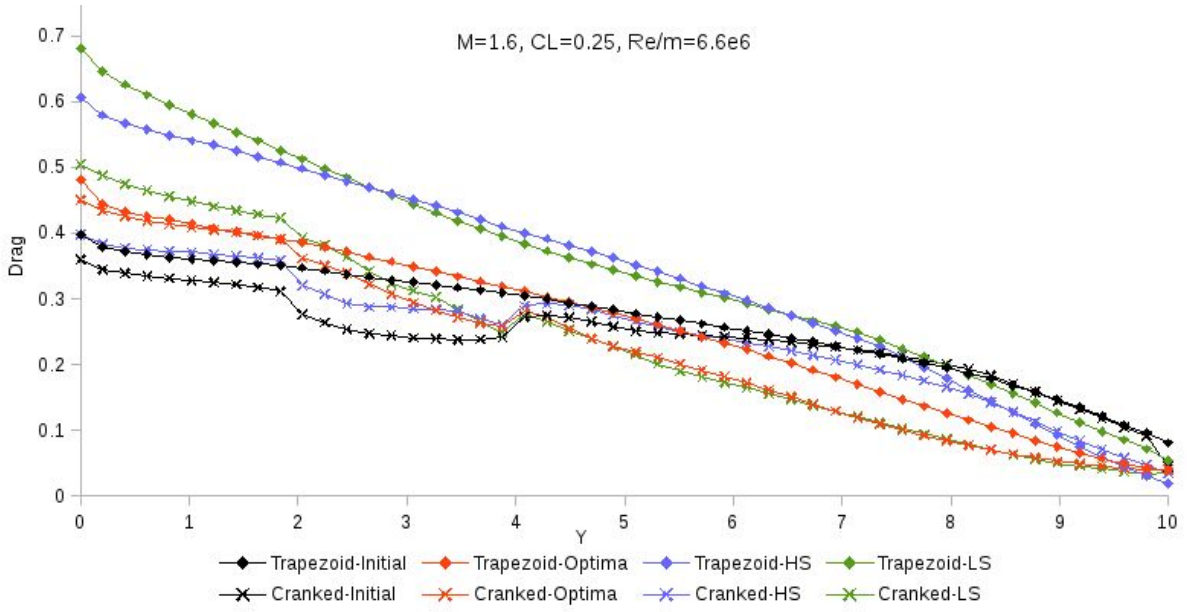

Fig 4.116 RANS spanwise drag distributions for each wing design at supersonic flight condition

Figure 4.116 shows the spanwise drag distributions of each wing design at the supersonic design point as calculated by the viscous RANS equations. The pitch-constrained trapezoid wings have the highest drag from the wing root out to Y=8m, where they both produce lower wingtip drag than the uncambered wings.

The supersonic CMy constrained trapezoid wing has the second-highest drag value at the root, however it has the highest drag in the mid-span 3m<Y<6m. At the wingtip Y>9.8m this wing has the lowest drag of any design. The transonic CMy constrained trapezoid wing has the highest root drag of any of the wing designs, and the highest drag of any of the cambered designs at the wing tip, however otherwise it's drag follows a similar distribution to that of the supersonic CMy constrained trapezoid wing.

The supersonic CMy constrained cranked wing has the lowest root drag of any cambered wing design, with a distribution resembling that of the uncambered cranked wing except shifted upwards by

around 0.05. At Y=3.4m this difference reduces and from Y=6m outwards the drag is less than the uncambered wing, although with a similar characteristic distribution shape. The overall drag distribution of his wing is broadly similar to the uncambered cranked wing except with a higher gradient so that the drag is higher at the root and lower at the tip.

The transonic CMy constrained cranked wing has a drag distribution which almost exactly follows that of the minimum drag wing except from the second crank location inwards. The drag gradually increases inwards along the span at the 75 degree swept section and inboard 50 degree swept section until it reaches a value of 0.5 at the wing root. This suggests that a compromise has been made between wing root drag and pitching moment.

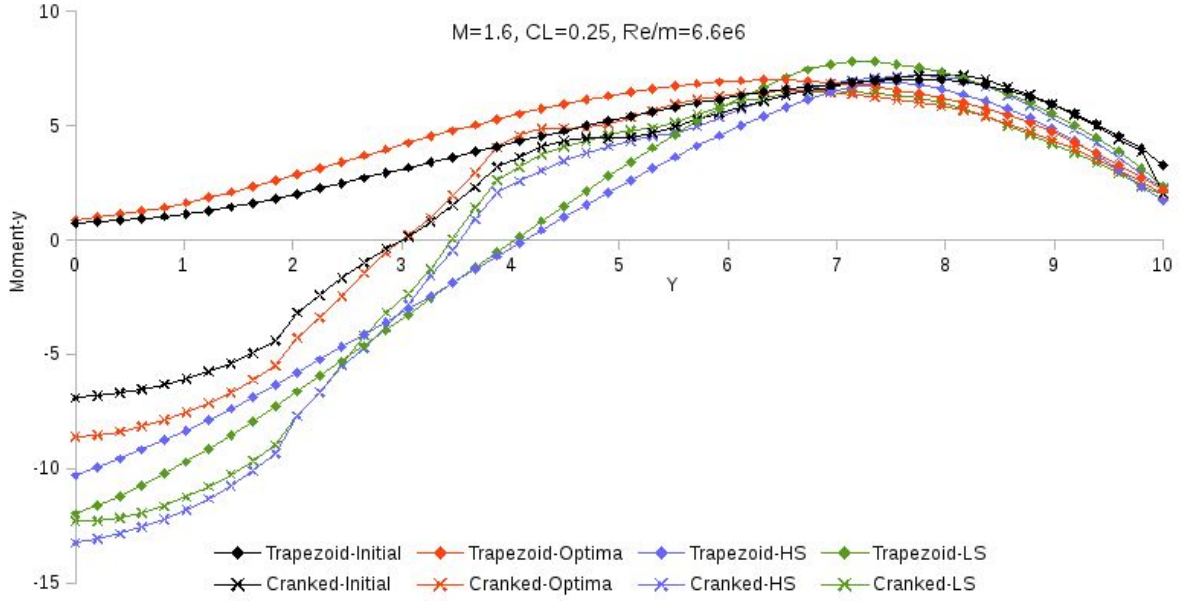

Fig 4.117 RANS spanwise pitching moment distributions for each wing design at supersonic flight condition

Figure 4.117 shows the spanwise pitching moment distributions of each wing design at the supersonic design point as calculated by the viscous RANS equations.

The uncambered trapezoid wing has a positive (nose down) pitching moment throughout its entire span, starting at a low value and gradually increasing until it reaches a maximum value at Y=8m, after which there is a gradual decrease until the wing tip. This wing has the highest pitching moment of any design at the tip Y=10m.

The minimum drag trapezoid wing has a slightly higher pitching moment than the uncambered trapezoid wing at the root, where it continues to increase at a higher gradient until its maximum point at Y=6.4m. From this point until the tip there is a gradual decrease in pitching moment.

The supersonic CMy constrained trapezoid wing has a negative pitching moment in the order of -10 at the wing root, with a linear increase until Y=6m where the gradient reduces and pitching moment reaches its maximum value at Y=7.6m. From this point on there is a steep reduction in pitching moment leading to the lowest wing tip pitching moment of any design. The pitching moment is zero at Y=4.2m.

The transonic CMy constrained trapezoid wing has a very similar pitching moment distribution to the supersonic CMy constrained wing, except that it has a lower value at the root, slightly steeper gradient towards it's higher maximum value at Y=7.4m and has a pitching moment of zero at Y=4m.

The uncambered cranked wing has the lowest magnitude negative (nose up) pitching moment at the wing root of any design. From the root to Y=1.8m there is a gradual nonlinear increase in pitching moment, after which there is a sharp increase to Y=2m. At the 75 degree swept wing section 2m<Y<4m, there is a moderate nonlinear increase in pitching moment, with zero moment at Y=3m. Just outboard of the second crank location, Y=4.5m, there is a plateau with no considerable change in pitching moment until Y=5m where it rises to almost exactly match the distribution shown by the uncambered trapezoid wing out to the tip. It's maximum pitching moment value is at Y=8m.
The minimum drag cranked wing shows a similar pitch distribution shape to the uncambered cranked wing, except with a more negative pitching moment at the wing root and a higher gradient. Pitching moment is zero at Y=3m as with the uncambered wing. The pitching moment distribution then follows that of the uncambered trapezoid wing in the region 4.5m<Y<7m, with its highest value at Y=7m, after which it gradually decreases towards the wing tip.
The supersonic CMy constrained cranked wing has the most strongly negative pitching moment at the wing root of any design, however it's pitching moment distribution shows the same characteristics as all of the cranked wing designs except with a much larger gradient in the region 0m<Y<5m and a pitching moment of zero at 3.5m. The maximum pitching moment value is at Y=8m with a steep reduction towards the tip.
The transonic CMy constrained cranked wing has a slightly higher pitching moment at the wing root than the supersonic CMy constrained cranked wing, however at the 75 degree swept region the distributions match very closely, with zero moment at Y=3.4m. It continues to have a slightly higher pitching moment until Y=6.8m, after which it follows the distribution of the minimum drag cranked wing all the way to the tip.

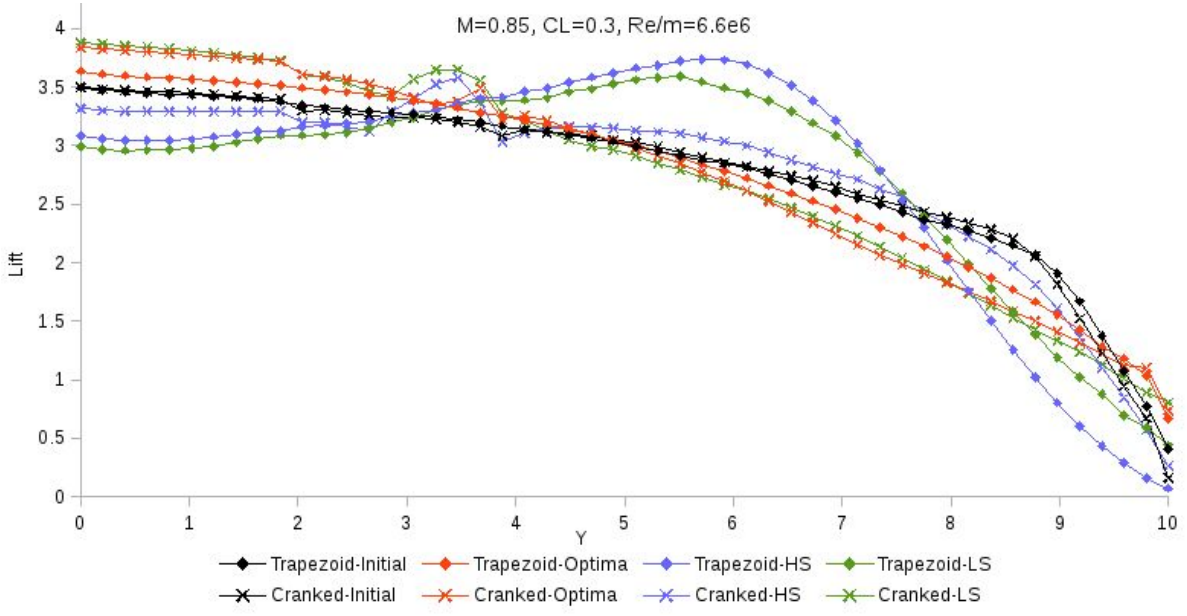

Fig 4.118 RANS spanwise lift distributions for each wing design at transonic flight condition

Figure 4.118 shows the spanwise lift distributions of each wing design at the transonic constraint point as calculated by the viscous RANS equations.

The uncambered trapezoid wing has a local lift value of 3.5 at the root, and gently slopes downwards to Y=8.6m where it has a value of just above 2. At this point, the slope increases dramatically towards the wingtip where it reaches a value of 0.5.

The minimum drag trapezoid wing has a slightly higher root loading than the uncambered wing, with a similar gradient until Y=3m, where the gradient begins to increase gradually with the lift distribution taking on an elliptical characteristic. There is a sharp reduction in lift between Y=9.8m and the wing tip, where it reaches a value of 0.75.

The supersonic CMy constrained trapezoid wing has the second-lowest loading at the wing root with a value of approximately 3.1. The loading then increases gradually until Y=6m where lift reaches a maximum value of 3.8. After this there is a sharp reduction in lift towards the wing tip where it reaches a value near zero.

The transonic CMy constrained trapezoid wing has a very similar lift distribution to the supersonic CMy constrained trapezoid wing, with the exception of having a slightly lower root loading of 3, a lower maximum lift value of 3.7 at Y=5.5m and a higher lift value at the wingtip of 0.5.

The uncambered cranked wing has a near-identical lift distribution to the uncambered trapezoid wing, except at the crank locations where there are slight perturbations in lift distribution and near the wingtip, where the sharp drop in lift begins at 8.4m and continues down to a lift value of 0.2 at the tip.

The minimum drag cranked wing has the second highest lift of any design at the wing root, with a gradual reduction to Y=2m where there is a sharp reduction in lift at the first crank location. Just before the second crank location at Y=3.8m there is a sharp positive perturbation in lift caused by the vortical flow in this region. From here out to Y=9.8m there is a moderate reduction in lift to a value of 1.25. At the wing tip there is a sharp reduction in lift to a value of 0.9.

The supersonic CMy constrained cranked wing has a slightly lower local lift value at the wing root to the uncambered cranked wing and a similar lift distribution until Y=2.8m, where there is a large increase in lift until Y=4m, again caused by the vortical flow in this region. Lift increases gradually once again from Y=4m to Y=5m, where it begins decreasing in an elliptical manner to the tip.

The transonic CMy constrained cranked wing has the highest lift value of any design at the root, however follows the lift distribution of the minimum drag cranked wing almost exactly with the exception of the high lift region caused by vortical flow at 3m<Y<4m and a slightly lower lift value near the wing tip at 8.4m<Y<9.8m. There is no sharp drop in lift at the wing tip.

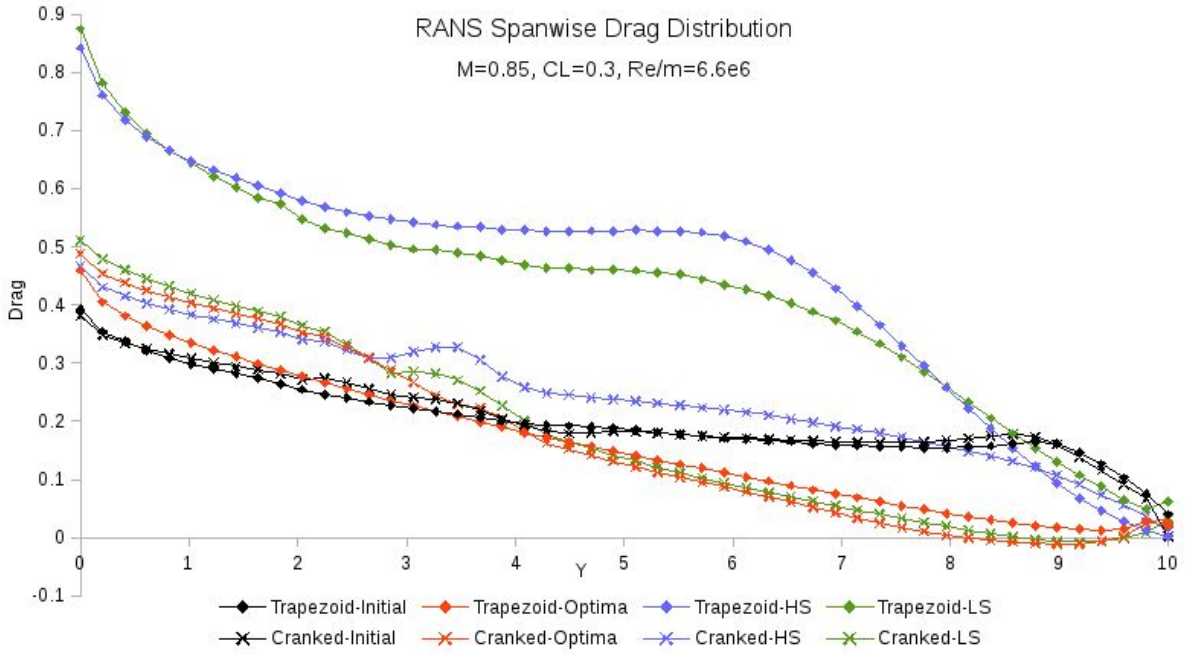

Fig 4.119 RANS spanwise drag distributions for each wing design at transonic flight condition

Figure 4.119 shows the spanwise drag distributions of each wing design at the transonic constraint point as calculated by the viscous RANS equations.

The uncambered trapezoid wing has the second lowest drag value at the wing root, gradually reducing to Y=4m where this reduction becomes almost imperceptible until Y=8m. At this point there is a small increase in drag with a local maximum at Y=8.8m and subsequent reduction towards the wing tip.

The minimum drag trapezoid wing has the lowest wing root drag of any of the cambered wings with a value of 0.45, and initially this value reduces rapidly to 0.4 within the first 0.2m of the span. From 0.2m to 9.4m there is a steady nearly linear decrease in drag to a very low positive value, with a small positive spike at Y=9.8m.

The supersonic CMy constrained trapezoid wing has the second highest root drag of any wing design, sharply reducing from the root at first and then holding steady at a value of 0.55 in the region 3m<Y<5.8m. From Y=6m to the tip there is a large reduction in drag resulting in the lowest wingtip drag of any of the wing designs.

The transonic CMy constrained trapezoid wing has the highest root drag of any of the wing designs, sharply reducing initially with a similar distribution shape to the supersonic CMy constrained trapezoid wing. There are some small perturbations in drag at the crank locations and a lower mid-span drag than the supersonic CMy constrained trapezoid wing. This wing has the highest wingtip drag of any of the wing designs.

The uncambered cranked wing has the lowest root drag of any wing design in this investigation, and has a lift distribution which generally follows the same trend as that expressed by the uncambered trapezoid wing. The differences are that the cranked wing has slightly higher drag in the region 0.5m<Y<3.8m due to the extended leading edge and a slight reduction in drag just outboard of the second crank location Y=4.2m.

The minimum drag cranked wing has a moderate root drag value of 0.495 with a gentle reduction in drag until Y=2.2m, where there is a sharper reduction in drag out to Y=9m with the exception of a

small increase in the region of the vortical flow structure at Y=3.7m. In the region 8m<Y<9.5m this wing has a negative drag value, indicating that this portion of the wing is producing a net thrust force.
The supersonic CMy constrained cranked wing has a wing root drag value of 0.46 with an initial reduction which is similar to the minimum drag cranked wing; however at Y=2.6m there is a moderate increase in drag due to the strong vortical flow. From this point to the tip the drag is significantly higher than either of the other cambered cranked cases, due to the highly separated flow on the leeside of the outer section of the wing.
The transonic CMy constrained cranked wing has the highest root drag of any of the cranked wing designs, with a drag distribution which closely resembles that of the minimum drag cranked wing for the entire span, with the exception of the region 3m<Y<4m where the strong vortical flow causes a moderate increase in drag. The region of negative drag is also smaller than that of the minimum drag wing, extending from Y=8.5m to Y=9.5m.

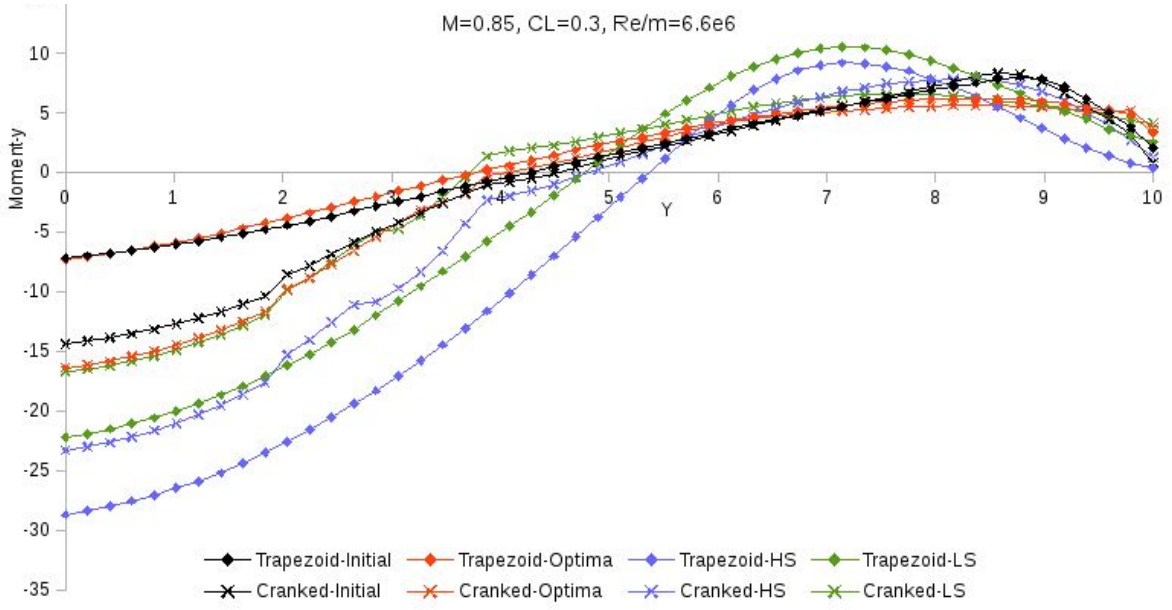

Fig 4.120 RANS spanwise pitching moment distributions for each wing design at transonic flight condition

Figure 4.120 shows the spanwise pitch moment distributions of each wing design at the transonic constraint point as calculated by the viscous RANS equations. Interestingly, at this transonic speed, all of the wing designs have a nose-up pitching moment at their root.
The uncambered trapezoid wing has the smallest negative root pitching moment of any of the designs, a value which gradually rises towards Y=8.8m where it reaches its maximum value of 10. There is a pitching moment of zero at Y=4.3m and a sharp reduction in pitching moment from Y=9m out to the tip.
The minimum drag trapezoid wing has a similar root pitching moment to the uncambered trapezoid wing, but initially increases with a stronger gradient along the span resulting in a pitching moment of zero at Y=3.7m. At Y=6m, the slope of dCMy/dY reduces and pitching moment reaches its maximum value of 7 at Y=8.6m, before gently reducing towards the wing tip.
The supersonic CMy constrained trapezoid wing has the most strongly negative pitching moment at the wing root of any of the wings, and even though there is a strong gradient dCMy/dY the pitching moment does not become zero until Y=5.4m - the furthest outboard zero-moment point of any design.

The strong gradient also results in the most inboard maximum pitching moment of any of the designs at Y=7.2m with a value of 10. The pitching moment then reduces towards the tip where it has a value of near-zero.

The transonic CMy constrained trapezoid wing has a very similar spanwise pitching moment distribution to the supersonic CMy constrained trapezoid wing - however shifted upwards on the axes shown. The difference in pitching moments between these two designs is large at the root but reduces towards the wing tip. The pitching moment is zero at Y=4.8m and has a maximum value of 12 at Y=7.2m; the highest maximum pitching moment value of any design at this flight condition.

The uncambered cranked wing has a more negative pitching moment at the wing root than the uncambered trapezoid wing, with a fairly constant difference in the innermost section 0m<Y<2m. Along the 75 degree swept section 2m<Y<4m, this difference reduces quickly so that on the outer 6m span of the wing, both CMy distributions match very closely.

The minimum drag cranked wing has a slightly more negative pitching moment at the root than the uncambered trapezoid wing but generally a similar distribution shape until Y=7m, where the gradient dCMy/dY reduces and the distribution follows that of the minimum drag trapezoid wing until the wing tip.

The supersonic CMy constrained cranked wing has the second most negative pitching moment at the root of any of these designs, however the shape of the moment distribution in the first 2.5m of the span follows a similar shape to that expressed by all of the cranked wing designs. At Y=2.5m there is a deviation from this shared trend where the pitching moment remains constant for 0.2m and then continues rising. This effect is due to the strong vortical flow on the leeside of this wing. At the inner span of the wing, the supersonic CMy constrained design has the highest gradient dCMy/dY of any of the cranked wing designs resulting in the highest pitching moment of any cranked wing design in the region 6.8m<Y<8.2m.

The transonic CMy constrained cranked wing has a pitching moment distribution which closely follows that of the minimum drag cranked wing for the first 3m of the span, however deviates in the region of the leeside vortical flow structure and increases at Y=4m. From this point outwards there is a higher pitching moment than the minimum drag wing until the wing tip, where in the outer 1.5m of the span their pitching moment distributions match each other closely once again.

4.3.8 RANS Force Polars

Now that the performance, flowfields and force distributions of each of the wing designs have been analysed in detail at the design point and constraint point using RANS evaluations, it is important to discover how these wings perform throughout a larger region of the flight envelope. In order to do this, RANS solutions have been generated for a series of incidence angles for each of the wing designs at both supersonic M=1.6 and transonic M=0.85 speeds. The lift, drag and moment forces on each wing at each condition have been displayed in force 'polars', shown below.

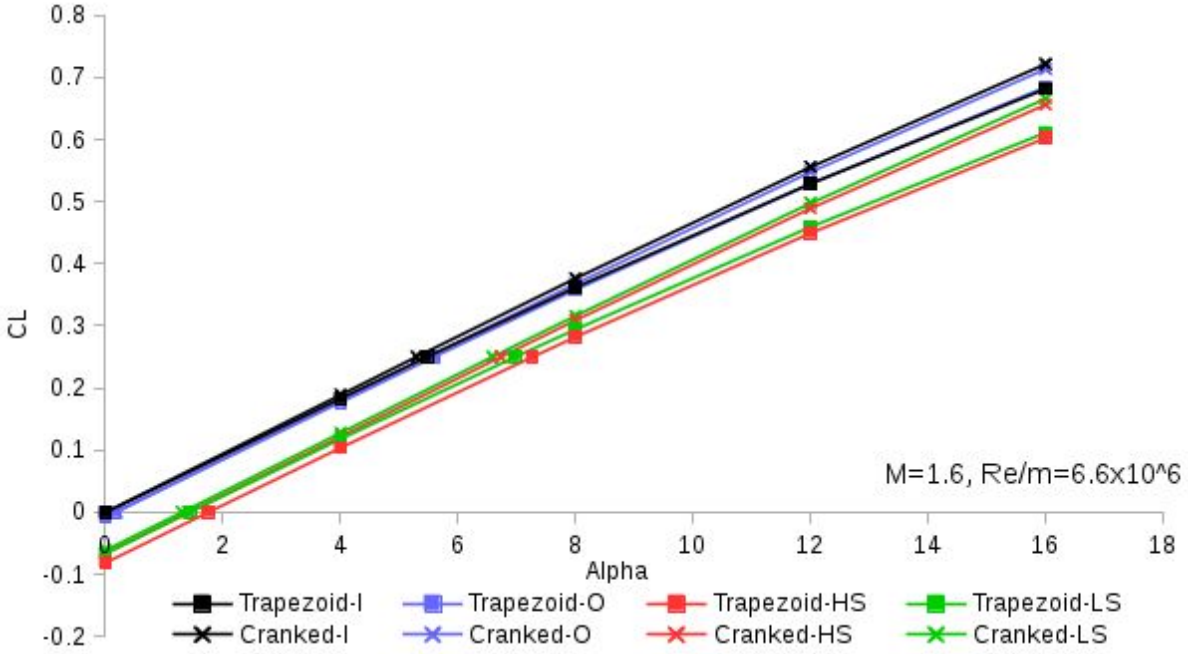

Fig 4.121 Supersonic lift polars of each wing design

Figure 4.121 shows the lift polar of each wing design at Mach 1.6. The region $0<\alpha<16$ has been included in this analysis, meaning that the stalling point of each wing has not been found at this speed and most of the polars shown in Figure 4.121 remain within the linear lift slope region of each design. The uncambered trapezoid and cranked wings both have zero lift at zero angle of attack, however the cranked wing has a slightly higher lift slope at low incidences and lacks the slight nonlinearity of the trapezoid wing lift slope at higher incidence angles. This means that the cranked uncambered wing has moderately higher lifting coefficients than the trapezoid uncambered wing at high incidence angles.

The minimum drag wing designs have supersonic lift polars which follow their uncambered counterparts very closely, except shifted downwards almost imperceptibly in figure 4.121 so that they produce zero lift at slightly positive α values. Other than this their lift slopes are identical.

The supersonic CMy constrained trapezoid wing has the lowest CL of any wing design at any incidence angle, requiring an incidence angle of 1.8 degrees to satisfy the zero-lift condition. However, this wing has a more linear lift slope than any of the other trapezoid wing geometries throughout the range tested meaning that the gradient $dCL/d\alpha$ does not reduce as much at higher incidence angles.

The supersonic CMy constrained cranked wing has a linear lift slope for the entire range of α values included in figure 4.121, producing zero lift at 1.4 degrees α and having a CL of 0.656 at 16 degrees α.

The transonic CMy constrained trapezoid wing has a slightly nonlinear lift slope, producing a higher CL of -0.067 at zero degrees α than the supersonic CMy constrained trapezoid wing but a similar CL of 0.61 at 16 degrees α.

The transonic CMy constrained cranked wing has a linear lift slope with a CL of -0.061 at zero degrees α and a CL of 0.665 at 16 degrees alpa.

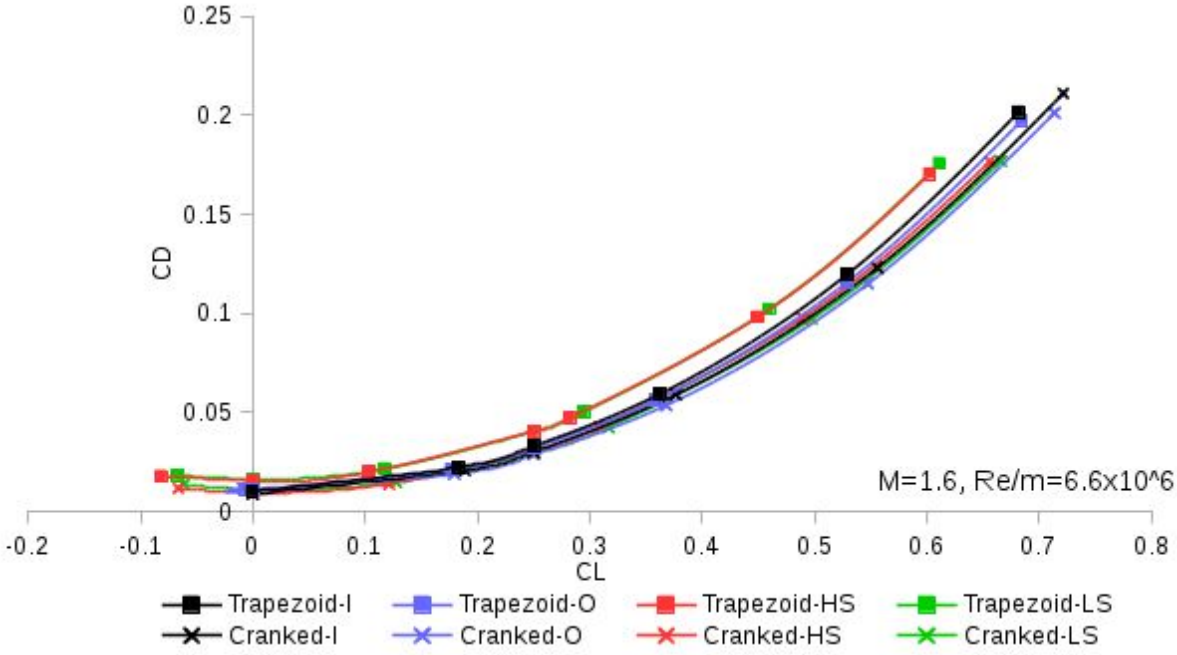

Fig 4.122 Supersonic drag polars of each wing design

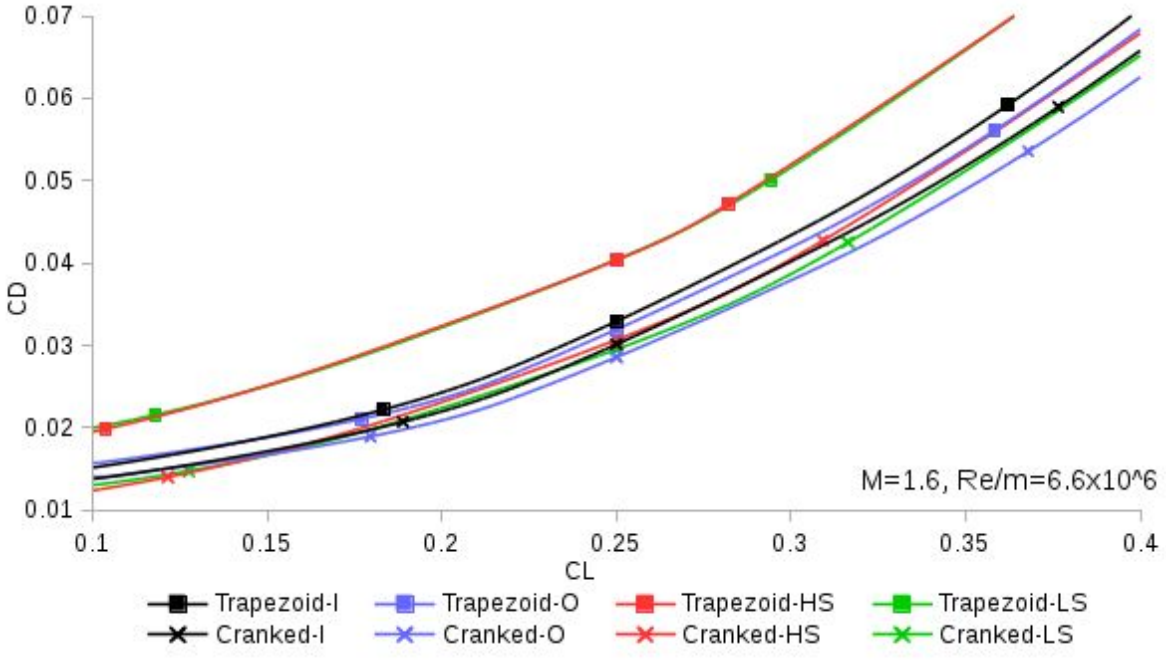

Fig 4.123 Zoomed view of the supersonic drag polars of each wing design

Figure 4.122 shows the drag polar of each wing design at Mach 1.6 in the region 0<α<16 degrees. The uncambered wings both have lower zero-lift drag than any of their cambered counterparts. Both of the pitching moment constrained trapezoid wings have significantly higher drag values at any given CL than any other wing design. At high lift coefficients, the transonic CMy constrained cranked wing and minimum drag cranked wing have the lowest drag values.

Figure 4.123 shows the drag polar of each wing design at Mach 1.6 in the region 0.1<CL<0.4. At low lift coefficients, the cranked pitching moment constrained designs have the lowest drag values. From CL=0.17 upwards the minimum drag cranked wing has the lowest drag value, however the transonic CMy constrained cranked wing comes very close in the region 0.25<CL<0.32. In the entire CL range shown in Figure 4.123, all of the cranked wings have lower drag values than any of the trapezoid wings - illustrating the influence of planform shape on aerodynamic performance at this Mach number.

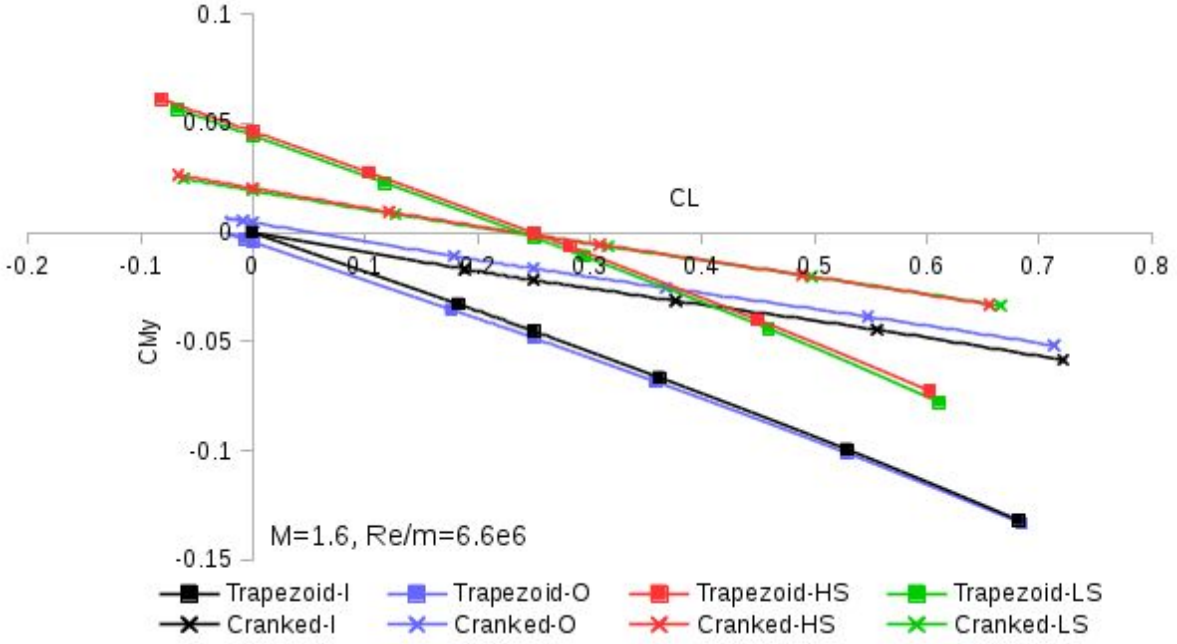

Fig 4.124 Supersonic pitching moment polars of each wing design

Figure 4.124 shows the pitching moment polar of each wing design at Mach 1.6 in the region 0<α<16 degrees. There are two notable locations where designs seem to produce zero pitching moment. The first is near CL~0 where the flat wings produce zero moment and the second is at CL=0.25 where the pitching moment constrained wings produce zero moment. The gradients dCMy/dCL seem to be relatively constant for each planform shape, suggesting that changes in wing camber only have the effect of translating the pitch moment slopes but will not significantly affect the gradient of the slopes. Both cranked CMy constrained wings have almost identical pitching moment polars, as do both trapezoid CMy constrained wings. The trapezoid minimum drag wing has a positive pitching moment at CL=0, whereas the cranked minimum drag wing has a negative pitching moment at CL=0.

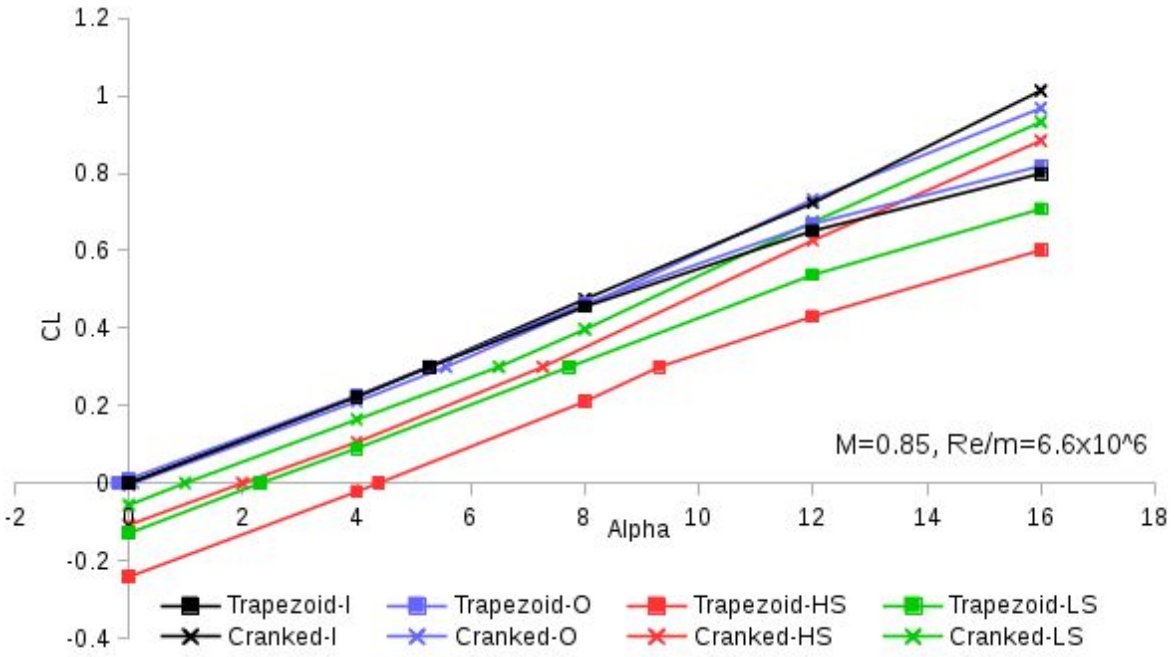

Fig 4.125 Transonic lift polars of each wing design

Figure 4.125 shows the lift polar of each wing design at Mach 0.85 in the region 0<α<16 degrees.
There is a very interesting difference between each planform, in that for incidence angles above 8 degrees the trapezoid wing lift slopes generally decrease, whereas the cranked wing lift slopes generally increase above this incidence angle.
The trapezoid supersonic CMy constrained design has the lowest CL at any incidence angle by a considerable margin, as with the supersonic evaluation. This is due to the large negative camber over the majority of the wing.
The trapezoid transonic CMy constrained design has the second lowest CL at any incidence angle, and the slope dCL/dα does not reduce until 12 degrees α.
The uncambered and minimum drag trapezoid and cranked wings have very similar lift slopes at low incidence angles, producing zero lift at near zero degrees α. At 8 degrees α, the trapezoid wings show a reduction in lift slope.
The pitching moment constrained cranked wings have the same lift slope gradients as the uncambered and minimum drag cranked wings, however shifted downwards so that the supersonic CMy constrained cranked wing produces zero lift at 2 degrees α and the transonic CMy constrained cranked wing produces zero lift at 1 degree α.

Figure 4.126 shows the drag polar of each wing design at Mach 0.85 in the region 0<α<16 degrees.
As with the supersonic evaluation, the trapezoid CMy constrained wings both have the highest drag values of any of these wings at all incidence angles. At high lift coefficients CL>0.5 the cranked minimum drag and cranked transonic CMy constrained wings have the lowest drag values. At zero lift, the uncambered trapezoid wing has the lowest drag value thanks to it's low wetted surface area, however this wing also has the third highest drag of any design at high CL values. The supersonic CMy constrained cranked wing has the highest drag of any of the cranked wings at all lifting coefficients included in this study.

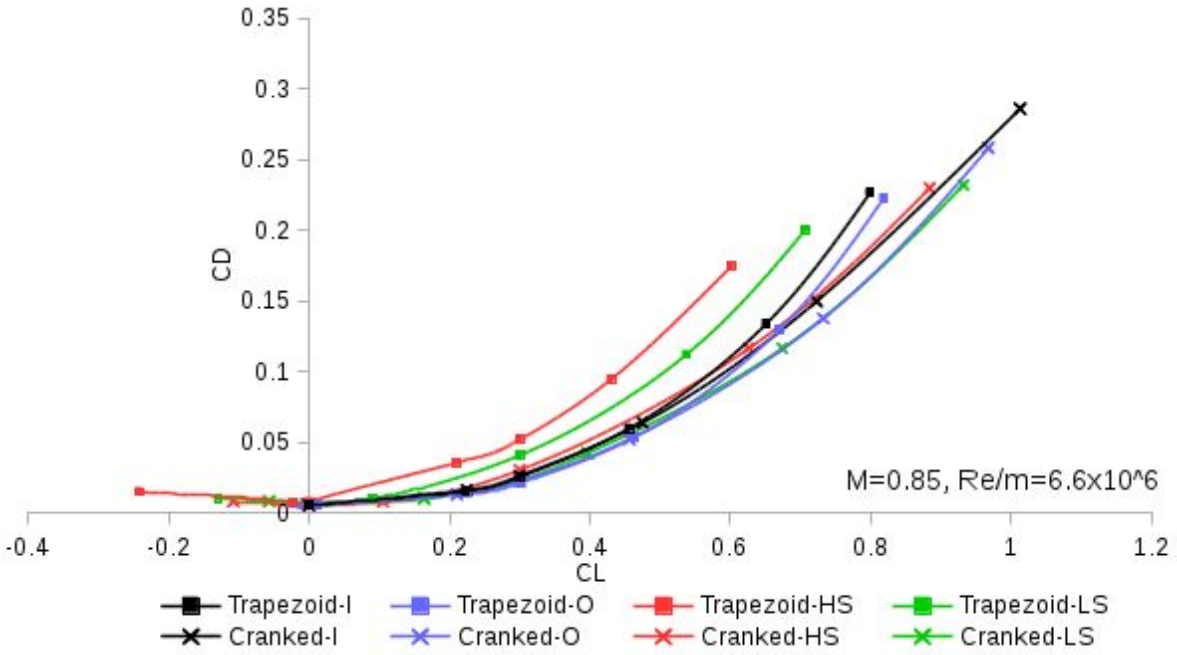

Fig 4.126 Transonic drag polars of each wing design

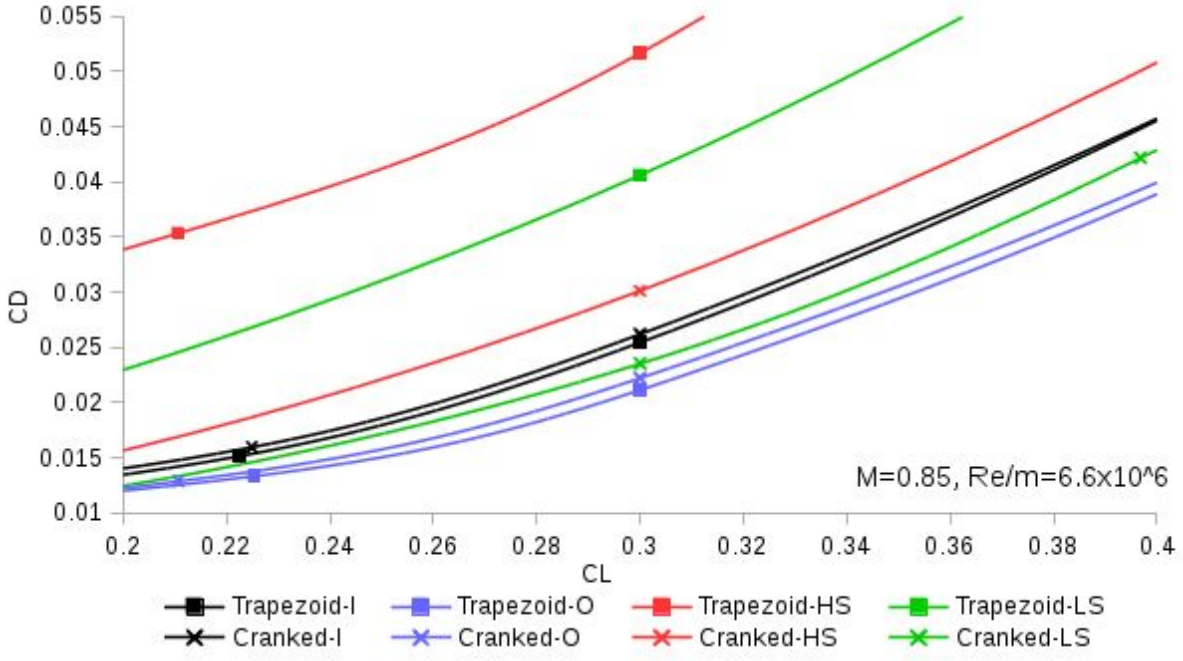

Fig 4.127 Zoomed view of the transonic drag polars of each wing design

Figure 4.127 shows the drag polar of each wing design at Mach 0.85 in the region 0.2<CL<0.4. At the design point lift coefficient, CL=0.3, the trapezoid minimum drag wing has the lowest drag value, closely followed by the minimum drag and transonic CMy constrained cranked wings. These results show that at this transonic speed, the leading edge extension has less of an influence on drag than wing camber shape - the opposite of what can be said for the supersonic speeds examined earlier. It is found that the trapezoid uncambered wing has lower drag at CL=0.3 than the cranked uncambered wing.

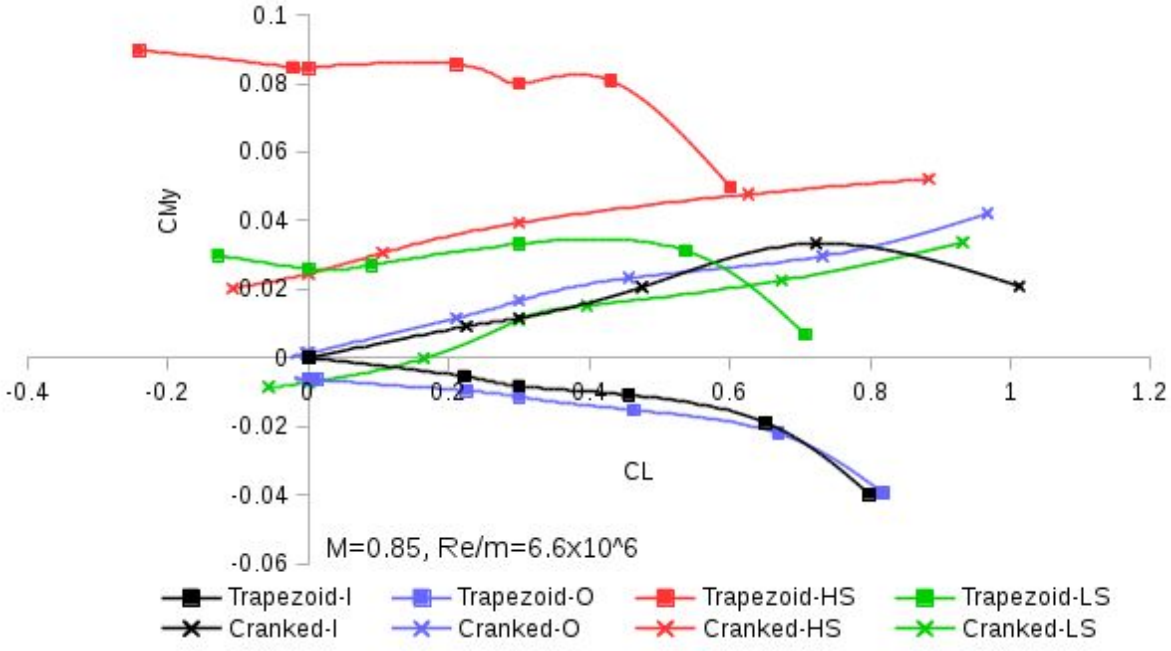

Fig 4.128 Transonic pitching moment polars of each wing design

Figure 4.128 shows the pitching moment polar of each wing design at Mach 0.85 in the region $0<\alpha<16$ degrees. Due to the fact that the moment reference point was chosen to be located at an approximation of the aerodynamic centre of the trapezoid wing at transonic speeds, most of the slopes dCMy/dCL are very small especially for the trapezoid wing designs at low CL values.

There are 3 wing designs which have near-zero pitching moment at zero lift: the uncambered wings and the cranked minimum drag wing. There are also only two designs which can be considered as statically stable about this moment reference point at this Mach number: the uncambered and minimum drag trapezoid wings. This is because the slope dCMy/dCL remains negative over the entire range of incidences.

The cranked wings are all statically unstable at the transonic flight condition due to their increased surface area ahead of the moment reference point. The CMy constrained trapezoid wings are also statically unstable at the design lift coefficient CL=0.3, this is due to their reflex camber which pushes the centre of lift further forwards.

None of the wings have successfully achieved the target of zero pitching moment at CL=0.3, but 4 of the wings have come quite close: the trapezoid uncambered and minimum drag wings have small negative CMy values whilst the uncambered and transonic CMy constrained cranked wings have small positive CMy values. Only one of these wings has low pitching moment values at both supersonic and transonic speeds - the transonic CMy constrained cranked wing. It is clear that the addition of the leading edge extension allows a camber design which provides favourable pitching moment characteristics and good aerodynamic efficiency at both supersonic and transonic flight conditions. This is not to say that the effects of sonic ‘Mach-tuck’ are completely negated, but rather significantly reduced without a large drag penalty.

4.3.9 Conclusions of Pitching Moment Constrained Optimisation Study

Additional hard constraints were added to the soft constrained optimisation strategy in order to control the pitching moment of optimised wing designs. Designs were produced with CMy constrained at both the supersonic design point and a transonic cruise condition. The design histories and final results showed that planform shape has a very strong effect on the ability of the camber design to satisfy constraints and improve performance of supersonic wings.

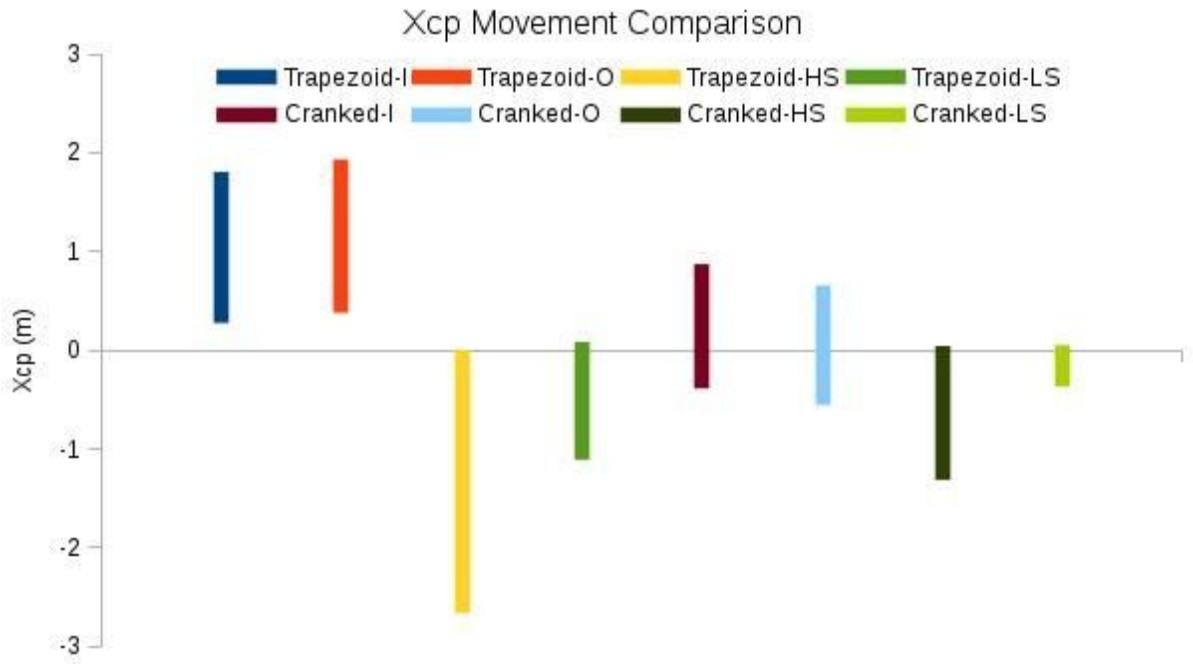

Fig 4.129 Comparison of centre of pressure movement between M=0.85, CL=0.3 and M=1.6, CL=0.25 for each wing design.

Figure 4.129 shows the centre of pressure locations of each wing design at both transonic and supersonic speeds. On this chart, a value of zero corresponds to X=7.88m on the trapezoid wing and X=12.88m on the cranked wing. This value, in both cases, equates to 8.82m forwards from the trailing edge - the low-speed aerodynamic centre of the flat trapezoid wing. This is the location where the centre of gravity of the aircraft would be located, meaning that positive Xcp locations would require nose-up pitch trim to achieve equilibrium and negative Xcp locations would require nose-down pitch trim. The magnitude of the difference reflects the magnitude of trim which would be required. In this plot, minimum Xcp values correspond with cruising transonic flight at CL=0.3 and maximum Xcp values correspond with manoeuvring supersonic flight at CL=0.25.

For both planforms, the minimum drag geometries produce similar Xcp locations to the uncambered wings, with the trapezoid min. drag wing having slightly higher Xcp values and the cranked min.drag wing having slightly lower Xcp values. In general, the trapezoid wings experienced an Xcp shift of around 1.5m between flight states. The cranked wings experienced an Xcp shift of around 1.2m between flight states.

The wings which were designed using only a supersonic pitching moment constraint both have near-zero Xcp at the supersonic manoeuvre condition, however they have the lowest Xcp values at the transonic condition due to their high degree of reflex camber.

The wings which were designed using two pitch constraints both achieved better performance values than the wings optimised with only one pitch constraint - potentially suggesting that they were forced to explore different regions of the design space in an attempt to satisfy all constraints and subsequently found more globally optimised shapes. Of the wings which were designed with both supersonic and transonic pitching moment constraints, only the cranked planform design can be seen as having come close to satisfying the pitch moment constraints. This wing design is described in more detail in the following section.

4.3.9.1 Novel Wing Design

In particular it is found that a cranked or LERX planform, when optimised using the multipoint-constrained adjoint method, is capable of high performance with only 0.42m change in centre of pressure from transonic to supersonic flight. This wing design achieves L/D=8.46 at CL=0.25, M=1.6, Re/m=6.6x10^6 and L/D=12.76 at CL=0.3, M=0.85, Re/m=6.6x10^6 which is remarkable performance given the 70% reduction in centre of pressure movement. It is hypothesized that further planform and wing thickness alterations might allow a wing design with almost insignificant difference in centre of pressure between two specified subsonic and supersonic flight conditions.

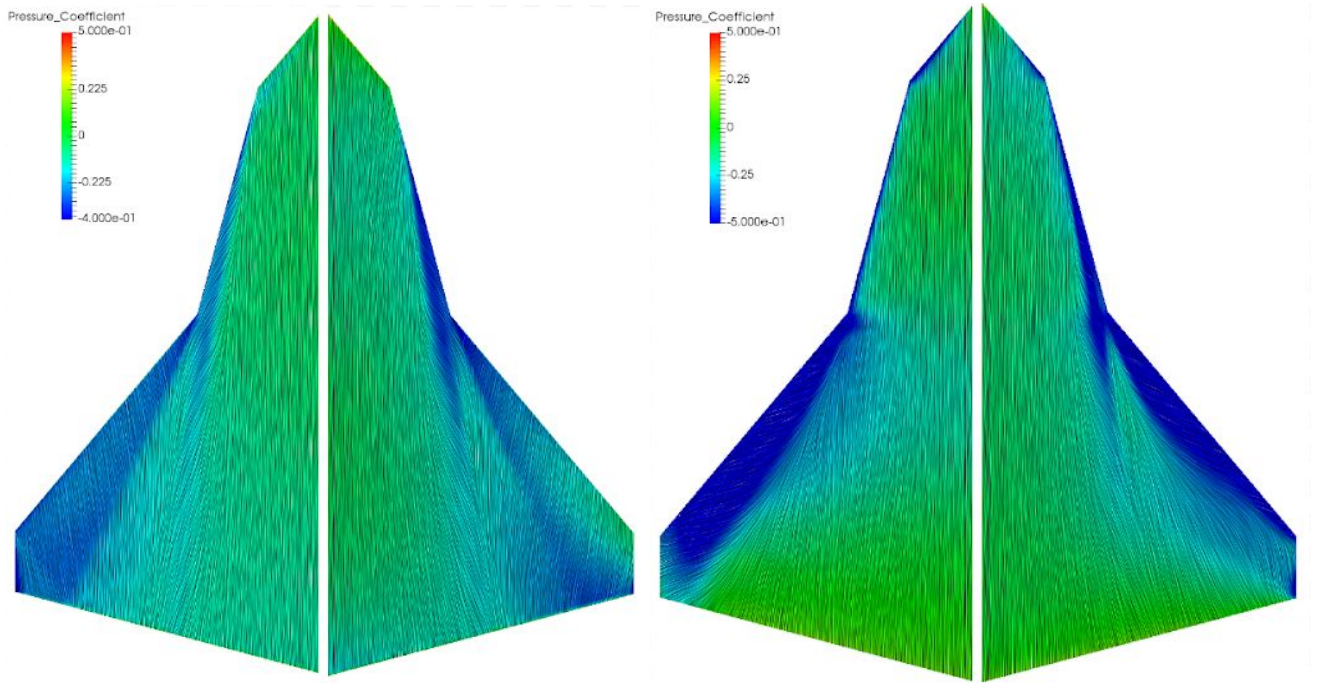

A. Uncambered B. Novel Design C. Uncambered D. Novel Design

Fig 4.130 RANS surface flows at M=1.6, CL=0.25, Re/m=6.6x10^6 (left) and M=0.85, CL=0.3, Re/m=6.6x10^6 (right)

Figure 4.130 demonstrates the lee-side surface flows of the novel cranked wing design at the supersonic and transonic design points and compares them with those of the uncambered cranked wing.

At the supersonic manoeuvre flight state, the novel wing design has a very similar surface flow pattern to the minimum drag design shown earlier, except for having slightly stronger cross-flow shockwaves and a slightly modified loading along the trailing edge. At the transonic flight state, the flow pattern on the surface of the novel design is quite different to that of the uncambered wing. The separation and subsequent vortical flow forms almost exactly the same structure at the 75 degree leading edge irrespective of whether it is transonic or supersonic. On the outboard section of the wing, a single strong shockwave has been replaced with two smaller shockwaves, one meeting the wingtip near the leading edge and another meeting the wingtip at the trailing edge. The leading edge flow on the outboard section of the wing is separated in both cases and reattaches just downstream of the first shockwave it passes.

Chapter 5 Conclusions

A simple lift constrained adjoint optimisation strategy has been presented and compared with another widely used adjoint optimisation constraint strategy, using Mason *et al*'s supersonic conical cambered wing as a test case. This method produced a conical wing with CDp=0.0569 at CL=0.4 in inviscid supersonic flow M=1.62 compared with CDp=0.0626 for the initial flat wing at the same lifting coefficient and Mach number, providing a 9.1% reduction in pressure drag. The 'soft' constrained optimisation strategy required less running time than the hard constrained strategy to reach a converged design solution; 28 hours instead of 46.8 hours - a substantial saving of 39.25% when run using the same number of CPU cores. The 'soft' method also produced a marginally better design (1 drag count) with similar geometrical characteristics, therefore confirming that it is the most efficient method for imposing a lift constraint in the supersonic adjoint optimisation case studied in this thesis. For this reason, the 'soft' method for imposing lift constraints was used for the remainder of the wing designs in the thesis.

RANS was used to evaluate the performance of the soft-constrained optimised wing, the initial flat wing and Mason et al's supersonic conical cambered manoeuvre wing. The adjoint optimum design had the highest performance of any of the wing designs investigated using RANS, with CD=0.06226 - improving upon the flat wing drag by 8.98% or 61 drag counts and Mason *et.al'*s minimum drag design by 2.12% or 13.5 drag counts. This demonstrated one of the many advantages of the adjoint numerical optimisation method over other wing design methods.

The soft constrained optimisation method was utilised to produce minimum pressure-drag camber designs for two supersonic wing planforms with fixed NACA 64A004 thickness distributions, providing a significant increase in the performance of each wing. The effect of planform on wing performance at supersonic speeds is found to be substantial with an 8.5% difference in drag between each planform with uncambered aerofoil. It is also found that the performance gained from camber optimisation is greater in the case of the cranked wing planform, with the trapezoid wing achieving a 3% drag reduction and the cranked wing achieving a 5.2% drag reduction. These designs can be seen as having the minimum pressure drag for their given planform shape, aerofoil thickness distribution and lifting coefficient. They were subsequently used as a benchmark to evaluate the performance of wings which are designed with additional constraints, as a manner of ascertaining the performance penalty of these additional constraints.

As with the conical wing drag reduction study, it has been found that a major source of drag at this Mach number was embedded crossflow shockwaves; which were reduced substantially by the adjoint optimisation process. It has also been found, however, that in a similar way to the conical wing, the minimum drag wings do indeed still feature weak crossflow shockwaves. It can be ascertained from this that other sources of pressure drag become equally as important as shockwave drag as the size of the shockwave reduces. A tradeoff has been made between embedded crossflow shock intensity and lift-induced or wingtip drag.

Additional hard constraints were then added to the soft constrained optimisation strategy in order to control the pitching moment of optimised wing designs. Designs were produced with CMy constrained

at both the supersonic manoeuvring design point and a transonic cruise condition. The design histories and final results showed that planform shape has a very strong effect on the ability of the camber design to satisfy constraints and improve performance of supersonic wings.

For both planforms, the minimum drag geometries produce similar Xcp locations to the uncambered wings at both the supersonic design condition and the transonic cruise condition. In general, the trapezoid wings experienced an Xcp shift of around 1.5m between flight states and the cranked wings experienced an Xcp shift of around 1.2m between flight states.

The wings which were designed using only a supersonic pitching moment constraint both have near-zero CMy (and therefore no trim requirement) at the supersonic manoeuvre condition, however they have the furthest forward Xcp values at the transonic condition of any of the designs due to their high degree of reflex camber, making them unstable in the transonic cruise condition with a large trim requirement.

The wings which were designed using two pitch constraints both achieved better performance values than the wings optimised with only one pitch constraint - potentially suggesting that they were forced to explore different regions of the design space in an attempt to satisfy all constraints and subsequently found more globally optimised shapes. Of the wings which were designed with both supersonic and transonic pitching moment constraints, only the cranked planform design can be seen as having come close to satisfying the pitch moment constraints.

It is found that a cranked or LERX planform, when optimised using the multipoint-constrained adjoint method, is capable of high performance with only 0.42m change in centre of pressure location from transonic to supersonic flight. This wing design achieves L/D=8.46 at CL=0.25, M=1.6, Re/m=6.6×10^{6} and L/D=12.76 at CL=0.3, M=0.85, Re/m=6.6×10^{6} with a 70% reduction in centre of pressure movement. In comparison, the minimum pressure drag wing of the same planform achieves L/D=8.74 at the supersonic condition and L/D=13.51 at the transonic condition. From this one can conclude that the penalty for 70% reduction in centre of pressure movement is a 3.2% decrease in performance (L/D) at the supersonic manoeuvre condition and a 5.5% decrease in performance at the transonic cruise condition. It is therefore hypothesized that further planform and wing thickness alterations might allow a wing design with almost insignificant difference in centre of pressure between two specified subsonic and supersonic flight conditions, with only marginal further performance penalties.
In summary, an adjoint-based lift-constrained optimisation strategy has been presented and shown to produce better conical supersonic manoeuvre wing designs than were designed through historical methods. This method was also found to require 39.25% less computational time than another widely used adjoint-based constrained optimisation strategy. Minimum pressure drag camber designs were found for two supersonic manoeuvre wing concepts using the previously presented lift-constrained adjoint optimisation strategy, revealing a balance between various sources of drag. Pitching moment constraints were then added to the optimisation process resulting in a novel camber design which has good supersonic and transonic performance with a difference of only 0.01244 in pitching moment coefficients between these two states. This trade-off between performance and stability was analysed and found to be a good design solution.

Future work

Some suggestions have been made as to directions for future studies below:

- RANS based optimisation of supersonic manoeuvre wings to include all physics.

It has been shown in this thesis that viscous effects have a significant impact on the flow fields around supersonic manoeuvre wings, causing features like shock-induced separation and boundary layer growth. The presence of subsonic boundary layers in the supersonic flow solution also present an interesting challenge for the adjoint solver; since the regions of influence in supersonic flow and subsonic flow are highly different - supersonic is downstream, with region of influence lying within Mach cones; whilst subsonic is both upstream and downstream, with regions of influence extending throughout the entire flow solution.

During the course of this project, the author was able to reliably calculate RANS discrete adjoint solutions for the conical supersonic manoeuvre wing case, meaning that this is a feasible route of exploration. However, the authors progress in using these solutions for optimisation was hampered by difficulties in deforming RANS boundary layer grids. For this reason those results have not been included in this thesis.

Successfully including these viscous effects in the design process might result in wings which have more efficiently balanced pressure and skin friction drag coefficients; as it has also been shown in this thesis that for the cases studied; minimum pressure drag wings usually had higher skin friction drag than the initial uncambered wings.

- Changes in thickness distribution and planform shape may still yield better wing designs

In this thesis, only wing camber has been used as a design variable for detailed surface parameterisation. It has been shown that wing camber can have a significant effect on the drag of the supersonic manoeuvre wing; however, it is hypothesised that further changes in planform and thickness distribution would yield even better wing designs due to increased design space.

- Pitching moment could be combined with drag as an objective function in order to reduce the number of hard constraints even further.

Combined objective functions could be implemented here in order to further reduce the computational expense of solving multiple adjoint solutions at the same flight condition, however would not reduce the expense of solving constraint functions at off-design flight conditions. It would also be interesting to try a minimisation of |CMy(supersonic)-CMy(transonic)| as an objective function with no other constraints in order to truly understand the fluid mechanics and performance tradeoffs associated with supersonic wings with no pitch trim requirements.

- More complete control of both transonic and supersonic pitching moment polars should be sought.

It has been found that in cases where both transonic and supersonic pitching moments were reduced to near-zero at the design points, the transonic pitching moment polar becomes unstable. This is detailed in figure 4.128, where it is clear that the nose-up pitching moment increases as the lift coefficient increases - which is undesirable in aircraft design. It should be investigated whether or not

it is possible to design a wing which has no difference in pitching moments between transonic and supersonic flight but also is stable throughout the entire flight envelope.

- Seeking more complete understanding of the link between crossflow shockwave drag, pressure drag associated with lift distribution and skin friction drag.

In this thesis a recurring theme has been the relationship between crossflow shockwave drag and lift induced drag. The ideal balance between these two forms of drag has been found for wings with high lifting coefficients, however further understanding of the relationship between them would potentially yield wing designs with even more favourable characteristics. Using an inverse design method with spanwise pressure coefficient distribution modes as targets in a conical supersonic wing case might yield better understanding.

References

[1] Kraft, D. “A Software Package for Sequential Quadratic Programming.” 1988.
[2] Jameson, A. “Aerodynamic Design via Control Theory.” Journal of scientific computing, Vol. 3, No. 3, 1988, pp. 233–260.
[3] Jameson, A., Shankaran, S., and Martinelli, L. “Continuous Adjoint Method for Unstructured Grids.” AIAA Journal, Vol. 46, No. 5, 2008, pp. 1226–1239.
[4] Jameson, A. “Control Theory for Optimum Design of Aerodynamic Shapes.” 29th IEEE Conference on Decision and Control. 1990. http://dx.doi.org/10.1109/cdc.1990.203571.
[5] Jameson, A. “Optimum Aerodynamic Design Using CFD and Control Theory.” 12th Computational Fluid Dynamics Conference. 1995. http://dx.doi.org/10.2514/6.1995-1729.
[6] Reuter, J., and Jameson, A. “Control Theory Based Airfoil Design for Potential Flow and a Finite Volume Discretization.” 1994. 32nd Aerospace Sciences Meeting and Exhibit. http://dx.doi.org/10.2514/6.1994-499.
[7] Reuther, J., and Jameson, A. “Aerodynamic Shape Optimization of Wing and Wing-Body Configurations Using Control Theory.” 1995. 33rd Aerospace Sciences Meeting and Exhibit. http://dx.doi.org/10.2514/6.1995-123.
[8] Jameson, A., and Reuther, J. “Control Theory Based Airfoil Design Using the Euler Equations.” 5th Symposium on Multidisciplinary Analysis and Optimization. 1994. http://dx.doi.org/10.2514/6.1994-4272.
[9] Jameson, A., Alonso, J., Reuther, J., Martinelli, L., and Vassberg, J. “Aerodynamic Shape Optimization Techniques Based on Control Theory.” 29th AIAA, Fluid Dynamics Conference. 1998. http://dx.doi.org/10.2514/6.1998-2538.
[10] Jameson, A. “Optimum Transonic Wing Design Using Control Theory.” IUTAM Symposium Transsonicum IV. 2002. 253–264. http://dx.doi.org/10.1007/978-94-010-0017-8_39.
[11] Jameson, A. Research Institute for Advanced Computer Science (U.S.). “A Comparison of Design Variables for Control Theory Based Airfoil Optimization.” 1995.
[12] Hicks, R. M. and Henne, P. A. “Wing Design by Numerical Optimization.” Journal of aircraft, Vol. 15, No. 7, 1978, pp. 407–412.
[13] Coppin, J. and Qin, N. “Adjoint Based Aerodynamic Optimisation of a UCAV.” 2013. 51st AIAA Aerospace Sciences Meeting including the New Horizons Forum and Aerospace Exposition https://doi.org/10.2514/6.2013-146
[14] Qin, N., Wong, S. and Le Moigne, A. “Adjoint-Based Optimisation of a Blended Wing Body Aircraft with Shock Control Bumps.” 2007. 45th AIAA Aerospace Sciences Meeting and Exhibit. doi: 10.2514/6.2007-57
[15] Hinchliffe, B. and Qin, N. “Using Surface Sensitivity from Mesh Adjoint for Transonic Wing Drag

Reduction.” AIAA Journal, Vol. 55, No. 3, 2017, pp. 818–831.
[16] Le Moigne, A. and Qin, N. “Variable-Fidelity Aerodynamic Optimization for Turbulent Flows Using a Discrete Adjoint Formulation.” AIAA Journal, Vol. 42, No. 7, 2004, pp. 1281–1292.
[17] Zhu, F. and Qin, N. “Using Mesh Adjoint for Shock Bump Deployment and Optimisation on Transonic Wings.” 2015. 53rd AIAA Aerospace Sciences Meeting. http://dx.doi.org/10.2514/6.2015-1488.
[18] Hinchliffe, B. L. and Qin, N. “Using Surface Sensitivity from Mesh Adjoint Solution for Transonic Wing Drag Reduction.” 2016. 54th AIAA Aerospace Sciences Meeting. http://dx.doi.org/10.2514/6.2016-0560.
[19] Vivarelli, G. Qin, N. and Shahpar, S. “Combined Hessian and Adjoint Error-Based Anisotropic Mesh Adaptation for TurboMachinery Flows.” 2017. 55th AIAA Aerospace Sciences Meeting. http://dx.doi.org/10.2514/6.2017-1946.
[20] Mura, G. L. Hinchliffe, B. L. Qin, N. and Brezillon, J. “Effect of Non-Consistent Mesh Movements and Sensitivities on a Discrete Adjoint Based Aerodynamic Optimization.” 55th AIAA Aerospace Sciences Meeting. 2017. http://dx.doi.org/10.2514/6.2017-0461.
[21] Mura, G. L. Hinchliffe, B. L. Qin, N. and Brezillon, J. “Nonconsistent Mesh Movement and Sensitivity Calculation on Adjoint Aerodynamic Optimization.” 2018. AIAA Journal. 4. Volume 56, 1541–1553. http://dx.doi.org/10.2514/1.j055904.
[22] Le Moigne, A. and Qin, N. “Aerofoil Profile and Sweep Optimisation for a Blended Wing-Body Aircraft Using a Discrete Adjoint Method.” 2006. The Aeronautical Journal. 1111. Volume 110, 589–604. http://dx.doi.org/10.1017/s0001924000001457.
[23] Vivarelli, G., Qin, N., Shahpar, S. and Radford, D. “Efficient Adjoint-Based Mesh Adaptation Applied to Turbo-Machinery Flows.” 2019. TurboMachinery Volume 2C. http://dx.doi.org/10.1115/gt2018-77066.
[24] Wong, W. S., Le Moigne, A. and Qin, N. “Parallel Adjoint-Based Optimisation of a Blended Wing Body Aircraft with Shock Control Bumps.” 2016. The Aeronautical Journal. 1117. Volume 111, 165–174. http://dx.doi.org/10.1017/s0001924000004425.
[25] Mura, G. L., Hinchliffe, B. L., Qin, N., and Brezillon, J. “Efficient Method to Eliminate Mesh Sensitivity in Adjoint-Based Optimization.” 2018. AIAA Journal. 4. Volume 55, 1140–1151. http://dx.doi.org/10.2514/1.j055212.
[26] Reuther, J., Alonso, J. J., Rimlinger, M. J. and Jameson, A. “Aerodynamic Shape Optimization of Supersonic Aircraft Configurations via an Adjoint Formulation on Distributed Memory Parallel Computers.” Computers & fluids, Vol. 28, No. 4-5, 1999, pp. 675–700.
[27] Munguia, B. C., Economon, T. D., and Alonso, J. J. “A Discrete Adjoint Framework for Low-Boom Supersonic Aircraft Shape Optimization.” 2017.18th AIAA/ISSMO Multidisciplinary Analysis and Optimization Conference, https://doi.org/10.2514/6.2017-3326
[28] Nadarajah, S. K., Jameson, A., and Alonso, J. J. “An Adjoint Method for the Calculation of Non-Collocated Sensitivities in Supersonic Flow.” 2009. Computational Fluid and Solid Mechanics. 921–925. http://dx.doi.org/10.1016/b978-008043944-0/50804-0.
[29] Nadarajah, S. K., Jameson, A., and Alonso, J. “Adjoint-Based Sonic Boom Reduction for Wing-Body Configurations in Supersonic Flow.” 2005. Canadian Aeronautics and Space Journal. 4. Volume 51, 187–199. http://dx.doi.org/10.5589/q05-014.
[30] Kim, H.-J., Sasaki, D., Obayashi, S., and Nakahashi, K. “Aerodynamic Optimization of Supersonic Transport Wing Using Unstructured Adjoint Method.” AIAA Journal, Vol. 39, 2001, pp. 1011–1020.
[31] Hu, R., Jameson, A., and Wang, Q. “Adjoint-Based Aerodynamic Optimization of Supersonic Biplane Airfoils.” Journal of aircraft, Vol. 49, No. 3, 2012, pp. 802–814.
[32] Nadarajah, S., Jameson, A., and Alonso, J. “Sonic Boom Reduction Using an Adjoint Method for Wing-Body Configurations in Supersonic Flow.” 2002. 9th AIAA/ISSMO Symposium on Multidisciplinary Analysis and Optimization https://doi.org/10.2514/6.2002-5547
[33] Miller, D. S., Mason, W. NASA Scientific and Technical Information Branch. “Pressure and Force

Data for a Flat Wing and a Warped Conical Wing Having a Shockless Recompression at Mach 1.62." 1981.
[34] Stanbrook, A., and Squire, L. C. "Possible Types of Flow at Swept Leading Edges." Aeronautical Quarterly, Vol. 15, No. 01, 1964, pp. 72–82.
[35] Squire, L. C. "Leading-Edge Separations and Cross-Flow Shocks on Delta Wings." AIAA Journal, Vol. 23, No. 3, 1985, pp. 321–325.
[36] Miller, D. S., and Wood, R. M. "Leeside Flows over Delta Wings at Supersonic Speeds." Journal of aircraft, Vol. 21, No. 9, 1984, pp. 680–686.
[37] Squire, L. C. "Flow Regimes over Delta Wings at Supersonic and Hypersonic Speeds." Aeronautical Quarterly, Vol. 27, No. 01, 1976, pp. 1–14.
[38] Ghorai, C. "Leading-Edge Vortices and Shock-Detachment Flow over Delta Wings." Journal of aircraft, Vol. 6, No. 3, 1969, pp. 228–232.
[39] Economon, T. D., Palacios, F., Copeland, S. R., Lukaczyk, T. W., and Alonso, J. J. "SU2: An Open-Source Suite for Multiphysics Simulation and Design." AIAA Journal, Vol. 54, No. 3, 2016, pp. 828–846.
[40] Boeing: "Autonomous Systems - X37B." https://www.boeing.com/defense/autonomous-systems/x37b/index.page. Accessed 01/2020.
[41] BAe Systems. "Combat Air Strategy." https://www.baesystems.com/en/product/combat-air-strategy. Accessed 01/2020.
[42] Stallings, R. "Low Aspect Ratio Wings at High Angles of Attack." AIAA Journal, Hampton, Virginia, 1986.
[43] Miller, D. S., Wood, R. M. "Lee-Side Flow over Delta Wings at Supersonic Speeds." 1985. Langley Research Center.
[44] Wood, R. M., Miller, D. S. "Experimental Investigation of Leading-Edge Thrust at Supersonic Speeds." 1983. National Aeronautics and Space Administration, Scientific and Technical Information Branch.
[45] Wood, R. M. "Influence of Airfoil Geometry on Delta Wing Leading-Edge Vortices and Vortex-Induced Aerodynamics at Supersonic Speeds." 1992. NASA Technical Paper 3105.
[46] Hadidoolabi, M., and Ansarian, H. "Computational Investigation of Vortex Structure and Breakdown over a Delta Wing at Supersonic Pitching Maneuver." Journal of the Brazilian Society of Mechanical Sciences and Engineering, 2018.
[47] Mason, W. Written Correspondence, 2017.
[48] Mason, W. "SC3 - A Wing Concept for Supersonic Maneuvering." AIAA Applied Aerodynamics Conference. 1983. http://dx.doi.org/10.2514/6.1983-1858.
[49] Middleton, W. D., and Carlson, H. W. "Numerical Method of Estimating and Optimizing Supersonic Aerodynamic Characteristics of Arbitrary Planform Wings." 1967. Journal of Aircraft. 4. Volume 2, 261–265. http://dx.doi.org/10.2514/3.43650.
[50] Miller, D., Carlson, H., and Middleton, W. "A Linearized Theory Method of Constrained Optimization for Supersonic Cruise Wing Design." 1976. Proceedings of the SCAR Conference, Part 1.
[51] Cenko, A. "Advances in Supersonic Configuration Design Methods." 1980. Journal of Aircraft. 2. Volume 17, 119–126. http://dx.doi.org/10.2514/3.57882.
[52] Pittman, J. L. "Supersonic Airfoil Optimization." 1987. Journal of Aircraft. 12. Volume 24, 873–879. http://dx.doi.org/10.2514/3.45532.
[53] Carlson, H., and Miller, D. "The Influence of Leading-Edge Thrust on Twisted and Cambered Wing Design for Supersonic Cruise." 1981. Aircraft Systems and Technology Conference. http://dx.doi.org/10.2514/6.1981-1656.
[54] Carlson, H., and Miller, D. "Numerical Methods for the Design and Analysis of Wings at Supersonic Speeds." 1974. NASA technical note 7713.
[55] Carlson, H. "A Numerical Method of Estimating and Optimizing the Supersonic Aerodynamic Characteristics of Wings of Arbitrary Planform." 1964. Transport Aircraft Design and Operations

Meeting. http://dx.doi.org/10.2514/6.1964-590.
[56] Robins, A., and Carlson, H. “High-Performance Wings with Significant Leading-Edge Thrust at Supersonic Speeds.” 1979. Aircraft Systems and Technology Meeting. http://dx.doi.org/10.2514/6.1979-1871.
[57] Mann, M., and Carlson, H. “An Assessment of Current Methods for Drag-Due-to-Lift Minimization at Supersonic Speeds.” 1991. 9th Applied Aerodynamics Conference. http://dx.doi.org/10.2514/6.1991-3302.
[58] Mason, W., and Miller, D. “Controlled Supercritical Crossflow on Supersonic Wings - An Experimental Validation.” 1980. 13th Fluid and Plasma Dynamics Conference. http://dx.doi.org/10.2514/6.1980-1421.
[59] Burgreen, G., and Baysal, O. “Three-Dimensional Aerodynamic Shape Optimization of Supersonic Delta Wings.” 1994. 5th Symposium on Multidisciplinary Analysis and Optimization. http://dx.doi.org/10.2514/6.1994-4271.
[60] Placio, F. “Stanford University Unstructured (SU2): Open Source Analysis and Design Technology for Turbulent Flows.” 2014.
[61] Schlichting, H. “Turbulent Boundary Layers at Zero Pressure Gradient.” 1951. In Boundary-Layer Theory, McGraw-Hill, p. 643.
[62] Baldwin, B., and Lomax, H. “Thin-Layer Approximation and Algebraic Model for Separated Turbulent Flows.” 1978. 16th Aerospace Sciences Meeting. http://dx.doi.org/10.2514/6.1978-257.
[63] Menter, F. R. “Two-Equation Eddy-Viscosity Turbulence Models for Engineering Applications.” 1994. AIAA Journal, Vol. 32, No. 8
[64] Menter, F. R. “Performance of Popular Turbulence Models for Attached and Separated Adverse Pressure Gradient Flows.” 1991. AIAA Journal. Volume 30, No. 8
[65] Spalart, P. R., and Allmaras, S. R. “A One-Equation Turbulence Model for Aerodynamic Flows.” 1992. 30th Aerospace Sciences Meeting and Exhibit, AIAA.
[66] Mellor, G. L., and Herring, H. J. “Two Methods of Calculating Turbulent Boundary Layer Behaviour Based on Numerical Solution of the Equations of Motion.” Presented at the Turbulent Boundary Layer Prediction Conference, Stanford, 1968.
[67] Allmaras, S. R., Johnson, F. T., and Spalart, P. R. “Modifications and Clarifications for the Implementation of the Spalart–Allmaras Turbulence Model.” 2012. Seventh International Conference on Computational Fluid Dynamics.
[68] Saad, Y., and Schultz, M. H. “GMRES: A Generalized Minimal Residual Algorithm for Solving Nonsymmetric Linear Systems.” 1986. SIAM Journal on Scientific and Statistical Computing. 3. Volume 7, 856–869. http://dx.doi.org/10.1137/0907058.
[69] Versteeg, H. K., and Malalasekera, W. “An Introduction to Computational Fluid Dynamics: The Finite Volume Method.” Pearson Education, 2007.
[70] Kong, C. “Comparison of Approximate Reimann Solvers.” University of Reading, 2011.
[71] Godunov, S. “A Finite Difference Method for the Computation of Discontinuous Solutions of the Equations of Fluid Dynamics.” Computational Mathematics (Russian), Vol. 47, 1959, pp. 357–393.
[72] Jameson, A. “Origins and Further Development of the Jameson–Schmidt–Turkel Scheme.” 2017. AIAA Journal. 5. Volume 55, 1487–1510. http://dx.doi.org/10.2514/1.j055493.
[73] Roe, P. L. “Approximate Riemann Solvers, Parameter Vectors, and Difference Schemes.” 1981. Journal of Computational Physics. 2. Volume 43, 357–372. http://dx.doi.org/10.1016/0021-9991(81)90128-5.
[74] Venkatakrishnan, V. “Convergence to Steady State Solutions of the Euler Equations on Unstructured Grids with Limiters.” Journal of computational physics, Vol. 118, No. 1, 1995, pp. 120–130.
[75] Van Leer, B. “Towards the Ultimate Conservative Difference Scheme. A Second-Order Sequel to Godunov’s Method.” 1979. Journal of Computational Physics. 1. Volume 32, 101–136. http://dx.doi.org/10.1016/0021-9991(79)90145-1.

[76] Bayliss, A., and Turkel, E. “Far Field Boundary Conditions for Compressible Flows.” 1982. Journal of Computational Physics. 2. Volume 48, 182–199. http://dx.doi.org/10.1016/0021-9991(82)90046-8.
[77] Armijo, L. “Minimization of Functions Having Lipschitz Continuous First Partial Derivatives.” 1966. Pacific Journal of Mathematics, Vol. 16, No. 1, . doi: 10.2140/pjm.1966.16.1.
[78] Nadarajah, S., and Jameson, A. “A Comparison of the Continuous and Discrete Adjoint Approach to Automatic Aerodynamic Optimization.” 2000. 38th Aerospace Sciences Meeting and Exhibit. http://dx.doi.org/10.2514/6.2000-667.
[79] Sederberg, T. W., and Parry, S. R. “Free-Form Deformation of Solid Geometric Models.” 1986. ACM SIGGRAPH Computer Graphics. 4. Volume 20, 151–160. http://dx.doi.org/10.1145/15886.15903.
[80] Chang, Y.-K., and Rockwood, A. P. “A Generalized de Casteljau Approach to 3D Free-Form Deformation.” 1994. Proceedings of the 21st annual conference on Computer graphics and interactive techniques - SIGGRAPH. http://dx.doi.org/10.1145/192161.192220.
[81] Hock, W., and Schittkowski, K. “Test Examples for Nonlinear Programming Codes.” Springer Science & Business Media, 1981. ISBN 978-3-642-48320-2

Appendix: SU2 configuration options and Python definitions

The lines in the SU2 configuration file which control the choice of governing equations are:

PHYSICAL_PROBLEM= EULER
PHYSICAL_PROBLEM= NAVIER_STOKES
MATH_PROBLEM= DIRECT

The lines in the SU2 configuration file which enable and control turbulence models are:

KIND_TURB_MODEL= SA_NEG
REYNOLDS_NUMBER= 6.6E6
REYNOLDS_LENGTH= 1.0

The line in the SU2 configuration file which enables the time discretisation method used in this work is:

TIME_DISCRE_FLOW= EULER_IMPLICIT

The lines in the SU2 configuration file which enable and control spatial discretisation methods are:

NUM_METHOD_GRAD= GREEN_GAUSS
CONV_NUM_METHOD_FLOW= JST
MUSCL_FLOW= YES
SLOPE_LIMITER_FLOW= VENKATAKRISHNAN
JST_SENSOR_COEFF= (0.5, 0.02)

The lines in the configuration file which control the boundary conditions to be used are:

MARKER_HEATFLUX= (UPPER, 0.0, LOWER, 0.0, TIP, 0.0)
MARKER_EULER= (UPPER, LOWER, TIP)
MARKER_FAR= (FAR)
MARKER_SYM= (SYM)

The example above would be for a wing with upper, lower and tip solid surfaces, a symmetry plane and a single farfield boundary in either inviscid or viscous flow. The zero values in ‘MARKER_HEATFLUX’ denote the value of heat flux at the cell faces for viscous flow solutions.

Lines in the SU2 configuration file which enable fixed-CL mode and control residual tolerances are:

FIXED_CL_MODE= YES
TARGET_CL= 0.25
DCL_DALPHA= 0.047
UPDATE_ALPHA= 5
CONV_CRITERIA= RESIDUAL
RESIDUAL_REDUCTION= 9
RESIDUAL_MINVAL= -12

The lines in the SU2 configuration file which are used to control which flow based value to use as an objective or constraint function are as follows:

OBJECTIVE_FUNCTION=DRAG
OPT_OBJECTIVE=DRAG*1.0

An example of the line in the custom python script which defines constraints is as follows:

Constraints = ({'type':'ineq', 'fun':funLift, 'jac':jacLift, ‘lb’:’0.4’})

The lines in the SU2 configuration script which control the use of the adjoint method are as follows:

MATH_PROBLEM= DISCRETE ADJOINT
LINEAR_SOLVER= FGMRES
LINEAR_SOLVER_PREC= LU_SGS
OBJECTIVE_FUNCTION=DRAG
CONV_NUM_METHOD_ADJFLOW= JST
ADJ_JST_SENSOR_COEFF= (0.5, 0.02)
TIME_DISCRE_ADJFLOW= Euler_IMPLICIT
MG_ADJFLOW= NO
MUSCL_ADJFLOW= YES
CFL_REDUCTION_ADJFLOW= 0.8

The lines in the SU2 configuration file which define the shape and use of the FFD box are as follows:

DV_KIND= FFD_CAMBER
DV_MARKER= (UPPER, LOWER, TIP)
DV_PARAM= (MAIN_BOX, 1, 0); … ; (MAIN_BOX, 1, 6)
DV_VALUE= 0.0
FFD_DEFINITION= (MAIN_BOX, 0.0, 0.0, 0.0, 1.0, 0.0, -0.05, 1.0, 0.7, -0.05, 0.0, 0.0, 0.0, 0.0, 0.0, 0.0, 1.0, 0.0, 0.05, 1.0, 0.7, 0.05, 0.0, 0.0, 0.0)
FFD_SYMMETRY_PLANE= YES
FFD_DEGREE= (10, 8, 1)
FFD_CONTINUITY= NO_DERIVATIVE
FFD_COORD_SYSTEM= CARTESIAN
DEFINITION_DV= (11, 1.0 | UPPER, LOWER, TIP | MAIN_BOX, 1, 0); … ; (11, 1.0 | UPPER, LOWER, TIP | MAIN_BOX, 1, 6)

The lines in the SU2 configuration file which control the volumetric grid deformation are as follows:

DEFORM_LINEAR_SOLVER= FGMRES
DEFORM_LINEAR_SOLVER_PREC= LU_SGS
DEFORM_LINEAR_ITER= 350
DEFORM_NONLINEAR_ITER= 1
DEFORM_CONSOLE_OUTPUT= YES
DEFORM_LINEAR_SOLVER_ERROR = 1E-17
DEFORM_STIFFNESS_TYPE= INVERSE_VOLUME